

**TECHNISCHE UNIVERSITÄT MÜNCHEN**  
**LEHRSTUHL FÜR LUFTFAHRTSYSTEME**

# **Modelling and Performance Aspects of Coandă Flap Systems**

Korbinian Franz Stadlberger

Vollständiger Abdruck der von der Fakultät für Maschinenwesen der Technischen Universität München zur Erlangung des akademischen Grades eines

Doktor-Ingenieurs (Dr.-Ing.)

genehmigten Dissertation.

Vorsitzender:

Univ.-Prof. Dr.-Ing. Florian Holzapfel

Prüfer der Dissertation:

1. Univ.-Prof. Dr.-Ing. Mirko Hornung

2. apl. Prof. Dr.-Ing. Christian Breitsamter

Die Dissertation wurde am 30.06.2016 bei der Technischen Universität München eingereicht und durch die Fakultät für Maschinenwesen am 26.10.2016 angenommen.



*Leider lässt sich eine wahrhafte Dankbarkeit  
mit Worten nicht ausdrücken.*

JOHANN WOLFGANG VON GOETHE (1749-1832)

# Hintergrund der Forschung

Die folgende Arbeit entstand während der Tätigkeit als wissenschaftlicher Mitarbeiter am Lehrstuhl für Luftfahrtsysteme der Technischen Universität München. Initiiert und zu großen Teilen finanziert durch das Unternehmen Airbus Defence and Space (ehemals Cassidian) wurden im Rahmen der nationalen Forschungskoooperation „SAGITTA“ von mehreren Partnerorganisationen unterschiedlichste Technologien untersucht, die für die zukünftige Nutzung von unbemannten Flugsystemen (UAS) von Bedeutung sind. Die Schwerpunkte lagen dabei in den Bereichen Autonomie, Kommunikation (Datenverbindung) und Systementwurf von niedrig gestreckten, unkonventionellen Flugzeugkonfigurationen. Speziell auf dem letztgenannten Gebiet des Flugzeugentwurfs soll die folgende Ausarbeitung mit den darin enthaltenen Erkenntnissen einen Beitrag dazu liefern, den Reifegrad von innovativen, technischen Lösungen zu erhöhen. Durch die Verbindung der Fachdisziplinen Aerodynamik, Flugantriebe, Flugmechanik und Gesamtsystementwurf entstand somit eine ganzheitliche Machbarkeitsstudie für einen aus der Literatur entnommenen Ansatz zur „klappenlosen“ Flugsteuerung.

# Zusammenfassung

Im Kontext von klappenlosen Flugsteuerungskonzepten gewinnt die aktive Strömungskontrolle mittels gezielter Ausblasung an der Flügelhinterkante zusehends an Bedeutung. Besonders ist hier die sog. „Coandă-Klappe“ als fluidisches Flugsteuerungssystem von Interesse, welches sich den Coandă-Effekt für die Manipulation der lokalen Zirkulation zu Nutze macht. Die technische Umsetzung im Flugzeugesamtsystem schließt jedoch grundsätzlich mehrere interagierende Subsysteme wie Triebwerk, Leitungssystem sowie die Coandă-Klappe selbst mit ein. Für deren gesamtheitliche Leistungsbeurteilung bietet diese Arbeit eine Modellierungskette, die den Anforderungen des Vorentwurfstadiums gerecht wird. Zu diesen zählen Robustheit, ausreichende Genauigkeit, geringe Berechnungsdauer und Automatisierbarkeit.

Der einleitende Überblick über den aktuellen Stand der Forschung beschreibt zunächst die relevanten Strömungsphänomene und deren messbare Wirkung auf aerodynamische Steuerkräfte und -momente, sowie den Einfluss von Entwurfsparametern und Umgebungsbedingungen. Die anschließende Diskussion über numerische Modellierungsversuche von Coandă-Profilen aus der Literatur legt die gewählte 2,5D-Modellierungsstrategie fest. Darin werden mittels eines eigens implementierten RANS-Finite-Volumen-Verfahrens mit modifiziertem Turbulenzmodell (Menter SST) automatisiert berechnete Profilpolare in einer weiterentwickelten potentialtheoretischen „Profilkrümmungsmethode“ (VLM) weiterverarbeitet. Dadurch können die aerodynamischen Steuerreaktionen auf einem (niedrig gestreckten) endlichen Flügel berechnet werden. Für die Triebwerksmodellierung liefert das mittels Skriptdateien ausgeführte, kommerzielle Programm GasTurb V12 den Einfluss der Zapfluftentnahme in allen wichtigen Betriebszuständen. Die Druckverluste durch viskose Effekte im Leitungssystem werden anhand eines quasi-eindimensionalen Finite-Volumen-Ansatzes in Verbindung mit empirischen Beziehungen abgeschätzt. Die Fusion der vorberechneten Datensätze in SIMULINK ermöglicht schließlich die flugdynamische Simulation (6 Freiheitsgrade) einer Flugzeugkonfiguration mit Coandă-Flugsteuerungssystem.

Als Anwendungsfall dient die niedrig gestreckte Nurflügelkonfiguration SAGITTA. Die Analyse der Berechnungsergebnisse erfolgt sowohl für die jeweils isolierten Subsysteme als auch für das Flugzeugesamtsystem. Für die untersuchte Konfiguration erwiesen sich die Coandă-Klappen zur Roll- und Nicksteuerung im Vergleich zu konventionellen Klappen als konkurrenzfähig. Die Giersteuerung ist mit dem neuartigen System jedoch nur eingeschränkt möglich. Eine abschließende Effizienzanalyse ergab, dass höhere Fluggeschwindigkeiten einen deutlichen Mehrverbrauch an Kraftstoff erfordern, während bei niedrigen Geschwindigkeiten ein Potential zur Einsparung identifiziert werden konnte.



TECHNISCHE UNIVERSITÄT MÜNCHEN  
INSTITUTE OF AIRCRAFT DESIGN

# **Modelling and Performance Aspects of Coandă Flap Systems**

Korbinian Stadlberger

Doctoral Thesis

Supervisor: Prof. Dr.-Ing. Mirko Hornung

2016



# Abstract

Active flow control technologies receive increased interest for flapless flight control applications. Their technical implementation inevitably consists of several interacting subsystems which have to be simulated in early design stages. Focusing on circulation control aerofoils, this document contains a set of modelling methods appropriate to meet the demands of preliminary design, as they are robustness, sufficient accuracy, computational efficiency and compatibility with automation. The application of these methods enables the substantive performance assessment of an overall aircraft system featuring flight control effectors based on the Coandă effect. Embodied sensitivity studies reveal the effect of design parameter changes on both effectiveness and efficiency.

The introductory literature review about experimental work on Coandă aerofoils describes the associated flow phenomena which occur on the blunt trailing edge, and summarises the trends in measured force and moment reactions. The subsequent discussion on related modelling approaches found in literature leads to the conclusion that a segregated 2.5D strategy is most suitable to meet the requirements of preliminary design. Hence, the results of automated two-dimensional CFD simulations of the aerofoil section flow are processed by a vortex lattice cambering method to obtain the finite wing aerodynamics. The overall system assessment additionally requires the modelling of the remaining critical subsystems, i.e. engine and duct. The engine modelling is achieved by the scripted execution of a commercial software package (GasTurb V12). The duct system is represented by a quasi-1D finite volume approach that incorporates empirical relations to account for pressure losses due to viscous effects. The 2D RANS modelling of the Coandă flap is realised through an incompressible second order finite volume method featuring a modified version of Menter's SST model for turbulence closure. The extrapolation of this 2D data set on the finite wing (of low aspect ratio) is performed by the specifically developed "Cambering Method" which relies on the Vortex Lattice Method (VLM). The assembly of all these precalculated submodel data tables in SIMULINK finally enables flight dynamics simulations (6DOF) of an aircraft configuration equipped with Coandă flaps.

The unmanned low-aspect-ratio flying wing configuration SAGITTA serves as use case for the application of the developed methods. The discussion of results is focused on the isolated submodels as well as on the overall flapless flight control system. For the tested configuration pitch and roll authority turned out to be comparable to conventional plain flaps while yaw authority is poor. In terms of fuel consumption, trim calculations revealed that the Coandă flap system is less efficient at higher velocities whereas potentials for fuel cost reduction could be identified at low velocities.



# Contents

<b>1</b>	<b>Introduction</b>	<b>1</b>
1.1	Motivation . . . . .	3
1.2	Objectives . . . . .	4
1.3	Structure of Work . . . . .	5
<b>2</b>	<b>Fundamentals of Coandă Flap Aerodynamics</b>	<b>7</b>
2.1	Wall Jet . . . . .	7
2.2	Trailing Edge Blowing and Circulation Control . . . . .	9
2.2.1	Influence of Trailing Edge Geometry . . . . .	11
2.2.2	Influence of Coandă Surface Roughness . . . . .	14
2.2.3	Influence of Slot Height . . . . .	15
2.2.4	Influence of Angle of Attack . . . . .	15
2.2.5	Stall Phenomena . . . . .	15
2.2.6	Influence of Free Stream Mach Number . . . . .	18
2.2.7	Pulsed Blowing . . . . .	19
2.2.8	Uncertainties of Wind Tunnel Experiments . . . . .	19
2.2.9	Circulation Control on Finite Wings . . . . .	20
2.3	Flying Demonstrators . . . . .	22
2.4	Modelling Approaches . . . . .	24
2.4.1	Potential Theory and Integral Methods . . . . .	24
2.4.2	Reynolds Averaged Navier-Stokes Approach (RANS) . . . . .	26
2.4.3	Large Eddy Simulation and Direct Numerical Simulation . . . . .	28
2.4.4	Conclusion for Coandă Flap Modelling . . . . .	28
<b>3</b>	<b>Coandă Flap System Modelling</b>	<b>31</b>
3.1	Investigated Coandă Flap Concept . . . . .	32
3.2	Modelling of the Engine and Bleed Air Supply . . . . .	36
3.3	Modelling of the Duct System . . . . .	38
3.3.1	Governing Equations . . . . .	38
3.3.2	Semi-Empirical Implementation . . . . .	39
3.3.3	Validation . . . . .	42
3.4	Modelling of the Coandă Aerofoil (2D) . . . . .	43
3.4.1	Governing Equations . . . . .	44
3.4.2	Baseline Turbulence Model . . . . .	45
3.4.3	Numerical Implementation . . . . .	46
3.4.4	Automatic Meshing and Calculation . . . . .	48
3.4.5	Turbulence Model Modifications . . . . .	53
3.4.6	Validation . . . . .	54
3.5	Modelling of the Finite Wing (3D) . . . . .	62
3.5.1	Governing Equations . . . . .	64

3.5.2	Calculation Procedure . . . . .	65
3.5.3	Validation . . . . .	71
3.6	Overall Modelling of the Flight Dynamic System . . . . .	73
<b>4</b>	<b>Test Case: SAGITTA</b>	<b>77</b>
4.1	Design Mission and Platform Requirements . . . . .	77
4.2	SAGITTA Configuration . . . . .	77
4.2.1	Flying Wing . . . . .	80
4.2.2	Propulsion System . . . . .	80
4.3	Conventional Reference Flap Layout . . . . .	81
4.4	Novel Coandă Flap Layout . . . . .	81
<b>5</b>	<b>Application and Discussion</b>	<b>83</b>
5.1	Preliminary Results for the Isolated Subsystems . . . . .	83
5.1.1	Intermediate Results of Engine Modelling . . . . .	83
5.1.2	Intermediate Results of Duct Modelling . . . . .	88
5.1.3	Intermediate Results of Coandă Aerofoil Modelling . . . . .	92
5.1.4	Intermediate Results of Finite Wing Reactions . . . . .	100
5.2	Final Results of the Overall System . . . . .	103
5.2.1	Pitch Authority . . . . .	104
5.2.2	Roll Authority . . . . .	106
5.2.3	Yaw Authority . . . . .	107
5.2.4	Efficiency . . . . .	109
<b>6</b>	<b>Conclusion</b>	<b>117</b>
6.1	Summary of Results . . . . .	117
6.2	Applicability and Validity . . . . .	119
6.3	Outlook . . . . .	120
	<b>References</b>	<b>121</b>
	<b>Nomenclature</b>	<b>133</b>
	<b>Appendix</b>	<b>147</b>
A	Bibliography: Conducted Experiments on Coandă Aerofoils . . . . .	149
B	Bibliography: Tested Turbulence Models . . . . .	151
C	Isentropic Flow Equations . . . . .	153
D	Validation of 2D RANS Code . . . . .	155
D.1	Lid-Driven Cavity Flow . . . . .	155
D.2	Turbulent Boundary Layer on a Flat Plate . . . . .	155
D.3	Unblown Coandă Aerofoil . . . . .	156

# 1 Introduction

*“These aeroplanes we have today are no more than a perfection of a child’s toy made of paper. In my opinion, we should search for a completely different flying machine, based on other flying principles. I imagine a future aircraft, which will take off vertically, fly as usual and land vertically. This flying machine should have no moving parts.”*

This statement given by Henri Marie Coandă (1886-1972) reflects his pioneer spirit and visionary thinking (TOOREN ET AL., 2009). At a symposium in 1967, he enthused about novel possibilities which innovative technologies and their underlying physical effects can provide. As Romanian inventor and eponym of the well-known fluid dynamic effect, he designed a great number of flying devices as his ducted fan aircraft “Coandă-1910” (Figure 1.1a), or his “flying saucer” named “Aerodina Lenticulara” (COANDA, 1961). The latter just relies on this famous Coandă effect which describes the fact that jets or jet sheets are prone to attach to sufficiently close walls and even tend to follow convex contours (Figure 1.2). Inside the wall jet flow, the centrifugal force on a fluid element equals the force generated by the pressure gradient normal to the curved wall. While firstly observed and documented in the 18th century (YOUNG, 1800), this effect was exploited during the Cold War when an advanced Canadian development named “VZ-9 AV Avrocar” (Figure 1.1b) generated lift and thrust from one central turborotor. It blew the exhaust out directly above the rim of the saucer-shaped aircraft to provide vertical take-off and landing (VTOL) capabilities. Beyond this classified project, the Coandă effect has further been of interest for practical aeronautical applications as it enables the entrainment of the surrounding fluid through relatively low mass flow rates, and this without any complex mechanical parts. The research on active flow control (AFC) has become an increasingly important research field seeking to improve the cost-benefit ratio of “aerodynamic morphing”. While in Germany and Great Britain the first experiments on blown flaps were conducted already before Second World War (WILLIAMS, 1955), intensive investigations on circulation control (CC) aerofoils began only in the late 1960s (ENGLAR, 1971). This unusual aerofoil type usually features blunt rounded trailing edges with tangential jet injection into the upstream boundary layer (Figure 1.3). As the Coandă effect significantly delays the separation of the upper surface flow, these aerofoils are

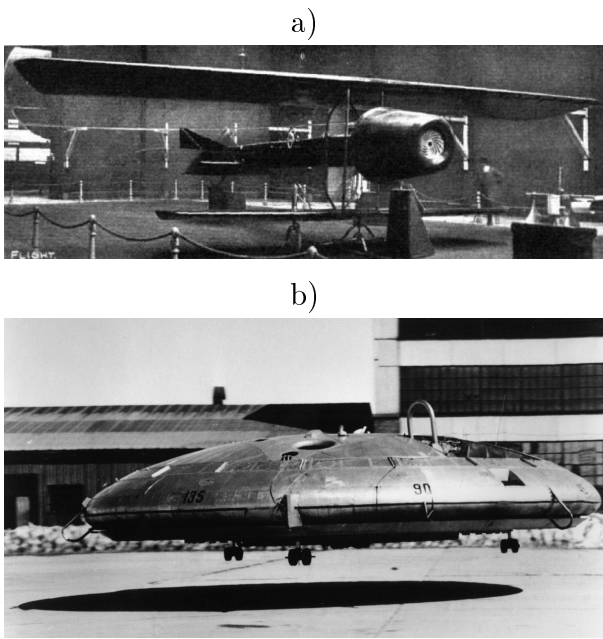


**Figure 1.1:** Turbine driven aircraft Coandă-1910 (a) (FLIGHT GLOBAL, 1910) and U.S. military project Avro Canada VZ-9 Avrocar (b) (USAF, 2008)

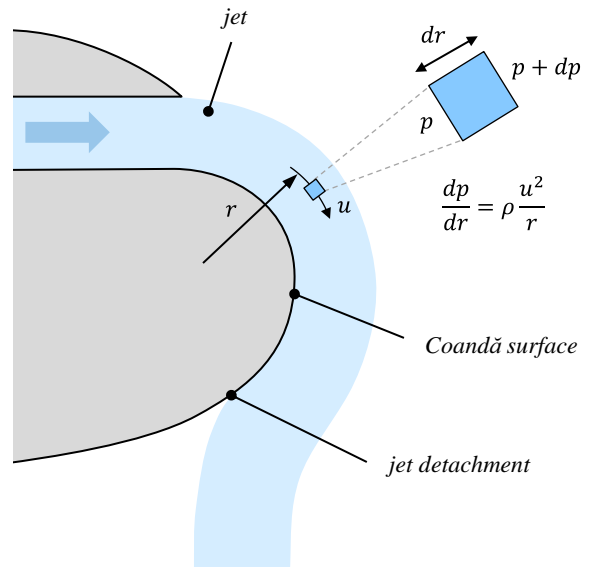


**Figure 1.2:** Illustration of Coandă effect

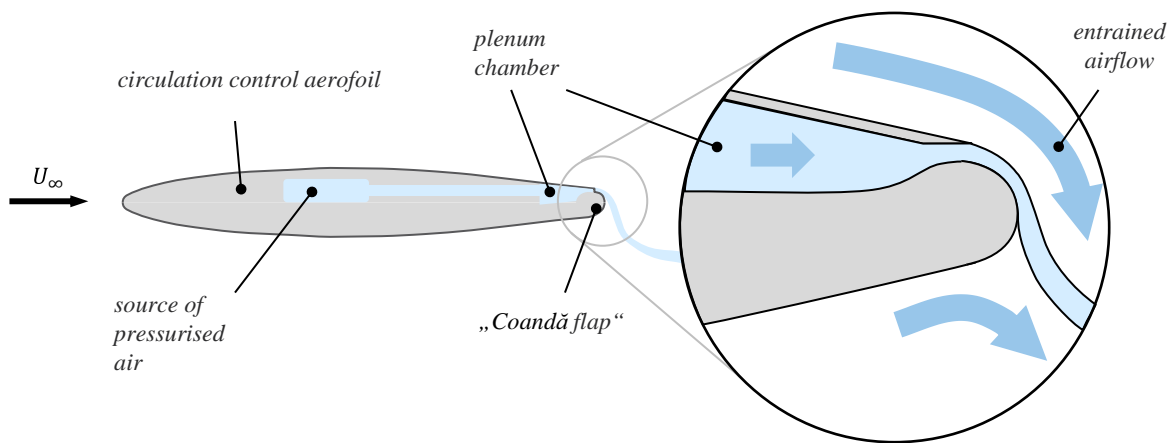


**Figure 1.3:** Illustration of a circulation control aerofoil / Coandă aerofoil (modified from STADLBERGER/HORNUNG, 2014, 2015a,b)

also often called Coandă aerofoils. As central issue of this concept, the momentum of the blowing jet controls the position of the rear stagnation point which causes a net increase in circulation around the aerofoil. Consequently, the notable gain in lift can be used for high lift system design in the field of short take-off and landing applications (STOL). While the associated high pitching moment constitutes a rather unfavourable parasite reaction for high-lift applications, it is particularly interesting for flight control purposes. Here, the round trailing edge can act as a “Coandă flap” comprising only a low number of moving mechanical parts. In this scope of “flapless” flight control, the motive of the present study is to contribute to the research on active flow control technologies by investigating the Coandă flap as an integral part of an aircraft system. For the applicability and performance assessment of this novel concept, preliminary modelling is the key discipline whose demand will be addressed along this document. Before, the following sections further introduce into the subject of this thesis by explaining its motivation, objective and structure.

## 1.1 Motivation

As already mentioned, the motivation of this work derives from the idea to use active flow control technology for flight control purposes. In the first instance, the concept of fixed blown trailing edges is particularly interesting for military applications as it enables flapless flight control with reduced observability. Conventional flaps inevitably imply surface discontinuities and gaps which are prone to radar scattering through diffraction and reradiation of traveling waves (RAYMER, 2012, p. 239f.). Of course, the necessary Coandă jet outflow openings cannot be omitted either, and a round trailing edge actually raises the specular return compared to a sharp trailing edge. However, the slots and Coandă surfaces can be aligned such that the increment of radar cross section (RCS) is limited to directions which coincide with the azimuth angle of the naturally existing trailing edge spike.

A further motivation is related to the potential savings in the number of moving parts within an aircraft system. A decrease in complexity and weight is advantageous in all aeronautical fields of application. Even if structural design and weight estimation are not part of this study, the cutback of complex and heavy kinematics promises potential weight reductions. Omitted actuators and hydraulic lines may outweigh the newly required air ducts and pneumatic structures which can be realised through lightweight and composite materials (e.g. carbon reinforced plastics) though. In addition, significant savings in maintenance cost are expected.

However, since the Coandă flap itself is only one single part of the fluidic flight control system, the concept raises questions about its effectiveness and efficiency when it is integrated into an existing aircraft concept. While experimental investigations of the isolated system

promise a high potential in control moment generation (chapter 2), feasibility studies for tangible use cases require a broader perspective, i.e. the extension of considered system boundaries. Interacting strongly with other subsystems (e.g. propulsion system, ducts, etc.) and environmental conditions (e.g. ambient pressure, flight velocity), the Coandă flap concept necessitates an integral model of the overall system to evaluate the concept's applicability for a given aircraft configuration. Especially during the preliminary design stages, computationally cheap and robust, though sufficiently accurate, modelling methods of the overall system contribute to quick substantial conclusions about performance, penalties and their sensitivity to free design parameters. However, present tools and methods in their basic form often do not provide sufficiently precise and robust results for the rapid creation of reliable Coandă flap system models (subsection 2.4.4). Moreover, no explicit approach has been found in present literature proposing an adequate strategy to combine the different subsystem models to an overall system model. Hence, this work is motivated by the need to find enhanced solutions in the field of integral Coandă flap modelling which are supposed to raise the technology readiness level (TRL) of the studied Coandă flap concept.

## 1.2 Objectives

The first objective of this study is to respond to the lack of available preliminary design methods which are capable to model Coandă flap systems including the interaction of their critical subsystems. Therefore, the following chapters aim to present and validate an adapted set of methods appropriate to meet the demands that arise from preliminary aircraft design:

- robustness
- sufficient accuracy
- computational efficiency
- compatibility with automation

As second objective, this work is supposed to deliver insight into the sensitivities of system behaviour through variation of the main design parameters of a Coandă flap system. Here, the deduction of general design rules is to be pursued inasmuch as the specific investigated use case allows the transfer of specific results on universal applications. This test case defines the environment and aircraft platform which the Coandă flap system is to be integrated into. An all-embracing performance analysis of the overall aircraft system shall provide clarity about the feasibility of the Coandă flap concept and its fuel flow demand.

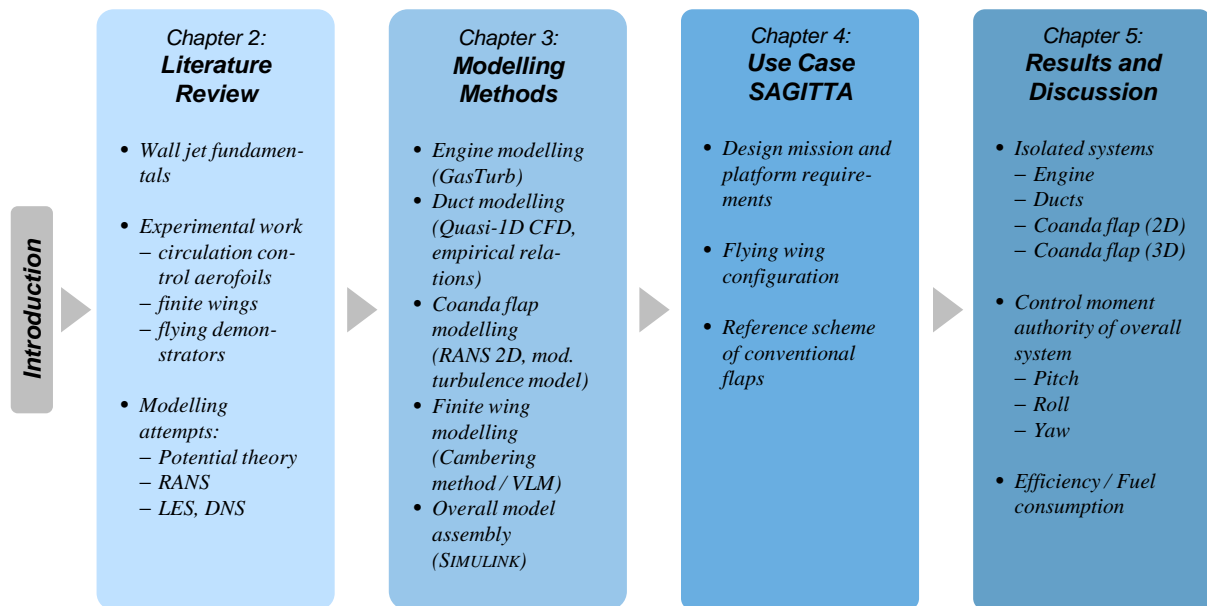


Figure 1.4: Structure of work

## 1.3 Structure of Work

As illustrated in Figure 1.4, this introductory chapter is followed by a literature review both on experimental facts and modelling methods related to Coandă flaps. Since the response and modelling of the other connected subsystems (engine, ducts) are already largely understood and straightforward, chapter 2 confines to summarising the state-of-the-art of circulation control aerofoils and the different modelling approaches as yet applied in literature. To assess these aerodynamic modelling methods in a later step, the first subsections embrace Coandă flap specific flow phenomena as well as their response in the form of aerodynamic forces and moments measured in the wind tunnel. A compressed synopsis about finite wing applications and flying demonstrators featuring fluidic circulation control systems closes the review of experimental experience. The second part of chapter 2 describes the various types of modelling attempts found in literature. They range from methods based on potential theory, over Reynolds averaged Navier-Stokes (RANS) representations up to far more computationally expensive methods as large eddy simulation (LES) and direct numerical simulation (DNS). The concluding subsection 2.4.4 finally draws the implications for the implemented modelling approach exposed in chapter 3.

In the context of flapless flight control, chapter 3 defines the critical subsystems and system boundaries of the engine, ducts and Coandă flap. The subsequent descriptions of the refined modelling methods focus on supplements and modifications that deviate from the respec-

tive sophisticated baseline methods. The underlying theoretical fundamentals are set out inasmuch as they had to be addressed during the respective implementation. The fully automated calculation routines ultimately enable the calculation of vast parameter variations. So, the assembly of precalculated data tables leads to the overall Coandă flap model which forms the base for flight mechanical (6DOF) performance assessments. The final section 3.6 further contains a summary of the most relevant assumptions and simplifications made for the overall system modelling.

Chapter 4 illustrates the use case for the previously presented methods and portrays the context of the SAGITTA research program. It includes the design mission as well as the concept of an unmanned flying wing configuration featuring a low aspect ratio. The most substantial requirements to be fulfilled by the flapless alternative can be derived from a conventional flap scheme which builds the reference for the subsequent performance analysis of the Coandă flap system.

In the context of SAGITTA, chapter 5 presents and discusses the results for the isolated submodels as well as for the overall flight dynamic model. Hence, while the first sections give insight into the subsystem sensitivities to design parameters, the second part of this chapter addresses the control authority of the installed Coandă flap in comparison to the conventional flap reference. The final study on fuel consumption and efficiency quantifies the penalties for low observable flapless flight.

# 2 Fundamentals of Coandă Flap Aerodynamics

The following literature review first portrays the experimental findings about the so called wall jet. This crucial flow phenomenon on the Coandă surface of a circulation control aerofoil is responsible for lift and pitching moment increments generated through trailing edge blowing. Subsequently, a synopsis of significant factors affecting Coandă aerofoil effectiveness is derived from published wind tunnel experiments. Further presentations of finite wing experiments and flying demonstrators complete the state-of-the-art before different approaches to model circulation control aerofoils are analysed. The final section of this chapter draws important conclusions for the modelling strategy pursued in chapter 3.

## 2.1 Wall Jet

As recurrent mechanism on all blown Coandă aerofoils, the internal, pressurised air leaves the upper slot with height  $h_u$  having a mean velocity  $U_{jet}$  (Figure 2.1). For subsonic outflow velocities, the jet bounds to the wall (Coandă effect) and mixes with the turbulent boundary layer flow arriving from the upper side of the aerofoil. This process has its onset right at the lower slot lip edge where eddies of large length scales and high levels of vorticity amplify turbulent mixing. Since large eddies are most effective in entraining external fluid, this results in a rapid broadening of the wall jet while its shape remains similar though (WETZEL ET AL., 2009). In wide zones downstream the slot, the boundary layer then features the typical wall jet velocity profile. As illustrated in Figure 2.2, the velocity distribution constitutes a two-layer shear flow which can be divided into an inner region ( $0 < y < y_m$ ) and an outer layer ( $y_m \leq y < \delta$ ). The inner region is characterised by a similar structure compared to a conventional turbulent boundary layer which usually exhibits a viscous sublayer, a buffer layer and a layer obeying the log law. The outer shear-layer shows the characteristics of free shear flow rather than one bounded by a wall. In addition, the upper surface boundary layer and the slot lip usually cause a velocity deficit (slot lip wake) that can be seen in the velocity profiles close to the slot. Even though the associated strong turbulent diffusion potentially increases the momentum transport between inner and outer region, the growth

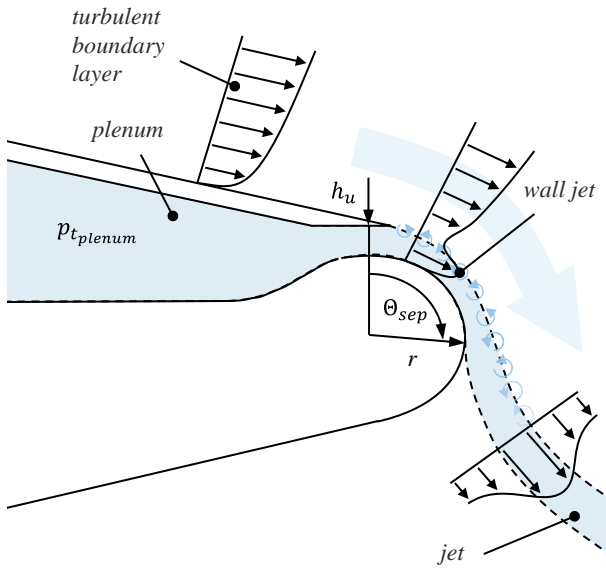


**Figure 2.1:** Illustration of outflow process and wall jet (modified from STADLBERGER/HORNUNG, 2012, 2014)

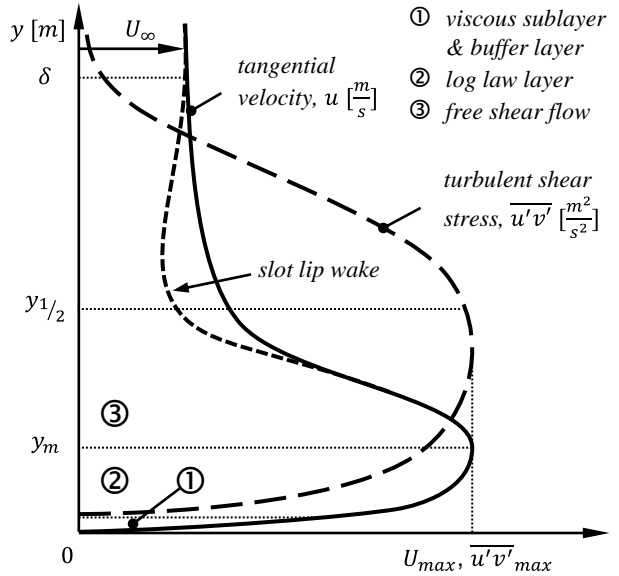


**Figure 2.2:** Typical velocity and turbulent shear stress profile of a wall jet

rate of a wall jet is significantly lower than the broadening of a jet in free shear flow. This is due to the damping of turbulent velocity fluctuations in the direction normal to the wall (LAUNDER/RODI, 1983).

In the end, however, the wall jet separates at an angle  $\Theta_{sep}$  before it aligns with the free stream. Further turbulent and viscous mixing processes alleviate the over velocities until complete assimilation in the far-field. Obviously, the point of separation depends on the integral jet momentum  $U_{jet}\dot{m}_{jet}$  ejected at the slot. However, during tests on a cylinder in still air the jet detachment angle  $\Theta_{sep}$  exhibited an asymptotic behaviour even for excessive blowing reaching maximum angles of  $\Theta_{sep} \approx 210deg$  (FEKETE, 1963). This suggests that viscous processes acting close to the Coandă surface are at least as important for jet separation as the bare blowing intensity. The separation angle  $\Theta_{sep}$  is of particular interest because it potentially defines the location of the rear stagnation point of the aerofoil flow. According to the Kutta-Joukowski theorem the generated lift and pitching moment increment of the Coandă aerofoil is supposed to respond quite sensibly to the position of jet detachment. Hence, the turbulent processes inside the wall jet are crucial for flow control effectiveness.

Considering a wall jet on a plane surface without pressure gradient, the shear stresses and associated eddy viscosities determine the development of the jet along the flat wall. In general, positive sense vorticity in the outer region acts to destabilise the flow, whereas negative sense vorticity, such as in the inner region, is highly stabilising (NOVAK ET AL.,

1987). Hence, if the momentum transport is able to expand from the velocity maximum into the viscous sublayer, the wall jet becomes stabilised and delays separation over a relatively long distance along the plane surface. External free stream additionally contributes to this stabilisation. Under conditions of external free stream instead of still air, the relative strength of the outer region and its unfavourable impact on the inner decreases due to the reduced velocity excess (LAUNDER/RODI, 1983).

In the present circulation control application, however, the turbulent wall jet experiences a convex stream line curvature around the Coandă surface (i.e. round trailing edge) as well as an adverse pressure gradient. Both intensify Reynolds stresses and turbulent mixing in the outer part of the flow (BRADSHAW/GEE, 1962; KOBAYASHI/FUJISAWA, 1983; NEUENDORF/WYGNANSKI, 1999). The increased turbulent transport between outer and inner region enhances the diffusion of the velocity excess into free stream. Hence, reduced wall jet stability has to be expected for Coandă aerofoils, aggravating with decreasing Coandă surface radius  $r$ . In general, the process of a possibly premature separation due to Coandă surface curvature is complex. The centrifugal instability due to the convex contour generates eddies of large length scales and enhances the turbulence level well beyond the norm in comparable plane wall jets (NEUENDORF/WYGNANSKI, 1999). This comes along with wall jet broadening and deceleration affecting the angle of jet detachment ( $\Theta_{sep}$ ) substantially. Furthermore, turbulence intensifies unfavourably arising from increased counter-pressure caused by external free stream arriving from the lower side of the aerofoil. While this is disadvantageous for maximum lift generation with a single-slotted aerofoil design, the premature separation could be desired for double-slotted aerofoil concepts. An opposing wall jet ejected from a lower slot enables the precise control of the separation point, thus lift and pitching moment generation. Outside the region of interaction, the flow characteristics of the curved wall jet revealed essentially the same as those of the conventional wall jets (REW/PARK, 1988). However, the thickness growth rate of both jets raise significantly when they approach the clash point.

It is particularly interesting for modelling and design purposes that the wall jet growth rate and jet separation angle exhibit only weak dependence on the jet Reynolds number (FEKETE, 1963; LAUNDER/RODI, 1983). In contrast, separation angle reductions of  $\Delta\Theta_{sep} \approx -40\text{deg}$  due to increased cylinder surface roughness could be observed (FEKETE, 1963). This suggests that surface quality of the round trailing edge is an issue for circulation control effectiveness.

## 2.2 Trailing Edge Blowing and Circulation Control

As stated in the previous section, the wall jet separation point on the bluff trailing edge is important for lift generation effectiveness. In fact, the relatively simple model of lift mani-

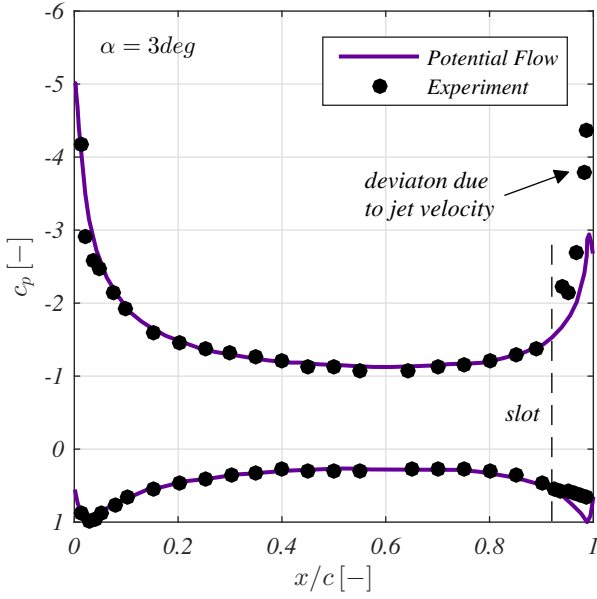


**Figure 2.3:** Experimental and potential pressure distribution of an elliptical ( $t/c = 15\%$ ) circulation control aerofoil (created with data from ENGLAR, 1971)

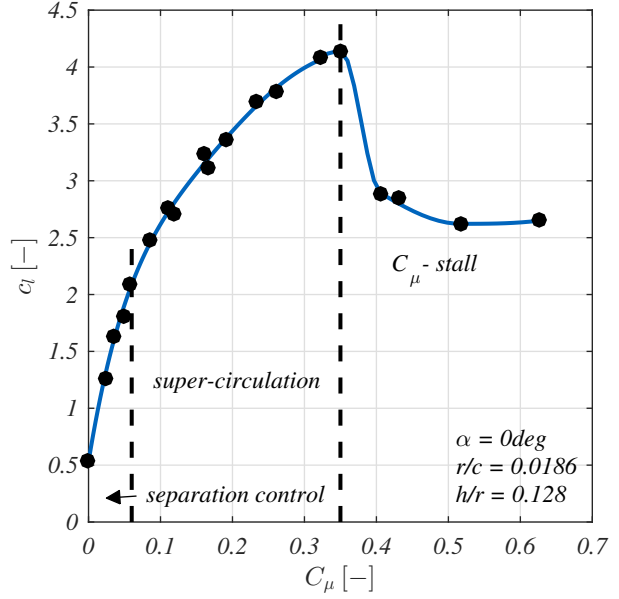


**Figure 2.4:** Lift increase due to blowing (created with data from ENGLAR, 1981)

pulation through displacement of the rear stagnation point provides quite accurate results as a first approximation. As can be seen in (Figure 2.3), separation control through tangential blowing enables viscous flow section properties very close to those predicted inviscidly by potential flow (WILLIAMS/HOWE, 1970; ENGLAR, 1971). However, some discrepancy can be found at the trailing edge downstream the slot. The jet velocity excess produces an additional suction peak which cannot be modelled by potential theory alone. In addition, the separation bubble at the lower surface trailing edge impedes the ideal inviscid pressure recovery. Nonetheless, sectional lift coefficients approaching the theoretical inviscid maximum of  $2\pi \left(1 + \frac{t}{c}\right)$  have been demonstrated (WOOD/NIELSEN, 1986). Further raise of the blowing rate causes the imaginary aft stagnation point to move towards the lower side of the Coandă aerofoil, thus enhancing the circulation through redefinition of the governing Kutta-condition. The separation control process thereby evolves into the so-called super-circulation regime (ENGLAR, 1971), where significant lift is generated even at zero angle of attack. As reproduced in Figure 2.4 and widely used in this work, it is common in literature to describe the attained aerodynamic force and moment reactions dependent on the normalised momentum flux of the outflow, i.e. the equivalent normalised thrust force. The flow momentum coefficient  $C_\mu$  therefore yields

$$C_\mu = \frac{\dot{m}_{jet} U_{jet}}{\frac{1}{2} \rho_\infty U_\infty^2 S_{ref}} \quad (2.1)$$

where  $\dot{m}_{jet}$  is the jet mass flow,  $U_{jet}$  the jet outflow velocity,  $\frac{1}{2}\rho_{\infty}U_{\infty}^2$  the free stream dynamic pressure and  $S_{ref}$  the lifting surface reference area. Usually, the dependency of produced lift  $\Delta c_l$  on the momentum coefficient  $C_{\mu}$  is approximately linear ( $\Delta c_l \sim C_{\mu}$ ) in the separation control region and clearly disproportionate ( $\Delta c_l \sim (C_{\mu})^{\frac{1}{n}}$ ,  $n \approx 2$ ) in the super-circulation regime.

During circulation control, both the forward and aft stagnation point are shifted such that the aerofoil experiences an increase in effective camber, in suction peak intensity and in associated lift. Indeed, due to super-circulation notably high lift coefficients of 8 and beyond could be measured during wind tunnel experiments (ENGLAR ET AL., 2009). However, too excessive blowing often ends up in the so-called “ $C_{\mu}$ -stall” which manifests itself in lift stagnation or even in a sudden lift drop (Figure 2.4). The causes can be manifold (e.g. leading edge separation (bubble), supersonic jet detachment, etc.) and are addressed later in subsection 2.2.5.

Numerous wind tunnel experiments on circulation control aerofoils have been performed during the past decades. A compendium is given in the appendix (section A) and contains selected published wind tunnel data including summarised geometrical specifications. In the 1960s, the beginning of extensive wind tunnel tests on elliptical circulation control aerofoils aimed to investigate the applicability of active flow control for helicopter rotors (WILLIAMS/HOWE, 1970). Cyclic blowing at the blades’ trailing edges should substitute the function of the swash plate and omit the associated complex kinematics. In addition, a vertically symmetric elliptic blade section was considered advantageous in the reverse flow regime at high advance ratios. Here, slots at both leading and trailing edge should prevent flow separation which leads to a significant base drag reduction compared to the unblown aerofoil. In terms of drag, the delay of flow detachment on the Coandă surface usually outstrips the bare jet thrust effect. Apart from rotary wing applications, Coandă aerofoils also gained increased interest in the research fields of high-lift systems and STOL aircraft design. For flight control purposes, the sensitivity of aerodynamic control reactions to geometrical and operational parameters is in the same way important as for high-lift applications. To this, the wind tunnel results of published experiments on circulation control aerofoils allow some general statements about lift generation effectiveness. Its qualitative dependencies on various parameters, in addition to blowing rate, are briefly discussed in the following paragraphs and are additionally summarised in Table 2.1.

### 2.2.1 Influence of Trailing Edge Geometry

The Coandă effect is limited by several parameters. One of them is the curvature of the Coandă surface the jet is supposed to bend around. Under subsonic flow conditions, constant (circular) trailing edge radii reach higher lift augmentations  $\frac{\partial \Delta c_l}{\partial C_{\mu}}$  and higher maximum

**Table 2.1:** Summary of qualitative circulation control sensitivities

	lift $c_l$	drag $c_d$	pitching moment $c_m$
Coandă surface geometry	<ul style="list-style-type: none"> <li>Circular trailing edges obtain higher <math>\frac{\partial \Delta c_l}{\partial C_\mu}</math> and higher <math>(\Delta c_l)_{max}</math> in subsonic free stream.</li> <li>Slender elliptical and biconvex trailing edges are more efficient in transonic free stream.</li> <li>The larger the trailing edge radius (<math>\frac{r}{c}</math>), the higher <math>\frac{\partial \Delta c_l}{\partial C_\mu}</math> and <math>(\Delta c_l)_{max}</math>.</li> <li>Strong curvatures increase the risk of supersonic jet detachment, i.e. <math>C_\mu</math>-stall.</li> </ul>	<ul style="list-style-type: none"> <li>Slender trailing edges (elliptic, biconvex) exhibit reduced drag.</li> <li>Strong curvatures increase the risk of supersonic jet detachment, i.e. sudden drag rise.</li> </ul>	<ul style="list-style-type: none"> <li>Circular trailing edges obtain higher <math>\frac{\partial  \Delta c_m }{\partial C_\mu}</math> and higher <math>( \Delta c_m )_{max}</math> in subsonic free stream.</li> <li>Slender elliptical and biconvex trailing edges are more efficient in transonic free stream.</li> <li>Strong curvatures increase the risk for supersonic jet detachment, i.e. sudden drop of <math> \Delta c_m </math>.</li> </ul>
aerofoil nose geometry	<ul style="list-style-type: none"> <li>Sharp nose geometries risk leading edge separation (bubbles) at moderate/high blowing rates and reduce <math>\frac{\partial \Delta c_l}{\partial C_\mu}</math> and <math>(\Delta c_l)_{max}</math>.</li> </ul>	<ul style="list-style-type: none"> <li>Sharp nose radii provoke leading edge separation (bubbles) at moderate/high blowing and increase drag.</li> </ul>	<ul style="list-style-type: none"> <li>Sharp nose geometries risk leading edge separation (bubbles) and influence pitching moment significantly.</li> </ul>
angle of attack	<ul style="list-style-type: none"> <li>The influence of moderate and negative angles of attack is small.</li> <li>Higher angles of attack reduce <math>\frac{\partial \Delta c_l}{\partial C_\mu}</math>.</li> </ul>	<ul style="list-style-type: none"> <li>The influence of moderate and negative angles of attack is small.</li> <li>Earlier separation (bubbles) at increasing angles of attack increase drag.</li> </ul>	<ul style="list-style-type: none"> <li>The influence of moderate and negative angles of attack is small.</li> <li>Earlier separation (bubbles) at increasing angles of attack influence pitching moment.</li> </ul>
slot height	<ul style="list-style-type: none"> <li>The smaller the slot height, the higher <math>\frac{\partial \Delta c_l}{\partial C_\mu}</math>.</li> <li>Larger slot heights increase risk of supersonic jet detachment, i.e. <math>C_\mu</math>-stall.</li> </ul>	<ul style="list-style-type: none"> <li>At low blowing momentum, only small influence is visible.</li> <li>At higher blowing condition, the influence tends to grow but no clear trend visible (dependence on turbulent mixing processes).</li> <li>Larger slot heights increase risk of supersonic jet detachment where drag rises significantly.</li> </ul>	<ul style="list-style-type: none"> <li>The smaller the slot height, the higher <math>\frac{\partial \Delta c_m}{\partial C_\mu}</math>.</li> <li>Larger slot heights increase risk of supersonic jet detachment, i.e. sudden drop of <math> \Delta c_m </math>.</li> </ul>
free stream compressibility	<ul style="list-style-type: none"> <li>Increasing the free stream Mach number <math>Ma_\infty</math> tends to increase <math>\frac{\partial \Delta c_l}{\partial C_\mu}</math>.</li> <li>Due to the risk of supersonic jet detachment, the maximum lift generation <math>(\Delta c_l)_{max}</math> diminishes with increasing free stream Mach number <math>Ma_\infty</math>.</li> </ul>	<ul style="list-style-type: none"> <li>The drag rise due to Mach number <math>Ma_\infty</math> is also present on circulation control aerofoils.</li> </ul>	<ul style="list-style-type: none"> <li>Increasing the free stream Mach number <math>Ma_\infty</math> tends to increase <math>\frac{\partial \Delta c_m}{\partial C_\mu}</math>.</li> <li>Due to the risk of supersonic jet detachment, the maximum pitching moment generation <math>(\Delta c_m)_{max}</math> diminishes with increasing free stream Mach number <math>Ma_\infty</math>.</li> </ul>
jet compression-ability	<ul style="list-style-type: none"> <li>Even though certain slot geometries and weak Coandă surface curvatures can alleviate the problem, supersonic jets tend to suddenly detach at certain Mach numbers <math>Ma_{jet} \gtrsim 1.2</math> of the fully expanded jet. Sudden lift loss is the consequence.</li> </ul>	<ul style="list-style-type: none"> <li>Supersonic jet detachment entails a sudden drag rise.</li> </ul>	<ul style="list-style-type: none"> <li>Supersonic jet detachment leads to a sudden loss in <math> \Delta c_m </math>.</li> </ul>
pulsed blowing	<ul style="list-style-type: none"> <li>An increase in lift augmentation is possible by choosing an appropriate frequency.</li> </ul>	<ul style="list-style-type: none"> <li>Drag reduction through pulsed blowing is possible.</li> </ul>	<ul style="list-style-type: none"> <li>An increase in pitching moment augmentation is possible.</li> </ul>

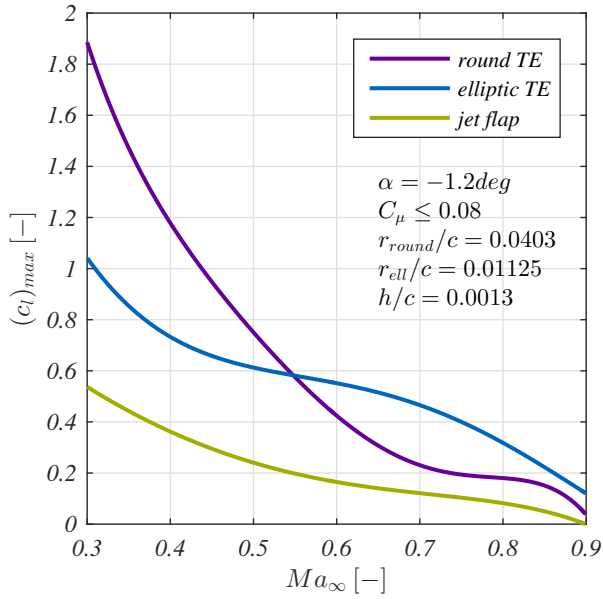


**Figure 2.5:** Maximum attained lift coefficient over free stream Mach number of an elliptical ( $t/c = 15\%$ ) circulation control aerofoil for different trailing edge shapes (created with data from ENGLAR, 1970)

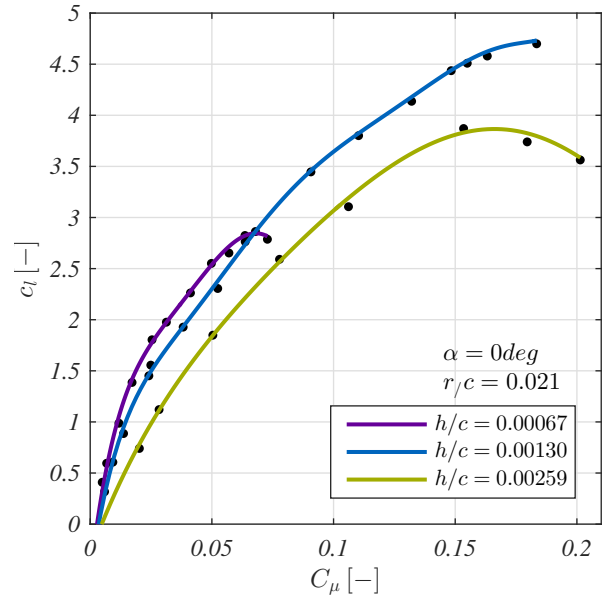


**Figure 2.6:** Lift coefficient over blowing coefficient of a circulation control aerofoil (CCW 244) for different slot heights (created with data from ENGLAR, 1975)

lift increments  $(\Delta c_l)_{max}$ . In contrast, elliptic or biconvex trailing edges are superior in transonic free stream as they alleviate unfavourable compressible effects (ENGLAR, 1970, 1971; ABRAMSON, 1977; JONES, 2005; SCHLECHT/ANDERS, 2007). More details on these effects will be given in subsection 2.2.5 and subsection 2.2.6. Figure 2.5 depicts the maximum attained lift coefficient  $(c_l)_{max}$  for a circular and elliptic trailing edge as a function of free stream Mach number  $Ma_\infty$ . For reference reasons, the maximum effectiveness of a simple jet flap is plotted additionally but is not able to compete throughout the entire velocity range. The reasons for the subsonic superiority of larger trailing edge radii can be found in the stronger trailing edge suction peaks which are consistently favourable for high lift augmentation  $\frac{\partial \Delta c_l}{\partial C_\mu}$  and high maximum lift increments  $(\Delta c_l)_{max}$  (ABRAMSON, 1977; ENGLAR, 1981). This sensitivity is generally more pronounced in the super-circulation regime and goes in line with optimisation attempts of an initially circular trailing edge contour (TAI/IDWELL, 1985). Under the design conditions of a cambered ellipse aerofoil, a deeply drooped blunt trailing edge ( $\frac{dr}{d\theta} < 0$ ) yielded an increase of 25% in maximum lift compared to an elliptic or spiralled ( $\frac{dr}{d\theta} > 0$ ) Coandă surface shape.

Similar to the lift increment characteristics, also pitching moment authority  $\frac{\partial |\Delta c_m|}{\partial C_\mu}$  and maximum attainable control moment  $(|\Delta c_m|)_{max}$  can be increased by the choice of larger radii (ENGLAR, 1971; JONES, 2005). As before, circular shapes dominate in subsonic free stream

where the trailing edge suction peaks contribute even more to high pitch-down moments. Analogous to lift generation, elliptical and biconvex trailing edge shapes revealed more efficient in transonic free stream though (ALEXANDER ET AL., 2005).

By contrast, section drag exhibits an inverse behaviour. Whereas leading edge suction is favourable in terms of drag, the trailing edge suction peaks are usually responsible for a significant drag rise. The larger the base area, i.e. Coandă radius, and the larger the jet turning angle, the higher drag values have to be expected as a consequence of the pressure distribution. However, the jet propulsive effect contributes to drag reduction and can even produce net thrust for high blowing conditions. Consequently, slender trailing edges (elliptic, biconvex) provide the potential of significant negative drag increments  $\Delta c_d < 0$  due to blowing (ENGLAR, 1971; ALEXANDER ET AL., 2005; JONES, 2005). The lower jet bending angles and reduced associated mixing losses alleviate the unfavourable rise in pressure and friction drag. Dual-slot-blowing on upper and lower surface extends this potential since the clashing jets form a region of high (stagnation) pressure in the zone of interaction. In the unblown case, smaller trailing edge radii obviously generate less drag but still suffer a clear penalty compared to conventional aerofoils with sharp trailing edges. However, the net drag of the blown aerofoil can be minimised to that of the baseline aerofoil through blowing at low  $C_{\mu}$ -values (ENGLAR, 1981). For flight control purposes, this is of particular interest since the fluidic system has to be designed for permanent operation to retain reactivity. In particular during long loiter and cruise phases, drag penalties severely impinge on fuel consumption and long-range performance. In transonic flight regimes, aerofoils with circular Coandă surfaces additionally experience a significant wave drag rise which, however, can be mitigated by use of elliptic trailing edge shapes (ENGLAR, 1970).

## 2.2.2 Influence of Coandă Surface Roughness

As already mentioned in the context of wall jets, FEKETE (1963) measured premature jet separation with increasing roughness on a cylinder surface in still air. However, no systematic tests have been performed on circulation controlled aerofoils. In the water tunnel test case from ROGERS/DONNELLY (2004), no loss in circulation control performance was visible when the Coandă surface was littered and scratched by file gouges. This suggests that surface irregularities have to exceed a certain height to observe a significant effect. For instance, a thick tape located at  $\Theta = 90deg$  along the trailing edge cylinder seriously degraded the jet effectiveness and caused more than 40% reduction in lift at high blowing coefficients (ENGLAR, 1979). This is particularly interesting for double-slotted aerofoil designs where the lower slot constitutes a significant disturbance when maximum force generation requires blowing solely through the upper slot. However, the wind tunnel experiments from ABRAMSON (2004) showed that the opposing slot edge had no impact on the aerodynamic performance.

### 2.2.3 Influence of Slot Height

The outcome of most wind tunnel experiments was that smaller slot heights  $h$  are able to produce the same lift or pitching moment at lower jet momentum coefficients than larger slot heights (ENGLAR, 1971, 1972, 1975; JONES, 2005; ALEXANDER ET AL., 2005; ENGLAR ET AL., 2009). This indicates that the velocity ratio  $\frac{U_{jet}}{U_\infty}$  of jet and free stream is more important than the amount of mass flow itself. An increased velocity difference at the slot tends to improve the mixing rate between the two streams, leading to higher lift augmentations  $\frac{\partial \Delta c_l}{\partial C_\mu}$  (WOOD/NIELSEN, 1986). As can be seen in Figure 2.6, the influence of slot height  $h$  is rather marginal for low momentum coefficients  $C_\mu$  (separation control) whereas it gains in importance in the super-circulation regime. At first sight, a system designer would aim for smaller slot heights in order to reduce the pneumatic power requirements. However, experiments on a supercritical aerofoil revealed that larger slot heights gain effectiveness on very small Coandă radii and outperform small slot heights before supersonic jet detachment occurs (ENGLAR, 1981). The resulting high mass fluxes at low pressure ratios make this configuration potentially compatible with turbofan bypass fan air.

Apart from the mass flow dependent thrust effect, the slot height has minor impact on drag at low blowing conditions. At higher  $C_\mu$  values, i.e. in the super-circulation region, no clear trend is visible since the integral drag coefficient measured with the wind tunnel balance does not separate thrust forces from possible viscous effects affecting the pressure distribution.

### 2.2.4 Influence of Angle of Attack

As given by potential theory, produced lift and pitching moment maintain their linear behaviour with angle of attack  $\frac{\partial c_l}{\partial \alpha}$  also under blowing conditions ( $C_\mu > 0$ ) (Figure 2.7). This holds if no significant viscous effects like leading edge separations are eminent. However, depending on the aerofoil nose shape, increased active circulation control can lead to premature angle-of-attack-stall (ENGLAR, 1971). High blowing rates diminish the stall incidence  $\alpha(c_{l_{max}})$  down to lower angles of attack which is addressed further in the next subsection.

### 2.2.5 Stall Phenomena

With enhanced blowing up to very high jet momentum coefficients, the lift increment begins to stagnate or even decreases (e.g. Figure 2.4). This so-called “ $C_\mu$ -stall” can have various causes:

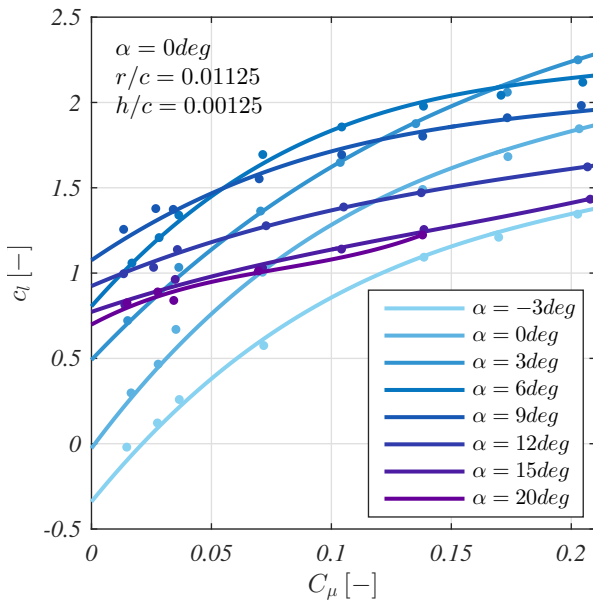


**Figure 2.7:** Lift coefficient over blowing coefficient of an elliptical ( $t/c = 15\%$ ) circulation control aerofoil for different angles of attack (created with data from ENGLAR, 1971)

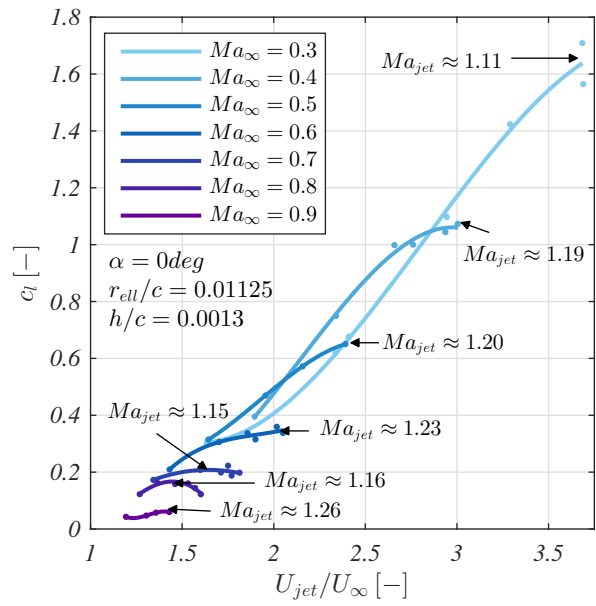


**Figure 2.8:** Lift coefficient over outflow velocity ratio of an elliptical ( $t/c = 15\%$ ) circulation control aerofoil for different free stream Mach numbers (created with data from ENGLAR, 1970)

**Jet Impingement in the Wind Tunnel** In wind tunnels, the test conditions can have significant impact on the measurements due to tunnel effects. While small clearance distances between the model and the floor/ceiling usually increase the Coandă aerofoil effectiveness, some surprising drops in lift could be attributed to unsuitably small test sections (ENGLAR, 1975; ABRAMSON, 1977). Depending on the ground clearance in the test facility, jet impingement on the floor can occur at high momentum coefficients. Then, a bound vortex under the lower surface causes a decrease of static pressure on the lower side, thus reducing lift (WILLIAMS/HOWE, 1970).

**Leading Edge Separation** Independently from the testing environment, well-known stall phenomena like leading edge separation can be responsible for stagnating or decreasing lift increments (Figure 2.9a). Whereas the risk of trailing edge separation is eliminated through counteracting blowing on the Coandă surface, the viscous processes near the leading edge gain in importance. Depending on the leading edge shape, angle of attack and turbulence characteristics (e.g. forced transition), separation bubbles can supersede the leading edge suction peak and grow until the recirculating region covers large portions of the upper surface (WILLIAMS/HOWE, 1970; ENGLAR, 1971; ABRAMSON, 1977; ENGLAR ET AL., 2009). The zone of low pressure at the trailing edge is sometimes able to recapture this widely separated flow. However, this effect is individual subject to aerofoil shape and rear suction peak

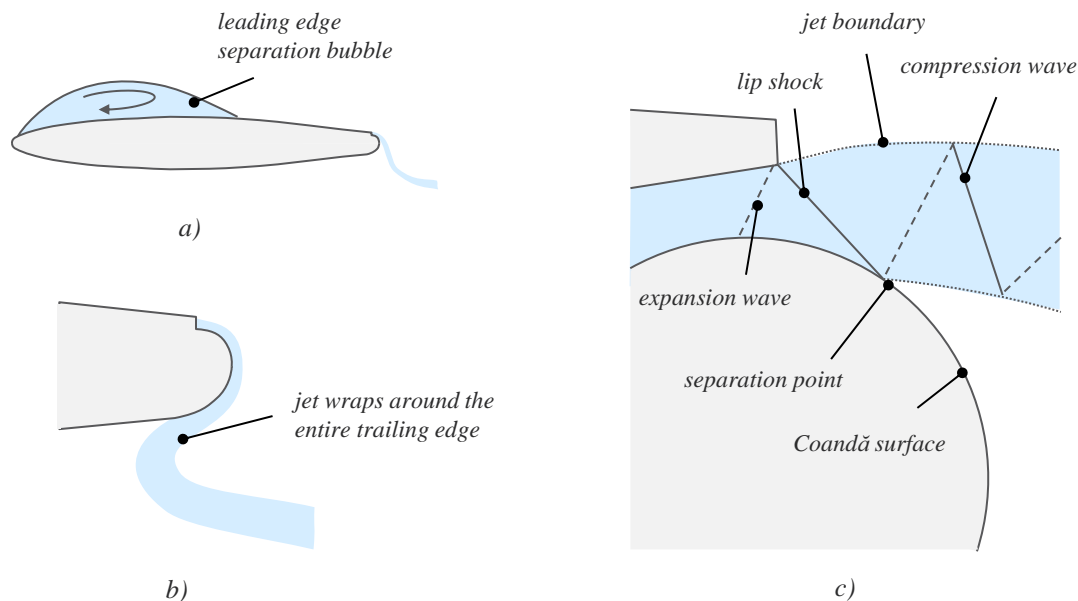


**Figure 2.9:** Illustration of possible  $C_{\mu}$ -stall phenomena: (a) leading edge separation, (b) jet wrap-around and (c) supersonic jet detachment (modified from CORNELIUS/LUCIUS (1994) and CARPENTER/SMITH (1997a))

strength. Experiments with constant blowing showed that, indeed, the trailing edge suction peak can alleviate the angle-of-attack-stall which then occurs at higher lift coefficients  $c_{l_{max}}$  but lower angles of attack  $\alpha(c_{l_{max}})$  (WILLIAMS/HOWE, 1970; ENGLAR, 1971).

**Jet Wrap-Around** Some wind tunnel tests gave indications that jets with relatively high outflow momentum can unfavourably influence the pressure distribution at the rear portion of the lower surface (ENGLAR, 1972; ABRAMSON, 1977; ROGERS/DONNELLY, 2004). The reason is attributed to the so-called “jet wrap-around” where wall jet separation is delayed such that the rear stagnation point is relocated onto the lower aerofoil surface (Figure 2.9b). The resulting “trailing edge pressure drawdown” appears to be limited to specific aerofoil shapes and test conditions as it was not visible in all references. Interestingly, this stall phenomenon due to excessive Coandă jet turning can be avoided by opposed blowing from a second slot on the lower side (ROGERS/DONNELLY, 2004; MIKLOSOVIC ET AL., 2012), which promotes double-slotted CC aerofoil designs.

**Supersonic Coandă Jet Detachment** When the blowing intensity clearly exceeds choked conditions ( $Ma_{jet,slot} = 1$ ), the underexpanded, supersonic jet is likely to detach due to expansion waves and recompression effects (ENGLAR, 1970, 1971, 1975; WILKERSON/MONTANA, 1982; ALEXANDER ET AL., 2005). With growing Mach number  $Ma_{jet}$  of the expanding jet, initial separation bubbles on the Coandă surface cause only a slight decline in circulation. The supersonic jet is able to reattach to the Coandă surface and still entrains the free stream flow (ENGLAR, 1971, 1972; CORNELIUS/LUCIUS, 1994). However, the excess of a specific

local expansion wave strength inside the underexpanded supersonic jet triggers jet detachment already in the proximity of the slot (Figure 2.9c). This results in a sudden loss of lift and pitching moment, while section drag rises significantly. As can be seen in Figure 2.8, the corresponding critical Mach number of the fully expanded jet  $Ma_{jet}$  can take relatively low values ( $Ma_{jet} \approx 1.2$ ) and, in addition, tends to reduce further with increasing free stream Mach number  $Ma_\infty$  (ENGLAR, 1970; ABRAMSON, 2004). Since the absolute values of the trailing edge suction peak pressure  $p_{static,slot}$  shrink with free stream velocity  $Ma_\infty$ , the local pressure ratio  $\frac{p_{t,plenum}}{p_{static,slot}}$  increases to the same extent. This causes the supersonic jet to accelerate additionally and inevitably leads to stronger compressible effects (ENGLAR, 1975). As already mentioned before, elliptic trailing edges revealed superior in transonic flight regimes and are also less prone to jet detachment effects due to reduced curvature (ENGLAR, 1970). In particular, the combination of slot height  $h$  and Coandă radius  $r$  seems to be crucial. Experimental data show that increasing slot-height-to-radius ratios  $\frac{h}{r}$  aggravate the risk of supersonic jet detachment (ENGLAR, 1975). The other way round, the critical pressure ratio of separation grows almost linearly with  $\frac{r}{h}$  where significant hysteresis effects could be observed (MATSUO ET AL., 1998). In summary, small slot heights  $h$  and large Coandă surface radii  $r$  are less prone to jet detachment. The reasons are due to viscous effects inside the supersonic wall jet. For smaller slot heights, the turbulent mixing processes at the boundaries of the supercritical wall jets are able to prematurely alleviate the velocity excess. The turbulent eddies intrude deeply enough into the cores of thinner jets to extenuate recompression shock waves which usually strengthen with tightened trailing edge curvature ( $r \downarrow$ ).

Certain constructive measurements applied on the slot geometry can further decrease the risk of supersonic jet detachment. CORNELIUS/LUCIUS (1994) found that a converging-diverging slot channel delayed jet separation and raised the limiting pressure ratio. Moreover, the introduction of a backstep between the slot and the Coandă surface appears to favourably extend the range of operation (CARPENTER/SMITH, 1997b). Unstepped slot outlets usually feature a lip shock emanating from the lower edge of the slot lip (Figure 2.9c). This incident shock generates a separation bubble which grows in size as the pressure ratio rises and ultimately causes breakaway to occur. A backstepped slot exit design eliminates this intensive recompression process and delays  $C_\mu$ -stall up to higher jet velocities  $Ma_{jet}$ .

## 2.2.6 Influence of Free Stream Mach Number

The influence of free stream Mach number becomes relevant beginning at approximately  $M_\infty = 0.4$ . Due to the previously presented supersonic jet detachment effects, the maximum attainable lift coefficient  $c_l$  decreases significantly when the circulation control aerofoil enters the transonic regime (Figure 2.8). The same applies for pitching moment authority. However, lift augmentation due to blowing  $\frac{\partial \Delta c_l}{\partial C_\mu}$  increases with Mach number under conditions of

attached jet (ENGLAR, 1970; WOOD/CONLON, 1983; ALEXANDER ET AL., 2005).

Also section drag experiences a pronounced variation with external Mach number. Especially, round trailing edges exhibit a significant drag rise at higher transonic Mach numbers which even aggravates with increasing blowing rates (ENGLAR, 1970). However, blowing over elliptical trailing edges can favourably reduce drag through rearward relocation of the upper surface shock (up to  $\Delta \frac{x}{c} = 20\%$ ) (ENGLAR, 1970; ABRAMSON, 2004). But once reached supersonic jet detachment, further growing plenum pressure ratios reverse this trend and push the shock location towards the nose (ALEXANDER ET AL., 2005).

### 2.2.7 Pulsed Blowing

Although early success in enhancing lift augmentation through pulsed blowing could not be reproduced consistently (ENGLAR, 1975), JONES/ENGLAR (2003) could confirm the performance benefit of unsteady jets. By use of modern high-speed solenoid valves, frequencies up to 200Hz were tested attaining jet peak velocities up to sonic conditions. An important result of the experiments was that performance was highly frequency dependent. For instance, a 50% reduction in mass flow could be realized using a frequency of 10Hz in the separation control regime. Further wind tunnel tests from WONG ET AL. (2006) indicate that pulsed blowing could lead to significant drag reductions while gains in lift and pitching moment are remained. However, trailing edge geometry revealed crucial in this context where the benefit of an elliptic trailing edge was clearly less (30%) than that of a circular shape (50%) (JONES, 2005). Interestingly, no potential for mass flow reduction was measurable with the biconvex trailing edge.

For permanently active Coandă flap systems, this method of unsteady blowing is of special interest. However, the mechanical implementation poses high challenges as high-speed valves usually entail significant losses of total pressure due to throttle effects. Similarly, solutions based on oscillating membranes have to be considered with caution, too, as they might not provide sufficient reliability and endurance.

### 2.2.8 Uncertainties of Wind Tunnel Experiments

In comparative studies, numerical results often underestimate the experimentally measured suction peak on the circular trailing edge. One cause is setting the momentum flux too low for the inflow boundary condition of the jet exit. The reason can be traced back to fact that the experimental jet outflow velocity is often determined analytically by use of the isentropic flow equations (see section C in the appendix). The ratio of plenum total pressure and static pressure at the slot exit define the outflow Mach number  $Ma_{jet}$ . For simplicity

reasons, test engineers often used the ambient pressure  $p_\infty$  instead of the real static pressure at the slot. However, under free stream conditions the static pressure at the trailing edge is significantly lower (suction peak) than the ambient static pressure and causes the Coandă jet to accelerate additionally. So, the estimated momentum flux coefficient might deviate from the higher real  $C_\mu$ -values, especially under extensive blowing conditions.

Furthermore, the interaction of the jet sheet with tunnel side walls can have an important 3D effect. The high pressure gradient causes vortices downstream the wing which then induce a net downwash on the aerofoil (ENGLAR, 1971; OWEN/OWEN, 2006). This effect intensifies with increasing blowing rate and could also be reproduced numerically (SWANSON ET AL., 2005; NISHINO/SHARIFF, 2010). The separation and roll-up of the boundary layers in the wing-sidewall juncture regions are a consequence of the strong adverse pressure gradients on the upper surface of the wing. Extreme circulation around the wing cause vortex shedding at the sidewall similar to a finite wing. These vortical structures induce a downwash along the span of the wing and significantly reduce the effective angle of attack (ENGLAR, 1971; SWANSON ET AL., 2005; OWEN/OWEN, 2006; ENGLAR ET AL., 2009; NISHINO/SHARIFF, 2010). This influence has to be kept in mind for the validation of sophisticated and new modelling approaches.

Finally, the determination of the section mass flow rate might be distorted by differing slot heights at the jet exit. These deviations from the nominal slot height vary along span and are due to non-uniform bending loads on the rear skin fractions (JONES ET AL., 2006; ENGLAR ET AL., 2009). As a consequence the estimated  $C_\mu$ -values are lower than the real flow momentum coefficient. This is particularly important for the spanwise location where the pressure sensors are installed for lift force integration.

## 2.2.9 Circulation Control on Finite Wings

This subsection provides a literature review on circulation control experiments and possible deviations in performance when Coandă aerofoils are installed on finite wings. Early wind tunnel experiments on finite wings (with body and tail) were conducted on a scaled (1:8.5) model of the “Grumman A-6 Intruder” in the 1970s (ENGLAR, 1979). Its wing and horizontal stabiliser were equipped with circulation control trailing edges being optimised during the tests. As anticipated before, the model achieved a maximum trimmed lift coefficient double that of the standard aircraft. In addition, operational aspects just as longitudinal and lateral characteristics of the circulation control configuration were addressed in this wind tunnel campaign.

More recent experiments on finite wings investigated the applicability of conventional potential theory on circulation control wings. ROGERS/DONNELLY (2004) tested a slightly

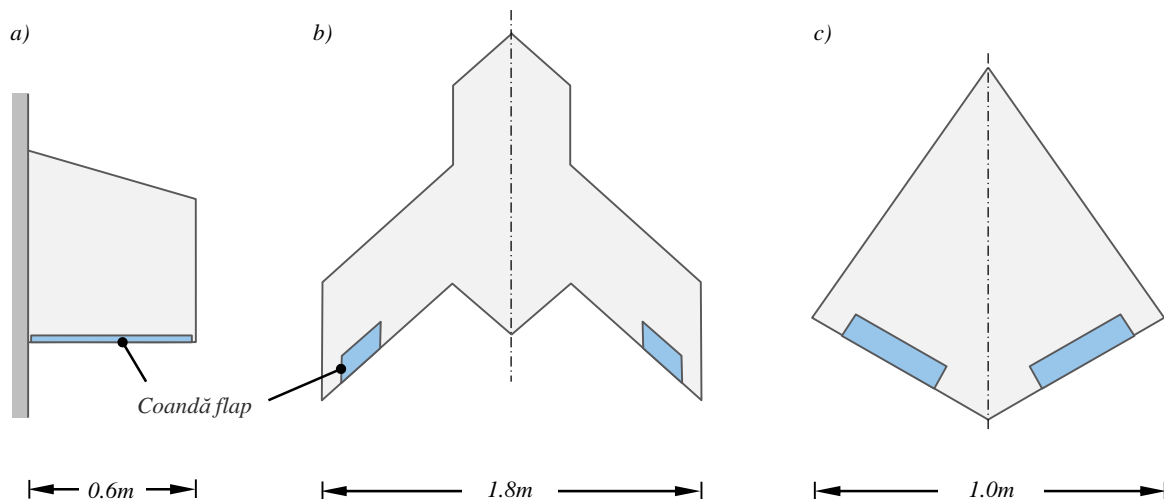


**Figure 2.10:** Illustration of finite wing wind tunnel models (planforms reproduced from ROGERS/DONNELLY (2004) (a), HARLEY ET AL. (2009) (b) and FRITH/WOOD (2004) (c))

tapered half wing ( $AR = 2$ ) with double-slotted elliptical section shape ( $\frac{t}{c} = 0.20$ ) in a water tunnel ( $Re = 2.1 \times 10^6$ ) (Figure 2.10a). In principle, linear potential theory revealed applicable also on circulation control wings with activated trailing edge blowing. The impact of low aspect ratio was essentially the same as on conventional wings. This conclusion was also made earlier by IMBER/ROGERS (1996), who examined a low aspect ratio wing with circular planform and  $360deg$  tangential fluid ejection. Induced drag measurements in the wind tunnel agreed with classical theory when full aft blowing was used. Moreover, HARLEY ET AL. (2009) confirmed that established semi-empirical data sheet methods (e.g. DATCOM), originally developed for conventional flaps, may be used to predict 3D planform characteristics from 2D circulation control section data. They tested a flying demonstrator in the wind tunnel whose planform was based on the Boeing X-45A concept (Figure 2.10b). However, ROGERS/DONNELLY (2004) found indications that the spanwise flow component is potentially lower for circulation control wings. This was most visible near the wing tips where the under-elliptical lift distribution induced surprisingly low effective angles of attack ( $\alpha_{local} \approx -14^\circ$ ). This effect annihilated the leading edge suction peaks and led to a reduced wing tip vortex strength. The only pressure gradient from the lower to the upper side stems from the remaining jet induced suction peak at the trailing edge. Additionally to this, a small vertical plate was attached at the wing tip covering solely the trailing edge cylinder. Acting like a trailing edge flow fence, this modification resulted in significant lift increase and drag reduction in the super-circulation domain.

For highly swept wings, especially the interaction of circulation control with non-linear lift and other 3D effects is of interest. FRITH/WOOD (2004) performed wind tunnel tests ( $Re = 1.3 \times 10^6$ ) on a diamond shaped wing with a leading edge sweep of  $\varphi_{0\%} = 55^\circ$  and a trailing edge sweep of  $\varphi_{100\%} = -30^\circ$  (Figure 2.10c). The pitch and roll moment performance showed

an essentially continuous behaviour that correlates with 2D section trends. It is interesting to note that effectiveness in the augmentation of lift, pitching moment and roll moment increased at higher angles of attack, i.e. in the non-linear lift region. The trailing edge blowing concept was able to favourably magnify the strength of the vortex system that originated from the highly swept sharp leading edge. Earlier wind tunnel investigations on delta half wings ( $\varphi_{0\%} = 50^\circ$ ) with sharp and rounded leading edges showed that the position of the vortex remains essentially unchanged whereas its diameter increased in size (FRITH/WOOD, 2003). Another finding was that the circulation control effectors are not sensible to its spanwise position even if pronounced 3D effects have to be expected on low-aspect-ratio wings. The spanwise relocation of the Coandă flaps had minor effect on lift augmentation.

## 2.3 Flying Demonstrators

This section provides a brief summary of published examples of demonstrators which successfully performed test flights with fully functional Coandă flaps. Note that blown-flap applications were excluded intentionally since practical implementations of simply round trailing edges are of explicit interest for this work. An early technical realisation of this circulation control type was successfully tested in flight by LOTH ET AL. (1976). The general aviation “WVU Flight Demonstrator” (Figure 2.11a) from West Virginia University was equipped with a deployable cylindrical Coandă surface mounted at the edge of a conventional flap. During cruise, it was retracted by folding forward to alleviate the penalty of section base drag. Under high-lift conditions, the hot bleed air was provided by an additionally installed turbine whose high-pressure compressor air was expanded through a high-mass ratio ejector. The associated suction was performed at the flap hinge line which had a positive effect on circulation control performance. The reduced thickness of the boundary layer arriving from the upper side delays wall jet separation and thus enhances circulation. In the



**Figure 2.11:** WVU Flight Demonstrator (a) and Grumman A-6A (b) as examples for flying circulation control demonstrators (LOTH, 2006)

end, satisfactorily high trimmed lift coefficients could be obtained at low aircraft attitude resulting in good pilot visibility.

A second example performed its test flights in the late 1970s. The modified carrier aircraft Grumman A-6A (Figure 2.11b) successfully demonstrated the high lift and STOL capability of the implemented circulation control wing concept (PUGLIESE/ENGLAR, 1979). The circular Coandă trailing edge was attached to the existing flap and received bleed air from both engines for blowing. The bleed air system comprised pressure regulating valves to ensure bleed air regulation independent from power setting. Engine ground tests revealed a thrust reduction of approx. 30% with full bleed. In order to extend the high-lift capability and safety margins, leading edge separation through excessive circulation was prevented by an enhanced wing SLAT system. Additionally, the horizontal stabiliser was enlarged and partially redesigned featuring inverted leading edge droop. Thus, lift coefficients could be doubled at high angle of attack and even tripled at moderate angle of attack. The achieved  $c_{L_{max}}$  was improved by 65% compared to the basic A-6 flaps. The enhanced high-lift capability led to an approach speed reduction of approx. 30kts yielding ground roll distances shortened by nearly 50% (ENGLAR ET AL., 1981). In addition, all failure modes tested in flights turned out to be fully controllable, including blowing- and single-engine failures. However, the intentionally constant slot heights varied significantly due to changing pressure load conditions. These structural deformations due to varying throttle and valve settings constitute an important risk when the real lift performance does not coincide with preceding estimations.

While the precedent examples exploit the Coandă effect for high-lift applications, one implementation was published which seeks to ensure fluidic flight control through permanent blowing. Flapless flight through active circulation control could be demonstrated within the FLAVIIR research project in 2010. The unmanned Demon demonstrator had a take-off mass of 80 kg and a diamond shaped wing plan-form of 2.5 metres in span (FIELDING ET AL., 2010; MONTERZINO/LAWSON, 2010). A particularly challenging requirement was that the vehicle must demonstrate an entire flight cycle without the use of conventional flight control surfaces. For this, the air vehicle was equipped with two pairs of circulation control units: one for roll at the outboard position and one for pitch at the inboard position. They comprised a double-slotted CC aerofoil design featuring a moving cylindrical trailing edge with eccentric pivot point. For yaw control, a conventional rudder was used. Since bleed air from the main engine was insufficient at low thrust levels (e.g. landing phase), a dedicated auxiliary power unit provided the required pressurised air on board. This concept successfully ensured fluidic roll and pitch control during all phases of the test flight.

## 2.4 Modelling Approaches

Except the previously presented examples found in literature, practical experience with circulation control systems is rather limited. But as common outcome of flight tests and experimental work, generally high mass flow demands were reported. This might be one reason why the Coandă flap concept has not been pursued for industrial applications so far. Another reason could originate from the uncertainty of turbulent processes which still are not completely understood, but determine circulation control effectiveness. Neither systematic data bases of aerodynamic data, nor general design rules for Coandă flap implementations are available at present. This fact underlines the need for reliable modelling methods which enable manifold optimisation activities in the preliminary design stages.

One important task of the preliminary design process is the exploration of the design space. In the context of a given aircraft configuration, the specification of Coandă flap parameters requires robust modelling methods which quickly provide sufficiently accurate aerodynamic data. The following literature review on modelling approaches confines to publications on two-dimensional sections due to the lack of numerical studies on finite wings. Of course, three-dimensional calculations gave insight into certain 3D effects, but they were conducted in the scope of supplemental calculations on section experiments. These simulations mainly tried to reproduce wind tunnel tests with blocked wing tip flow rather than real finite wing cases or even entire aircraft configurations.

As also summarised in STADLBERGER/HORNUNG (2014), the following subsections review the most relevant modelling approaches found in literature. Still, vast parameter variations during preliminary aircraft design are usually achieved by simplified, quick methods based on analytical and semi-empirical relations as well as on potential flow. However, with growing computational power also more detailed methods become interesting for early design stages. Therefore, this review also includes methods of computational fluid dynamics (CFD) and assesses their performance and sensitivities. Concluding remarks finally deduce the most promising modelling approach for the scope of this study. So, the final subsection builds the bridge to the subsequent chapter which then describes the chosen modelling procedure and involved methods.

### 2.4.1 Potential Theory and Integral Methods

Right at the beginning of intensive experimental research on circulation control technology in the 1960s, simultaneous analytical modelling approaches have been applied on the wall jet behaviour along a curved Coandă surface (DUNHAM, 1968; LEVINSKY/YEH, 1972). According to the potential theory practice, a vortex superimposed on a doublet was used to describe the global flow field around a tangentially blown cylinder in free stream. On the windward

surface, parametrised velocity profiles were prescribed both for laminar and turbulent regions. This enabled the application of an integral method to model the main characteristics of the well-known boundary layer shapes. A similar approach was chosen for the regions that are affected by the wall jet. The particular wall jet velocity profile was divided into four layers in order to solve the momentum equations analytically (LEVINSKY/YEH, 1972). In the standard boundary layer approximation, vertical pressure variations are usually neglected. The developed multi-strip integral method, however, accounted for curvature effects which manifest themselves in normal pressure gradients. However, this calculation method still produced significant deviations from experimental data, especially at high jet momentum.

In the end of the 1970s, the investigated circulation control aerofoils were represented by a vortex lattice arrangement with additional source distribution to account for boundary layer thickness (DVORAK/KIND, 1979). The boundary layer flows on the lower and the upper surface upstream the slot were calculated using integral methods. These were able to distinguish laminar and turbulent regions through transition point estimation. On the Coandă surface, a finite difference technique of the Crank-Nicholson type estimated the jet flow behaviour from ejection until separation. For turbulence modelling, a modified Van Driest eddy viscosity model was applied on the inner region of the jet while the outer region underlay a newly formulated eddy viscosity model (DVORAK, 1973). The boundary layer on the remaining fraction of the Coandă surface was modelled as a nominal boundary layer under adverse pressure gradient. The combined technique explicitly accounted for both normal pressure gradients and curvature effects. Convergence of the iterative calculation process was attained when the upper and lower separation pressure on the Coandă surface both coincided within a prescribed tolerance, i.e. when the estimation of the rear stagnation point was sufficiently correct. This program named CIRCON was able to predict jet separation and associated aerofoil flow field quite accurately for the simulated blowing conditions. Over time, the calculation tool has been extended for transonic free stream conditions. Both calculations of potential theory and boundary layer were adapted to account for compressibility effects on the aerofoil surface (DVORAK/CHOI, 1983). However, supersonic wall jets still could not be modelled and the semi-empirical turbulence modelling approach was not sufficiently sensitive to detect changes in pressure distributions arising from small changes in geometry. Therefore, most recent modifications comprised the introduction of the curvature corrected  $k$ - $\varepsilon$ -turbulence model for the outer layer of the wall jet (DVORAK ET AL., 1987). This modelling method thus reached a complexity level not far from finite-difference simulations which solve the Reynolds Averaged Navier-Stokes equations (RANS) on fully discretised flow domains (SHREWSBURY, 1986).

## 2.4.2 Reynolds Averaged Navier-Stokes Approach (RANS)

As already mentioned in section 2.1, the external free stream plays an important role in the overall mixing of the different wall jet layers. The viscous processes therein exhibit a dependency on the boundary layer shape coming from the upper side of the aerofoil (NOVAK/CORNELIUS, 1986). Therefore, a segregated modelling approach of the wall jet without global flow field interaction may lead to favourably low computational efforts, but might not reach sufficient accuracy for arbitrary aerofoil shapes. Here, the simultaneous solution of the conservation equations for the entire aerofoil flow field (2D) appears more promising. Computing times rise significantly but should be feasible also for vast parameter variations. Hence, the compendium in this subsection is confined to the most recent modelling activities in the field of numerical fluid dynamics. The following computational investigations solve the Reynolds Averaged Navier-Stokes equations (RANS) by use of one- and two-equation turbulence closures. Algebraic turbulence models are excluded as they usually require case dependent calibration and therefore lack in generality (PULLIAM ET AL., 1985).

It is common practice to reproduce wind tunnel experiments using CFD methods. Simulation results can provide a deeper insight into flow topology and turbulent processes. Figure 2.12 gives an example of a simulated flow field (a) with respective pressure distribution (c). Whereas some modelling efforts indicate a certain success in using RANS to predict trends and selected details (BAKER/PATERSON, 2006), there have been more failures of RANS models than successes (FASEL ET AL., 2006; SWANSON ET AL., 2006; ZACHAROS/KONTIS, 2006; CHANG ET AL., 2006; STADLBERGER/HORNUNG, 2014). Failures typically manifest themselves in a wall jet which stays attached on the Coandă surface too long up to a non-physical extent. In the first instance, this leads to an excessive overprediction of the lift coefficient, but then turns into a gross underprediction of lift. The latter is due to wrong modelling of the wall jet that wraps around the entire trailing edge (Figure 2.12b) and deteriorates the pressure distribution of the lower side (Figure 2.12d). Here, tangential grid refinement at the Coandă surface can help but does not always cure the problem (SWANSON/RUMSEY, 2009). It is the turbulence model used for RANS closure which is decisive for the final result. The model dependent eddy viscosity predictions inside the wall jet determine the location of jet separation. Unfortunately, a distinct all-embracing statement about the most appropriate turbulence model for circulation control is not possible if one has to give a final conclusion of available literature at present. It is of interest that the more complex full Reynolds stress model (RSM) did not turn out to be superior despite its anisotropic representation of turbulence (CHANG ET AL., 2006; ZACHAROS/KONTIS, 2006). By theory, it should be more suitable for the wall jet problem (LAUNDER/RODI, 1983). Also, the attempt to adjust the constant coefficients of the  $k$ - $\omega$ -turbulence model could not improve the

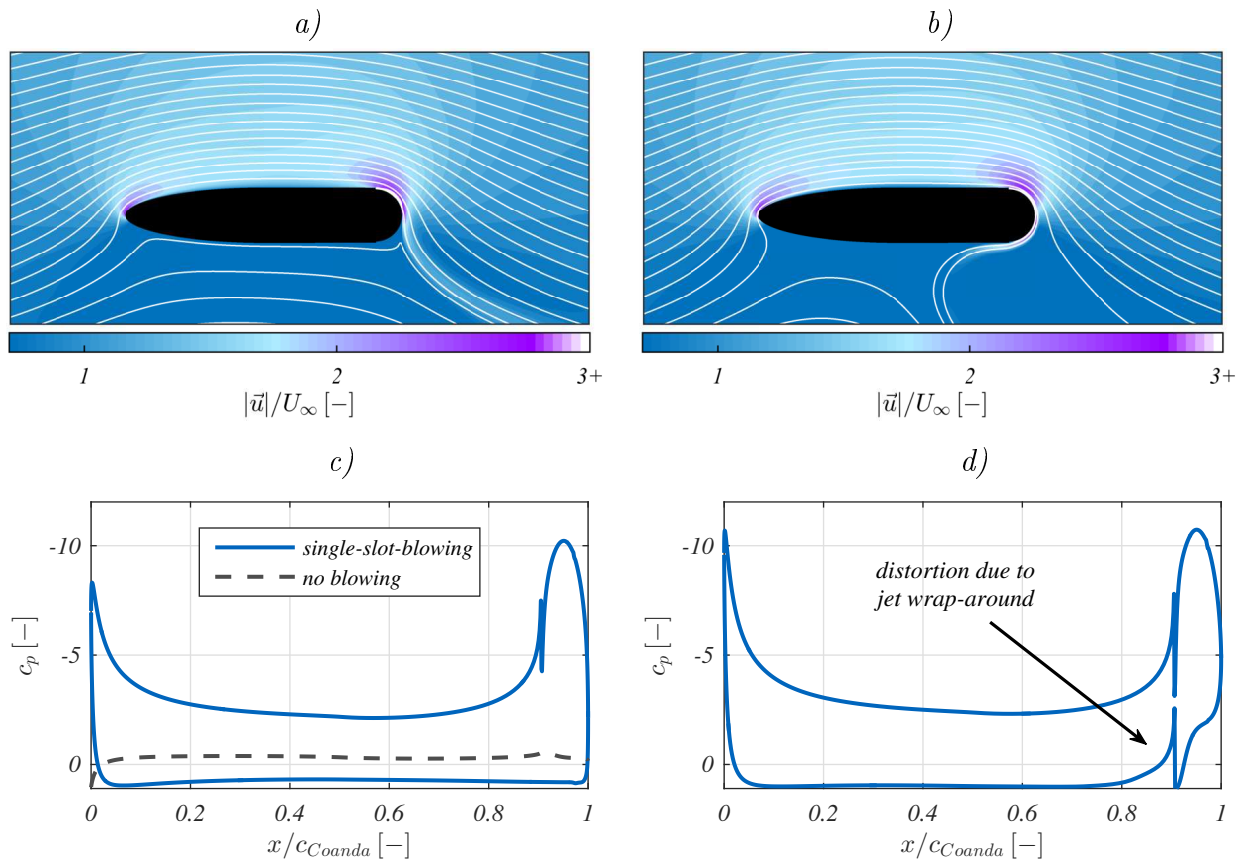


**Figure 2.12:** Flow fields (a,b) and pressure distributions (c,d) of successful (left) and failed (right) RANS simulations reproducing the wind tunnel test case from ENGLAR ET AL. (2009),  $\alpha_\infty = 0deg$ ,  $\frac{U_{jet}}{U_\infty} = 6$ ,  $\frac{h_u}{c_{Coanda}} = 0.0022$  (simulated with the RANS method presented in section 3.4)

predictability of a general aerofoil design (PAJAYAKRIT/KIND, 2000). However, turbulence models with implemented flow curvature correction (e.g. HELLSTEN (1998), SHUR ET AL. (2000)) tend to alleviate the problem of non-physical solutions at high blowing rates but give no guarantee (SWANSON ET AL., 2005, 2006; FASEL ET AL., 2006; RUMSEY/NISHINO, 2011; AROLLA/DURBIN, 2013).

Systematic calculations of MIN ET AL. (2009) indicate that the order of spatial discretisation has minor effect on the accuracy of the final results. Similarly, the inclusion of the plenum chamber upstream the slot exit showed no significant difference compared to the simple assignment of boundary conditions directly at the vertical slot plane. However, the lift performance revealed visibly sensitive to the prescription of turbulence level at the slot exit boundary. Furthermore, calculations performed by NISHINO/SHARIFF (2012) investigate the influence of jet nozzle lip thickness and underline the importance of turbulent processes in the region close to the slot. Their results showed that the jet profile across the nozzle exit is insensitive to the nozzle lip thickness. However, the jet flow downstream the nozzle exit and circulation control effectiveness are to some extent dependent on the lip thickness due to the varying momentum losses.

FORSTER/STEIJL (2015) carried out RANS simulations under transonic free stream conditions which also implied numerical investigations of the supersonic Coandă jet. While the numerical results for  $Ma_\infty = 0.3$  agreed essentially well with experimental data, the position of the shock wave on the upper side of the aerofoil could not be predicted accurately under blowing conditions. However, in terms of supersonic jet detachment, the favourable effect of both a converging-diverging nozzle shape and a backstep between slot and Coandă surface could be confirmed numerically (see also subsection 2.2.5). Moreover, a gradient based contour optimisation of the trailing edge could increase the attained lift coefficient by 8%. In contrast, a weaker curvature close to the slot accomplished to prevent supersonic jet detachment (FORSTER ET AL., 2015).

### 2.4.3 Large Eddy Simulation and Direct Numerical Simulation

Theoretically, the extremely fine resolution of the wall jet should reproduce nearly every turbulent aspect by directly calculating eddies down to very small length scales. Prediction accuracy is supposed to be highest with these modelling strategies. However, the considerable increase of computational effort by performing Large-Eddy-Simulations (LES) (NISHINO ET AL., 2010) or Direct Numerical Simulations (DNS) (MADAVAN/ROGERS, 2010) could not outperform the RANS methods. Surprisingly, significant deviations of pressure distribution still exist at high blowing rates. Hence, the statement of SWANSON/RUMSEY (2009) has to be extended at present: “the current prediction capability with numerical methods for circulation control flows over Coandă surfaces is not ready for a general design procedure”, neither with RANS methods nor with LES or DNS approaches.

### 2.4.4 Conclusion for Coandă Flap Modelling

The first part of this chapter presented the aerodynamic phenomena that have been experienced on Coandă aerofoils during wind tunnel experiments. The summary of published modelling attempts in the second part attested poor capability of the present modelling methods to accurately reproduce the aerodynamic forces and moments up to high blowing rates. Computationally intense methods (LES, DES, DNS) might be the obvious way to improve accuracy by exactly resolving the complex turbulent processes inside the shear layers. However, sufficient reliability still could not be achieved in the context of circulation control aerofoils. Moreover, to meet the objectives of this work, a far quicker CFD method has to be found in view of the computational power provided by current standard desktop machines. Potential flow combined with discretised boundary layer representation on the Coandă surface appears promising in the first approach. The adapted zero-equation turbulence model provided remarkably reliable results. However, the underlying procedure would have to be

adapted and extended to cover modified CC aerofoil concepts as double-slotted designs for flight control applications. Since the outcome of this path would have been too uncertain, the focus was set on calculation methods which represent the modern standard of aerodynamic modelling. Methods implying turbulence models that rely on transported turbulence quantities in a discretised domain (e.g.  $k$ - $\varepsilon$ ,  $k$ - $\omega$ ) provide more flexibility even though automated high quality meshing is not trivial. Since modelling attempts based on RANS struggled with high blowing rates, hitherto untested modifications and corrections of local turbulence (e.g. eddy viscosity) are considered to be necessary to obtain sufficiently accurate results. Of course, these corrections could also be inspired by robust zero-equation models. As baseline turbulence model Menter's sophisticated SST model was judged to be the most promising candidate for customisation. To this, the subsequent chapter will present a solution which has been elaborated to enable more accurate and robust simulations of wall jet flows. Furthermore, the option of pulsed blowing is abandoned in this study because of the associated higher computational effort. Also, in terms of reliability a suitable mechanical implementation is still uncertain including the required moving parts (e.g. membranes, valves etc.). Hence, steady blowing is regarded as a sufficiently representative baseline configuration for flight control purposes. The quicker convergence rate supports large-scale parameter variations even though the performance values turn out somewhat conservative. Consequently, this work confines to the modelling of steady state aerodynamics to study the feasibility of Coandă flap systems.

Experimental findings revealed that compressible effects are crucial for circulation control effectiveness. Nevertheless, the modelling of the external stream was reduced to incompressible flow. The extension to fully compressible flow had to be abandoned in favour of overall system modelling aspects. Additional challenges would have been the additional solution of the energy equation, the automated local grid refinement for shock capturing, and the general difficulty of transonic flow convergence. Obviously, the incompressible implementation is not able to correctly represent supersonic jets and their tendency to detach ( $C_{\mu}$ -stall). Indeed, these points constitute important topics for future studies. In this work, however, priority is given to the exploration of the overall system behaviour. Incompressible flow still covers most of the relevant system reactions over large portions of the flight envelope.

Furthermore, fully three-dimensional CFD simulations go beyond the scope of preliminary aircraft design as they exceed computational capacity and manageability. However, the compromise of two-dimensional RANS calculations with subsequent extrapolation on the finite wing is considered to be feasible. Different methods in literature based on potential theory already responded to the need of viscous section data transfer onto finite wings. By means of custom modifications, they can be adapted for the modelling of Coandă flaps.



### 3 Coandă Flap System Modelling

The previous chapter reviewed the available practical experience with circulation control aerofoils including published modelling attempts. No matter which type of active flow control concept is under consideration, they all have in common the need for additional pneumatic systems. For instance, each technology that relies on blowing requires a source of pressurised air for synthetic jet formation. So, circulation control systems usually consist of a compressor, ducts and some sort of fluidic effector element, e.g. the trailing edge device of a Coandă flap. Since the overall performance of the fluidic flight control system naturally depends on the behaviour of these subcomponents, they have to be represented adequately within the overall system model. Figure 3.1 illustrates the simplified system breakdown for a low-aspect-ratio flying-wing configuration. In this case, the pressurized air is directly supplied by the engine rather than by a decentralized solution with electrically driven compressors (e.g. in SEUME ET AL. (2013)). The relatively low distances to be covered by power lines favour one central source with pneumatic ducts instead of electrical wiring with peripheral, smaller compressors. The mass penalty of decentralised compressor systems tends to outweigh the benefits of reduced ducting mass (JABBAL ET AL., 2010; JABBAL/TOMASSO, 2014). The associated lower complexity and development cost additionally consolidate the concept of engine bleed as single source for pressurised air.

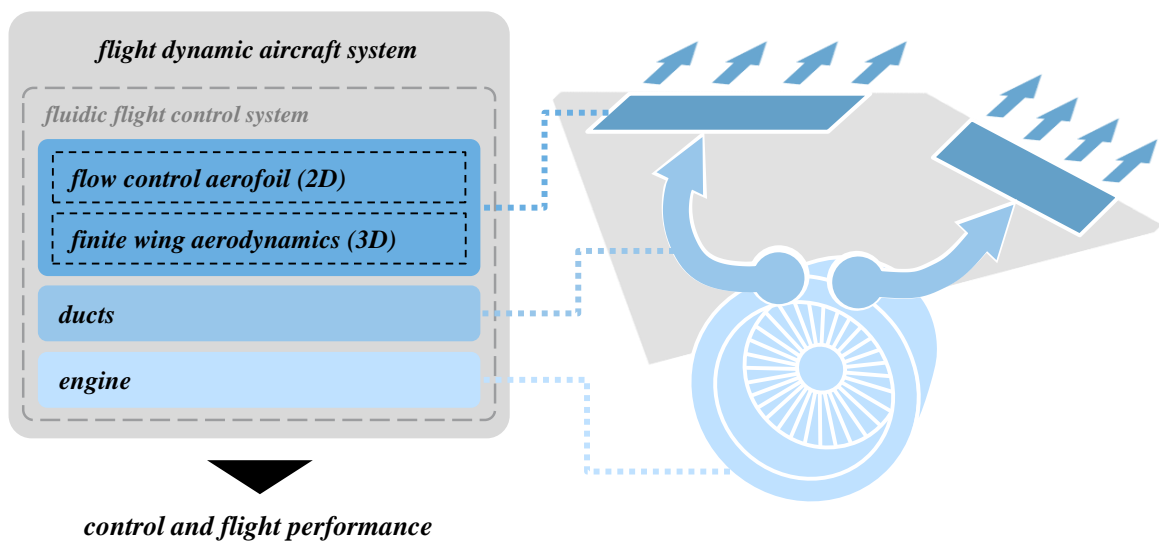


**Figure 3.1:** Illustration of main subsystems of the fluidic flight control system

To establish the data basis for the simulation of the overall aircraft system, several submodels generate data tables which are combined and reprocessed in succession. Figure 3.2 gives an overview of the modelling sequence involving five submodels. For preliminary design purposes, the models of both engine (compressor) and duct system can be established by use of sophisticated tools and methods as will be seen in section 3.2 and section 3.3, respectively. Here, computational efforts are low compared to the computing power demands that arise from CFD calculations. As explained in subsection 2.4.4, RANS methods are judged to be most appropriate for the aerodynamic modelling of the Coandă aerofoil effectiveness (subsection 2.4.4). The three-dimensional finite wing reactions are then attained by use of potential theory. The underlying methods are described in section 3.4 and section 3.5, respectively. Both imply custom enhancements of sophisticated techniques. Several modifications have been necessary to obtain reliable results for blown round trailing edges applied on low-aspect-ratio wings. By means of automated calculation procedures, the submodels then provide large data tables. They can be assembled in SIMULINK to establish an overall model of the fluidic flight control system. A fully dynamic flight simulation (6-DOF) of the aircraft (section 3.6) finally enables the analysis of the overall system performance in the scope of a given aircraft configuration and design mission.

The first introductory section of this chapter describes the studied double-slotted version of the Coandă flap concept and specifies the physical interactions between the subsystem models. The remaining sections explain in detail the modelling approaches used for engine, air ducts, Coandă aerofoil section aerodynamics (2D), finite wing aerodynamics (3D), and overall system flight dynamics.

## 3.1 Investigated Coandă Flap Concept

In chapter 2 the basic principle of the Coandă aerofoil, its sensitivities and potential for high lift and control moment generation have been reviewed. This concept of circulation control is further adapted for the use as flapless flight control technique. In contrast to high-lift applications, the ability to generate control moments in both positive and negative direction becomes crucial to attain sufficient control authority. Therefore, the studied Coandă flap is designed as a (symmetric) double-slotted version of a Coandă aerofoil which can act similarly to a conventional plain flap (Figure 3.3). As a matter of concept, the momentum vector can be bended both upwards or downwards. This design may also be suitable for yaw control when the air outflow momentum is controlled differentially on the wing half spans. Note that the detailed constructive realisation of the Coandă flap is not part of this work.

For the fluid mechanic modelling during preliminary design stages, it is sufficient to define the upper and lower slot sizes. Both outlets are supplied by the same pressurised plenum cham-

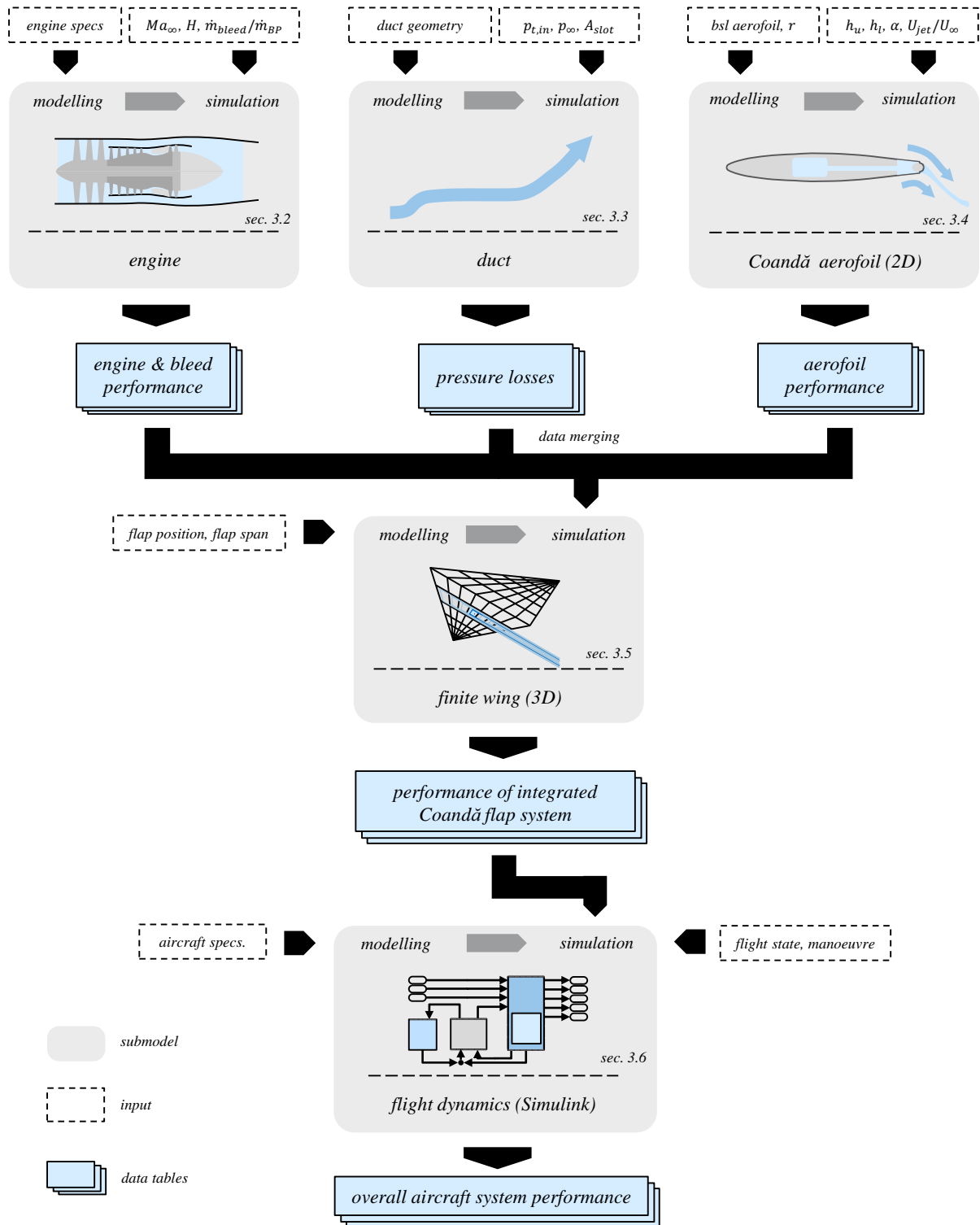
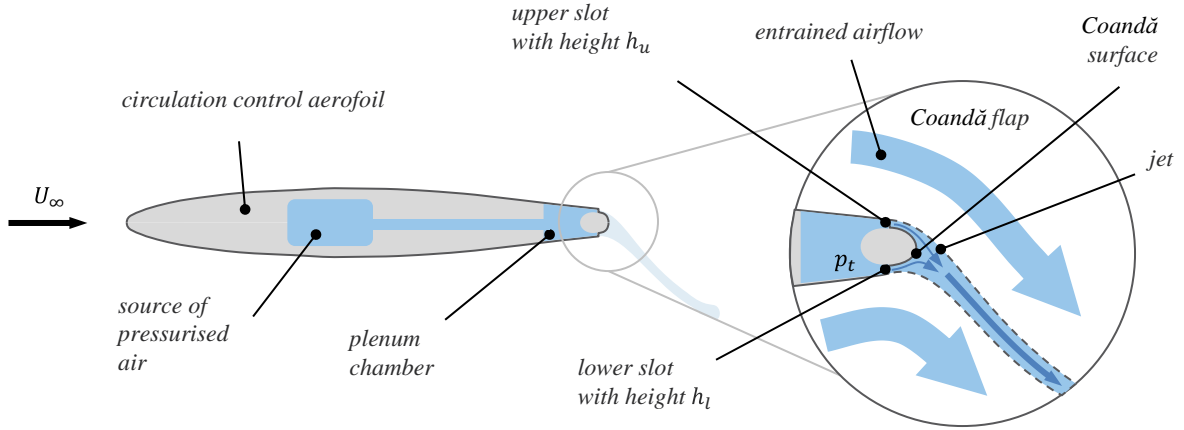


Figure 3.2: Overview of the overall system modelling process



**Figure 3.3:** Illustration of investigated Coandă flap concept (modified from STADLBERGER/HORNUNG, 2014, 2015a,b)

ber. So, the common outflow velocity solely depends on the pressure ratio defined by the total pressure  $p_{t,plenum}$  inside the plenum. The mass flow, and thereby the outflow momentum, can then be controlled by deformation of the flexible rear parts of the upper and lower skin, respectively. The vertical positions of the lips set the actual slot heights  $h_u$ ,  $h_l$  and specify the outflow momentum coefficients  $(C_\mu)_u = f(p_{t,plenum}, h_u)$  and  $(C_\mu)_l = f(p_{t,plenum}, h_l)$ . Depending on the outflow momentum ratio  $\frac{(C_\mu)_u}{(C_\mu)_l}$  of the upper and lower slot, the rear stagnation point (where both jets clash) is shifted downwards or upwards. Given a constant plenum pressure ratio, the control forces and moments are then determined by the combination of upper and lower slot sizes. Finally, the Coandă flap effectiveness depends on three control factors

$$(\Delta C_l, \Delta C_m, \Delta C_n)_{Coanda} = f(p_{t,plenum}, h_u, h_l) \quad (3.1)$$

where  $h_u$  and  $h_l$  can be adjusted directly and independently. In contrast, the plenum pressure  $p_{t,plenum}$  is subject to thrust setting  $\delta_T$  and subsystem interactions inside the fluidic flight control system. These interactions are illustrated in (Figure 3.4). At Mach number  $Ma_\infty$  and altitude  $H$ , the steady flight state requires a certain amount of net thrust  $F_N$ . With the associated throttle setting  $\delta_T$ , the engine compressor generates a total pressure  $p_{t,compr}$  which is further reduced along the ducts due to viscous losses. Inside the plenum chamber, it finally takes the value  $p_{t,plenum}$  and, together with the ambient pressure  $p_\infty$ , defines the jet outflow velocity at the trailing edge. Depending on the current slot heights  $h_u$  and  $h_l$ , the Coandă jet mass flow  $\dot{m}_{Coanda}$  leaves the slot exits having a total outlet area  $A_{slots}$ . Since the viscous pressure losses and the engine performance are a function of bleed mass flow  $\dot{m}_{bleed} = \dot{m}_{Coanda}$ ,

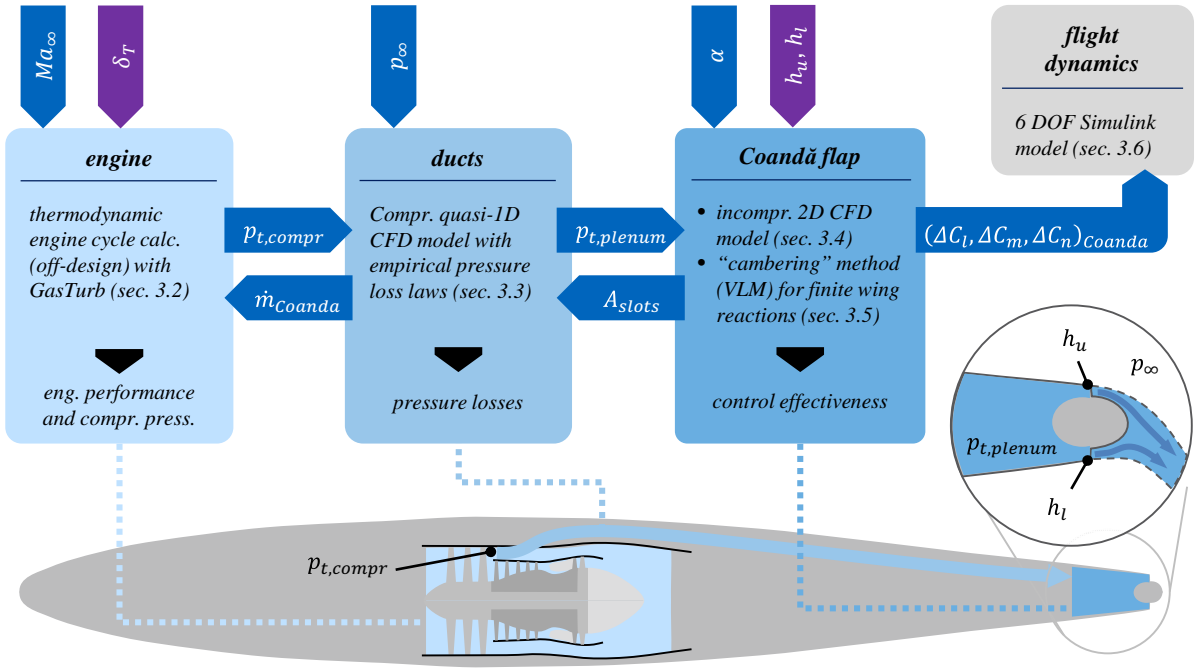


**Figure 3.4:** Illustration of subsystem model interactions

the final control moment authority  $(\Delta C_l, \Delta C_m, \Delta C_n)_{Coanda}$  is a result of subsystem coupling and fluid mechanical interactions. Under steady conditions, the overall system will attain a state of equilibrium which can be assessed in terms of control effectiveness.

Even though the overall system behaviour is a central part of this study, the flow control potential of the Coandă flap element is particularly interesting as well. Parametric studies will provide new insights as no extensive and systematically collected data is available in literature. In order to increase the informative value of the associated numerical results, the control factors  $h_u$  and  $h_l$  are translated into a combination of two equivalent parameters. For this, a new control parameter  $\eta_\mu$  is introduced which yields

$$\eta_\mu = \frac{(C_\mu)_u - (C_\mu)_l}{(C_\mu)_u + (C_\mu)_l} \quad (3.2)$$

This relative outflow momentum ratio is defined to be equivalent to a plain flap deflection and ranges from  $-1$  (flap deflected 100% upwards) to  $1$  (flap deflected 100% downwards). In the case of one common plenum pressure, the control parameter reduces approximately to the following expression

$$\eta_\mu \approx \eta_h = \frac{h_u - h_l}{h_{total}} \quad (3.3)$$

where  $h_{total} = h_u + h_l$  is the sum of upper and lower slot height  $h_u$  and  $h_l$ , respectively.

Again, the control parameter  $\eta_h$  spans the operational range from completely closed upper slot ( $h_l = h_{total} \rightarrow \eta_h = -1$ ) to completely closed lower slot ( $h_u = h_{total} \rightarrow \eta_h = 1$ ). These both borderline cases of asymmetric single slot blowing typically provide maximum control reactions.

Finally, the Coandă flap effectiveness can be described as a function of  $\eta_h$  and  $h_{total}$

$$(\Delta C_l, \Delta C_m, \Delta C_n)_{Coanda} = f(p_{t,plenum}, \eta_h, h_{total}) \quad (3.4)$$

This translation of  $(h_u, h_l)$  into  $(\eta_h, h_{total})$  increases the comparability to conventional plain flaps and simplifies the analysis of sensitivities.

## 3.2 Modelling of the Engine and Bleed Air Supply

For active flow control in the subsonic regime, the required bleed air is preferably taken from the bypass channel of a turbofan engine (Figure 3.5). Bleeding from the core engine usually leads to severe perturbations of the thermodynamic cycle and counteracts efficient thrust generation (GOLOGAN, 2009). Above all, the increased turbine entry temperature is critical for the structural stability of the high pressure turbine stage (RAHMAN, 2009, p. 91ff). Moreover, when air is bled after the first core engine compressor stages, the subsequent stages are prone to reduced surge margins. Of course, these penalties could be partially alleviated through customised engine design that explicitly aims for higher bleed fractions. But as bleed air demand varies significantly throughout the mission, a globally optimised core engine is difficult to realise. Especially in the current application, the low pressure

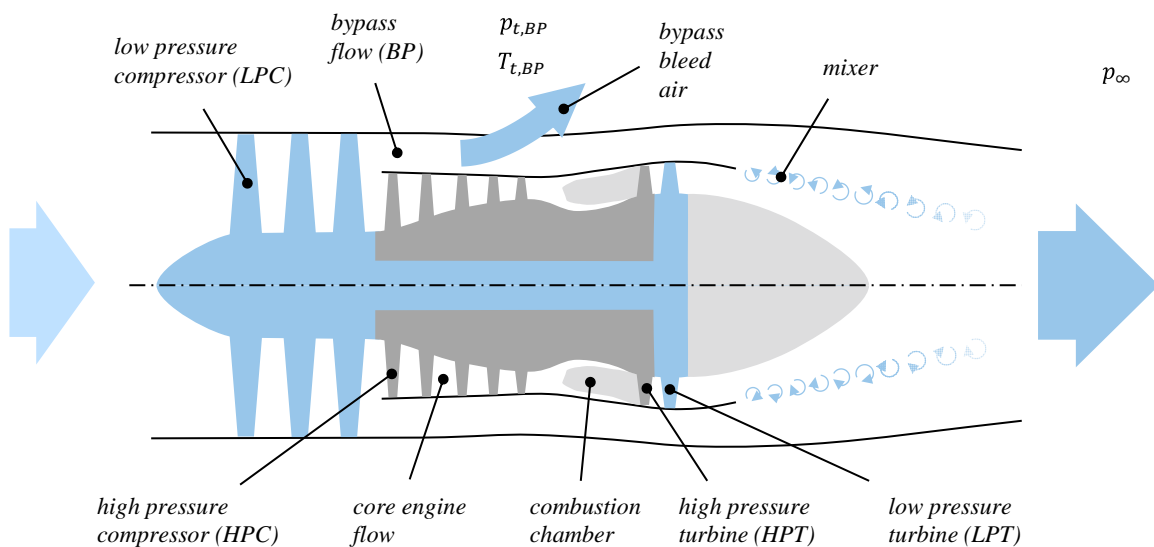


**Figure 3.5:** Illustration of a turbofan engine with bypass bleed concept

compressor (LPC = “fan”) of the intended engine provides adequate total pressure ratios  $\Pi = \frac{p_t}{p_\infty} \approx 2$ . They essentially lie inside the margins of secure blowing operation without supersonic jet detachment ( $Ma_{jet} \lesssim 1$ ). In principle, high pressure ratios from the high pressure compressor (HPC) would reduce friction losses inside the ducts. But this benefit is eliminated under the consideration of the necessary throttles which naturally cause an even stronger drop in total pressure. Moreover, the associated higher local temperatures are likely to cause structural complication with hot ducting through lightweight composite structures (e.g. CFRP). The same applies for exhaust offtake from the mixed nozzle flow. Therefore, the chosen bypass bleed approach is considered to be most appropriate for the studied aircraft and engine configuration. This conclusion is consolidated by refs. BARBERIE ET AL. (2013) and WICK ET AL. (2013) where a similar bleed concept was investigated numerically and experimentally for a STOL configuration.

The engine and bleed data set was calculated by use of the commercial software package GasTurb V12. Amongst other features, it allows to simulate the design and off-design performance of gas turbines (KURZKE, 1995), to optimise their thermodynamic cycle (KURZKE, 1999), and to estimate their transient behaviour (KURZKE, 2011). Since 1991, GasTurb has been developed by Dr. Joachim Kurzke at the turbine engine manufacturer MTU (german: MOTOREN- UND TRIEBWERKE UNION) and calculates the properties of a variety of predefined engine configurations (e.g. turbojet, turboshaft, separate- or mixed-stream turbofan, geared turbofan, etc.). Many of the formulae and algorithms used within GasTurb can be found in MÜNZBERG/KURZKE (1977). Considering real gas properties, the program estimates mass flows, pressures and efficiencies of the engine cycle. Input parameters are the studied engine geometry, the boundary conditions, and either the spool rotation speed or the turbine entry temperature. Moreover, the engine off-design performance can be retrieved by looping over altitude, Mach number, throttle position and various other operational parameters. Here, the software package also enables the processing of script files and the automated calculation of the correct pressures, temperatures and rotation speeds by performing internal iteration loops. For this work, the GasTurb scripts have been created by an automation algorithm in MATLAB and executed manually in GasTurb. Four parameters, prescribing the operating conditions, have been varied: altitude  $H$ , flight Mach number  $Ma$ , bypass bleed fraction  $\frac{\dot{m}_{bleed}}{\dot{m}_{BP}}$ , and throttle setting. The latter is represented by the normalised high pressure (HP) spool speed  $\Omega_{HP}^* = \frac{\Omega_{HP}}{(\Omega_{HP})_{design}}$ . The output data was retranslated into a MATLAB lookup table building the base of the engine subsystem model. Note that excessive bleed mass flows ( $\frac{\dot{m}_{bleed}}{\dot{m}_{BP}} \geq 0.5$ ) can lead to convergence problems. These points have been complemented by cubic spline interpolation or extrapolation.

For all calculations in the scope of this study, the implemented standard compressor and turbine maps have been used. The results for the isolated engine subsystem, including its sensitivity to bypass bleed, can be found in subsection 5.1.1.

### 3.3 Modelling of the Duct System

The duct system connects the compressor (engine LPC) with the Coandă flap element at the wing trailing edge. Dependent on the pipe geometry and ducted air mass flow, pressure losses have to be expected due to viscous effects (e.g. friction, local separations). In general, local curvatures and diameter changes should be designed as smooth as possible respecting the limited available space. Moreover, due to the risk of internal shocks, the pipe diameters should be chosen such that the smallest cross sectional area is located at the slot exit. Intermediate throats in duct systems can significantly increase the penalties of compressible effects when the mass flow rates reach critical values.

In the field of hydraulic system engineering, it is common to estimate the pressure losses by use of the theory of flow filament. Bernoulli's incompressible flow equation is combined with empirical pressure loss coefficients given for different shapes of pipe segments (SIGLOCH, 2003, p. 111ff). For general gas flows with changing density, however, this incompressible approach is invalid. Therefore, the compressible Navier-Stokes-Equations (subsection 3.3.1) are solved for a discretised, but reduced model of the pipe geometry. Under the assumption of an adiabatic quasi-1D flow of an ideal and perfect gas, the equations can be simplified such that their solution requires insignificant computational efforts. The implementation of the iterative solution procedure as well as the incorporation of empirical pressure loss coefficients is described in subsection 3.3.2. The application of this method can be found in subsection 5.1.2.

#### 3.3.1 Governing Equations

According to the finite volume method (VERSTEEG/MALALASEKERA, 2007, p. 9ff) the compressible fluid transport equations can be written in an integral form by using Gauss's divergence theorem. The continuity equation then is given by

$$\int_{CV} \frac{\partial \rho}{\partial t} dV + \int_A \vec{n} \cdot (\rho \vec{u}) dA = 0 \quad (3.5)$$

where the normal vectors on the control volume's (CV) boundary surfaces  $A$  are denoted by  $\vec{n}$ .

The Reynolds averaged momentum equation yields

$$\int_{CV} \frac{\partial (\rho u_i)}{\partial t} dV + \int_A \vec{n} \cdot (\rho u_i \cdot \vec{u}) dA = - \int_{CV} S_{p_i} dV + \int_A \vec{n} \cdot (\mu_{eff} \text{grad} u_i) dA + \int_{CV} S_{u_i} dV \quad (3.6)$$

where  $S_{p_i} = \frac{\partial p}{\partial x_i}$  constitutes the pressure source term and  $S_{u_i}$  an arbitrary momentum source

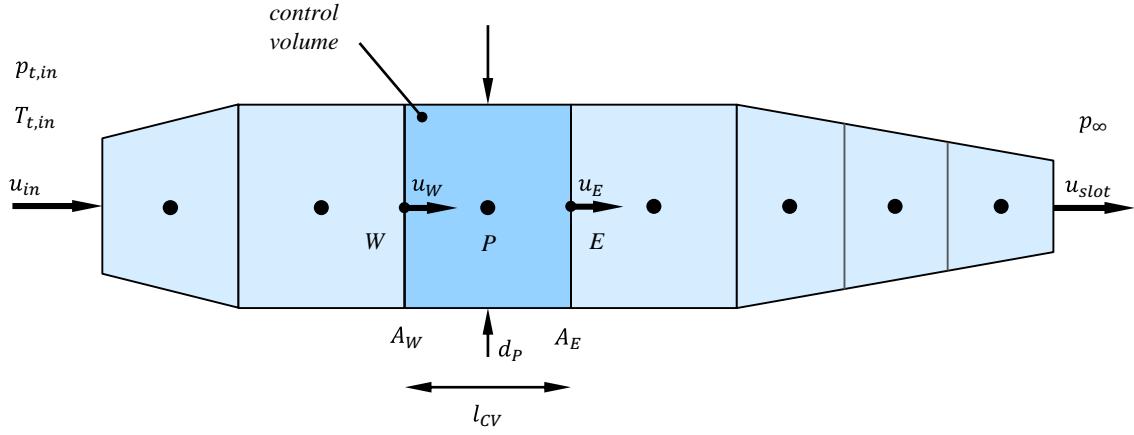


**Figure 3.6:** Illustration of duct model with discrete control volumes

term. Note that, according to the Boussinesq assumption, the effective viscosity  $\mu_{eff} = \mu + \mu_t$  contains the laminar viscosity  $\mu$  of the fluid and the eddy viscosity  $\mu_t$  due to time averaged turbulent fluctuations.

In analogy, the energy equation yields

$$\int_{CV} \frac{\partial(\rho C_v T)}{\partial t} dV + \int_A \vec{n} \cdot (\rho C_v T \cdot \vec{u}) dA = - \int_{CV} p \operatorname{div} \vec{u} dV + \int_A \vec{n} \cdot (k_{T,eff} \operatorname{grad} T) dA + \int_{CV} S_i dV \quad (3.7)$$

where  $S_i$  represents an arbitrary heat source term.

For an ideal gas, its density can be derived from the ideal gas law

$$p = \rho RT \quad (3.8)$$

### 3.3.2 Semi-Empirical Implementation

Considering a quasi-1D control volume of steady flow (Figure 3.6), Equation 3.5 and Equation 3.6 can be simplified to

$$\rho_W u_W A_W = \rho_E u_E A_E \quad (3.9)$$

$$p_W A_W + \rho_W u_W^2 A_W + \int_{A_W}^{A_E} p dA = p_E A_E + \rho_E u_E^2 A_E + \int_V S_u dV \quad (3.10)$$

As the cross section area along the duct is not constant, the pressure integral  $\int_{A_W}^{A_E} p dA$  for the upper (north) and lower (south) cell face still has to be determined. It is approximated

by  $\int_{A_W}^{A_E} p \, dA \approx \bar{p}(A_E - A_W)$ . The mean cell pressure  $\bar{p}$  can be approximated by  $\bar{p} \approx \frac{p_W + p_E}{2}$ .

Under the assumption of an adiabatic flow of ideal and perfect gas, i.e. no heat exchange through the pipe walls, the energy equation (Equation 3.7) can be converted to the following isentropic equation

$$T = T_0 \left( 1 + \frac{\kappa - 1}{2} Ma^2 \right)^{-1} \quad (3.11)$$

where the total temperature  $T_0$  is considered to be constant along the entire duct. The remaining isentropic equations can be found in the appendix (section C).

The pressure losses due to friction and turbulent processes inside the ducts are approximated by empirical relations. The pressure decrement  $\Delta p$  along a pipe segment with length  $L$  and hydraulic diameter  $D_{hydr}$  can be modelled by

$$\Delta p = -\frac{1}{2} \rho \bar{u}^2 \lambda_{visc} \frac{L}{D_{hydr}} \quad (3.12)$$

where  $\lambda_{visc}$  denotes the pressure loss factor due to viscous effects which has to be determined by empirical laws covering different pipe segment shapes. Note that the cross sections of the ducts are assumed to be of circular shape, i.e.  $D_{hydr} = 2R_{pipe}$ . The integral momentum sink term  $\int_V S_u \, dV$  in (Equation 3.10) can then be modelled by

$$\int_V S_u \, dV = \int_A \Delta p \, dA \approx \frac{1}{2} \rho u_P^2 \lambda_{visc} \frac{l_{CV}}{d_P} A_P = \frac{\pi}{8} \rho u_P^2 \lambda_{visc} l_{CV} d_P \quad (3.13)$$

where  $l_{CV}$  denotes the length of the control volume.  $u_P$ ,  $d_P$  and  $A_P$  represent the flow velocity, the diameter and cross sectional area at the control volume centre, respectively. The pressure loss coefficient  $\lambda_{visc}$  is defined by

$$\lambda_{visc} = \lambda_{fric} (1 + f_{bend}) + \lambda_{sep} \quad (3.14)$$

where the Darcy/Weisbach friction factor  $\lambda_{fric}$  represents the pressure losses due to friction and shear stresses inside the developed boundary layer. The additional pressure loss supplement  $f_{bend}$  introduces increased pressure losses due to three-dimensional effects and separations inside pipe bends.  $\lambda_{sep}$  further accounts for possible flow detachments and recirculations that likely occur in diverging duct segments. The respective coefficients are given as follows:

For laminar flow ( $Re_d < 2320$ ) the friction factor  $\lambda_{fric}$  is given by the Hagen/Poiseuille law

(SIGLOCH, 2003, p. 114) and can be modelled by

$$\lambda_{fric} = \frac{64}{Re_d} \quad (3.15)$$

with the pipe segment Reynolds number  $Re_d = \frac{u_P \bar{d}_P}{\nu_P}$ .

For turbulent flow the friction factor  $\lambda_{fric}$  can be estimated according to Colebrook/White (SIGLOCH, 2003, p. 120)

$$\frac{1}{\sqrt{\lambda_{fric}}} = -2 \log \left( \frac{2.51}{Re_d \sqrt{\lambda_{fric}}} + 0.27 \frac{k_s}{d_P} \right) \quad (3.16)$$

According to Herring (WAGNER, 2012, p. 99f.) the pressure loss supplement  $f_{bend}$  of a pipe bend with radius  $r_{bend}$  and bend angle  $\vartheta_{bend}$  can be approximated by

$$f_{bend} = c_{bend} \sqrt{\frac{\vartheta_{bend} \bar{d}_P}{\pi/2} \frac{1}{L}} \quad (3.17)$$

where the coefficient  $c_{bend}$  depends on the bend aspect ratio  $\sigma_{bend} = \frac{r_{bend}}{d_P}$  and is given by

$$c_{bend} = \begin{cases} \frac{15.2}{\frac{3}{4}} & \sigma_{bend} < 2 \\ \sigma_{bend} & 2 \leq \sigma_{bend} \leq 8 \\ \frac{12.8}{\sqrt{\sigma_{bend}}} & 2 \leq \sigma_{bend} \leq 8 \\ 1.6\sigma_{bend} & \sigma_{bend} \geq 8 \end{cases} \quad (3.18)$$

The influence between two successive pipe bends was neglected in the scope of this work.

The separation loss factor  $\lambda_{sep}$  approximates the pressure losses caused by separations inside diverging pipe segments (diffusor) (CZICHOS/HENNECKE, 2004, p. E145) and is given by

$$\lambda_{sep} = k_\phi \left( 1 - \left( \frac{d_W}{d_E} \right)^2 \right) \frac{\bar{d}_P}{L} \quad (3.19)$$

where the empirical correction factor  $k_\phi$  can be interpolated using the values in Table 3.1. Pressure losses inside throats which likely occur after converging pipe segments were not taken into account. It is assumed that the only converging nozzle segment is situated at the end of the duct system.

The presented theory and empirical relations were implemented in the MATLAB environment from MATHWORKS. The developed function processes an arbitrary discretised duct geometry, i.e. the pipes are divided into a chosen number of control volumes. Input parameters are the inlet total pressure  $p_{t,in}$ , the inlet total temperature  $T_{t,in}$ , and the static pressure  $p_{s,exit}$  at the duct exit. For robustness reasons, the unconditionally stable upwind

**Table 3.1:** Empirical correction factor  $k_\phi$ 

Diffusor angle $\phi_{diff}$ [deg]	Correction factor $k_\phi$ [-]
5	0.13
7.5	0.14
10	0.16
15	0.27
20	0.43
40	1
180	1

differencing scheme is employed which prevents numerical instabilities due to coarse discretisation. To avoid non-physical, discretisation induced pressure oscillations, a staggered grid approach was chosen for velocity components and scalar parameters (HARLOW/WELCH, 1965). A coupled pressure-based solver strategy, implying a combined system of linear equations (SLE), has been implemented. The built-in MATLAB function `mldivide` solves the SLE of the momentum (Equation 3.10) and continuity (Equation 3.9) equations simultaneously. Then Equation 3.11 is used to update the static temperature after each iteration. The boundary conditions are determined by the total pressure  $p_{t,in}$  and the total temperature  $T_{t,in}$  at the duct inlet as well as by the static pressure  $p_{s,exit}$  at the outlet, i.e. slot. For purely subsonic flow, the inlet velocity  $u_{in}$  is set according to the pressure ratio  $\left(\frac{p_t}{p}\right)_{in}$  at the inlet and has to be updated at each iteration step. With increasing bypass pressure ratio  $\Pi_{BP} = \frac{p_{t,BP}}{p_{s,exit}} = \frac{p_{t,in}}{p_{s,exit}}$  at the duct inlet, the flow reaches critical conditions  $Ma^* = 1$  at the section featuring minimum cross section area  $A^* = A_{min}$ . Under “choked” conditions, the inlet velocity  $u_{in}$  is given by the mass flow rate  $\dot{m}_{in} = \dot{m}^* = \rho^* u^* A^*$ . Note that the static pressure boundary condition at the outlet also has to be readjusted for supercritical flow, when the air at the exit is underexpanded. The exit pressure then yields  $p_{s,exit} = p^*$  where the critical static pressure is a function of the total pressure at the outlet  $p^* = f(p_{t,out})$ . The involved isentropic flow equations can be found in the appendix (section C).

### 3.3.3 Validation

For validation purposes, the inviscid results ( $\int_V S_u dV = 0$ ) of the MATLAB implementation were compared with results given by the isentropic flow equations (section C in the appendix). The tested duct system geometry is given in Figure 5.5 on page 88. Figure 3.7 shows the relative deviation of the local flow parameters which, in the isentropic case, are a function of total conditions and local Mach number. Maximum discrepancy is found in regions of significant cross section area change but remains well below 0.5%. In order to check the impact of discretisation, the number of discrete control volumes was varied for

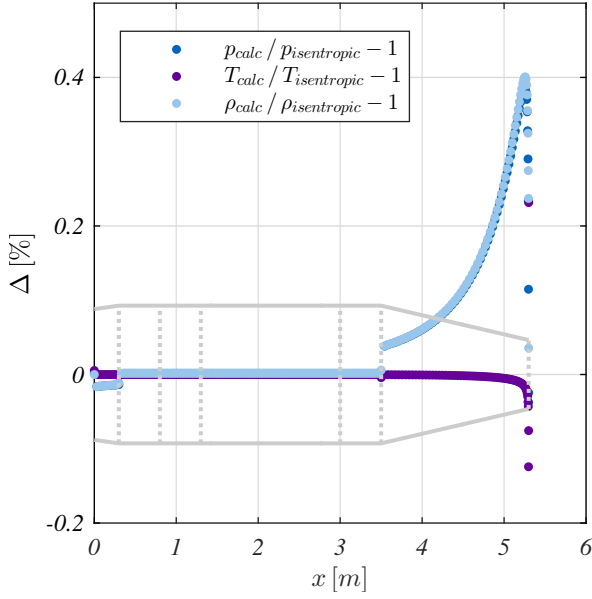


**Figure 3.7:** Relative deviation of inviscid results from isentropic flow equations

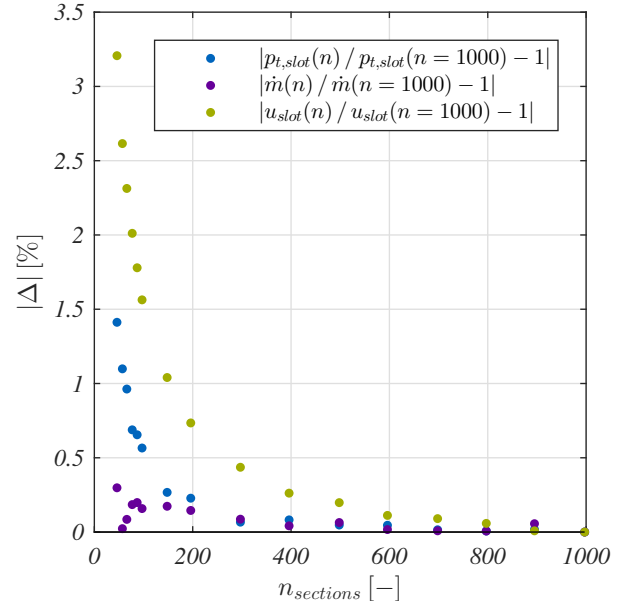


**Figure 3.8:** Relative variation of results as function of discretisation

identical boundary conditions. As can be seen in Figure 3.8, the relative difference of the most relevant flow properties drops below 1% for a number of 200 duct sections. For this comparison, the results of the finest grid ( $n_{sections} = 1000$ ) served as reference. Therefore, a discretisation of  $n_{sections} = 200$  was used for subsequent calculations whose results can be found in subsection 5.1.2. A possible error of 1% was judged to be acceptable in view of the simplifications made within the underlying semi-empirical method.

## 3.4 Modelling of the Coandă Aerofoil (2D)

According to the chosen segregated approach of Coandă flap modelling, the flow control potential is modelled and studied in the two-dimensional case first. Later, the 2D aerofoil data can be translated to three-dimensional aerodynamic reactions of the finite wing (section 3.5). The following subsections therefore describe the method used to estimate the 2D section aerodynamics under different blowing conditions, i.e. plenum pressures. Once the total pressure in the plenum chamber of the Coandă flap element is defined (section 3.2 and section 3.3), the jet exit velocity  $U_{jet}$  can be retrieved by use of the isentropic flow equations (section C in the appendix). The latter assume isentropic expansion up to the slot exit position where the Coandă jet is finally ejected to free stream. This simplification is considered to be valid for strongly accelerating, relaminarised flow in the Coandă flap nozzle.

With given slot heights  $h_u$ ,  $h_l$  and free stream conditions  $U_\infty$ , the resulting blowing inten-

sity  $C_\mu$  (Equation 2.1) determines the lift ( $\Delta c_l$ ), drag ( $\Delta c_d$ ) and pitching moment ( $\Delta c_m$ ) increments of the affected wing sections. For the estimation of these forces and moments on the 2D Coandă aerofoil, the steady Reynolds Averaged Navier-Stokes (RANS) equations (subsection 3.4.1) are processed numerically (subsection 3.4.3). In general, most of the underlying theory and its numerical treatment presented in this section relies on fundamentals compiled by FERZIGER/PERIĆ (2002) and VERSTEEG/MALALASEKERA (2007). Turbulence closure is achieved through a modified version of Menter's SST turbulence model (subsection 3.4.2 and subsection 3.4.5). As already mentioned before (subsection 2.4.4), the fluid of the given flow problem is considered as an incompressible Newtonian fluid to reduce computational efforts and to stabilise convergence. Past numerical studies have shown negligible influence of jet compressibility up to at least exit velocities of  $Ma_{jet} = 0.64$  (RUMSEY/NISHINO, 2011). The implementation of the 2D modelling method also comprises an automated mesher and convergence detection (subsection 3.4.4). Finally, the method's applicability is to be proven on wind tunnel test cases from literature (subsection 5.1.3). Parts of this section can also be found in STADLBERGER/HORNUNG (2014) and STADLBERGER/HORNUNG (2015b).

### 3.4.1 Governing Equations

For the steady simulation of an incompressible fluid, the continuity equation (Equation 3.5) reduces to

$$\int_A \vec{n} \cdot \vec{u} dA = 0 \quad (3.20)$$

Neglecting any further surface and body forces (e.g. gravity force, centrifugal force, Coriolis force), the momentum equation (Equation 3.6) then finally yields

$$\int_A \vec{n} \cdot (u_i \cdot \vec{u}) dA = - \int_{CV} S_{p_i} dV + \int_A \vec{n} \cdot (\nu_{eff} \text{grad } u_i) dA \quad (3.21)$$

where the effective viscosity is given by  $\nu_{eff} = \nu + \nu_t$ . For the determination of the kinematic eddy viscosity  $\nu_t$ , i.e. for the closure of the RANS equations, Florian Menter's  $k$ - $\omega$ -models (BSL/SST) (MENTER, 1994; MENTER ET AL., 2003) were selected. They estimate the extra turbulent stress terms evolving from time-averaged turbulent velocity fluctuations. The details of the implemented turbulence model are described in subsection 3.4.2 and subsection 3.4.5.

**Table 3.2:** Turbulence model coefficients of Menter's BSL model

coefficient	$k$ - $\omega$ -model ( $F_1 = 1$ )	$k$ - $\varepsilon$ -model ( $F_1 = 0$ )
$\sigma_k$	0.5	1
$\sigma_\omega$	0.5	0.856
$\beta$	3/40	0.0828
$\beta^*$	0.09	0.09
$\gamma$	5/9	0.44

### 3.4.2 Baseline Turbulence Model

The steady state, incompressible formulation of Menter's original turbulence model (MENTER, 1994) consists of two transport equations. The turbulent kinetic energy  $k$  is given by

$$\operatorname{div}(k \vec{u}) = \operatorname{div}[(\nu + \sigma_k \nu_t) \operatorname{grad} k] + (\nu P)_k - \beta^* k \omega \quad (3.22)$$

with the production term  $P = 2 \left[ \left( \frac{\partial u}{\partial x} \right)^2 + \frac{1}{2} \left( \frac{\partial u}{\partial y} + \frac{\partial v}{\partial x} \right)^2 + \left( \frac{\partial v}{\partial y} \right)^2 \right]$ .

The turbulence frequency  $\omega$  is given by

$$\operatorname{div}(\omega \vec{u}) = \operatorname{div}[(\nu + \sigma_\omega \nu_t) \operatorname{grad} \omega] + \gamma P - \beta \omega^2 + 2(1 - F_1) \frac{\sigma_\omega}{\omega} \left( \frac{\partial k}{\partial x} \frac{\partial \omega}{\partial x} + \frac{\partial k}{\partial y} \frac{\partial \omega}{\partial y} \right) \quad (3.23)$$

where the blending function  $F_1$  is defined by

$$F_1 = \tanh \left\{ \left\{ \min \left[ \max \left( \frac{\sqrt{k}}{\beta^* \omega d_w}, \frac{500\nu}{d_w^2 \omega} \right), \frac{4\rho\sigma_\omega k}{CD_{k\omega} d_w^2} \right] \right\}^4 \right\} \quad (3.24)$$

with  $CD_{k\omega} = \max \left( 2\rho \frac{\sigma_\omega}{\omega} \left( \frac{\partial k}{\partial x} \frac{\partial \omega}{\partial x} + \frac{\partial k}{\partial y} \frac{\partial \omega}{\partial y} \right), 10^{-10} \right)$  and  $d_w$  as the distance to the nearest wall.  $F_1$  is equal to zero away from the surface ( $k$ - $\varepsilon$ -model) and switches over to one inside the boundary layer ( $k$ - $\omega$ -model). The constants of the model are blended accordingly using

$$c_i = F_1 c_{k-\omega} + (1 - F_1) c_{k-\varepsilon} \quad (3.25)$$

whose original coefficients for the BSL model are given in Table 3.2.

To prevent the build-up of turbulence in stagnation regions, the production term of turbulent kinetic energy  $(\nu P)_k$  is limited using

$$(\nu P)_k = \min((\nu P)_k, 10\beta^* \rho k \omega) \quad (3.26)$$

For the baseline model (BSL), the turbulent eddy viscosity finally yields

$$\nu_t = \frac{k}{\omega} \quad (3.27)$$

For the shear-stress-transport-model (SST), the constant coefficient  $\sigma_k$  changes to 0.85 and the eddy viscosity is limited through the following expression

$$\nu_t = \frac{a_1 k}{\max(a_1 \omega, \sqrt{P} F_2)} \quad (3.28)$$

where the constant  $a_1$  equals 0.31 and  $F_2$  is a second blending function which is defined as

$$F_2 = \tanh \left[ \max \left( \frac{2\sqrt{k}}{\beta^* \omega d_w}, \frac{500\nu}{d_w^2 \omega} \right)^2 \right] \quad (3.29)$$

The boundary condition for the turbulent kinetic energy  $k$  on no-slip walls is  $(k)_{wall} = 0$ . For  $\omega$ , the boundary condition values are calculated according to HELLSTEN (1998) and yield

$$(\omega)_{wall} = \frac{u_\tau^2}{\nu} S_R \quad (3.30)$$

where  $u_\tau$  is the friction velocity  $u_\tau = \sqrt{\tau_w/\rho}$  and  $S_R$  is a non-dimensional function defined as

$$S_R = \begin{cases} (50/\max(k_s^+, k_{s,min}^+))^2 & \text{for } k_s^+ < 25 \\ 100/k_s^+ & \text{for } k_s^+ \geq 25 \end{cases} \quad (3.31)$$

Here,  $k_s^+$  is the non-dimensional sand-grain height  $k_s^+ = u_\tau k_s/\nu$  where its lower limit is given by  $k_{s,min}^+ = 2.4(y^+)_{wall}^{0.85}$  for ideally smooth surfaces. This limit depends on the non-dimensional height  $(y^+)_{wall}$  of the first computational cell adjacent to the wall.

### 3.4.3 Numerical Implementation

The following paragraphs describe the strategy pursued for the implementation of the previously presented theory.

**Differencing Scheme and Staggered Grid** The current implementation relies on the hybrid differencing scheme which combines both upwind and central differencing schemes (SPALDING, 1972). Depending on the local Peclet number, the second-order accurate central differencing scheme or the unconditionally stable upwind differencing scheme is employed.

This method prevents numerical instabilities due to coarse discretisation. Furthermore, to avoid a non-physical discretisation induced “checker-board” pressure field, a staggered grid approach for velocity components and scalar parameters has been implemented (HARLOW/WELCH, 1965).

**Development Environment and Coupled Solver** The steady incompressible RANS equations (subsection 3.3.1) are processed inside the MATLAB environment from MATHWORKS. A coupled solver strategy with a combined system of linear equations (SLE) was set up solving the momentum and continuity equations simultaneously. MATLAB includes an ample library of regularly optimised built-in functions which help to treat common mathematical and geometrical problems in a naturally parallelised manner. During the iterative process, the solution of the SLE constitutes the main fraction in terms of computational cost. The corresponding function `mldivide` is based on FORTRAN subroutines (UMFPACK) and calculates this step at high performance. Unfortunately, it is only partially parallelised up to now so that the full computational power of a cluster cannot be exploited yet. However, for large calculation campaigns the calculations can be parallelised in macro scale. Each of these simulations is launched on only one single CPU core instead of processing one calculation on several cores.

**Under-Relaxation** Although a stabilising coupled approach is used for the solution of the flow field, the non-linear character of the partial differential equations (PDEs) usually requires under-relaxation to assure a robust calculation process. Therefore, the velocity field  $\vec{u}^n$  is updated by only a portion of the new SLE solution  $\vec{u}_{new}$ .

$$\vec{u}^n = f_{\Delta}^n \vec{u}_{new} + (1 - f_{\Delta}^n) \vec{u}^{n-1} \quad (3.32)$$

The under-relaxation factor  $f_{\Delta}^n$  is permanently adapted according to the following expression

$$f_{\Delta}^n = \frac{\left(\frac{|\Delta \vec{u}|}{U_{\infty}}\right)_{max}}{\max(|(u, v)_{new} - (u, v)^{n-1}|_{i,j}) / U_{\infty}} \quad (3.33)$$

where the maximum allowed velocity change  $\left(\frac{|\Delta \vec{u}|}{U_{\infty}}\right)_{max}$  has to be predefined. Here, a compromise has to be made between convergence rate and robustness. In this implementation, the velocity change is redefined at each iteration  $n$  according to the relations given in Table 3.3. Depending on the jet velocity excess  $\frac{U_{jet}}{U_{\infty}}$ , the allowed velocity change increases during the first 20 iterations and decreases to low levels when a number of 250 iterations is exceeded. This assures robustness during the first iterations where the flow field is still

**Table 3.3:** Law of under-relaxation for PDE solution

$n_{iter}$	$\left(\frac{ \Delta \vec{u} }{U_\infty}\right)_{max}$
1	
↓	$0.2 \cdot \frac{U_{jet}}{U_\infty}$
5	
↓	$0.5 \cdot \frac{U_{jet}}{U_\infty}$
20	
↓	$\min\left(0.1 \cdot \frac{U_{jet}}{U_\infty}, 0.4\right)$
50	
↓	$\min\left(0.05 \cdot \frac{U_{jet}}{U_\infty}, 0.2\right)$
250	
↓	$\min\left(0.02 \cdot \frac{U_{jet}}{U_\infty}, 0.1\right)$
350	
↓	$\min\left(0.01 \cdot \frac{U_{jet}}{U_\infty}, 0.05\right)$
$\infty$	

characterised by unbalanced velocity gradients. Then, increasing velocity changes accelerate the solution process until  $n = 50$  and finally flatten a possibly volatile convergence behaviour when a large number of iterations ( $n \geq 250$ ) has already been calculated. These calculation rules constantly gave satisfactory results throughout the numerous simulations performed within this study.

### 3.4.4 Automatic Meshing and Calculation

For automation, several features have been implemented as the tool is intended to be used for large calculation campaigns consisting of more than 10 000 simulations. The widespread parameter variations therein have to be calculated on several machines simultaneously. For this, a MATLAB script creates batch job files that can be processed by the available machines/CPUs (“workers”) in a parallelised manner. Besides various simulation settings, the job files contain Coandă aerofoil geometry data (i.e. baseline aerofoil, Coandă radius  $r$ , slot sizes  $h_u, h_l$ ), free stream conditions ( $U_\infty, \alpha_\infty$ ) and an array of jet outflow velocities  $\left(\frac{U_{jet}}{U_\infty}\right)_i$ . After the launch of the calculation campaign, each worker performs the following steps (see also Figure 3.9):

Based on the given geometry data, an automated meshing algorithm creates an orthogonalised structured curvilinear baseline grid (❶). Then, the nodes close to the slots are compressed and stretched according to the given slot heights (❷). After the definition of the free stream conditions (❸) and the estimation of the initial flow field properties through poten-

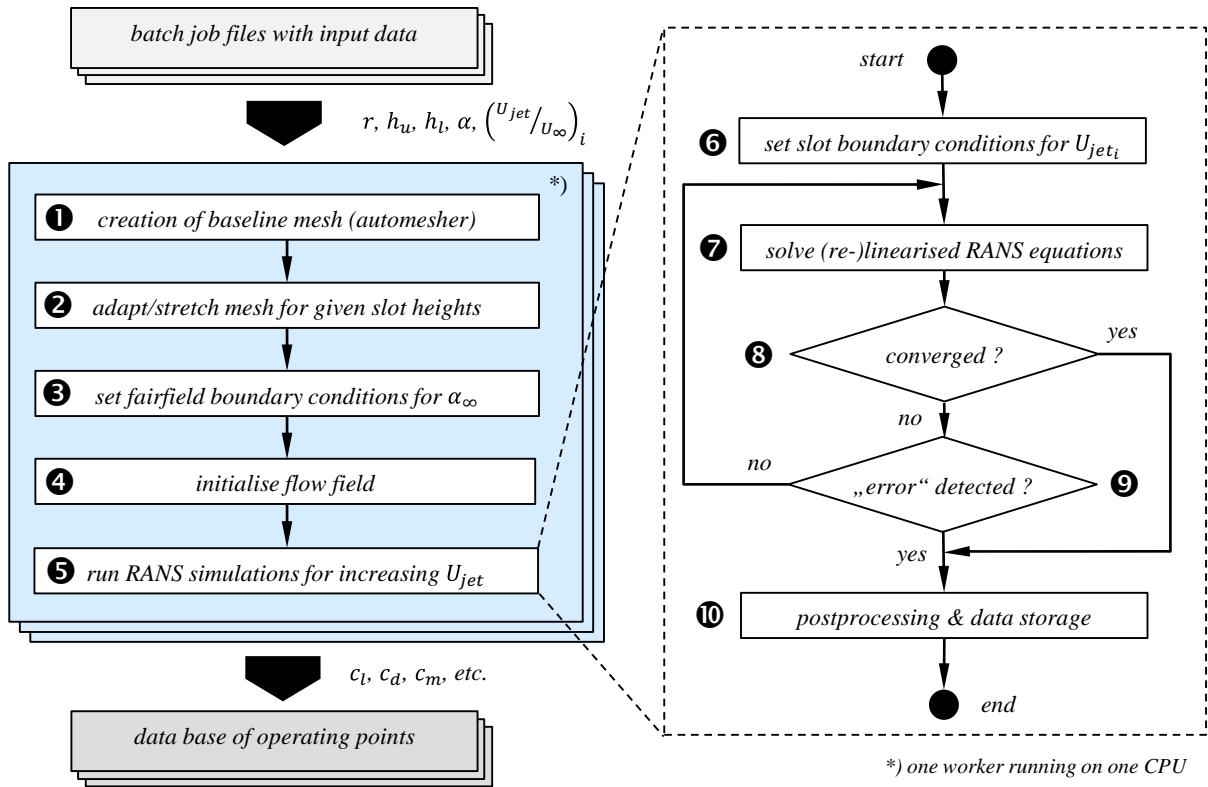


**Figure 3.9:** Illustration of the calculation procedure during a calculation campaign

tial flow (4), the actual simulation process starts (5). The batch job files are structured such that one file contains the information for a sequence of simulations with increasing jet outflow velocity  $\left(\frac{U_{jet}}{U_{\infty}}\right)_i$  while all other settings are kept constant. So, the subsequent calculations can be initialised by the precedent solutions to speed up convergence. Only the slot boundary conditions have to be updated (6). As illustrated in the detailed flow chart on the right hand side of Figure 3.9, each simulation is monitored at runtime. After each intermediate solution of the linearised RANS equations (7), i.e. solution of the SLE, automated checks are performed to identify proper convergence (8) or irregularities as jet wrap-around and leading edge separation (9). Both of them can terminate the current simulation process which is followed by post-processing and data storage (10). Finally, the successfully converged simulation files build the basis for the assembly of the aerodynamic data table that contains most of the operating points earlier defined by the input batch job files. The following paragraphs provide more details about the most noteworthy methods involved in this calculation procedure.

**Meshing (1, 2)** At first, a coordinate list of contour points is read in for the definition of an arbitrary baseline aerofoil geometry. Alternatively, the contour coordinates of the NACA families can be retrieved automatically by means of an integrated external NASA tool (naca456). On the basis of further geometry information as trailing edge radius  $r$  and

nominal slot heights  $(h_u, h_l)_0$ , the trailing edge of the baseline aerofoil is cut at the  $x$ -position where the aerofoil thickness equals  $t = r + (h_u)_0 + (h_l)_0 + h_{lip,u} + h_{lip,l}$ . The subsequent modelling of the new blunt trailing edge shape (circular or elliptic) finally defines the new contour of the Coandă aerofoil. An automated mesher then creates a structured grid for nominal slot opening conditions (“baseline grid”:  $(h_u, h_l) = (h_u, h_l)_0$ ) (1). For this, an algebraic initialisation with controllable density functions for varying grid point distributions provides an initial curvilinear grid featuring node refinement towards walls. In general, increased accuracy and robustness of the solution can be obtained by use of orthogonalised meshes. Therefore, a subsequent orthogonalisation process has been implemented according to THOMPSON ET AL. (1999, chapter 6). The coordinate functions  $\vec{x}(\xi, \eta) = \begin{pmatrix} x(\xi, \eta) & y(\xi, \eta) \end{pmatrix}^T$  of the grid points on the curvilinear grid lines along  $\xi$  and  $\eta$  are iteratively relaxed until they satisfy the following quasi-linear elliptic system of equations

$$g_{22}(\vec{x}_{\xi\xi} + P\vec{x}_{\xi}) - 2g_{12}\vec{x}_{\xi\eta} + g_{11}(\vec{x}_{\eta\eta} + Q\vec{x}_{\eta}) = 0 \quad (3.34)$$

where

$$\begin{aligned} g_{11} &= x_{\xi}^2 + y_{\xi}^2, \\ g_{12} &= x_{\xi}x_{\eta} + y_{\xi}y_{\eta}, \\ g_{22} &= x_{\eta}^2 + y_{\eta}^2. \end{aligned}$$

After discretisation of the derivatives  $x_{\varphi} = \frac{\partial x}{\partial \varphi}$ ,  $x_{\varphi\varphi} = \frac{\partial^2 x}{\partial \varphi^2}$  and reordering, the resulting SLE is solved by use of the MATLAB embedded function `mldivide`. At each iteration, the grid points are shifted towards a uniformly spaced orthogonal curvilinear grid. Note that under-relaxation is necessary to stabilise the solution process. To retain the non-uniform spacing (e.g. refinement inside boundary layers) of the initial algebraic grid, the orthogonal control functions  $P$  and  $Q$  have to be found by solving the following linear system

$$\begin{pmatrix} g_{22}x_{\xi} & g_{11}x_{\eta} \\ g_{22}y_{\xi} & g_{11}y_{\eta} \end{pmatrix} \begin{pmatrix} P \\ Q \end{pmatrix} = \begin{pmatrix} 2g_{12}x_{\xi\eta} - g_{22}x_{\xi\xi} - g_{11}x_{\eta\eta} \\ 2g_{21}y_{\xi\eta} - g_{22}y_{\xi\xi} - g_{11}y_{\eta\eta} \end{pmatrix} \quad (3.35)$$

However, to assure orthogonality at the boundaries, the functions  $P$  and  $Q$  are evaluated at these nodes using

$$\begin{pmatrix} P \\ Q \end{pmatrix} = \begin{pmatrix} -\frac{\vec{x}_{\xi} \cdot \vec{x}_{\xi\xi}}{g_{11}} - \frac{\vec{x}_{\xi} \cdot \vec{x}_{\eta\eta}}{g_{22}} \\ -\frac{\vec{x}_{\eta} \cdot \vec{x}_{\eta\eta}}{g_{22}} - \frac{\vec{x}_{\eta} \cdot \vec{x}_{\xi\xi}}{g_{11}} \end{pmatrix} \quad (3.36)$$

and interpolated to the interior. At each iteration, the different values of  $P$  and  $Q$  from

Equation 3.35 and Equation 3.36 must be smoothly blended from the boundary to the interior using an appropriate blending function.

To speed up the meshing of different slot geometries, this orthogonalisation process is performed only on the baseline grid defined by  $r$  and  $(h_u, h_l)_0$ . The current slot sizes  $h_u, h_l$  are introduced by manipulation of the nodes close to the slots (❷). The efficiency of this approach relies on the fact that the baseline meshes can be stored and reloaded to avoid the computational expensive orthogonalisation process for subsequent simulations. In the slot regions, the compressed and stretched grid finally represents the contour of the bended rear fraction of the aerofoil skin. According to the fundamental solution of the fixed beam problem, the bended contour line was approximated by a cubic spline. As the node displacements are relatively small, the initial grid orthogonality is not affected significantly. Examples of automatically created grids by use of the presented method can be found in Figure 3.12 and Figure 5.9.

**Flow Field Initialisation (❹)** In order to increase robustness and convergence rate at the first operating point given by  $\left(\frac{U_{jet}}{U_\infty}\right)_i$ , the flow field is initialised by an approximated inviscid solution evolving from potential theory. Discrete potential vortices and respective control points are distributed along the aerofoil contour. They model the inviscid flow field which finally is defined by the Kutta condition at the trailing edge. A guessed angle  $\Theta'_{sep}$  sets the aft stagnation point on the Coandă surface and closes the SLE to determine the potential vortex strengths.

**Convergence Detection (❸)** A convergence detection enables the premature completion of each single calculation and leads to significant time savings. The stop criteria are based on the history chart of the lift coefficient. The variance  $|c_l - \bar{c}_l|$  and slope  $|\frac{dc_l}{dn_{iter}}|$  of its 1<sup>st</sup> order regression (line) are used to terminate the calculation if both of the following conditions are true

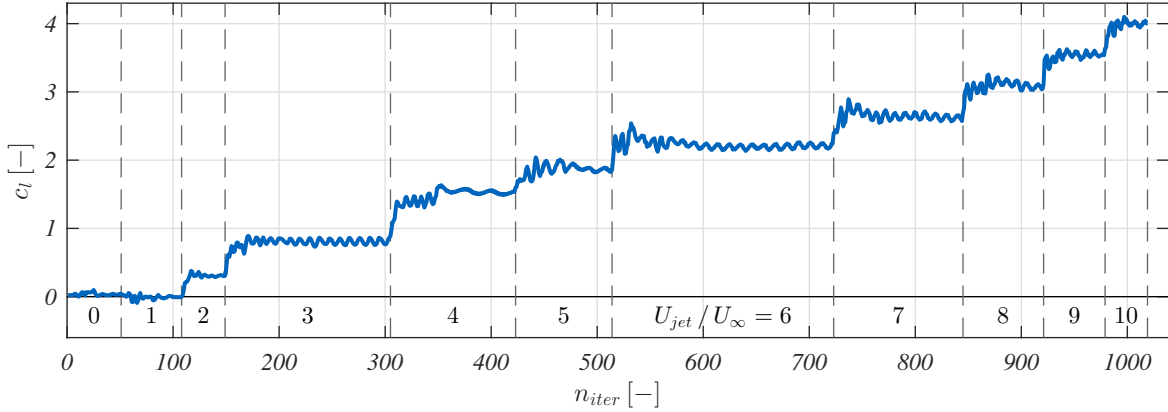
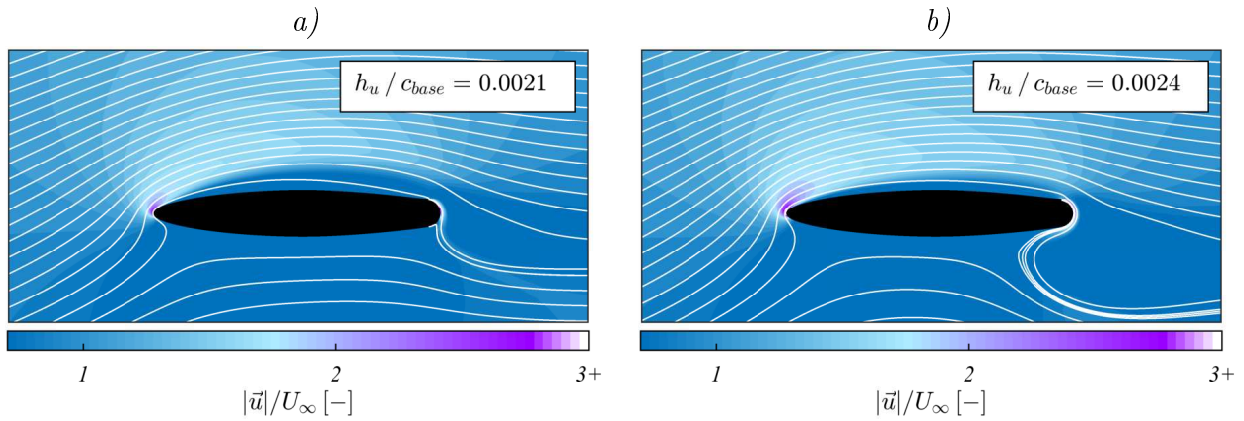
$$\left|\frac{dc_l}{dn_{iter}}\right| < \sigma_1 \vee \left|\frac{dc_l}{\bar{c}_l}\right| < \sigma_2 \quad (3.37)$$

$$\max(|c_l - \bar{c}_l|) < \sigma_3 \vee \max\left(\frac{|c_l - \bar{c}_l|}{|\bar{c}_l|}\right) < \sigma_4 \quad (3.38)$$

Either the absolute or the relative representation of the variance and slope values can trigger the compliance of each condition to cover a wide range of blowing conditions  $\frac{U_{jet}}{U_\infty}$ . High jet velocities usually imply strong variations in  $c_l$ . For the calculation campaigns performed within this study, the threshold values of Table 3.4 provided satisfactory results. As a compromise between robustness and convergence speed, the history of the precedent 20 iterations

**Table 3.4:** Proposed threshold values for convergence detection

$\sigma_1$	$5 \times 10^{-4}$
$\sigma_2$	$5 \times 10^{-3}$
$\sigma_3$	$2 \times 10^{-2}$
$\sigma_4$	$2 \times 10^{-2}$

**Figure 3.10:** Lift coefficient history of an exemplary calculation with increasing jet outflow velocity ratios  $U_{jet}/U_{\infty}$ **Figure 3.11:** Flow field of “erroneous” calculations with leading edge separation (a) and jet wrap-around (b),  $\alpha = 10deg$ ,  $\frac{r}{c_{base}} = 0.035$ ,  $\frac{U_{jet}}{U_{\infty}} = 5$ ,  $\frac{h_l}{c_{base}} = 0$ 

was evaluated. Figure 3.10 shows the lift coefficient history of an exemplary calculation with automated convergence detection for increasing jet outflow velocity ratios  $0 \leq \frac{U_{jet}}{U_{\infty}} \leq 10$ . The vertical dashed lines indicate the completion of each operating point before the slot boundary conditions are changed for the subsequent jet velocity  $\frac{U_{jet}}{U_{\infty}}$  (Ⓔ).

**“Error” Catching (Ⓕ)** In addition, problem specific flow phenomena as leading edge separation (Figure 3.11a) and jet wrap-around (Figure 3.11b and subsection 2.4.2) are detected at runtime. These “errors” are identified through flow direction checks on the front half of the aerofoil surface and through monitoring of the jet separation angle  $\Theta_{sep}$ , respectively.

Both phenomena usually entail instabilities and the inability to converge properly. Their detection contributes to robustness and acceleration of the automated calculation campaigns as failed branches are stopped. So, the subsequent operation points remaining in  $\left(\frac{U_{jet}}{U_\infty}\right)_i$  are cancelled once jet wrap-around or leading edge separation has occurred.

### 3.4.5 Turbulence Model Modifications

Initial test calculations with high jet outflow ratios  $\frac{U_{jet}}{U_\infty}$  led to results deteriorated by the aforementioned jet-wrap-around phenomenon (Figure 2.12b and Figure 3.11b). The jet remains attached to the Coandă surface too long, completely wraps around and shifts the rear stagnation point to the lower side of the aerofoil. The reasons for this non-physical solution are associated with the eddy viscosity prediction inside the characteristic wall jet (Figure 2.1). Initially, two modifications from literature have been tested. The ‘‘Separation Bubble Fix’’ from RUMSEY (2009) and the correction of the viscous sublayer from CELIC/HIRSCHHEL (2006), however, did not cure the problem of jet-wrap around. Finally, the detailed numerical investigation of this phenomenon yielded an own solution. The following subsections therefore propose two modifications for Menter’s SST turbulence model. At high blowing rates, they alleviate the encountered problems and contribute to accuracy and robustness of convergence.

**Wall Jet Correction (WJC)** First results indicate that the original version of Menter’s blending function (Equation 3.24) is inconvenient for the treatment of fluid over-speeds near the wall. The wall jet sheet is partly modelled by the  $k$ - $\varepsilon$ -model, even in regions close to the wall where the  $k$ - $\omega$ -model should dominate. For boundary layer flows, and especially for separating flows in adverse pressure gradient, the  $k$ - $\omega$ -model is superior to the  $k$ - $\varepsilon$ -model in terms of accuracy (MENTER, 1994). The latter often is prone to the wrong prediction of delayed separation. To mark the entire wall jet zone to be treated by the  $k$ - $\omega$ -model, the following expression provided robust results in the scope of the tested cases.

$$F_D = \tanh \left[ \left( v \cdot \frac{D\nu}{U_\infty^2} \right)^3 \right] \quad (3.39)$$

where  $D$  is the norm of the fluid element deformation tensor yielding  $D = \sqrt{\frac{\partial u_i}{\partial x_j} \frac{\partial u_j}{\partial x_i}}$ . This ensures that the mixing layer is selected ( $F_D \approx 1$ ) due to its strong velocity gradients relative to the free stream velocity  $U_\infty$ . The amplification factor  $v$  was calibrated from numerical experiments and was set to the value of  $1 \times 10^4$  for the present calculations. This wall jet

marker function was introduced into Equation 3.24 which then yields

$$F_1 = \tanh \left\{ \left\{ \min \left[ \max \left( \frac{\sqrt{k}}{\beta^* \omega d_w}, \frac{500\nu}{d_w^2 \omega} + F_D \right), \frac{f_{SG} \rho \sigma_\omega k}{CD_{k\omega} d_w^2} \right] \right\}^4 \right\} \quad (3.40)$$

Note that the safeguard term  $\frac{f_{SG} \rho \sigma_\omega k}{CD_{k\omega} d_w^2}$  of the baseline model takes very low values inside the wall jet and dominates the blending function  $F_1$  there. To avoid the undesired allocation to the  $k$ - $\varepsilon$ -model in these regions, the factor  $f_{SG}$  inside the safeguard term was increased from originally 4 to 40 000.

**Modification of SST-Model Formulation (SSTMod)** The application of the original shear-stress-transport model (SST) leads to reduced eddy viscosities in the mixing layers of the downstream wall jet near the slot lip. The extraordinarily high strain rates in the lip wake make Equation 3.28 act like an eddy viscosity limiter in this mixing layer region. Too low eddy viscosity values therein prevent the wall jet from momentum diffusion into the aerofoil free stream. The wall jet can preserve its overspeed up to non-physical distances and detaches too late or even not at all. Therefore, a modified formulation of  $F_2$  is proposed to deactivate the SST eddy viscosity limitation in the mixing layer regions of the wall jet. Equation 3.28 is extended by  $F_D$  (Equation 3.39) and yields

$$\nu_t = \frac{a_1 k}{\max \left( a_1 \omega, \sqrt{P} (F_2 - F_D) \right)} \quad (3.41)$$

### 3.4.6 Validation

The baseline RANS method was validated by standard test cases (lid-driven cavity flow, turbulent boundary layer on a flat plate, unblown aerofoil) as can be found in the appendix (section D). The validation of the final method including its turbulence model modifications is presented in the following paragraphs. Englar and Jones' wind tunnel experiments found in ref. ENGLAR ET AL. (2009) served as test cases.

**Grid** The aerofoil geometry and used grid topology are given in Figure 3.12. For the circulation control aerofoil, the O-grid mesh topology reduces grid distortions and skewed cells to a minimum. The normal grid spacing inside the boundary layers was resolved such that the first nodes adjacent to the wall fulfil the requirement  $y^+ < 1$ . Especially for high velocity wall jets, this leads to very small distances. The longitudinal grid size was varied by use of three different meshes. Their properties are given in Table 3.5.

CC aerofoil from ENGLAR ET AL. (2009)	
$t/c_{Coanda}$	20%
<i>camber</i>	0%
$r/c_{Coanda}$	0.095
$c_{Coanda}$ [m]	0.22
$Re$	$\sim 500\,000$
$h_u$ [mm]	0.23, 0.33, 0.46, 0.66, 1.09
$h_{lip}$ [mm]	0.25

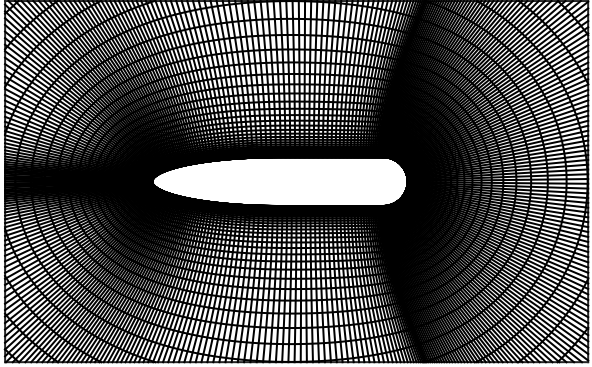


**Figure 3.12:** Circulation control aerofoil geometry of validation test case and used grid topology (STADLBERGER/HORNUNG, 2014)

**Table 3.5:** Mesh sizes of mesh refinement study

	coarse	medium	fine
Total number of longitudinal points	400	500	700
Number of long. points on Coandă surface	145	180	250
Total number of vertical points	180	200	200
Number of vert. points from Coandă surface to outer lip edge	80	90	90

**Boundary Conditions** The internal plenum was not modelled in this study. Instead, the jet inflow boundary condition was set directly at the vertical slot boundary below the slot lip. According to the wind tunnel experiments, the free stream velocity  $U_\infty$  was set to low subsonic conditions yielding a Reynolds number of 500 000. The calculated values for the mean jet outflow velocity ratio  $\frac{U_{jet}}{U_\infty}$  ranged from 0 to 10. The jet inflow velocity profile was approximated by a simple polynomial function of degree 10. Test calculations indicated insignificant dependence on the degree. Inflow turbulence parameters  $k$  and  $\omega$  at the slot exit were set to laminar flow conditions. The measured slot exit velocity profile indicates that the strong acceleration of the fluid inside the nozzle leads to relaminarised turbulence conditions in this zone (ENGLAR ET AL., 2009). The sand-grain height was set to  $k_s = 0.05\text{mm}$  for wall boundaries on the entire aerofoil including the Coandă surface.

**Curvature Correction** In some references, turbulence models with implemented flow curvature correction (e.g. HELLSTEN (1998), SPALART/SHUR (1997)) tend to alleviate the problem of non-physical solutions at high blowing rates (SWANSON ET AL., 2005, 2006; FASEL ET AL., 2006; RUMSEY/NISHINO, 2011). However, they give no general guarantee for successful simulations and accurate results. Initial calculations with Hellsten’s correction (HELLSTEN, 1998) exhibited a volatile behaviour with unstable convergence. The highly curved streamlines around the nose provoked significant differences in the turbulence predictions of the upper boundary layer. Since the turbulence parameters of the wall jet are

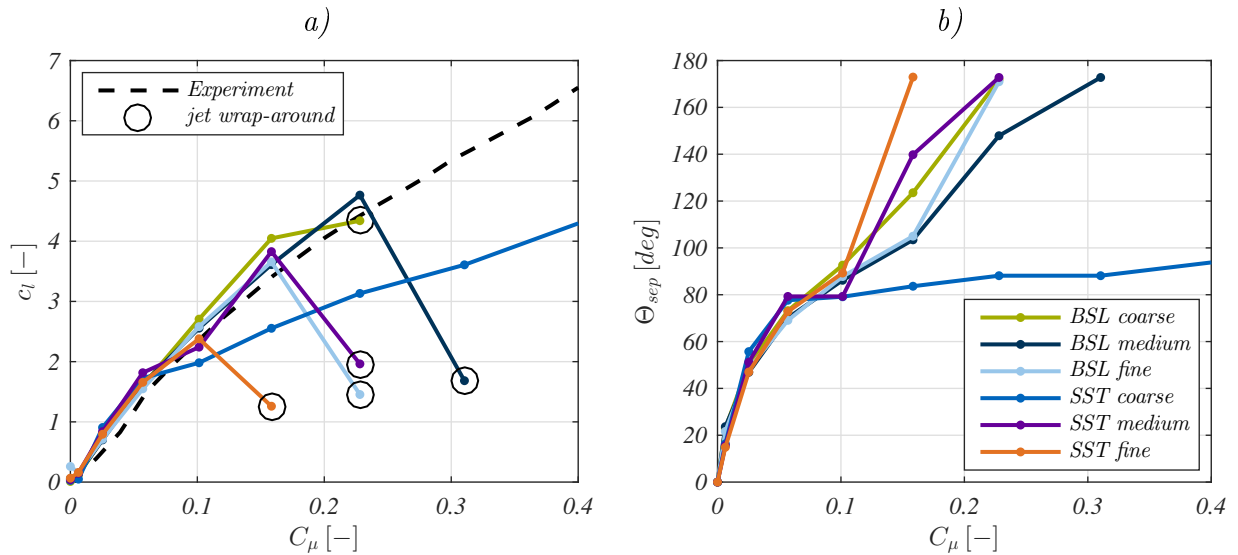


**Figure 3.13:** Lift coefficient increment (a) and wall jet separation angle (b) with original turbulence model versions (BSL, SST) for different mesh sizes,  $h_u = 0.5mm$ ,  $\alpha = 0deg$

sensitive to these upstream turbulence conditions, their unsteady interaction led to low convergence rate and poor accuracy. The variation of the curvature model constant did not cure this problem either. Therefore, curvature corrections have not been activated further in this study.

**Hardware and Computational Performance** The calculations in the scope of this study were performed on in-house desktop machines equipped with Intel Core i7-4770 processors (quad core, 3.40Ghz) and 8GB RAM. One iteration took between 5s and 10s where convergence was attained after 40 to 80 iterations in the majority of cases. The convergence criterion was based on the fluctuation and evolution of the lift coefficient (subsection 3.4.4).

## Results

First, an initial mesh refinement study illustrates the behaviour of the original turbulence model (BST, SST). Then, the subsequent paragraphs describe the impact of the turbulence model modifications (WJC, SSTMod) on the lift generation  $c_l$  as well as on the implied wall jet profiles.

**Mesh Refinement Study with Original Turbulence Model (BSL, SST)** The longitudinal grid size was varied during an initial mesh refinement study employing the original BSL and SST turbulence model. Figure 3.13a shows the section lift  $c_l$  over the blowing momentum flux coefficient  $C_\mu$ . For blowing rates up to  $C_\mu = 0.1$ , most of the BSL and SST lift increment curves exhibit a similar trend until they suddenly drop to lower levels when

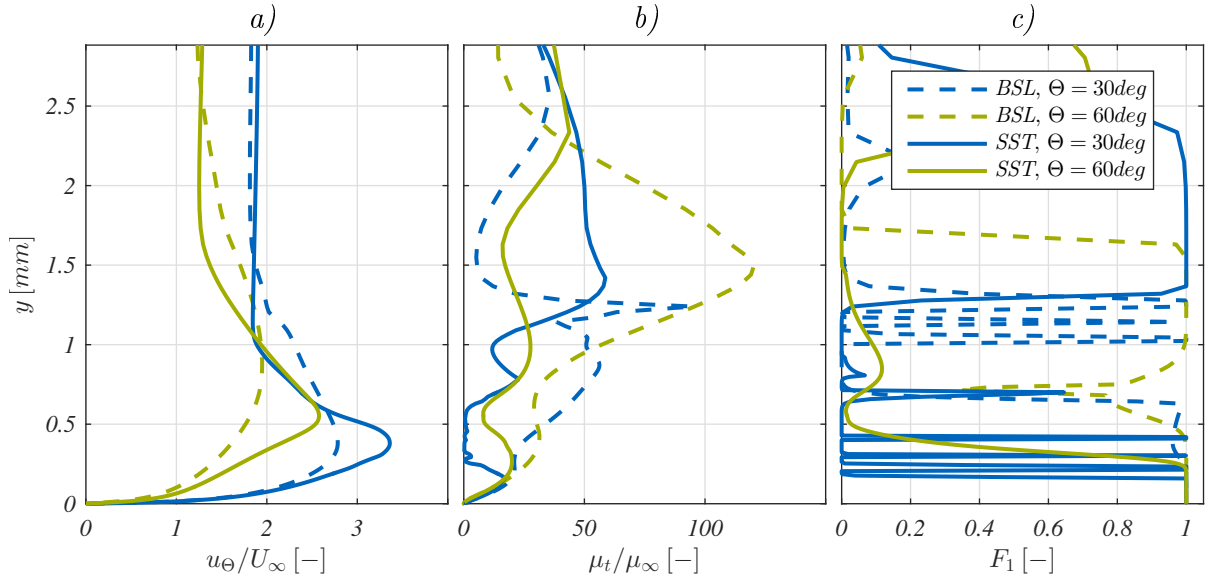


**Figure 3.14:** Velocity (a), eddy viscosity (b) and blending function (c) of the wall jet with original turbulence model (BSL, SST), medium mesh size,  $\frac{U_{jet}}{U_{\infty}} = 3$ ,  $C_{\mu} = 0.057$ ,  $h_u = 0.5mm$ ,  $\alpha = 0deg$

higher blowing rates ( $C_{\mu} > 0.15$ ) are reached. Figure 3.13b reveals that the simulations are corrupted by the well-known jet-wrap-around phenomenon indicated by  $\Theta_{sep} > 170^{\circ}$ . The coarse SST case was not affected by this instability but the lift generation deviated significantly from experimental results at higher blowing rates. In general, the original baseline model (BSL) performed better than the original SST model while in both cases the impact of different mesh sizes becomes more significant only at higher  $C_{\mu}$ -values. The finest grids aggravated the tendency to early jet wrap-around. However, coarse meshes cannot guarantee robust and accurate results either. Finally, the medium grids constitute the least problematic compromise between predictability and computational cost.

The examination of the medium grid wall jets gives indications about the reasons for instability and inaccuracy. While the velocity profiles (Figure 3.14a) of the baseline case (BSL) appear plausible, the associated eddy viscosity profiles  $\mu_t$  (b) and blending function values  $F_1$  (c) exhibit a volatile behaviour, especially close to the slot. For the SST case, these fluctuations are even more pronounced already beginning at low blowing rates ( $C_{\mu} \approx 0.05$ ). The associated jet velocity profiles show a non-physical deformation in the zones between the viscous sublayer and velocity peak (Figure 3.14a). In these peak regions, the eddy viscosity  $\mu_t$  (b) exhibits lower values compared to the BSL case. The fluid obviously follows the way of least resistance and forms the non-physical, tapered velocity profile. Interestingly, at the downstream position  $\Theta = 60deg$  the blending function  $F_1$  (c) reduces from 1 ( $k-\omega$ ) to almost 0 ( $k-\varepsilon$ ) well before the zone of velocity peaks ( $y \approx 0.5mm$ ). The change between the  $k-\omega$ -model and the  $k-\varepsilon$ -model inside the wall jet is assumed to have a significant impact on the determination of turbulence values. Above all, the turbulence onset in the zone close to the slot exit is supposed to be crucial for the downstream evolution of eddy viscosity.

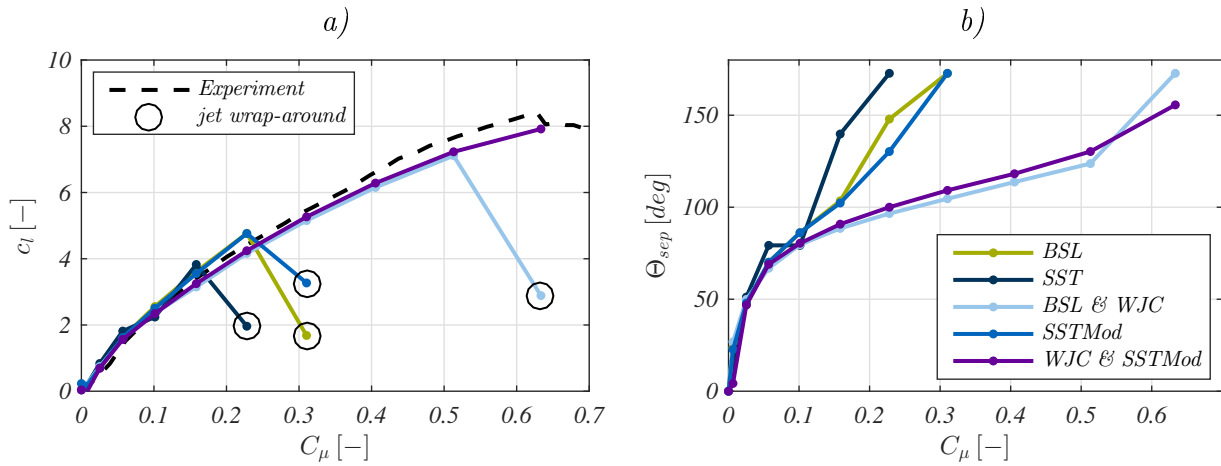


**Figure 3.15:** Lift coefficient increment (a) and wall jet separation angle (b) with turbulence model modifications activated individually and in combination for the medium mesh size,  $h_u = 0.5\text{mm}$ ,  $\alpha = 0\text{deg}$  (modified from STADLBERGER/HORNUNG, 2015b)

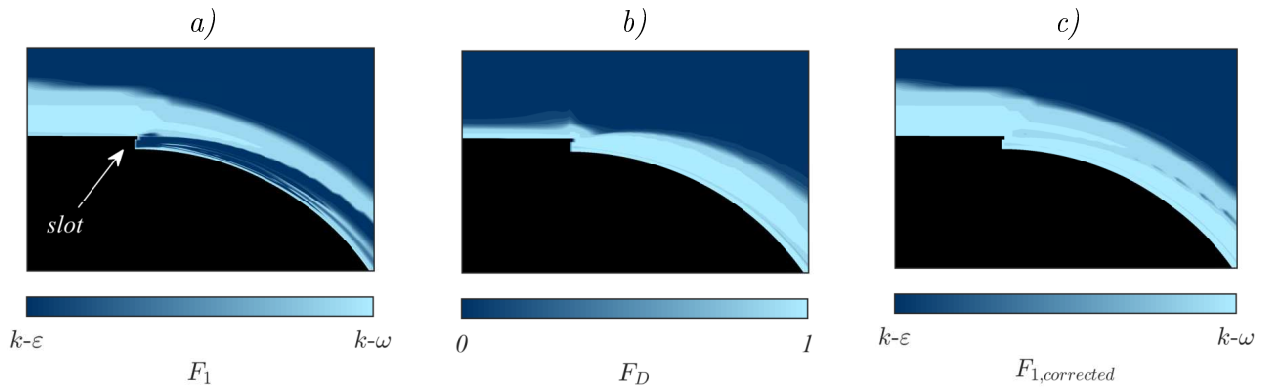


**Figure 3.16:** Baseline blending function  $F_1$  (a), corrective function  $F_D$  (b) and corrected blending function  $F_{1,corrected}$  (c) in the upper slot region of the blown trailing edge

In particular, the original SST formulation is prone to reduce the eddy viscosity in these regions such that the turbulent mixing along the Coandă surface is inhibited. In summary, the original formulation of the blending function visibly favours the  $k-\varepsilon$ -model inside the wall jet and leads to deteriorated turbulence and velocity profiles.

**Wall Jet Correction (WJC)** For the subsequent numerical studies, the medium grid size was chosen to assess the performance of the proposed turbulence model modifications. By introducing the wall jet correction (WJC), jet-wrap-around can be delayed up to very high blowing rates ( $C_\mu \approx 0.5$ ) and, despite a general underprediction, lift results compare essentially well with experimental data (Figure 3.15). As described in subsection 3.4.5, this modification of the blending function formulation aims to retain the use of the  $k-\omega$ -model throughout the entire wall jet. Figure 3.16 depicts the upper fraction of the Coandă surface close to the slot. In this example of a failed solution, the erroneous behaviour of the baseline

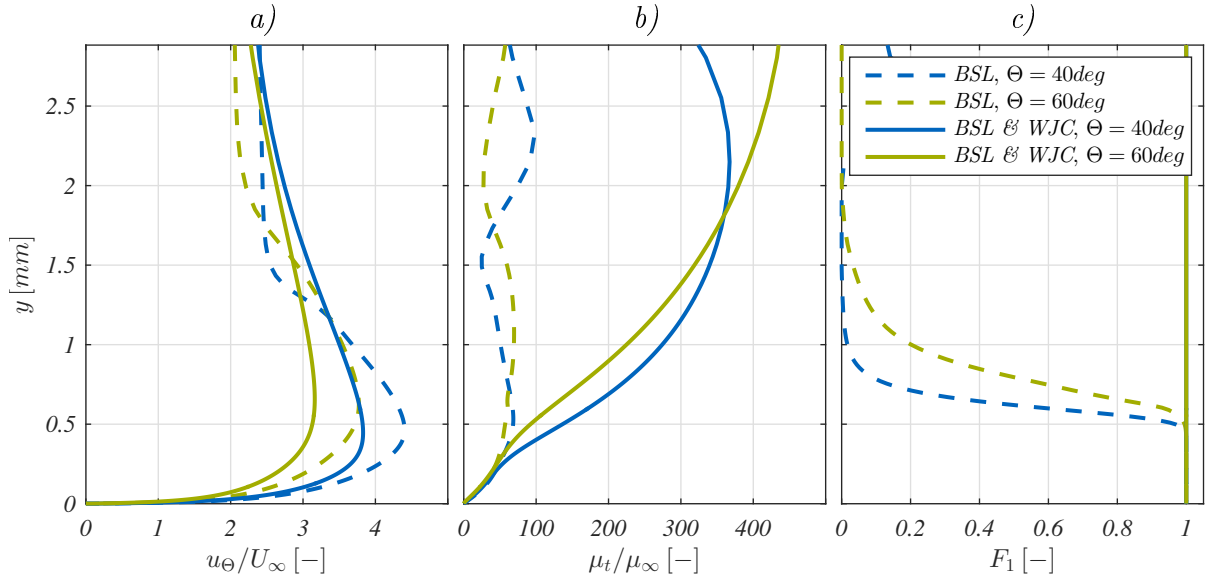


**Figure 3.17:** Velocity (a), eddy viscosity (b) and blending function (c) of the wall jet with activated WJC, medium mesh size,  $\frac{U_{jet}}{U_\infty} = 5$ ,  $C_\mu = 0.158$ ,  $h_u = 0.5mm$ ,  $\alpha = 0deg$  (modified from STADLBERGER/HORNUNG, 2015b)

function  $F_1$  (Figure 3.16a) wrongly assigns fractions of the wall jet to the  $k$ - $\varepsilon$ -model. The corrective function  $F_D$  identifies these regions (Figure 3.16b) and enforces the use of the  $k$ - $\omega$ -model inside the entire wall bounded jet (Figure 3.16c). A more detailed wall jet examination reveals that, compared to the BSL model, the jet velocity peaks with activated WJC attenuate visibly along the Coandă surface (Figure 3.17a). The modified blending function  $F_1$  triggers the  $k$ - $\omega$ -model throughout the entire wall jet profile (Figure 3.17c) and leads to significantly higher eddy viscosity values in the mixing layer ( $y > 0.5mm$ ) (Figure 3.17b). This enhances momentum transport towards free stream and prevents the wall jet from jet-wrap-around at higher blowing rates ( $C_\mu > 0.1$ ).

**SST Model Modification (SSTMod)** The modification of the SST formulation (SST-Mod) aims to deactivate its original turbulence limiting behaviour inside the wall jet regions. But it also seeks to preserve its well established function in the remaining flow domain including standard boundary layers under adverse pressure gradients. As can be seen in Figure 3.18c, the marker function  $F_D$  identifies the wall jet zone and deactivates the SST limiter in these regions as given by the term  $F_2 - F_D$  in Equation 3.41. The velocity profiles with modified SST formulation (SSTMod) exhibit an almost identical shape as the baseline model (BSL). However, eddy viscosity values differ significantly and still retain a volatile behaviour (Figure 3.18b). Note that WJC is not activated in this comparison and jet-wrap-around still occurs at blowing rates of  $C_\mu > 0.2$  (Figure 3.15).

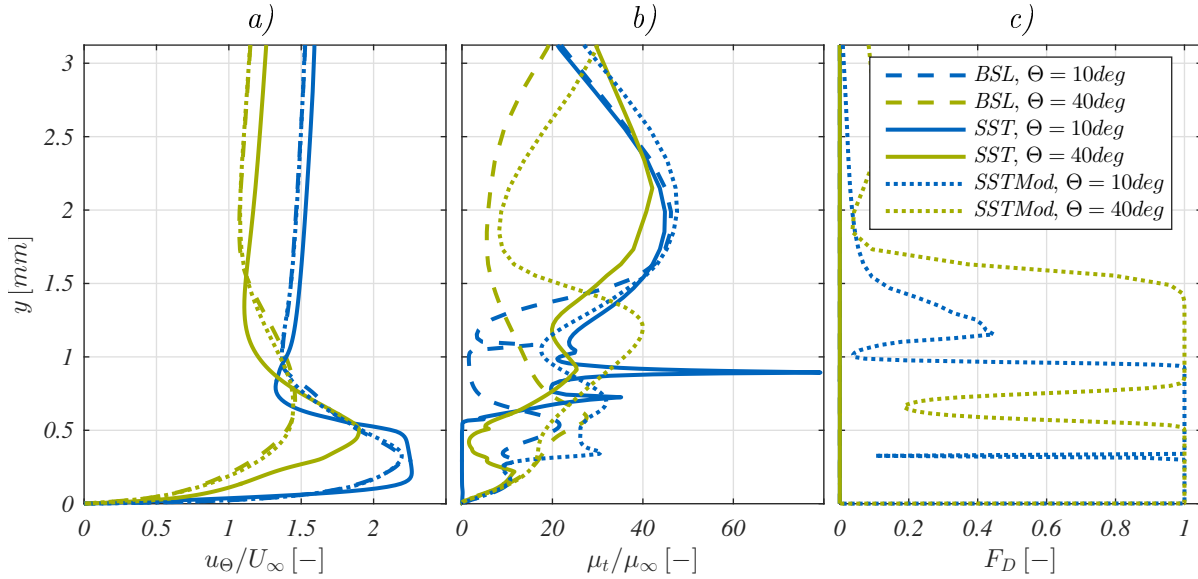


**Figure 3.18:** Velocity (a), eddy viscosity (b) and SST modification function (c) of the wall jet with modified SST formulation for the medium mesh size,  $\frac{U_{jet}}{U_\infty} = 2$ ,  $C_\mu = 0.025$ ,  $h_u = 0.5mm$ ,  $\alpha = 0deg$  (modified from STADLBERGER/HORNUNG, 2015b)

**Combined Activation** Finally, the two modifications were activated simultaneously in addition to Menter’s SST-model. This setting gave the most robust results up to the maximum of simulated blowing rates ( $C_\mu \approx 0.63$ ) (Figure 3.15) and has been applied for additional slot heights (Figure 3.19). The results of the presented RANS method were compared with wind tunnel data and, additionally for  $h_u = 0.3mm$ , with numerical results calculated with the commercial solver Ansys CFX. Details on the latter can be found in BERNHARDT (2015) whose simulations rely on a grid consisting of approximately  $1.1 \times 10^6$  elements. Here, a mesh block representing the geometry of the internal plenum is also part of the computational flow domain. Inside the CFX preprocessor, Menter’s original SST model was selected for turbulence modelling. As can be seen in Figure 3.19, both solvers are able to predict the generated lift quite accurately in the regime of low blowing rates ( $C_\mu < 0.1$ ). However, at higher blowing conditions ( $C_\mu > 0.1$ ), the numerical results deviate significantly from wind tunnel measurements. The author’s method reveals more conservative and underestimates the Coandă flap effectiveness. In contrast, the CFX solver overestimates the lift increase even with activated curvature correction (RCC) (SPALART/SHUR, 1997). At least, RCC could prevent the jet-wrap-around phenomenon up to blowing rates of  $C_\mu \approx 0.35$ . Further calculations with solely the author’s method led to results for additional slot sizes as depicted in Figure 3.19b. The predicted values agree quite well with experimental data for larger slot sizes up to blowing rates of  $C_\mu \approx 0.3$ . However, the reduced lift generation for the smallest slot height could not be reproduced numerically. Again, for all slot sizes the results exhibit a visible discrepancy at high blowing rates where jet-wrap-around could not be avoided for the largest tested slot height. Note that wind tunnel data for active flow control aerofoils

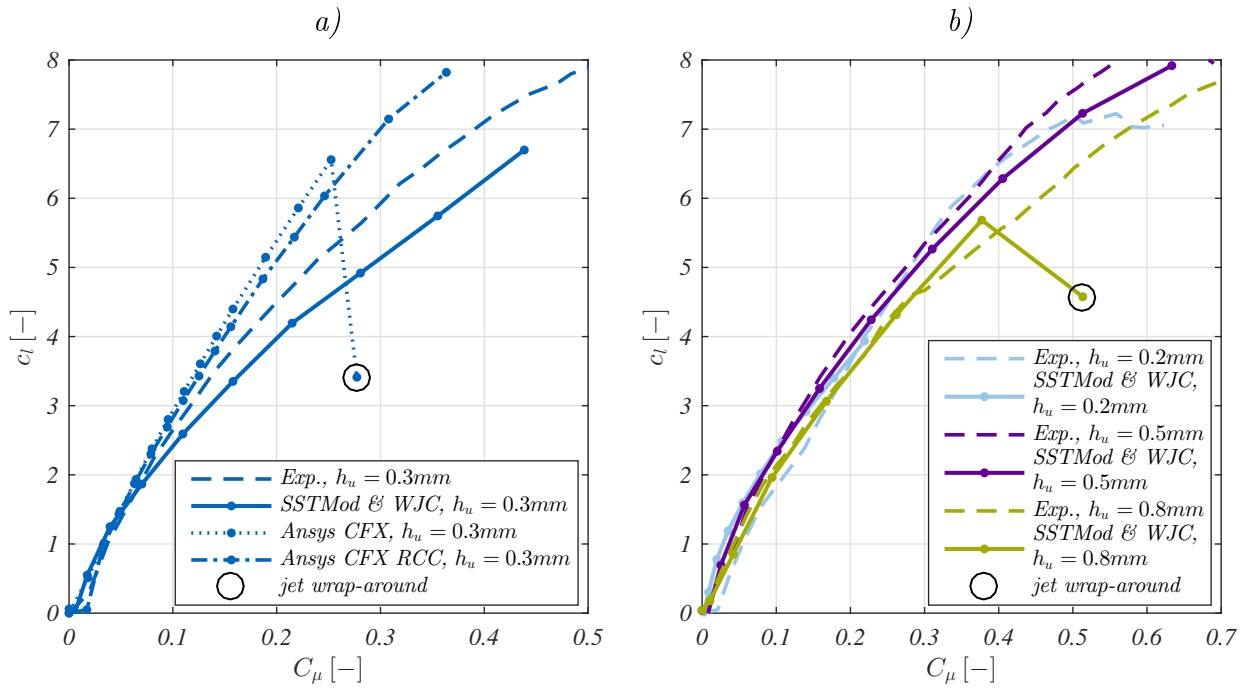


**Figure 3.19:** Lift generation of the Englar/Jones test case (ENGLAR ET AL., 2009) due to blowing for different slot heights, calculated with the medium mesh size for the author’s RANS method,  $\alpha = 0\text{deg}$  (modified from STADLBERGER/HORNUNG (2015b) with data from BERNHARDT (2015))

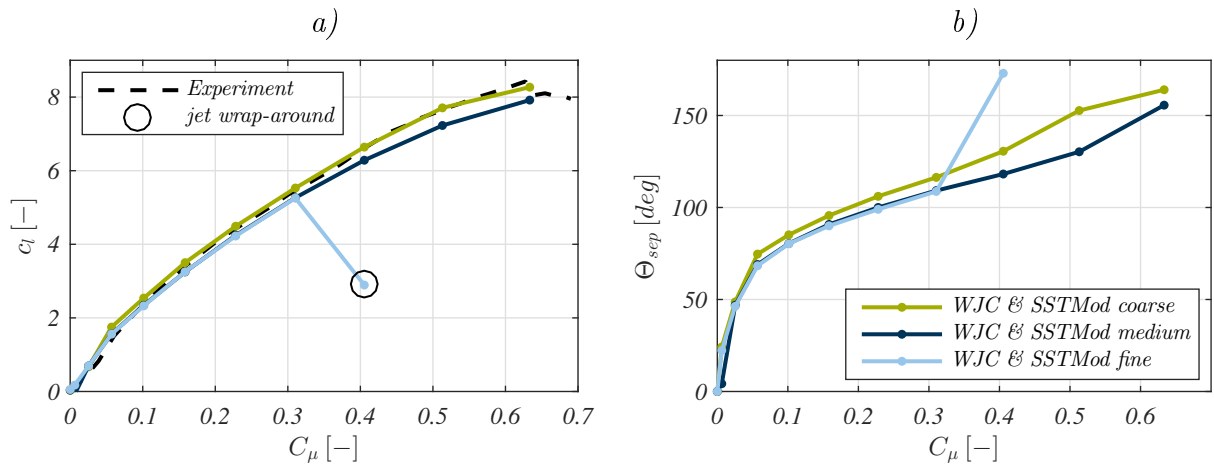


**Figure 3.20:** Lift coefficient increment (a) and wall jet separation angle (b) with turbulence model modifications WJC and SSTMod for different mesh sizes,  $h_u = 0.5\text{mm}$ ,  $\alpha = 0\text{deg}$

generally imply several uncertainties (subsection 2.2.8). Especially when high lift increments are attained, the experimental  $C_\mu$ - values tend to be underrated significantly.

Finally, the proposed turbulence model modifications were reinvestigated in terms of grid size sensitivity (Figure 3.20). While the coarse grid resulted in generally higher lift values, the medium and fine mesh sizes produced almost identical results up to  $C_\mu \approx 0.3$ . However, the fine grid promotes an earlier occurrence of jet-wrap-around when reaching excessive blowing conditions ( $C_\mu > 0.3$ ). Even though the destabilising effect of mesh refinement is

still present, the onset of jet wrap-around could be delayed to very high jet outflow velocity ratios ( $\frac{U_{jet}}{U_\infty} > 7$ ). For technically relevant applications in the field of flight control or high-lift systems,  $\frac{U_{jet}}{U_\infty}$ -values are assumed not to exceed  $\frac{U_{jet}}{U_\infty} < 4-6$ . The restrictions coming from possible supersonic jet detachment (subsection 2.2.5) hardly allow values beyond  $\frac{U_{jet}}{U_\infty} > 6$  at reasonable flight speeds. Considering the aforementioned uncertainties of the baseline wind tunnel experiments and the reduced precision requirements during preliminary design stages, the proposed RANS method was judged to be sufficiently accurate and robust to proceed to sensitivity studies (subsection 5.1.3).

### 3.5 Modelling of the Finite Wing (3D)

The transfer of two-dimensional wing section data onto the finite wing by means of potential flow was chosen to meet both requirements of sufficient accuracy and computational efficiency. Linear methods as Prandtl's Lifting Line Theory (PRANDTL, 1923) or the Vortex Lattice Method (VLM) (FALKNER, 1952) give quick results for finite wing aerodynamics. Accuracy is good if the aerofoil section can be expected to produce the theoretical lift force of an inviscid flat plate ( $c_{l_\alpha} = \frac{\partial c_l}{\partial \alpha} = 2\pi$ ) throughout the investigated range of angle of attack. However, viscous effects leading to non-linear polars for lift and pitching moment are not taken into account by the pure potential theory. On this topic, iterative approaches have been developed to introduce real section data into the linear solution process of potential flow. The objective was to model stall phenomena and low Reynolds number effects (SIVELLS/NEELY, 1947; ANDERSON, J. D./CORDA, 1980). The modern adaptations of the lifting line method use discrete horseshoe vortices and iteratively adjust the collocation point position. The section lift curve slope ( $c_{l_\alpha}$ ) is thereby tuned such that it corresponds to viscous aerofoil data and local angle of attack (PHILLIPS/SNYDER, 2000). However, the estimation of the 3D force and moment reactions on a low aspect ratio wing additionally requires the modelling of circulation strengths in the chordwise direction (Figure 3.21). A vortex lattice more accurately accounts for cross flows due to low aspect ratios rather than one single lifting line. Therefore, the vortex lattice method is more appropriate as theoretical basis for the studied flying wing configuration.

The following subsections describe the “cambering” method which has been developed for this study on the basis of ref. MUKHERJEE/GOPALARATHNAM (2006). This approach iteratively introduces the non-linear section data into the solution of discrete horseshoe vortices. Mukherjee and Gopalarathnam used the expression “Decambering Approach” as wing sections are virtually “decambered” when flow separations occur in the post-stall region. Inside their method, the vortex lattice geometry is manipulated such that, for the final solution, the calculated values of local lift force and pitching moment coefficients  $(c_l, c_m)_{pot}$  are consistent

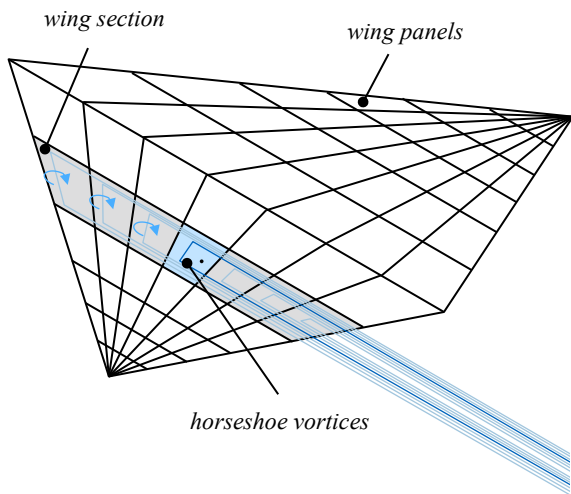


**Figure 3.21:** Illustration of a vortex lattice for a low aspect ratio wing (STADLBERGER/HORNUNG, 2015a)

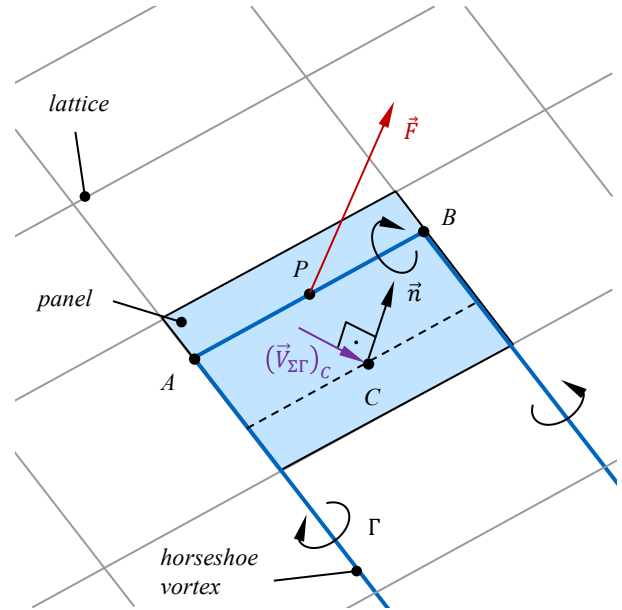


**Figure 3.22:** Illustration of one horseshoe vortex (STADLBERGER/HORNUNG, 2015a)

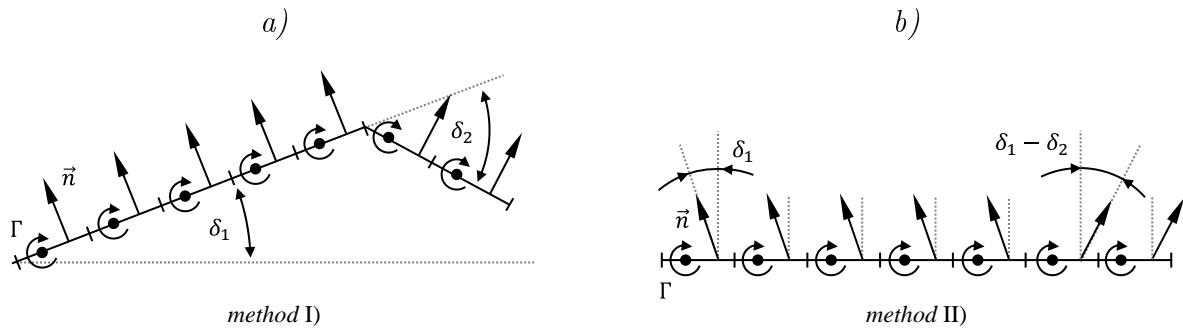


**Figure 3.23:** Panel modification method I) from MUKHERJEE/GOPALARATHNAM (2006) and present method II) (modified from STADLBERGER/HORNUNG, 2015a)

with viscous section data  $(c_l, c_m)_{visc}$ . After each iteration, the discrete vortices are rotated around the leading edge and around a virtual flap hinge line to change the incidence and camber of each wing section (Figure 3.23a). The rotation angles are determined by use of linearised analytical expressions which are derived from the classical solution of the lifting problem (KATZ/PLOTKIN, 2001).

In the scope of the present research activities, a new method is sought to incorporate the forces and moments generated by novel flight control technology, rather than a technique to investigate the post-stall regime. For the following method, the expression “cambering” approach was chosen. This comes from the fact that the aerofoil section is cambered through positive deflection of a plain flap or through an aerodynamically equivalent flight control

effector, e.g. a Coandă flap. The following subsections describe the method used to establish a three-dimensional aerodynamic data set for a finite wing. The algorithm was implemented in MATLAB and is linked with an object-oriented parametric wing model. So, it enables quick results for arbitrary wing planforms including swept low aspect ratio wings. The subsequent comparison of results from validating calculations with those from wind tunnel experiments finally assesses the accuracy of the presented method. Most of this section's content can also be found in STADLBERGER/HORNUNG (2015a).

### 3.5.1 Governing Equations

In the vortex lattice theory, the lifting surface is divided into a discrete number of panels in both chordwise and spanwise direction (Figure 3.21). In general, the wing aerodynamics are modelled by a lattice of horseshoe vortices whose lateral filaments are placed on the panel quarter-chord-lines. The two associated longitudinal filaments are aligned to the freestream velocity and represent the wake sheet (Figure 3.22). The differential form of the Biot-Savart law can be integrated to yield the induced velocity  $(\vec{V}_{\Gamma_j})_C$  in point  $C$  of one of these vortex filaments  $j$  ranging from  $A$  to  $B$

$$(\vec{V}_{\Gamma_j})_C = -\frac{\Gamma_j}{4\pi} \cdot \frac{\vec{r}_{AC} \times \vec{r}_{BC}}{\|\vec{r}_{AC} \times \vec{r}_{BC}\|^2} \cdot \left[ (\vec{r}_{AB})^T \cdot \left( \frac{\vec{r}_{AC}}{\|\vec{r}_{AC}\|} - \frac{\vec{r}_{BC}}{\|\vec{r}_{BC}\|} \right) \right] \quad (3.42)$$

where  $\Gamma_j$  is the vortex strength of the vortex filament  $j$ . Hence, the velocity  $(\vec{V}_{\Sigma\Gamma})_{C_i}$  in point  $C_i$  induced by all  $N$  vortex filaments can be determined by

$$(\vec{V}_{\Sigma\Gamma})_{C_i} = \sum_{j=1}^N (\vec{V}_{\Gamma_j})_{C_i} + \vec{V}_{\infty} \quad (3.43)$$

where  $\vec{V}_{\infty}$  is the free stream velocity. Then a Neumann boundary condition is established at all collocation points  $C_i$  that forces the flow velocity to be aligned with the respective panel surface, i.e. to be perpendicular to the normal vector  $\vec{n}_{C_i}$ . It yields

$$(\vec{V}_{\Sigma\Gamma})_{C_i} \cdot \vec{n}_{C_i} = 0 \quad (3.44)$$

Note that the collocation points are located at the midpoint of the 3/4-chord line which theoretically results in a lift curve slope of  $c_{l\alpha} = 2\pi$  for one panel in the two-dimensional case. Finally, the solution of the emerging system of linear equations (SLE) enables the determination of the vortex strengths  $\Gamma_j$  of each horseshoe vortex. The discrete forces  $\vec{F}_i$  acting on the midpoints  $P$  of the lateral filaments  $AB$  can be calculated by use of the

Kutta-Joukowski theorem

$$\vec{F}_i = \rho \cdot \Gamma_i \cdot \left( \left( \vec{V}_{\Sigma\Gamma} \right)_{P_i} \times \vec{r}_{AB} \right) \quad (3.45)$$

provided that 3D effects are negligible. The global  $(C_L, C_D, C_Y, C_m, C_n, C_l)$  and local section values  $(c_l, c_d, c_m)$  of the force and moment coefficients are determined by integration and decomposition into the respective directions.

### 3.5.2 Calculation Procedure

The basic idea of the cambering or decambering approach is to change the camber and incidence of the vortex lattice such that the section lift force and pitching moment calculated by potential theory corresponds to the viscous aerofoil data at the estimated local angle of attack. The simplest practice is to introduce two angles  $\delta_1$  and  $\delta_2$  that model a simple flap ( $\delta_2$ ) for pitching moment generation and change the incidence of the entire wing section ( $\delta_1$ ) for lift force correction. Figure 3.23a illustrates a modified section according to the method used by ref. MUKHERJEE/GOPALARATHNAM (2006). The vortices as well as the collocation points and normal vectors are rotated (method I) around the respective pivot points. However, for swept wings this method can induce non-physical lateral forces and moments if the virtual hinge lines are not perpendicular to the free stream direction. Therefore, the present method II only tilts the normal vectors to obtain the necessary local change in lift and pitching moment as depicted in Figure 3.23b. The details of the complete calculation procedure are described in the following paragraphs while the iterative process is additionally illustrated in Figure 3.24.

#### Initial calculations:

As a matter of principle, the following algorithm requires a correlation between the modification angles  $\delta_1, \delta_2$  and their impact on the 2D section aerodynamics  $(c_l)_{pot}, (c_m)_{pot}$ . Mukherjee and Gopalarathnam used two linearised analytical expressions to calculate the two-dimensional reactions  $(c_l)_{pot} = f_{analytical}(\delta_1, \delta_2)$  and  $(c_m)_{pot} = f_{analytical}(\delta_1, \delta_2)$ . As can be seen in Figure 3.25, the linearised analytical solutions of the lift (a) and pitching moment (b) coefficient deviate significantly from the 2D discrete vortex solutions applying method I. Especially at high deflection angles of  $\delta_2$ , discrepancy is high. In fact, the investigated fluidic flight control concept promises very high lift increments leading to increasingly inaccurate solutions at high values of  $\delta_1, \delta_2$ . The deviation is even higher when solely the normal vectors are tilt as intended (method II). This proves that the linearised approach is not valid anymore when high modification angles have to be expected. Hence, the two-dimensional

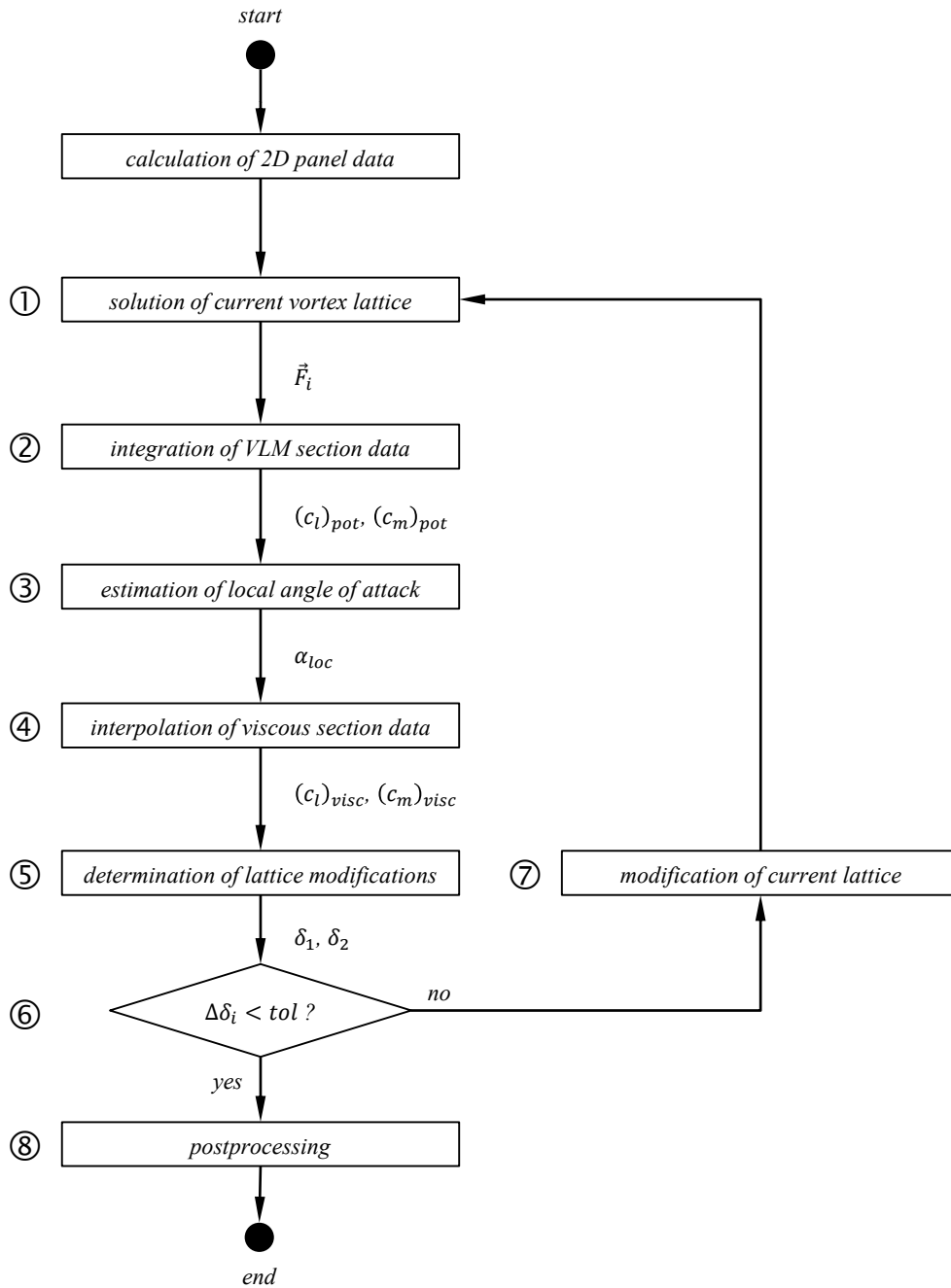


**Figure 3.24:** Flow chart of the cambering method calculation process (STADLBERGER/HORNUNG, 2015a)

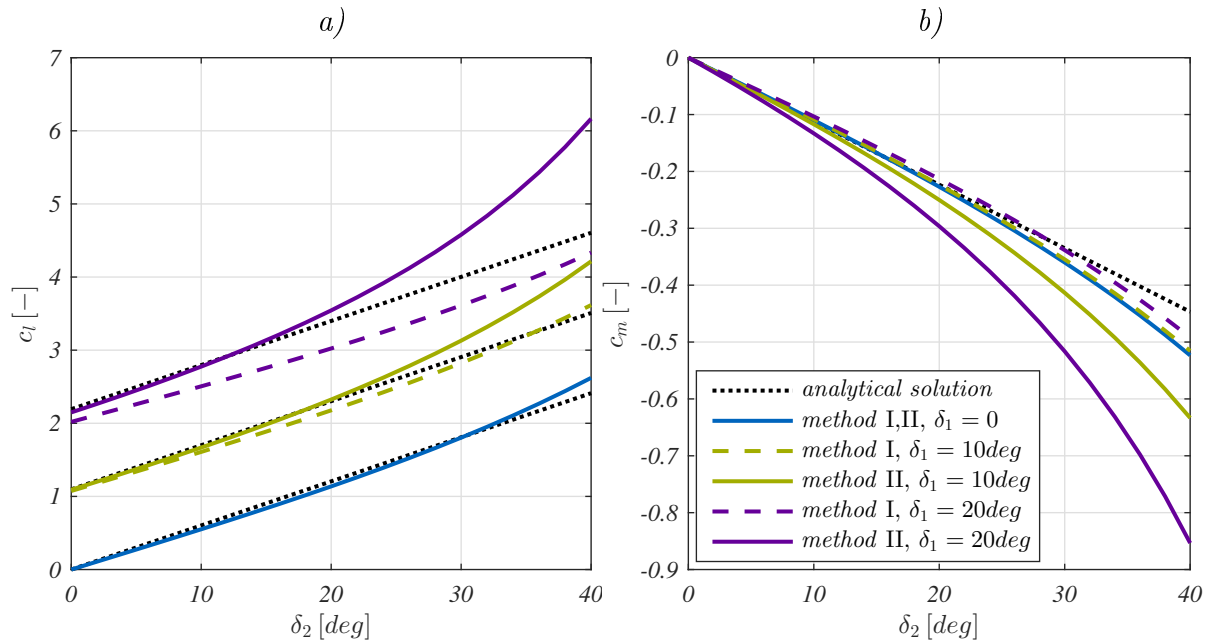


**Figure 3.25:** Comparison of lift (a) and pitching moment (b) coefficient for the different 2D panel modification methods,  $\alpha_\infty = 0deg$ ,  $\frac{x_{hinge} \delta_2}{c} = 0.8$  (modified from STADLBERGER/HORNUNG, 2015a)

reactions of the 2D baseline section have to be calculated with discrete vortices and stored in a look-up-table before the iteration process starts. This implies that the 2D panel problem (Figure 3.23b) is solved for a fine grid of  $\delta_1, \delta_2$ -values. This subfunction inside the calculation tool is represented by  $f_{2D\ panel}$  and provides

$$\left( (c_l)_{pot}, (c_m)_{pot} \right)_{2D} = f_{2D\ panel}(\delta_1, \delta_2) \quad (3.46)$$

Note that the panel fractions along the chordwise direction of the complete finite wing lattice as well as the respective virtual hinge line positions  $\frac{x_{hinge} \delta_2}{c}$  for  $\delta_2$  have to be identical to the precalculated baseline 2D panel section of Equation 3.46. In addition, the global angle of attack  $\alpha_\infty$  affects the discrete vortex solution with normal vector tilt. For that reason, the look-up-table has to be precalculated at the same angle of attack as given by the flight condition of the entire finite wing. In principle, these initial calculations for the 2D panel section can be performed once before larger calculation campaigns are launched. Reloading the stored 2D panel data, preferably directly from memory, at the beginning of the respective operating point ( $\alpha_\infty$ ) might save computation time. Unfortunately, the modification angles are constrained such that the matrix of the SLE becomes singular when a normal vector is tilted by  $90deg$ , i.e.  $\delta_1 + \delta_2 = 90deg$ . However, in practice this limit has never been reached.

**Step ①:**

The initial processing of the unmodified vortex lattice follows the theory presented in the previous section. Its first solution provides the force vectors  $\vec{F}_i$  acting on each panel.

**Step ②:**

These forces are integrated along each section to determine the local section lift and pitching moment coefficients  $((c_l)_{pot}, (c_m)_{pot})$  delivered by potential theory. The lift coefficient yields

$$(c_l)_{pot} = T_{G \rightarrow A} \cdot \frac{1}{qS_{section}} \sum_k \frac{\left(\vec{F}\right)_k}{(\varepsilon_{CP})_k} \quad (3.47)$$

where  $k$  denotes the panels contained in the processed wing section.  $T_{G \rightarrow A}$  is the transformation matrix from the global to the aerodynamic coordinate system,  $q$  is the dynamic pressure and  $S_{section}$  is the section area. Note that the discrete forces  $\left(\vec{F}\right)_k$  have to be corrected for sweep effects if the wing panels have a non-rectangular planform. Since the lift increment depends on the perpendicular distance from the collocation point  $C$  to the lateral vortex filament  $AB$ , it changes when the panel is swept. To enable the comparison with the viscous section data, the forces are corrected by  $(\varepsilon_{CP})_k$  according to the deviation from perpendicularity. This correction factor is based on trigonometric relations and yields

$$\varepsilon_{CP} = \sqrt{1 - \left( \frac{\vec{r}_{AB} \cdot \vec{r}_{PC}}{\|\vec{r}_{AB}\| \|\vec{r}_{PC}\|} \right)^2} \quad (3.48)$$

Further, the pitching moment coefficient yields

$$(c_m)_{pot} = \frac{1}{qS_{section}c_{section}} \sum_k \frac{\left(\left(\vec{F}\right)_k \times \Delta\vec{x}_k\right) \cdot \begin{pmatrix} 0 & 1 & 0 \end{pmatrix}^T}{(\varepsilon_{CP})_k} \quad (3.49)$$

where  $c_{section}$  is the mid section chord length and  $\Delta\vec{x}$  the distance from point  $P$  to the reference point at the mid section quarter-chord point.

**Step ③:**

Now, the calculated sectional coefficients can be used to estimate the local angle of attack  $\alpha_{loc}$  at each section. As the results of  $(c_l)_{pot}$  and  $(c_m)_{pot}$  from the initial calculations (Equation 3.46) are monotonic w.r.t.  $\delta_1$  and  $\delta_2$  (if  $\delta_1 + \delta_2 < 90\text{deg}$ ), the local angle of attack

can be estimated easily by inverse interpolation inside the look-up-tables.

$$(\delta_1^*, \delta_2^*) = f_{2D\ panel}^{-1} \left( (c_l)_{pot}, (c_m)_{pot} \right) \quad (3.50)$$

$$\alpha_{loc} = \delta_1^* + \alpha_\infty - \delta_1^{n-1} \quad (3.51)$$

#### Step ④:

The viscous section data  $(c_l)_{visc}$  and  $(c_m)_{visc}$  is thereupon retrieved by interpolation inside the non-linear viscous data tables which had been obtained by CFD calculations, wind tunnel experiments or other methods

$$(c_l)_{visc} = f_{l\ visc\ data}(\alpha_{loc}) \quad (3.52)$$

$$(c_m)_{visc} = f_{m\ visc\ data}(\alpha_{loc}) \quad (3.53)$$

#### Step ⑤:

Then, the vortex lattice is modified such that the local coefficients of the potential theory solution correspond to the response of the viscous data set. For a high aspect ratio wing with minor 3D effects, one would impose the condition  $(c_l)_{pot} = (c_l)_{visc}$  and  $(c_m)_{pot} = (c_m)_{visc}$ . After inverse interpolation as already performed before, this leads to a new set of angles  $\delta_1^n, \delta_2^n$  for each section (Equation 3.50).

$$(\delta_1^n, \delta_2^n) = f_{2D\ panel}^{-1} \left( (c_l)_{visc}, (c_m)_{visc} \right) \quad (3.54)$$

However, for low aspect ratio wings, the associated 3D effects due to flap deflections or equivalent control moment generation induce a virtual additional camber rather than the sole change of local angle of attack. Thus, the local pitching moment increases while the local lift decreases compared to a high aspect ratio wing. This effect also manifests itself in a discrepancy between  $\delta_2^*$  and  $\delta_2^n$  on the affected span fractions. When 3D effects are negligible, these angles are usually expected to be approximately identical. To account for possible difference, however, the input values of the inverse interpolation (Equation 3.54) are corrected as follows

$$(\delta_1^n, \delta_2^n) = f_{2D\ panel}^{-1} \left( (c_l)_{visc} + (\Delta c_l)_{corr}, (c_m)_{visc} + (\Delta c_m)_{corr} \right) \quad (3.55)$$

where the corrections  $(\Delta c_l)_{corr}$ ,  $(\Delta c_m)_{corr}$  are estimated by

$$(\Delta c_l)_{corr} = (c_l)_{pot} - (c_l)_{expected} \quad (3.56)$$

$$(\Delta c_m)_{corr} = (c_m)_{pot} - (c_m)_{expected} \quad (3.57)$$

with

$$\left( (c_l)_{expected}, (c_m)_{expected} \right) = f_{2Dpanel}(\delta_1^*, \delta_2^{n-1}) \quad (3.58)$$

This avoids an overestimation of the viscous section data used for the subsequent lattice modification. The corrections thus enable the consideration of certain 3D effects for low aspect ratio wings where not only the effective local angle of attack, but also the effective camber of the wing sections is affected.

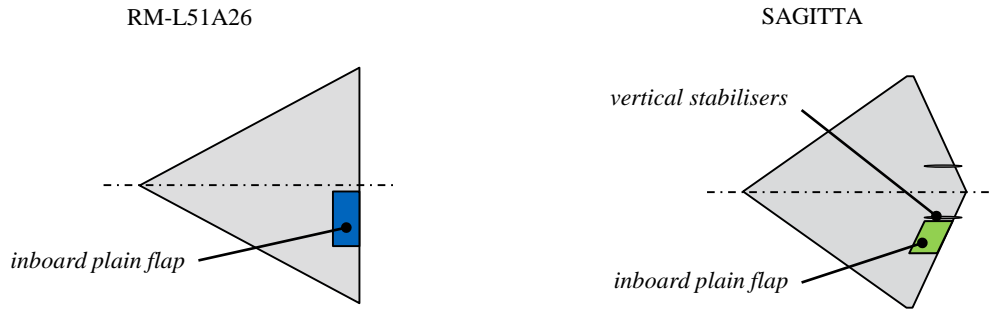
### Step ⑥ and ⑦:

If the change in modification angles  $\Delta\delta_i = |\delta_i^n - \delta_i^{n-1}|$ , compared to the previous iteration, exceeds a certain tolerance (e.g.  $tol = 0.02deg$ ), the vortex lattice is modified according to the current angles  $\delta_1^n, \delta_2^n$ . For stability reasons, it is recommended to use underrelaxation here ( $(\delta_i^n)_{applied} = v \cdot \delta_i^n + (1-v) \cdot \delta_i^{n-1}$  with e.g.  $v = 0.8$ ). Else, the results of the last VLM solution are postprocessed to obtain the detailed aerodynamic data.

### Step ⑧:

The final postprocessing routine extracts the global force and moment coefficients including coordinate system transformations as well as local parameters along span. Note that the viscous drag retrieved from the viscous section data set ( $(c_d)_{visc} = f_{d_{visc\ data}}(\alpha_{loc})$ ) is added to the induced drag component calculated by vortex lattice theory.

Compared to other methods based on potential theory, the applicability of the present method is extended but still restricted. This method of virtual cambering accounts for viscous effects in the subsonic regime that can be modelled in the two-dimensional case. Thus, it is possible to represent zonal separations (e.g. at the wing tips on highly tapered wings) near stall and even in the post-stall regime. Here, studies have shown that smoothing along span of the retrieved viscous data can stabilise the calculation process. The non-linear section data usually does not exhibit a monotonic behaviour (sink) after stall and therefore produces wiggles in the spanwise distributions due to hysteresis effects. However, highly three-dimensional viscous phenomena like non-linear vortex lift on swept wings cannot be



	RM-L51A26	SAGITTA
planform	delta	diamond
aspect ratio, $AR$	2.31	2.0
sweep (LE), $\varphi_0\%$	60deg	55deg
taper ratio, $\lambda$	0	$\sim 0$
aerofoil	NACA 65010	NACA 64A012
Re (M.A.C.)	$6.0 \times 10^6$	$2.2 \times 10^6$
flap span fraction	0.25	0.15
reference point, $x_{ref}$	$0.417 \cdot c_{root}$	$0.25 \cdot c_{MAC}$

**Figure 3.26:** Planforms and specifications of conventional flap validation test cases RM-L51A26 (HAWES/MAY JR, RALPH W, 1951) and SAGITTA (HÖVELMANN ET AL., 2014) (modified from STADLBERGER/HORNUNG, 2015a)

modelled easily by potential theory. Hence, the present method for subsonic flow is restricted to geometries and angles of attack that are not prone to leading edge separation with associated generation of a stable vortex system.

### 3.5.3 Validation

The presented calculation method is validated by comparing calculated results with available wind tunnel data from two subsonic test cases. Both low aspect ratio wings are equipped with conventional plain flaps and feature high sweep angles as well as low taper ratios. The first case comprises a large-scale delta wing having a leading edge sweep angle of 60deg and an aspect ratio of 2.31 (HAWES/MAY JR, RALPH W, 1951). The SAGITTA diamond wing depicts the second test case having a leading edge sweep angle of 55deg and an aspect ratio of 2.0 (HÖVELMANN/BREITSAMTER, 2012; HÖVELMANN ET AL., 2014). A summary of further specifications is given in Figure 3.26.

An initial discretisation study on the SAGITTA model revealed that chordwise panel numbers beyond  $N_x > 5$  do not lead to further significant changes in the aerodynamic reactions.

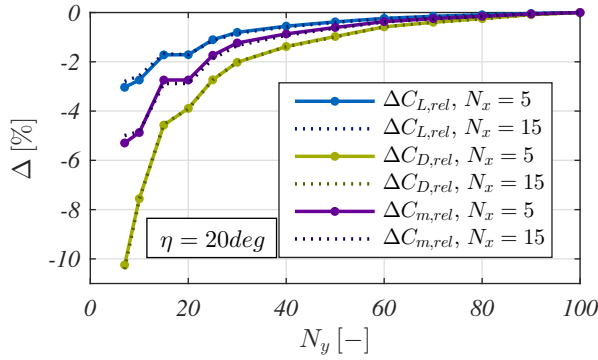


**Figure 3.27:** Relative change in aerodynamic reactions as a function of spanwise panel number

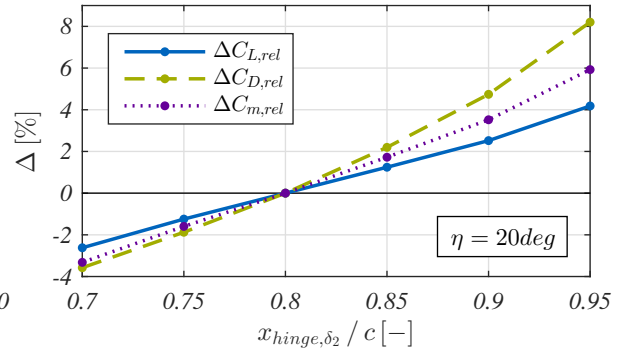


**Figure 3.28:** Relative change in aerodynamic reactions as a function of the relative hinge line position of  $\delta_2$ ,  $N_x = 10$ ,  $N_y = 30$

As can be seen in Figure 3.27, the respective lines of  $N_x = 5$  and  $N_x = 15$  nearly coincide. However, the forces and moments change visibly with the spanwise number of panels, especially below  $N_y < 20$ . As expected, the deviations from reference values ( $N_y = 100$ ) decrease asymptotically with increasing panel numbers. Furthermore, the influence of the relative hinge line position of  $\delta_2$  in chordwise direction was investigated. As depicted in Figure 3.28, the results change inside the range of about  $\pm 4\%$  when the hinge position is varied between  $0.7 \leq \frac{x_{hinge,\delta_2}}{c} \leq 0.9$ . The reference position is  $\frac{x_{hinge,\delta_2}}{c} = 0.8$ . Note that drag was affected most in both sensitivity studies.

For the subsequent validating calculations, each half span of both vortex lattices was modelled by 20 panels in spanwise direction and 10 panels in chordwise direction. The non-linear viscous 2D data of the respective baseline aerofoils were calculated by XFOIL (DRELA, 1989). The lift, drag and pitching moment increments due to flap deflection on a two-dimensional section were estimated by a semi-empirical DATCOM method from ref. FINK (1978). For both cases, the iterative calculation process converged after about 10 iterations (RM-L51A26: 9-10 iterations, SAGITTA: 5-9 iterations). As can be seen in Figure 3.29a, lift increments could be predicted quite accurately up to flap deflection angles of  $\eta = 20deg$ . Beyond, the numerical results underestimate the lift generation. This is due to the semi-empirical method (FINK, 1978) used for the modelling of two-dimensional flap effectiveness. Trailing edge separations at higher flap deflections seem to occur far later in the wind tunnel experiments than in the semi-empirical model. Induced drag prediction also exhibits acceptable accuracy (Figure 3.29b). Note that for comparison reasons a drag increment  $\Delta C_{D0}$  was added to the numerical drag results of the RM-L51A26 case as zero lift drag was underestimated significantly. In contrast, the zero lift drag for the SAGITTA case could be reproduced very well. Moreover, the pitching moment curves show fairly good agreement between calculated and experimental results (Figure 3.29c). However, similar to the lift curves, the semi-empirical

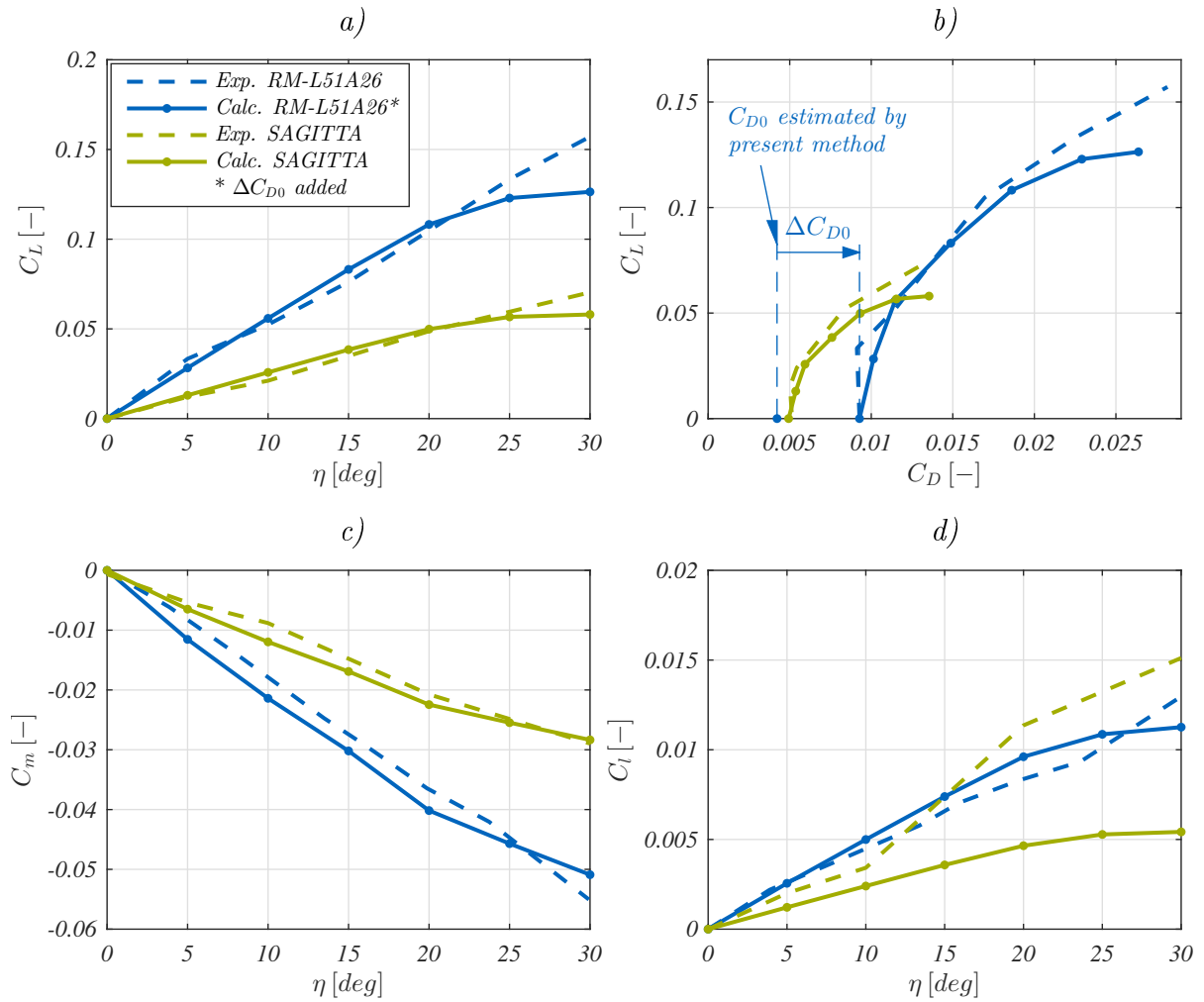


**Figure 3.29:** Comparison of numerical results with experimental data for conventional flaps,  $\alpha_\infty = 0deg$ ,  $\beta_\infty = 0deg$  (modified from STADLBERGER/HORNUNG, 2015a)

underestimation of flap effectiveness is also present for pitching moment beyond  $\eta = 20deg$ . While the roll moment curves show acceptable agreement for the RM-L51A26 case, the SAGITTA curves deviate strongly beginning at  $\eta = 10deg$  (Figure 3.29d). Note that the flap reactions of the SAGITTA wing were measured with mounted vertical stabilisers right next to the flap (Figure 3.26). The discrepancy could be due to interactions that affect the spanwise lift distribution and thus influence the resulting roll moment.

## 3.6 Overall Modelling of the Flight Dynamic System

To combine all previously presented submodels to an overall system model, their input and output data have to be connected inside a simulation environment. For this, a 6-DOF flight dynamic model of the SAGITTA configuration has been established in MATLAB/SIMULINK (R2015b). It allows the investigation of trimmed flight states as well as the real-time simula-

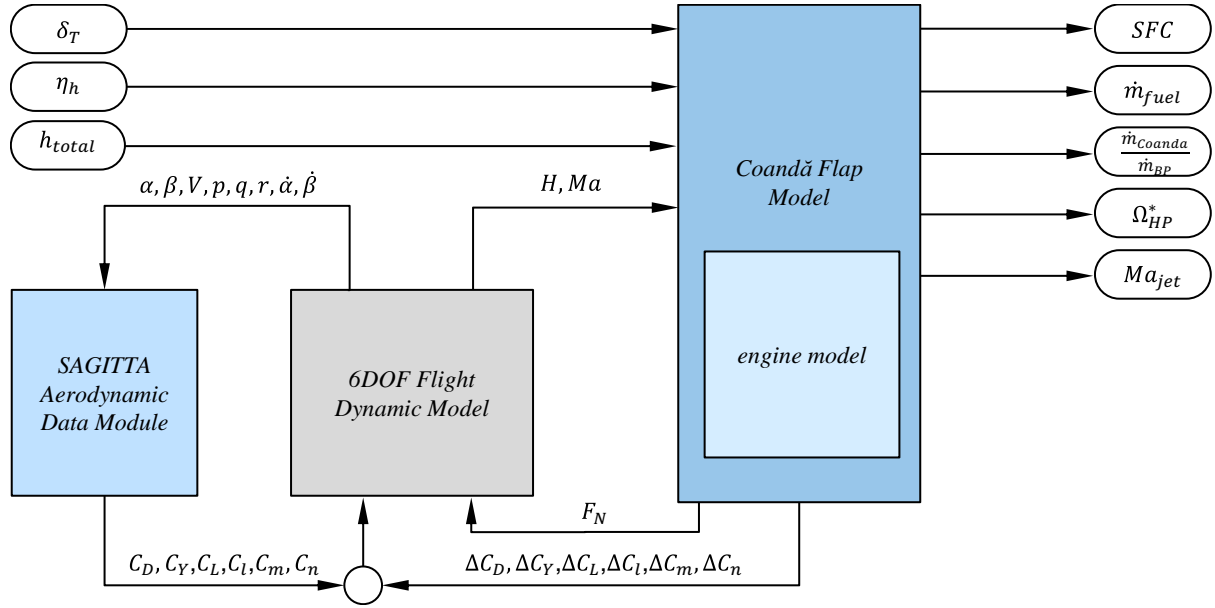


**Figure 3.30:** Main blocks and signal flows inside the SIMULINK model

**Table 3.6:** Main specifications of the SAGITTA wind tunnel model and test conditions

tested Reynolds number	$\sim 1\,700\,000$
free stream velocity	$40 \frac{m}{s}$
measured angles of attack	$-18deg \leq \alpha_\infty \leq 18deg$
measured sideslip angles	$-14deg \leq \beta_\infty \leq 14deg$
wing span	$1m$
fuselage length	$1m$
wing reference area	$0.53m^2$
aspect ratio	$2.1$
mean aerodynamic chord	$0.67m$
outer wing aerofoil	<i>NACA 64A012</i>
wing relative section thickness	$0.12$

tion of flight dynamics. As depicted in Figure 3.30, the aerodynamic data module (ADM) of the clean configuration and the Coandă flap model constitute the main external inputs. The 6-DOF model itself is straightforward and by default available as template in the aerospace toolbox of MATHWORKS. The ADM contains the results of wind tunnel experiments that have been performed on a scaled model (HÖVELMANN/BREITSAMTER, 2012). Its main specifications and test conditions are listed in Table 3.6. Note that the zero lift drag has been adapted for the full scale configuration where Reynolds numbers are significantly higher.

The two-dimensional force and moment increments generated by the Coandă flap are calculated in advance and stored in look-up tables according to the method described in section 3.4. For performance reasons, computationally expensive iterations at simulation

runtime should be avoided. This is especially relevant for the engine-duct linkage. Therefore, precedent matching of pressure ratios  $\frac{p_{BP}}{p_\infty}$  and control parameters ( $A_{slots} = f(h_{total})$ ) is necessary to estimate the bleed and outflow conditions for different altitudes, flight velocities and thrust settings. Here, the system operating line ( $(\Omega^*, \dot{m}_{bleed}, \frac{U_{jet}}{U_\infty}) = f(A_{slots}, H, Ma_\infty, F_{N,req})$ ) for constant engine thrust  $F_{N,req}$  dependent on the outflow area ( $A_{slots} = f(h_{total})$ ) is interpolated by matching two data sets for each flight state ( $H, Ma_\infty, F_{N,req}$ ). As given by the number of dimensions, this corresponds to an intersection of two surfaces, i.e.

$$\Pi_{BP} = f_{engine}(\dot{m}_{bleed}, \Omega^*)_{T_{req}} \cap \dot{m}_{bleed} = f_{duct}(\Pi_{BP}, A_{slots}) \quad (3.59)$$

The resulting outflow velocity is introduced into the 3D Coandă flap modelling process (section 3.5) which then provides data tables containing the six force and moment increments for all input parameters.

$$(\Delta C_D, \Delta C_Y, \Delta C_L, \Delta C_l, \Delta C_m, \Delta C_n) = f_{Coanda\ system}(\eta_h, A_{slots}, H, Ma_\infty, F_{N,req}) \quad (3.60)$$

Finally, a SIMULINK block representing the Coandă flap model is constructed and integrated into the flight dynamic aircraft model. Trimmed flight states can now be found by the automated trim function (e.g. `fmincon`) that solves an optimisation problem. The latter implies the search of feasible input and state variables by use of the gradient descent method with elimination. Starting at trimmed flight states, various dynamic manoeuvres (e.g. roll, pull-up, etc.) can be simulated and analysed as will be shown in chapter 5.

The combination of the previously presented methods implies several assumptions for the overall model:

- Compressibility of the air is neglected for external aerofoil flow, i.e. no corrections (e.g. Prandtl-Glauert) are applied on control force and moment increments. On the one hand, this depicts a conservative approach as lift and moment increments tend to increase with the free stream Mach number up to  $M_\infty = 1$ . On the other hand, possible penalties through shock waves on the upper side due to the transonic flight regime are not taken into account.
- The risk of supersonic Coandă jet detachment is neglected, i.e. under-expanded jets can accelerate on the Coandă surface up to their theoretic velocity  $Ma_{jet} > 1$ . This expansion is assumed to be isentropic without any compressible flow phenomena as shocks or expansion waves. The resulting velocity ratio  $\frac{U_{jet}}{U_\infty}$  is used for the evaluation of the incompressible Coandă aerofoil data set. As already mentioned in subsection 2.2.5, supersonic Coandă jets risk to detach prematurely which entails a sudden loss in circulation control effectiveness. Therefore, results at high transonic flight velocities have

to be regarded with caution when jet Mach numbers have to exceed  $Ma_{jet} > 1.2$  to generate sufficient control forces.

- The control force and moment increments ( $\Delta C_D, \Delta C_Y, \Delta C_L, \Delta C_l, \Delta C_m, \Delta C_n$ ) are assumed to be independent from angle of attack  $\alpha$  and sideslip  $\beta$ . For the sensitivity to  $\alpha$ , this assumption is true up to angles of attack of  $\alpha = 10deg$  as shown in subsection 2.2.4. But even if trailing edge blowing can expand the possible  $\alpha$ -range ( $\alpha_{max}$ ) significantly up to higher incidences, Coandă flap effectiveness reduces at higher  $\alpha$ -values. Leading edge separation still cannot be prevented at extreme angles of attack. The highly increased circulation strength through blowing might lead to premature leading edge stall if the aerofoil nose radius is too sharp.
- Penalties coming from a possible embedded design of the propulsion system are neglected. The propulsion system is modelled by uninstalled engine characteristics without any consideration of possible viscous effects inside inlets or nozzles.

## 4 Test Case: SAGITTA

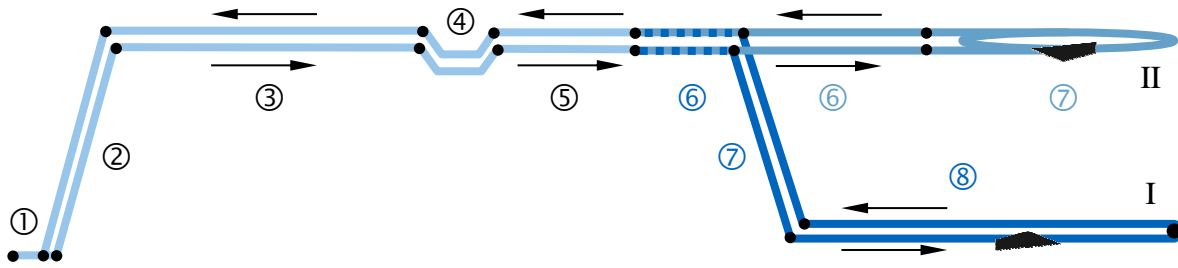
The previously presented methods are to be applied on a flying wing configuration named SAGITTA. To give an overview of this test case, the following sections describe its design mission and performance requirements as well as the most important characteristics of the studied flying-wing configuration. The final two sections seek to define both the conventional reference and the studied novel Coandă flap layout. The results of the comparative performance assessment will be given in the subsequent chapter.

### 4.1 Design Mission and Platform Requirements

The design mission scales the platform size as it determines the required fuel mass to reach the prescribed range or loiter time. In the scope of SAGITTA, the scenario stipulates aerial refuelling as imperative functionality of future stealth UAS. Therefore, the actual drivers for sizing are defined by the mission segments between refuelling as illustrated in Figure 4.1. Here, the two alternatives of low altitude dash flight (I) and high altitude loiter (II) are two sizing examples inside the large collection of possible scenarios. A conventional transfer flight of  $1700nm$  implying fuel reserves for loiter ( $30min$ ) additionally defines the performance requirements given in Table 4.1.

### 4.2 SAGITTA Configuration

The main specifications of the studied SAGITTA configuration are given in Table 4.2 while Figure 4.2 contains the associated 3-view. This unmanned aerial system (UAS) is intended to carry approximately  $3to$  of payload with transonic speeds up to  $Ma_\infty = 0.8$ . It is explicitly designed for low observability demands where all edges are oriented towards two predominant directions. In addition, all vertical surfaces, as stabilisers, are omitted to reduce the radar cross section. This inevitably leads to the necessity of artificial lateral stabilisation through the flight control system. This holds even though highly swept wings naturally exhibit increased weathercock stability. Not only for this reason, the SAGITTA configuration imposes challenging requirements on the intended fluidic flight control system



① → warming up, taxi, take-off /  
← landing, taxi, shutdown

② → acceleration, climb to 30 000ft /  
← descent, deceleration

③ cruise of 1500nm

④ aerial refuelling in 25 000ft (30min)

⑤ cruise of 100nm at Mach 0.8

Mission alternative I :

⑥ cruise of 150nm at Mach 0.8

⑦ → descent to 1000ft /  
← climb to 30 000ft

⑧ dash of 350nm at Mach 0.8

Mission alternative II :

⑥ cruise of 200nm at Mach 0.8

⑦ loiter of 5h

**Figure 4.1:** Illustration of the SAGITTA design mission

**Table 4.1:** Requirements imposed on the SAGITTA configuration

<b>Performance requirements</b>	
min. range (no refuel)	1700nm
radius of action (1000ft – 15 000ft)	500nm – 700nm
low level max dash speed (3000ft)	Ma 0.9
max. take-off field length	2400m
max. landing distance	1500m
sustained turn performance (STR)	3g @ Ma 0.7, 3000m
climb performance	15m/s @ MTOW, SL
<b>Life cycle requirements</b>	
max. temperature	ISA + 35 @ SL
service life	5000h (40 years)
average mission duration	10h
expected cycles (T/O & landing)	1000
max. manoeuvre g-load	±4.5g

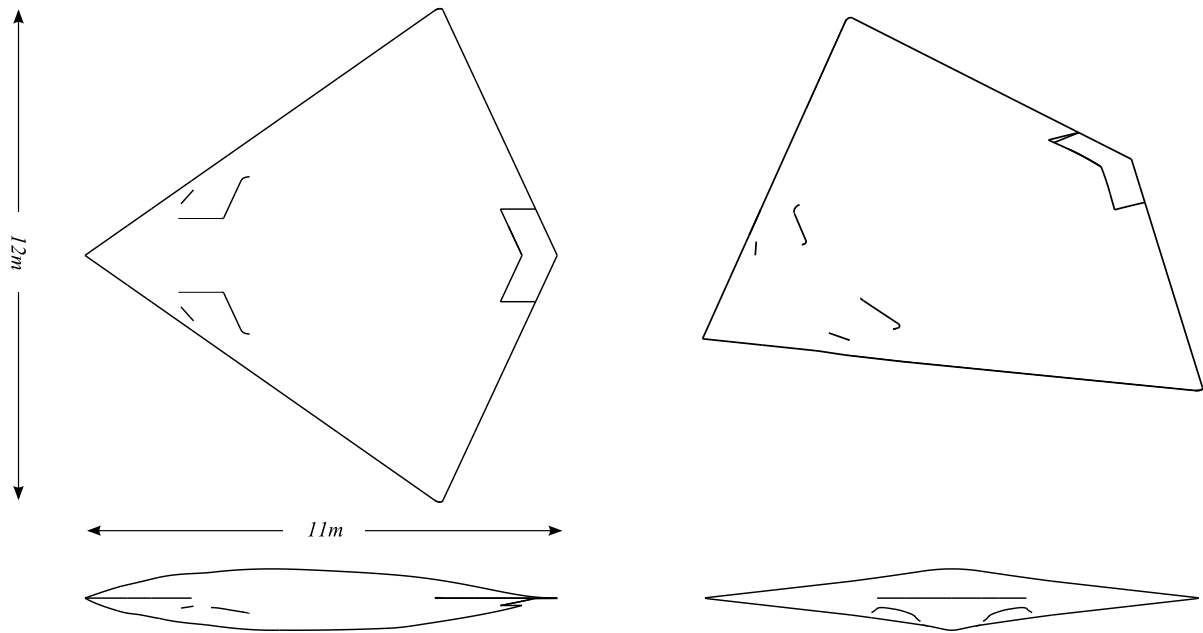


**Figure 4.2:** 3-view of the SAGITTA configuration

**Table 4.2:** Main specifications of the SAGITTA configuration

maximum take-off weight (MTOW)	$m_{MTOW}$	16.7to
wing span	$b$	11.8m
(fuselage) length	$l_{A/C}$	11.2m
height	$h_{A/C}$	2.3m
wing reference area	$S_{ref}$	66.0m <sup>2</sup>
aspect ratio	$AR$	2.1
mean aerodynamic chord	$\bar{c}$	7.45m
wing relative section thickness	$t/c$	0.125
wing loading (T/O)	$m/S_{ref}$	260 kg/m <sup>2</sup>
thrust-to-weight-ratio (T/O)	$F_N/m$	0.34
moments of inertia	$\begin{pmatrix} I_{xx} \\ I_{yy} \\ I_{zz} \end{pmatrix} \begin{pmatrix} 3, 1 \\ 7, 6 \\ 10, 6 \end{pmatrix} \times 10^4 kgm^2$	

(STADLBERGER/HORNUNG, 2012). As the characteristic wing and the envisaged propulsion system mainly determine the performance of the studied Coandă flap system, they are addressed in more detail in the following subsections.

### 4.2.1 Flying Wing

The flying wing configuration is characterised by a diamond planform featuring a low aspect ratio ( $AR = 2.1$ ) and a moderate leading edge sweep angle ( $\varphi_{0\%} = 55deg$ ). In general, the relatively low wing loading promises a considerable potential for high control authority. Aerodynamic forces are high compared to the aircraft's inertia. However, the low aspect ratio provides only short moment arms which diminish this advantage.

While the root sections feature sharp leading edges for radar signature reasons, the outer wing sections are based on the NACA64A aerofoil series whose round nose shape alleviates induced drag penalties. Since the wing also has to perform adequately during upside-down flight, the aerofoil camber line is restricted to only slight S-shapes (reflexed trailing edge). Therefore, flight control devices (conventional/novel flap systems, thrust vectoring) have to be employed to attain zero pitching moment for trimmed flight. The more asymmetric the aerofoil shape, the more the flight control system is challenged during inverted flight.

### 4.2.2 Propulsion System

The propulsion system consists of two embedded jet engines with serpent duct intakes and shielded nozzle sections. The twin engine configuration increases redundancy and enables one single central payload bay which avoids a lateral shift in c.g. position. The transonic flight regime ( $Ma_{\infty} \leq 0.85$ ) suggests the installation of a turbofan engine with increased bypass ratio promising high efficiency (low SFC) and extended range. In addition, lower exit temperatures and low exit speeds are favourable in terms of infra-red (IR) and noise signature. This additionally contributes to the low observable aircraft design. However, the available space for the two engines is limited by the low section thickness in the wing root zone. Due to this engine diameter constraint, only low bypass ratios can be realised for the present flying wing configuration. An appropriate engine (model AI-222-28) of suitable size was developed by IVCHENKO-PROGRESS since 1999 which had its first run in 2003. For this study, a slightly modified numerical representation in form of a generic engine was modelled in GasTurb (section 3.2) whose specifications are given in Table 4.3.

**Table 4.3:** Specifications of generic engine

Geometry		
LPC number of stages		3
fan area	$A_{fan}$	$0.317 m^2$
bypass area	$A_{BP}$	$0.104 m^2$
HPC number of stages		5
HPT number of stages		1
LPT number of stages		1
maximum diameter	$D_{engine}$	$0.88 m$
Parameters at design point (ISA0m, $Ma_\infty = 0$ )		
thrust (ISA0m)	$(F_N)_{ISA0}$	$26.25 kN$
bypass ratio	$\frac{\dot{m}_{BP}}{\dot{m}_{core}}$	1.5
air mass flow	$\dot{m}_{engine}$	$50.2 kg/s$
fan pressure ratio	$\Pi_{BP}$	2.16
HPC pressure ratio	$\Pi_{HPC}$	14.7
turbine inlet temperature	$T_{t,4}$	$1600 K$
nominal spool speed HP	$\Omega_{HP}$	$22\ 800 rpm$
nominal spool speed LP	$\Omega_{LP}$	$14\ 600 rpm$
specific fuel consumption	$SFC$	$17.84 g/kNs$

### 4.3 Conventional Reference Flap Layout

For the subsequent assessment of the studied Coandă flap system, a conventional flap scheme (Figure 4.3, top) serves as reference. These conventional flaps have also been implemented on the SAGITTA wind tunnel model for testing (Figure 4.4). They include inboard and midboard elevons for pitch and roll control as well as tip split flaps to assure yaw control. Under the assumption of a symmetric aerofoil, the flap geometry of the inboard plain flaps have been sized such that their necessary exclusive deflection for longitudinal trim at  $\alpha = 10deg$  does not exceed  $\eta_{inboard} \leq 20deg$ . The midboard plain flaps and tip split flaps compete for available space along span. Their final spanwise extension constitutes a compromise to attain sufficient roll and yaw authority for steady sideslip flight at  $\beta = 10deg$ .

### 4.4 Novel Coandă Flap Layout

As fundamental part of the novel flight control concept, the midboard elevon is replaced by flow control effectors including the necessary ducts that originate at the engine's bypass (Figure 4.3, bottom). The conventional inboard plain flaps are designed as a moving but

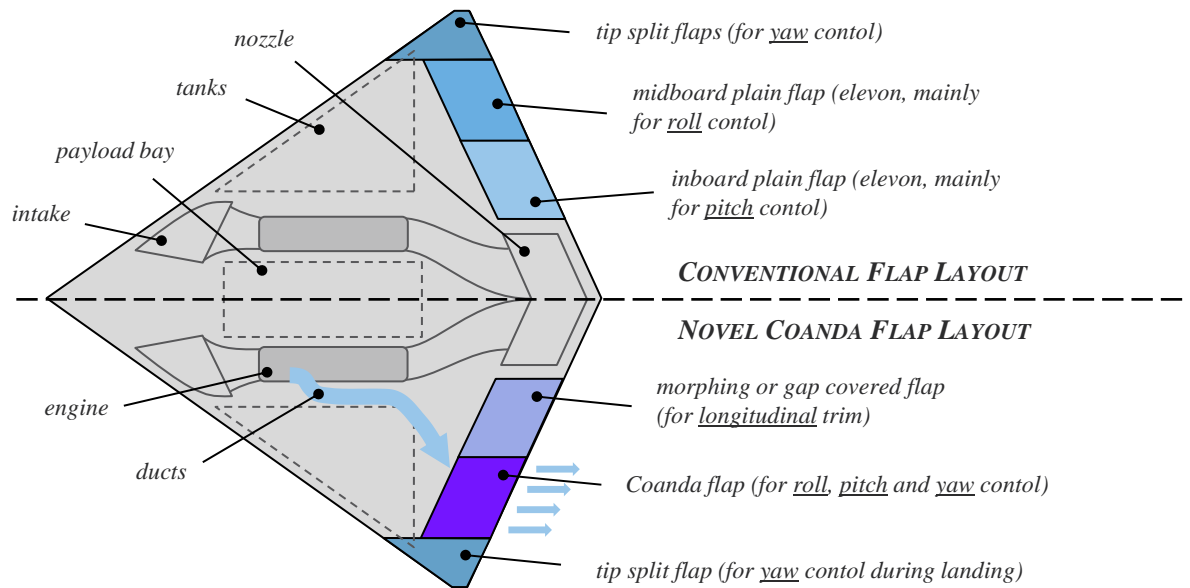


**Figure 4.3:** Illustration of the conventional reference flap scheme (top) and Coanda flap flight control concept (bottom) (modified from STADLBERGER/HORNUNG, 2014, 2015a)



**Figure 4.4:** SAGITTA wind tunnel model with conventional plain flaps and two different types of tip split flaps (left: abandoned concept, right: investigated vortex flap concept)

gapless solution (e.g. DA ROCHA-SCHMIDT/BAIER (2013); GRAMÜLLER ET AL. (2014)). Since the inboard elevon flap performs better for pitch control than for roll or yaw moment generation, the technology of flexible gap covers or morphing structures appears applicable for longitudinal trim. Slow-moving systems are acceptable here. Highly dynamic manoeuvres in pitch, roll and yaw are performed by the midboard Coandă flap. The vortex split flap on the “dirty” side (with all other openings) is retained to assure sufficient safety margins for yaw control under conditions of high sideslip angles (e.g. crosswind landing). It is assumed not to affect the cruise flight radar cross section excessively when it is completely closed.

# 5 Application and Discussion

The previously presented SAGITTA configuration serves as test case for the application of the modelling methods that are described in chapter 3. By discussing the results for the isolated subsystems, this chapter gives insight into their respective performance and sensitivities. The latter thereby enable the deduction of preliminary design rules. The evaluation of the overall system in terms of feasibility and efficiency requires studies on the control authority as well as on the fuel consumption of the complete Coandă flap system. For this, the conventional plain flaps build the reference case.

## 5.1 Preliminary Results for the Isolated Subsystems

In accordance to the definition of relevant submodels (chapter 3), the following subsections discuss the intermediate results for the engines, ducts, Coandă aerofoil sections and finite wing.

### 5.1.1 Intermediate Results of Engine Modelling

This subsection investigates the impact of bypass bleed on the performance of the studied propulsion system (Table 4.3). The three stages of the low pressure compressor (LPC) charge the bypass air to pressure ratios  $\Pi_{BP} = \frac{p_{t,BP}}{p_\infty}$  of 1.3 up to 4. This pressurised air can be exploited for circulation control concepts that are based on trailing edge blowing. For standard conditions (ISA  $H = 0m$ ,  $Ma = 0$ ), Figure 5.1a illustrates the reduction in total pressure inside the bypass duct for different relative high pressure (HP) spool speeds  $\Omega_{HP}^* = \frac{\Omega_{HP}}{(\Omega_{HP})_{design}}$  when bypass air is bled off after the LPC. The engine net thrust decreases due to reduced nozzle mass flow and loss of total pressure. The latter can be traced back to the characteristics of the LPC compressor responding to the increased bypass mass flow.

To evaluate the impact of bypass bleed on the thermodynamic cycle, the thrust force is related to the fuel consumption  $\dot{m}_{fuel}$  yielding the specific thrust  $\frac{F_N}{\dot{m}_{fuel}}$ . The solid lines in Figure 5.1b represent the specific thrust based on solely the thrust force produced by the engine nozzle. As expected, under bleed conditions, specific thrust diminishes rapidly with

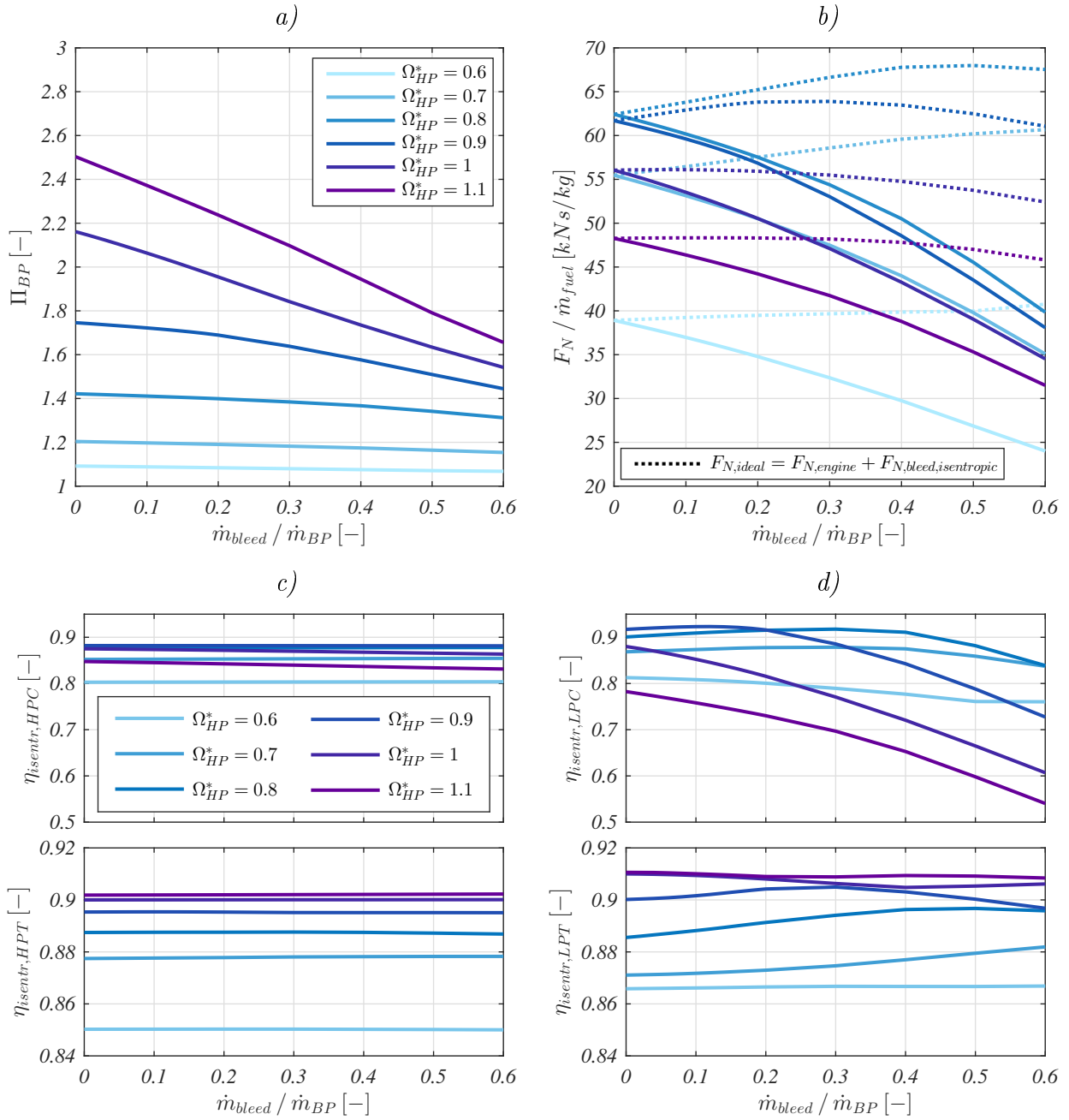


**Figure 5.1:** Bypass pressure ratio (a), specific thrust (b) and isentropic efficiencies (c, d) as a function of bypass bleed at standard conditions ( $H = 0m$ ,  $Ma = 0$ )

decreasing available nozzle thrust force. However, in the scope of the studied Coandă flap concept, the bled air is not completely lost and still can produce a contributing thrust force when ejected at the trailing edge. Assuming an ideally adapted nozzle for the bleed air and an isentropic expansion of the ideal gas without any viscous losses, an imaginary total thrust force  $F_{N,ideal} = F_{N,engine} + F_{N,bleed,isentropic}$  can be derived by use of the isentropic flow equations (section C in the appendix). For this calculation, the total pressure and the total temperature of the bypass air are taken from the output of the GasTurb simulation. The associated specific ideal thrust is represented by the dotted lines in Figure 5.1b. Up to regions of moderate bleed fractions ( $\frac{\dot{m}_{bleed}}{\dot{m}_{BP}} < 0.3$ ), the specific ideal thrust remains constant or even grows for low off-design spool speeds ( $\Omega_{HP}^* \leq 0.9$ ).

Despite the declining mixing efficiency of the remaining cold bypass and hot core engine flow (FAROKHI, 2009, p. 294ff), bypass bleed seems to have a favourable impact on the engine overall efficiency. The reasons can primarily be found in the new operating points of the most critical subcomponents. For standard conditions ( $H = 0m$ ,  $Ma_\infty = 0$ ), Figure 5.2 and Figure 5.3 depict the compressor (a) and turbine (b) maps of the HP and LP spool, respectively. The coloured solid lines represent the operating lines, i.e. the component's pressure ratio  $\Pi$  as a function of corrected mass flow  $\dot{m}_{corr}$ . While the operating points in the HP compressor and turbine maps are affected only slightly (Figure 5.2), the impact on the LP spool is more pronounced (Figure 5.3). Increased LPC mass flow and LP spool speeds in the off-design regime shift the operating points to higher adiabatic efficiencies both in the LPC turbine and compressor maps. However, close to the design points, bypass bleed leads to a cutback in adiabatic efficiency. These trends can be seen additionally in Figure 5.1c and Figure 5.1d which illustrate the isentropic efficiencies of the HP (c) and LP (d) spool. Above all the gain in LP turbine efficiency improves the overall engine efficiency under the assumption of ideal bleed air exploitation. In reality, significant reductions have to be expected because of viscous effects at the bleed air separator, inside the duct system, and inside the plenum chamber at the wing trailing edge.

During operation, the thrust loss due to bypass bleed will have to be partially compensated by higher throttle settings. Figure 5.4a shows the relative HP spool speed  $\Omega_{HP}^*$  as a function of bleed air fraction that is necessary to maintain the required thrust at three different flight states. Under the assumption of zero thrust recovery from bleed air (100% lost), the throttle setting has to be increased more than linearly. The higher rotational speed of the compressors counterbalances the nominal decline in total pressure seen in Figure 5.1a. In reality, the engine speed is naturally limited due to mechanical constraints (bearings, static strength, fatigue, etc.). Thus, there is a maximum feasible bleed fraction that reduces with increasing thrust demand. As the generated thrust is approximately proportional to the total pressure ratio inside the engine nozzle, the settled bypass pressure ratio on the operation line does not vary dramatically (Figure 5.4b).

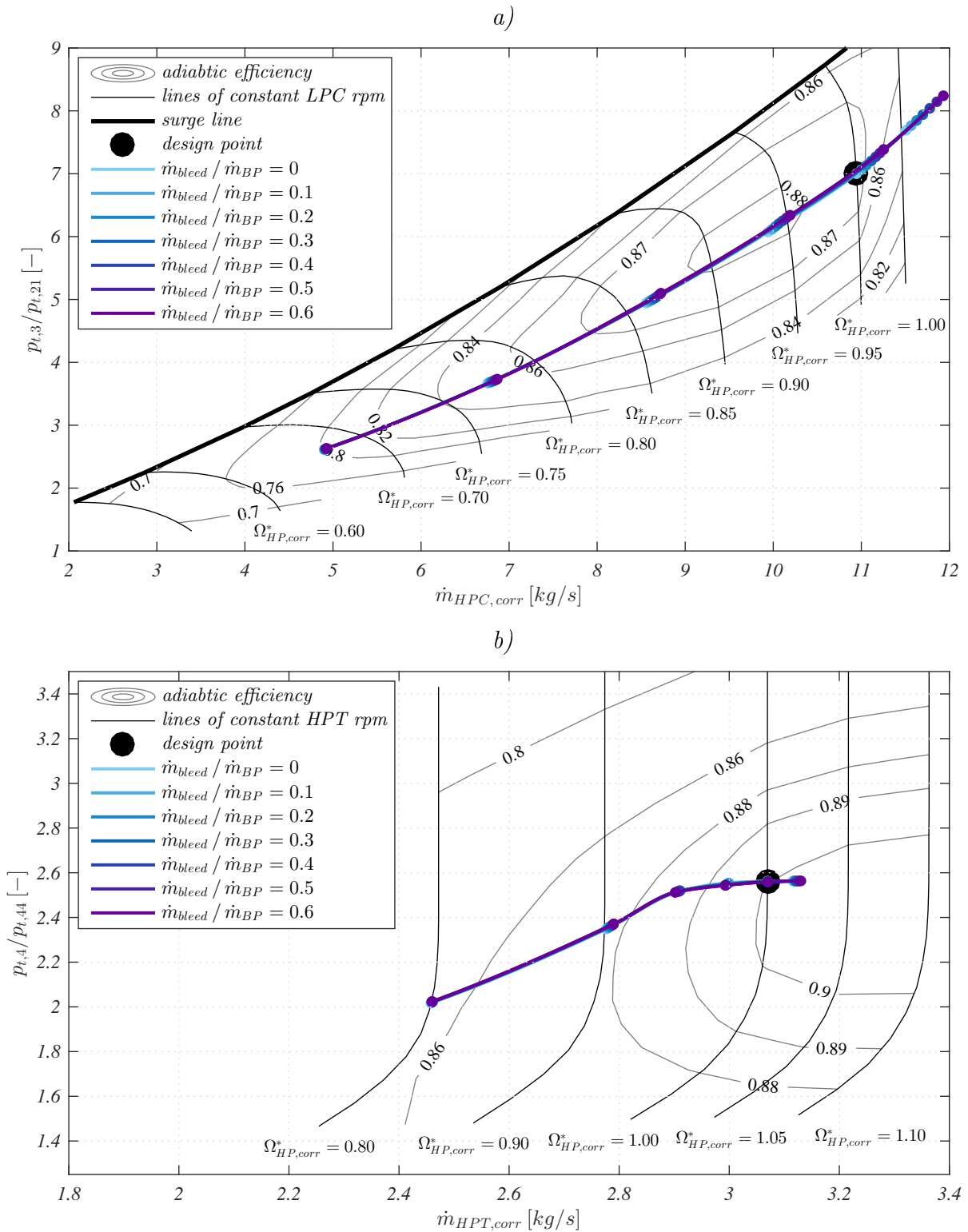


**Figure 5.2:** High pressure compressor (a) and turbine (b) map with operating lines for different bleed fractions at standard conditions ( $H = 0m, Ma = 0$ )

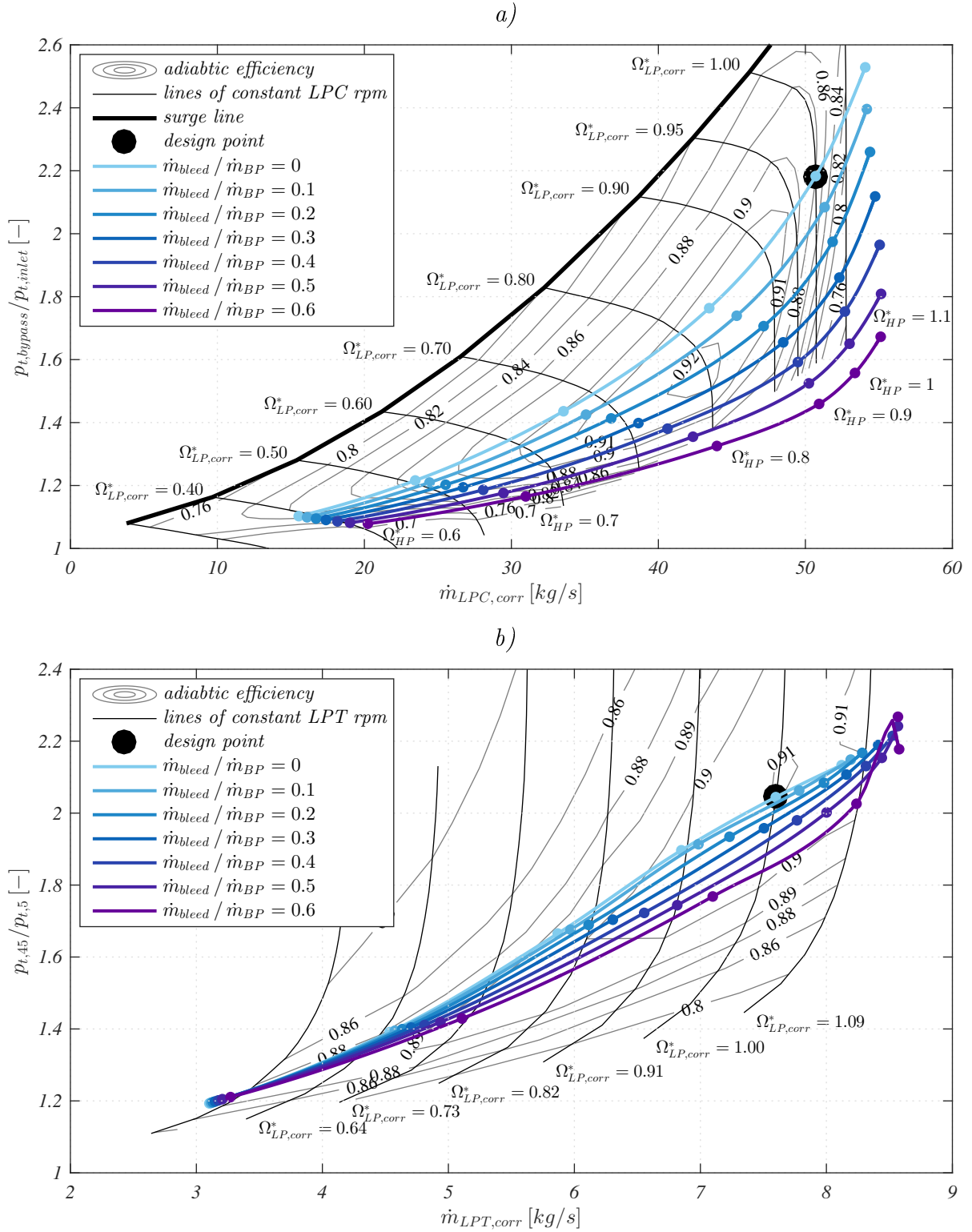


**Figure 5.3:** Low pressure compressor (a) and turbine (b) map with operating lines for different bleed fractions at standard conditions ( $H = 0m$ ,  $Ma = 0$ )

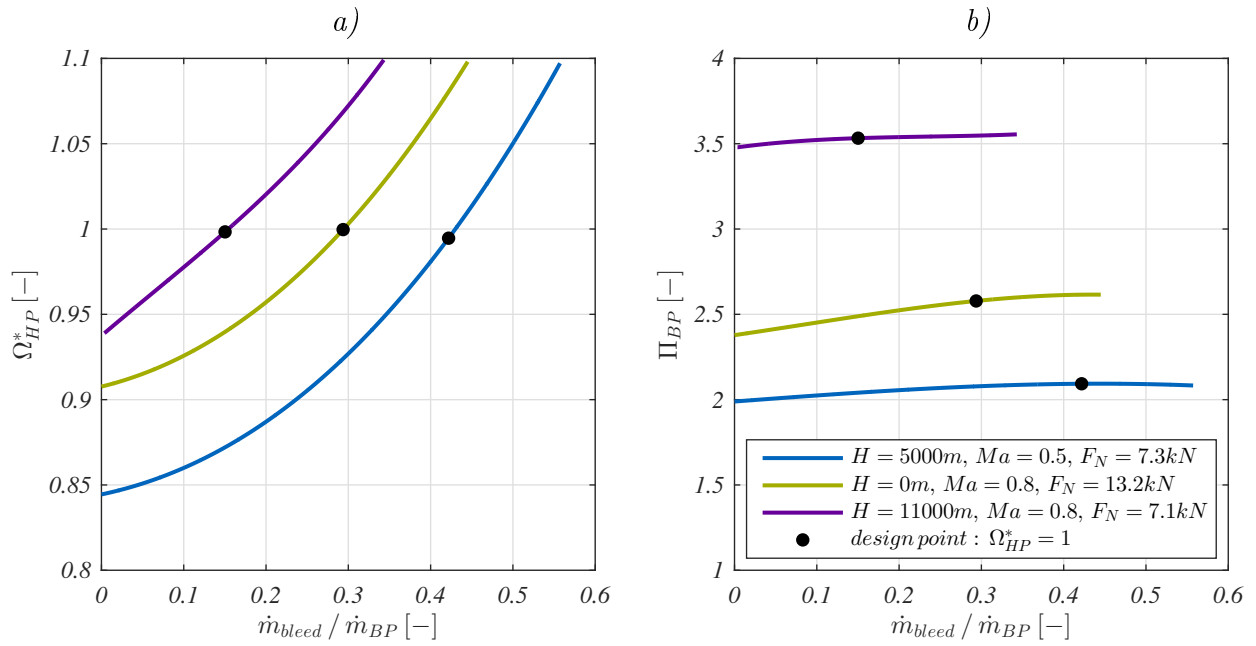


Figure 5.4: Relative HP spool speed (a) and bypass pressure ratio (b) as a function of bypass bleed fraction

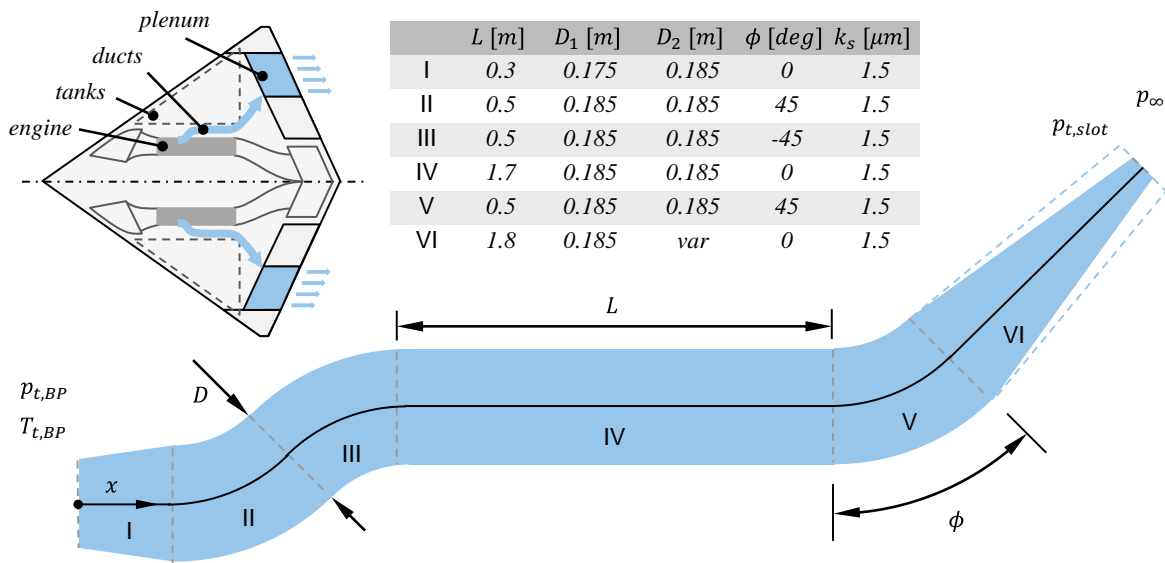


Figure 5.5: Illustration of studied duct system

### 5.1.2 Intermediate Results of Duct Modelling

The method proposed in section 3.3 is applied on the SAGITTA duct geometry. The pipe system is designed to fit inside the wing loft respecting the space demands of other subsystems (e.g. tanks). By definition, it connects the engine bypass with the Coandă flap at the trailing edge. Each half span is supplied by only one engine, i.e. no redundancy through cross-feed was postulated in the scope of this work. The studied duct shape, including the different pipe segments I-V, is illustrated and dimensioned in Figure 5.5. The nominal diameter

$D_{nom} = D_{II-V}$  of the majority of the pipe length (II-V) was specified such that the duct cross section area corresponds to 25% of the engine bypass duct area. This fraction was chosen somehow arbitrarily and was supposed to lead to reasonable dimensions that can be translated into a realisable design of the bleed air separator device. The viscous losses inside this device are modelled by a simple linear relation ( $p_{t,in} \approx (1 - 0.06 \frac{\dot{m}_{bleed}}{(\dot{m}_{bleed})_{max}}) \cdot p_{t,BP}$ ). Hence, the bleed off process is assumed to produce pressure losses of about 6% at the highest observed mass flow rate. Similar values have been measured by BARBERIE ET AL. (2013) and WICK ET AL. (2013).

In contrast to an isentropic flow (subsection 3.3.3), the total pressure of the real bleed air flow decreases continuously along its way through the duct system. These pressure losses of the given geometry (Figure 5.5) are illustrated in Figure 5.6d along the pipe's centreline ( $x$ ). The impact of the different pipe segments (I-VI) is clearly visible. In particular, the pipe bends lead to increased equivalent friction factors which are more than doubled compared to straight pipe sections (Figure 5.6b). As the pressure loss is mainly a function of flow velocity (Figure 5.6f), the most significant drop in total pressure can be seen in the most aft sections at the converging nozzle (VI). The flow parameter evolutions of static pressure (Figure 5.6c), static temperature (Figure 5.6e) and air density (Figure 5.6g) additionally illustrate the fact that the flow accelerates mainly along the final metre. In general, the pressure losses are fairly low ( $\sim 2\%$ ) for the tested equivalent slot diameter ratio of  $\frac{D_{slot}}{D_{nom}} \approx 0.5$ . Low mass flow rates and velocities over large parts of the total duct length lead to only minor viscous losses.

The present Coandă flap concept comprises the individual and independent adjustment of the slot heights, i.e. of the outflow section area  $A_{slot}$ . Under the assumption of isentropic flow, the outlet section area solely determines the mass flow while the outflow velocity is given by the pressure ratio  $\Pi_{BP}$ . In the viscous representation, however, the reduction of total pressure at the slot exit also implies a reduction of outflow velocity and mass flow which, in turn, influences the viscous pressure losses. Figure 5.7a shows the relative pressure ratio  $\frac{\Pi_{slot}}{\Pi_{BP}}$  at the slot exit as a function of input pressure ratio  $\Pi_{BP}$  for different outflow area ratios  $\frac{A_{in}}{A_{out}}$ . In the subcritical region ( $\Pi_{BP} \lesssim 1.9$ ), the pressure losses increase for higher flow velocities, i.e. growing mass flows. These are due to, either an increased bypass pressure ratio, or an increased outflow cross section area. However, under choked conditions the flow velocity inside the duct remains approximately constant with increasing pressure ratio. Consequently, the pressure losses change insignificantly once  $Ma = 1$  is reached at the outlet. With growing static pressure and air density throughout the entire duct, the local Reynolds numbers rise (Figure 5.6h) and lead to slightly reduced friction factors  $\lambda_{fric}$  (Figure 5.6b). For processing speed reasons, it is therefore convenient to freeze the pressure loss ratio  $\frac{p_{t,outlet}}{p_{t,inlet}}$  at the value of critical slot conditions ( $Ma_{slot} = 1$ ). In Figure 5.7a this approximation is illustrated by the respective dotted lines. With this, the remaining flow

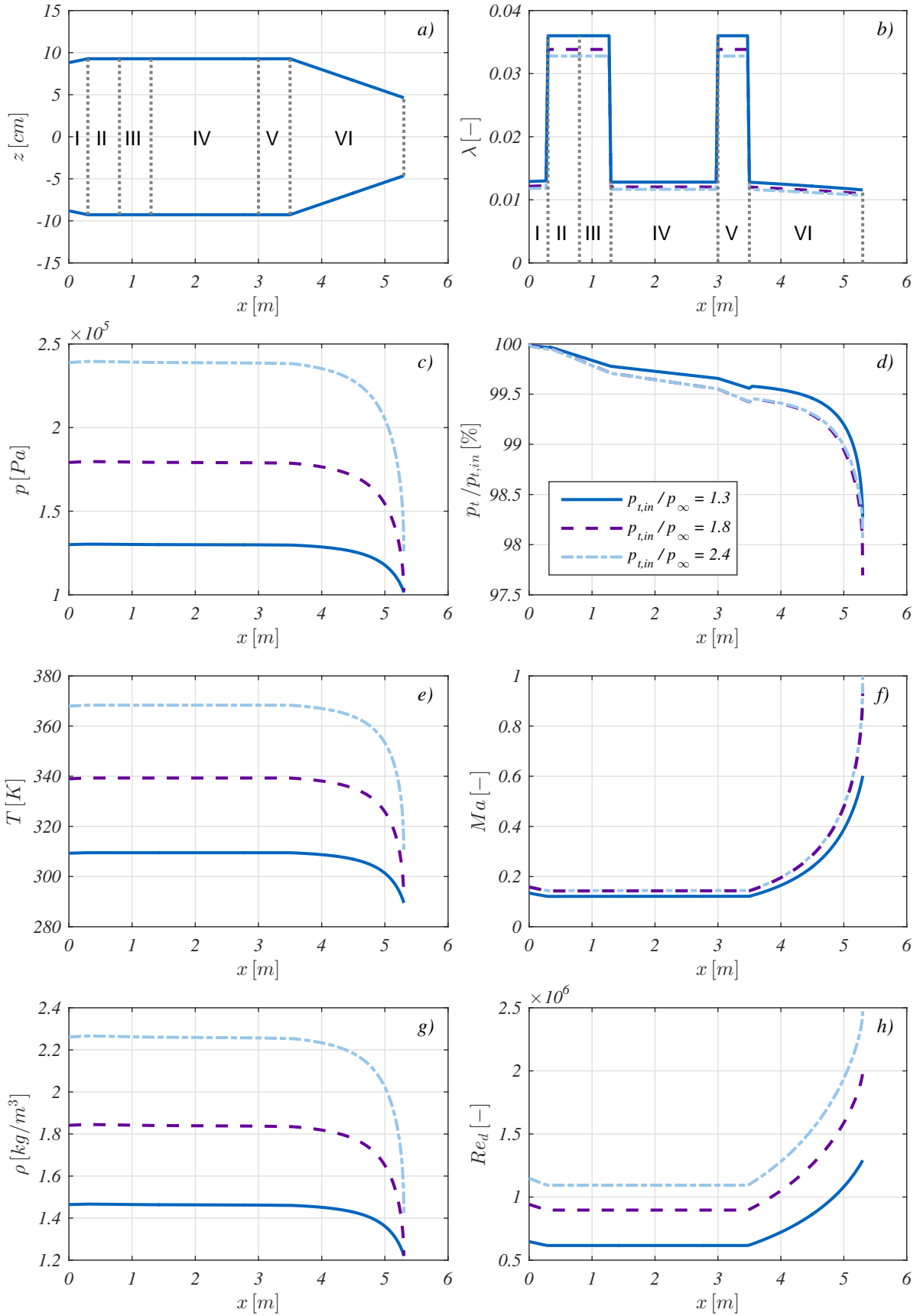
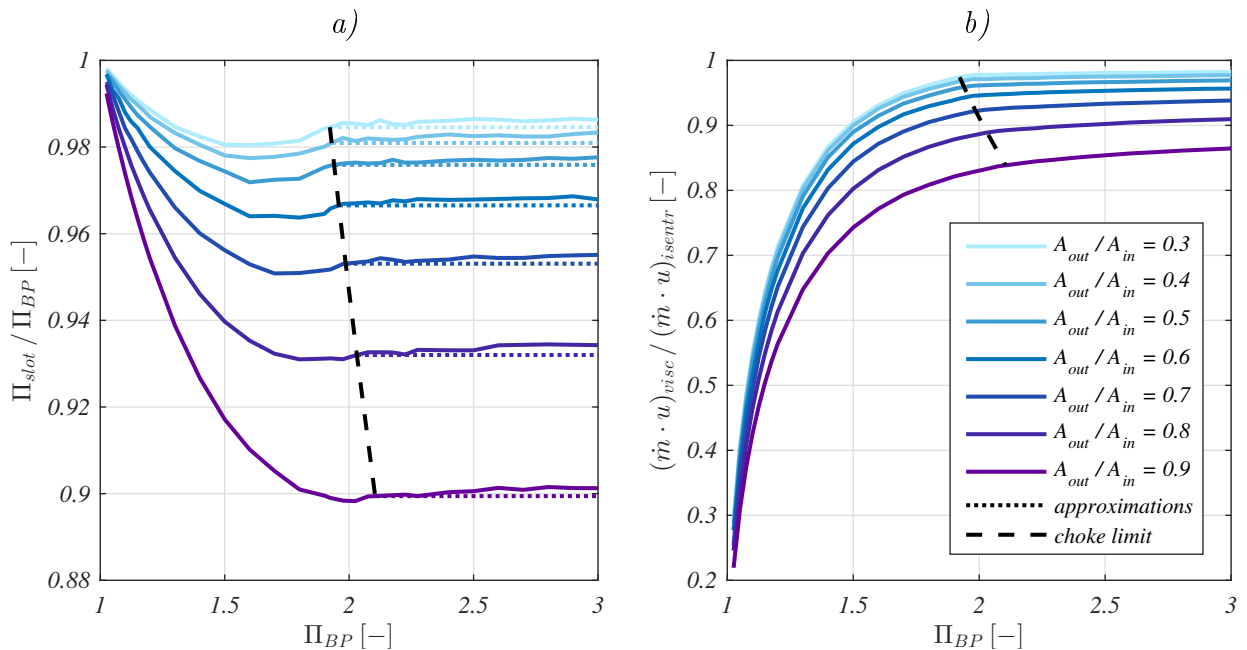


Figure 5.6: Flow parameters along duct at ISA0m



**Figure 5.7:** Relative pressure ratio (a) and relative momentum flux (b) at slot exit w.r.t. duct entrance values for different slot outlet areas

parameters can be simply calculated by use of the isentropic flow equations without the necessity of iterations. In general, the magnitude of total pressure losses (1% – 10%) seems to have reasonable values that were also found in wind tunnel tests on an optimised duct system for a similar application (WICK ET AL., 2013).

Figure 5.7b depicts the dependency of the relative outflow momentum flux  $\frac{(\dot{m} \cdot u)_{visc}}{(\dot{m} \cdot u)_{isentr}}$  on the inlet pressure ratio. The already introduced blowing momentum coefficient  $C_\mu$  (section 2.2) directly depends on the jet momentum flux and determines Coandă flap effectiveness. As can be seen, the relative losses in jet momentum are most severe for low pressure rates but alleviate for higher pressure ratios and virtually stagnate under choked conditions. Note that in case of choked flow, the outflow momentum flux  $(\dot{m} \cdot u)_i$  is calculated with the outflow velocity  $u_{out}$  of the completely expanded jet. The expansion is assumed to follow isentropic rules. This simplification no longer holds for higher pressure ratios when significant compressible effects (shocks etc.) have to be expected. In summary, jet momentum losses up to approx. 20% (for maximum slot opening) have to be expected in view of relevant pressure ratios provided by the engine bypass flow.

As already mentioned before, the nominal duct diameter  $D_{nom} = D_{II-V}$  is set to the value which corresponds to the maximum feasible fraction of bypass cross section area. The empirical relations demand maximum diameters for minimum pressure losses (Equation 3.16). This correlation is illustrated in Figure 5.8a where the relative outlet pressure ratio  $\frac{\Pi_{slot}}{\Pi_{BP}}$  decreases with decreasing diameter  $D_{II-V}$ . Note that the impact of the nominal diameter reduces under choked conditions as flow velocities increase only slightly with further in-

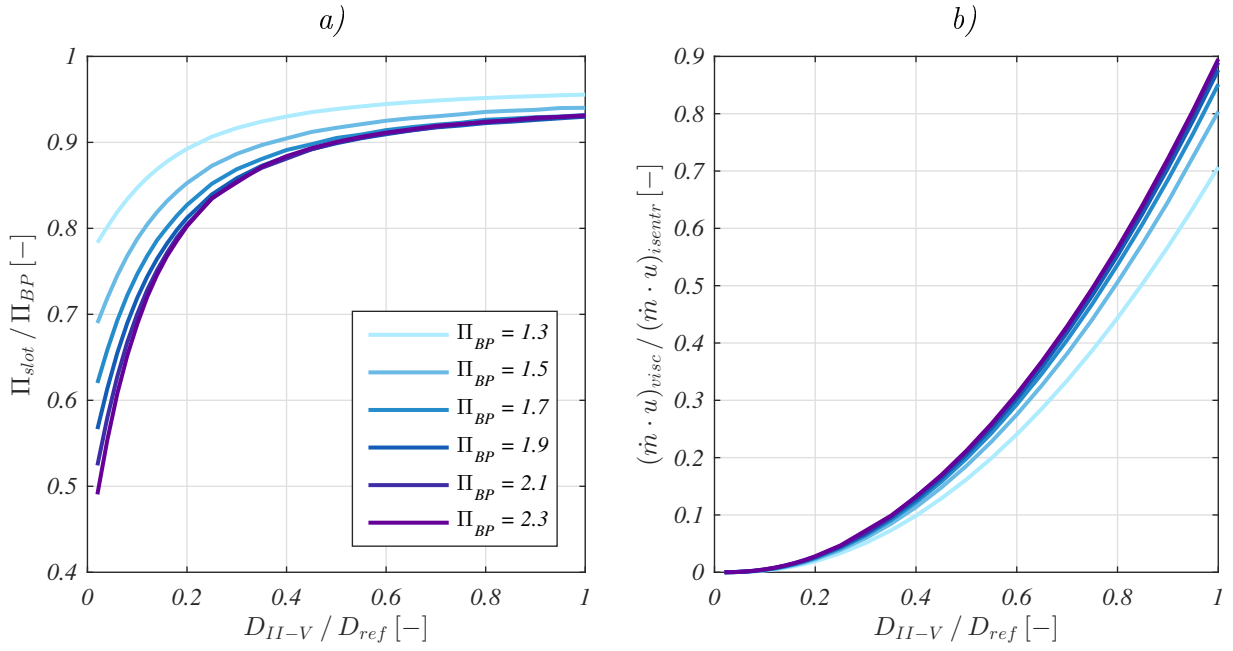


**Figure 5.8:** Relative pressure ratio (a) and relative momentum flux (b) at slot exit w.r.t. duct entrance values for different diameter sizes of the nominal duct pipe,  $D_{ref} = 0.185m$

creasing pressure ratio. While the loss in total pressure yields approx. 10% for a diameter reduction of 50%, the loss in jet momentum is dramatically higher (approx. 80%) as can be seen in Figure 5.8b. The curves underline the necessity to choose the duct diameters as large as possible. Moreover, pipe bend angles and diverging segments should be reduced to a minimum. Of course, these measures are constrained by available space and duct system mass limitations.

### 5.1.3 Intermediate Results of Coandă Aerofoil Modelling

The method for 2D Coandă aerofoil modelling presented in section 3.4 is now applied on the NACA 64A012CC aerofoil whose geometry data are given in Figure 5.9. Most of the results and discussions on this test case can also be found in STADLBERGER/HORNUNG (2015b). For the symmetric contour of the Coandă surface, a conventional circular shape has been chosen even though elliptic trailing edges revealed more suitable for transonic flight (section 2.2). The reason for this choice is mainly due to the fact that the incompressible RANS modelling represents only subsonic speeds and does not account for possible compressible effects on the aerofoil surface (subsection 2.2.6) or inside the wall jet (subsection 2.2.5). Thus, for the investigation of the full control force potential in the incompressible low speed regime, the circular trailing edge is more representative (subsection 2.2.1). For transonic flight, the resulting aerofoil polar data constitute an optimistic model in terms of control effectiveness but a conservative model in terms of drag. So, in the compressibility dominated flow regime,

NACA 64A012CC

$t/c_{base}$	12%
<i>camber</i>	0%
$c_{base}$ [m]	1
$r/c_{base}$	0.01 – 0.04
$Re$	$\sim 4 \times 10^6$
$h_u/t$ [mm]	0.1 – 1.9
$h_{lip}$ [mm]	0.5

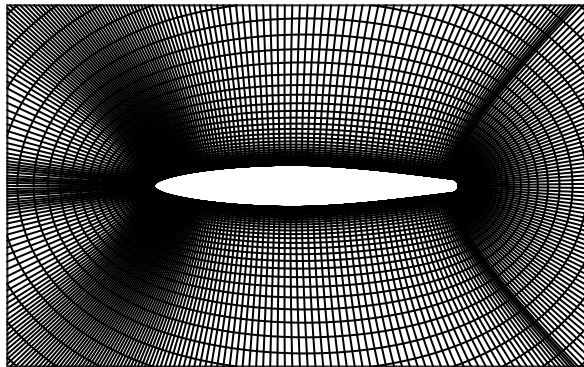


**Figure 5.9:** Geometry of the studied NACA 64A012 circulation control aerofoil and used grid topology (STADLBERGER/HÖRNUNG, 2015b)

the final results have to be taken with caution when further processed in the subsequent feasibility study (section 5.2).

During this calculation campaign, the used grid had a total longitudinal point number of about 350 around the entire surface with approximately 70 to 100 of these points concentrated on the Coandă trailing edge. The grid sections covering the wall jets had approximately 90 points in the normal direction to the Coandă surface giving a total grid point number of about 70 000 for each of the investigated meshes. The calculations were performed on the same machines as specified in subsection 3.4.6. One iteration took between 4s and 6s where a converged lift coefficient was attained after an average number of 60 iterations. Parameter variations of the Coandă radius  $r$ , the slot heights ( $h_u, h_l$ ), the blowing velocity  $\frac{U_{jet}}{U_\infty}$ , and the angle of attack  $\alpha$  have been investigated during the completely automated calculation campaign. The 18 quad-core desktop machines enabled a total number of 72 simultaneous simulations. Finally, the results of 30 000 calculated data points are available for performance analysis. In contrast to the previous validation case (subsection 3.4.6), the concept of the present circulation control aerofoil features both an upper and lower slot. This double-slotted Coandă aerofoil design thereby enables control moment reactions in both senses. The following paragraphs, however, discuss only one operating direction of the symmetric baseline aerofoil.

Note that the aerodynamic forces and moments acting on the aerofoil have been determined by integration of pressure and shear stress forces along the outer aerofoil skin (Figure 5.10). Therefore, the aerodynamic coefficients do not include the thrust force which is generated through the jet momentum flux passing the control volume at the slots. This is especially important for the interpretation of the drag coefficient curves. Furthermore, the aerodynamic coefficients are generally based on the Coandă aerofoil chord length  $c_{Coanda}$  (and not on the baseline chord length  $c_{base}$ ).

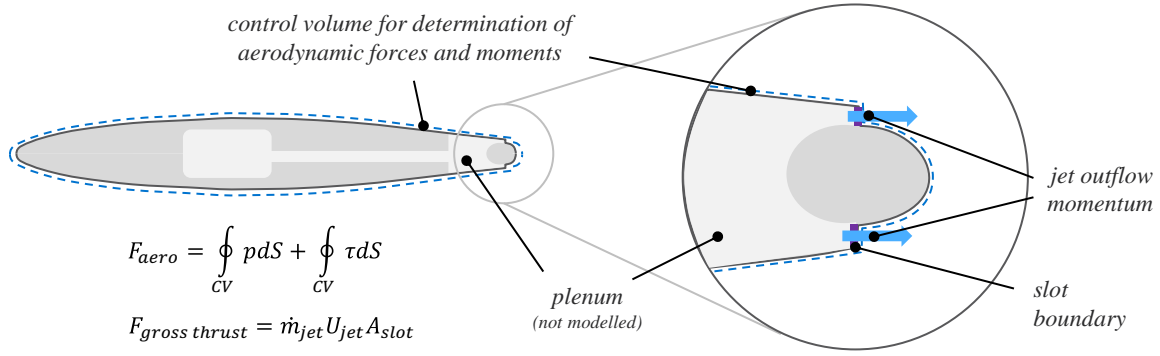


**Figure 5.10:** Illustration of control volume used for the calculation of aerodynamic forces and moments

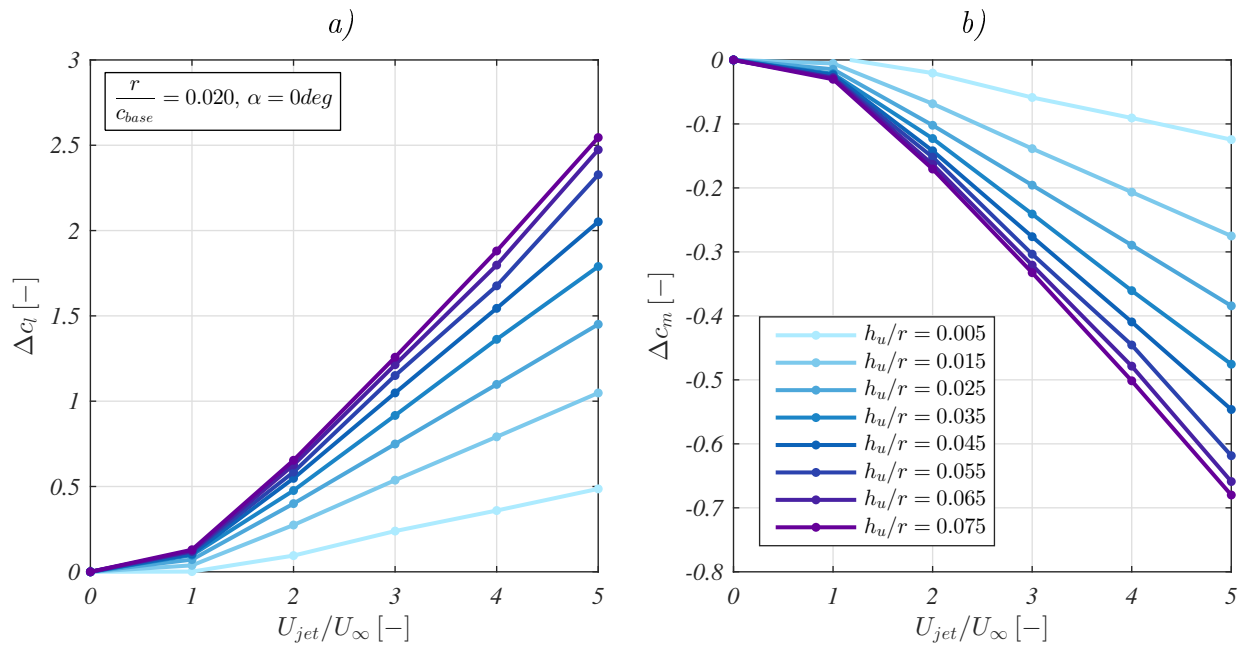


**Figure 5.11:** Lift (a) and pitching moment (b) due to blowing through upper slot over jet velocity ratio ( $\eta_h = 1$ ) (modified from STADLBERGER/HÖRNUNG, 2015b)

**Maximum Effectiveness ( $\eta_h = 1$ )** For the present concept, maximum control effectiveness is expected to be attained through single-slot-blowing ( $\eta_h = 1$ ), i.e. the lower slot is closed and only the upper slot height is varied. Figure 5.11 shows the evolutions of lift (a) and pitching moment (b) generation for a constant Coandă radius ( $\frac{r}{c_{base}} = 0.02$ ) and different upper slot heights  $h_u$ . The growing slot outflow velocity  $U_{jet}$  represents an increasing plenum pressure ratio. As can be seen, the jet velocity must exceed the free stream velocity  $U_\infty$  to produce significant lift and pitching moment increments. For larger Coandă radii, even slightly negative lift has been simulated with jet velocity ratios of  $\frac{U_{jet}}{U_\infty} = 1$ . But exceeding  $\frac{U_{jet}}{U_\infty} > 1$ , effectiveness grows with jet outflow velocity in an approximately linear manner. Moreover, the curve slopes become steeper with increasing slot height, i.e. increasing outflow

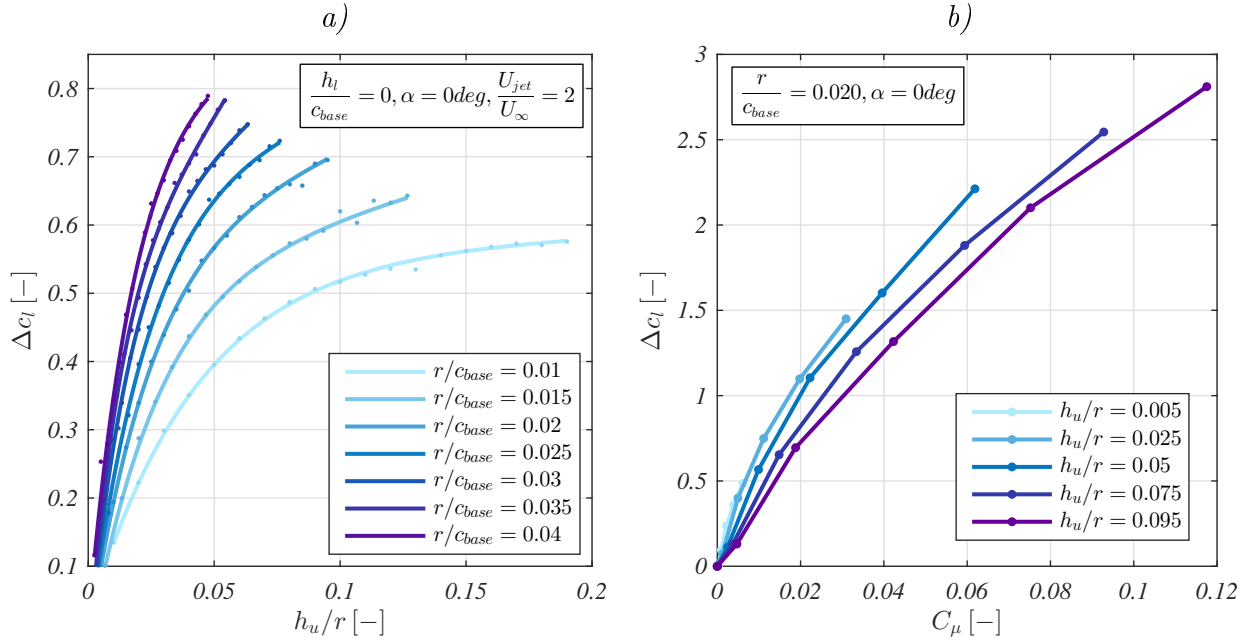


**Figure 5.12:** Lift due to blowing through upper slot for different slot heights and Coandă radii (a) and momentum flux coefficient (b) ( $\eta_h = 1$ ) (modified from STADLBERGER/HORNUNG, 2015b)

momentum. However, the attainable curve slope seems to be limited even if the slot height is further increased. The regression lines in Figure 5.12a confirm this behaviour for a variety of Coandă radii. Further opening of the slot might not lead to the desired gain of lift when the slot size has already exceeded reasonable margins. Assuming that the wall jet detachment angle  $\Theta_{sep}$  defines the (imaginary) rear stagnation point and thus lift, the momentum transport from the wall jet velocity peak into the viscous sublayer becomes crucial (section 2.1). Whereas increased jet velocities are favourable in this context, the sole increase of wall jet thickness (i.e. slot height) does not contribute to a desired delay of jet separation. Extending the velocity excess too far away from the Coandă surface has only little effect on the favourable turbulent processes close to the wall. So, lower slot heights exhibit higher lift forces for a given value of momentum flux ( $C_\mu$ ) which goes in line with wind tunnel measurements (subsection 2.2.3). To this, Figure 5.12b depicts the lift production dependent on the outflow momentum flux coefficient  $C_\mu$  and confirms the advantages of small slot heights. These are most visible in the separation control regime (section 2.2) when the trailing edge radius is kept constant. However, the integral outflow momentum becomes more important when longer distances ( $\Delta x = \Theta_{sep}r$ ) have to be covered by the wall jet to reach the same angle of separation  $\Theta_{sep}$ . With increasing Coandă radius, thicker wall jets become more beneficial as they better resist the turbulent mixing processes at the upper boundary of the wall jet. Consequently, larger trailing edge radii in combination with larger slot heights show an increased potential for lift and pitching moment generation (Figure 5.12a). This also relies on the fact, that the value of theoretically achievable circulation increases when the distances between

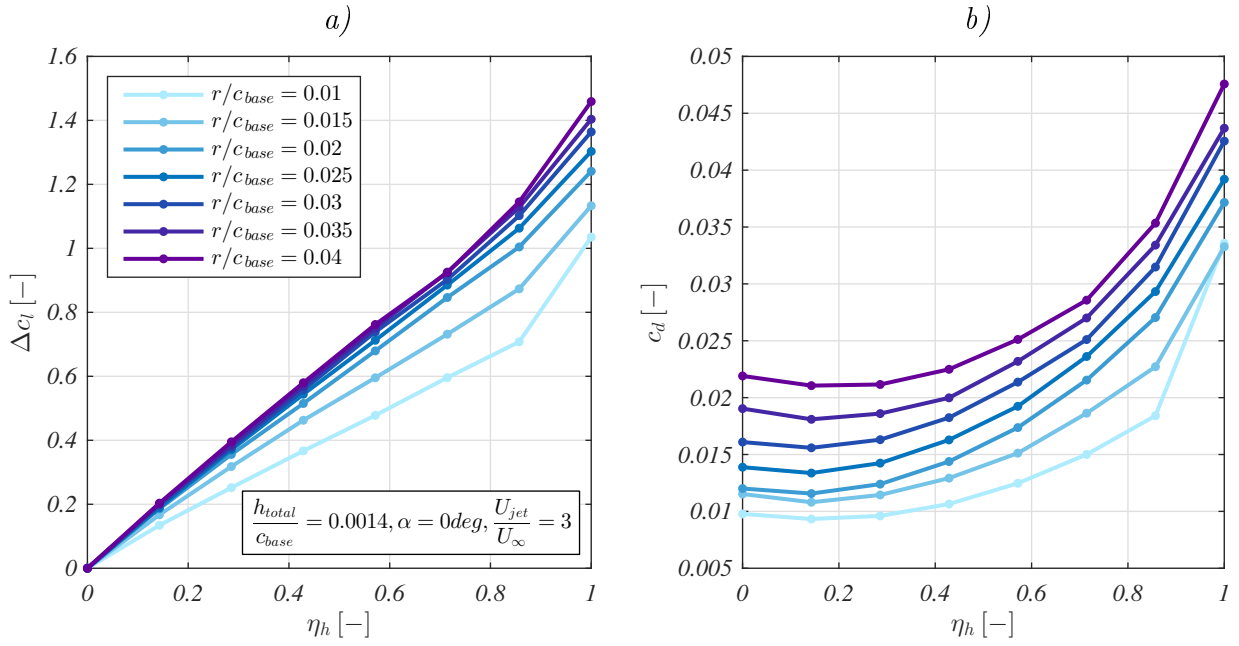


**Figure 5.13:** Lift (a) and drag (b) due to double-slot-blowing for different Coandă radii (modified from STADLBERGER/HORNUNG, 2015a,b)

the two stagnation points are reduced, i.e. when the Coandă aerofoil chord  $c_{Coanda}$  shrinks due to increasing  $r$  (subsection 3.4.4). In the associated aerofoil pressure distributions, this manifests itself in a growing relative importance of the low pressure zone near the trailing edge.

**Asymmetric Blowing ( $0 \leq \eta_h \leq 1$ )** For aircraft control purposes, lift and pitching moment are meant to be controlled by adjusting both upper and lower slot independently. Figure 5.15 depicts an exemplary flow field around a trailing edge under double-slot-blowing conditions. It also illustrates the zone of increased pressure ( $c_P > 0$ ) on the Coandă surface where both jets clash.

For an arbitrary slot setting, the geometrical configuration of the Coandă aerofoil can be described by the total slot height  $h_{total}$  and the ratio of upper and lower slot defined by the control parameter  $\eta_h$  (section 3.1). Given the pneumatic conditions, i.e. the total pressure inside the plenum, the jet outflow velocity ratio  $\frac{U_{jet}}{U_{\infty}}$  is set for both slots. The total slot height  $h_{total}$  then determines the total jet mass flow. Figure 5.13 shows the lift and drag force as a function of  $\eta_h$  for different Coandă radii. Except at high slot ratio values  $\eta_h$  (where the lower slot is nearly closed), the lift coefficient exhibits an approximately linear behaviour with increasing control factor  $\eta_h$  for all Coandă-radius-to-chord-ratios  $\frac{r}{c_{base}}$ . At  $\eta_h = 1$  the simulation results show an enhanced lift generation indicating that even low counter-pressures imposed by the lower jet cause premature detachment of the upper jet. Furthermore, Coandă flap effectiveness ( $\frac{\partial c_l}{\partial \eta_h}$ ) grows with increasing Coandă radius. However,

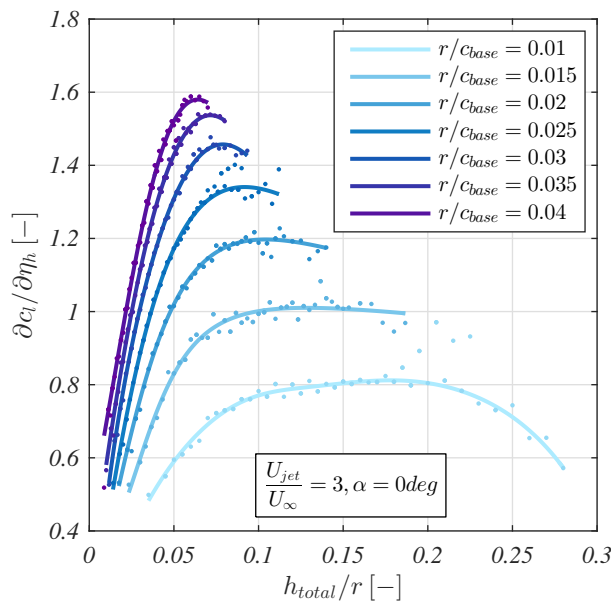


**Figure 5.14:** Lift increase due to control parameter  $\eta_h$  for different total slot heights and Coandă radii (modified from STADLBERGER/HORNUNG, 2015b)

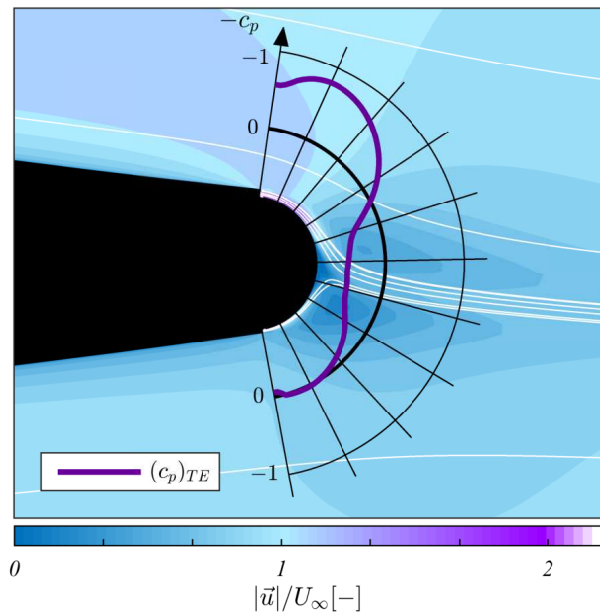


**Figure 5.15:** Flow field and  $c_p$  on the trailing edge under double-slot-blowing conditions,  $\frac{r}{c_{base}} = 0.02$ ,  $\frac{U_{jet}}{U_{\infty}} = 2$ ,  $\eta_h = 0.6$  (modified from STADLBERGER/HORNUNG, 2015b)

the effectiveness gain seems to saturate at a radius to chord ratio of approx.  $\frac{r}{c_{base}} = 0.02$ . A more general illustration of this behaviour is provided in Figure 5.14. For a given Coandă radius, the control force gain  $\frac{\partial c_l}{\partial \eta_h}$  cannot be increased arbitrarily by opening both slots excessively. Hence, the total slot height  $h_{total}$  should be chosen inside reasonable margins relative to the Coandă radius. Furthermore, as can be seen in Figure 5.13b, the aerofoil section drag decreases slightly until  $\eta_h = 0.2$  before it disproportionately rises to its maximum value at  $\eta_h = 1$ . Generally, drag grows with increasing Coandă radius where the present circular trailing edge geometry constitutes a conservative case compared to elliptical or biconvex shapes (subsection 2.2.1). Note that the section drag coefficient  $c_d$  only includes the integrated friction and pressure forces acting on the aerofoil and Coandă surface skin. The thrust force effect through blowing is not added (Figure 5.10).

**Dependency on Angle of Attack** Simulations revealed that the dependency of control effectiveness on the angle of attack is insignificant up to  $\alpha$ -values of  $5deg$ . Figure 5.16 shows the lift generation through single-slot-blowing for three different angles of attack. While lift increments are nearly identical for  $\alpha = 0deg$  and  $\alpha = 5deg$ , lift production under strong blowing conditions seems to be limited at high angles of attack ( $\alpha = 10^\circ$ ). However, the lift coefficients still are substantially higher than the maximum lift coefficient of the unblown lift polar (Figure 5.20a). The lift increase under double-slot-blowing exhibits

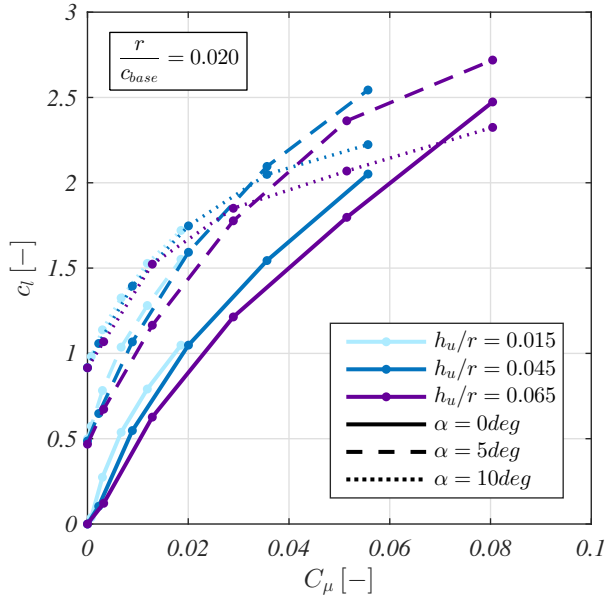


**Figure 5.16:** Dependency of lift generation on angle of attack (modified from STADLBERGER/HORNUNG, 2015b)

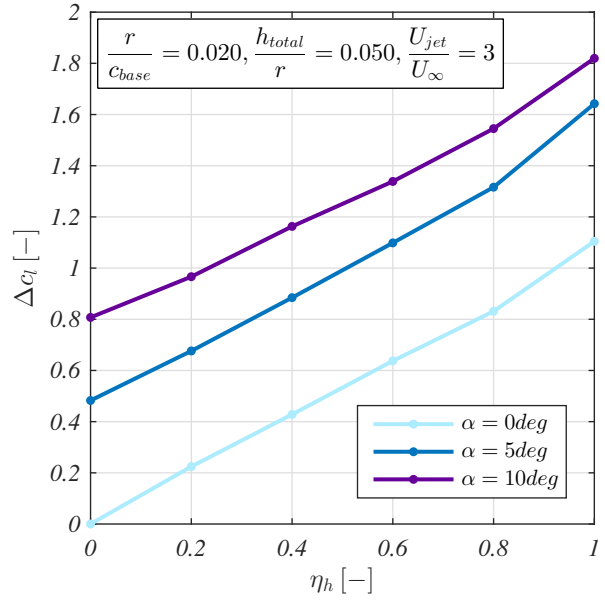


**Figure 5.17:** Dependency of lift of Coandă flap effectiveness on angle of attack (modified from STADLBERGER/HORNUNG, 2015b)

a similar dependency (Figure 5.17). Only at  $\alpha = 10deg$ , the Coandă flap lift gain  $\frac{\partial c_l}{\partial \eta_h}$  is slightly lower than for lower angles of attack. Note that circulation control aerofoils are prone to leading edge separation when high circulations are attained (subsection 2.2.5). Stall phenomena still are difficult to predict accurately by RANS calculations, especially under fully turbulent settings without transition model. Hence, the presented results are supposed to overestimate control effectiveness at high angles of attack.

**Efficiency** The performance of a circulation control concept not only includes maximum effectiveness but also efficiency in terms of necessary resources, i.e. pressurised air. In this study, the momentum flux coefficient  $C_\mu$  is used as a measure for engine bleed air demand. Figure 5.18 shows the regressed curves of lift augmentation  $\frac{\partial c_l}{\partial C_\mu}$  in the single-slot-blowing case as a function of slot height under different blowing conditions. For a given Coandă radius ratio  $\frac{r}{c_{base}}$ , a specific blowing rate exists that provides a maximum in efficiency over the major range of slot heights (in this case  $\frac{U_{jet}}{U_\infty} \approx 2$ ). Except at low blowing conditions ( $\frac{U_{jet}}{U_\infty} \approx 1$ ), smaller slot sizes enable a more economic lift generation. Hence, it is recommended to choose the slot height ratio  $\frac{h_u}{r}$  at reasonably low levels in order to maintain the required jet mass flow at low rates. Likewise, it can be seen in Figure 5.19 that the ratio of Coandă flap effectiveness and momentum coefficient  $\frac{\partial c_l / \partial \eta_h}{C_\mu}$  is higher for low total slot heights when the aerofoil is operated in the double-slot-blowing mode. The regression curves indicate that low Coandă radii with relatively large total slot heights can achieve higher efficiencies than large radii with relatively small slot heights.

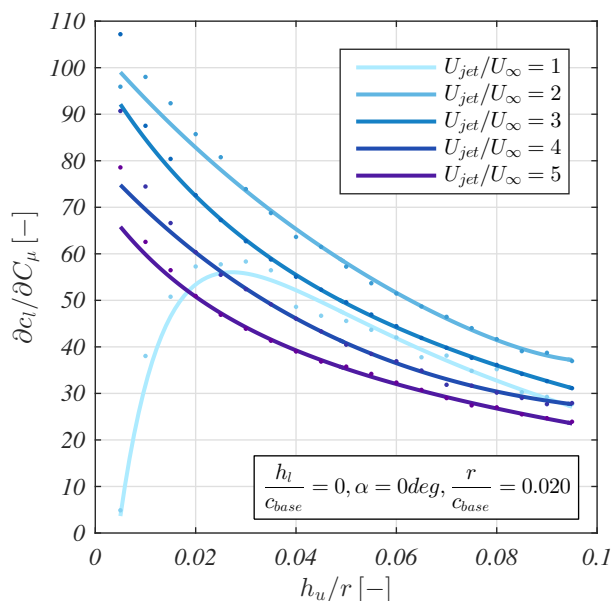


**Figure 5.18:** Dependency of lift augmentation on slot height and blowing conditions ( $\eta_h = 1$ ) (modified from STADLBERGER/HORNUNG, 2015b)

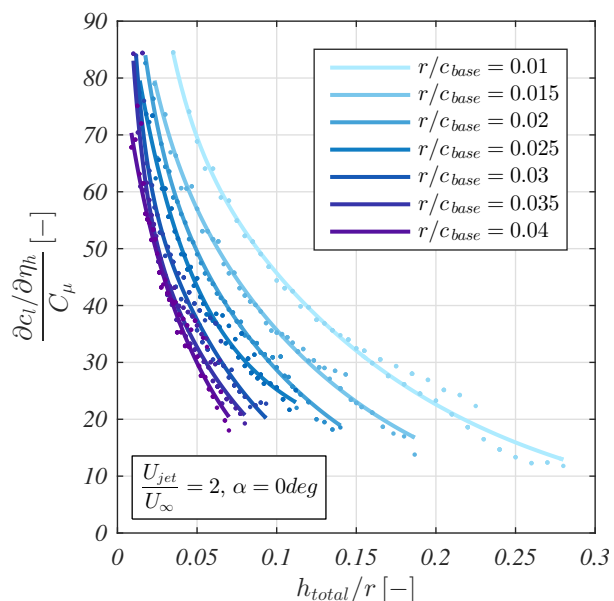


**Figure 5.19:** Ratio of Coandă flap effectiveness and momentum coefficient for different slot heights and Coandă radii (modified from STADLBERGER/HORNUNG, 2015b)

**Symmetric Blowing ( $\eta_h = 0$ )** Of course, effectiveness and efficiency of the Coandă aerofoil is particularly important for flight phases where the aircraft is facing high control moment requirements, e.g. during final approach. However, cruise phases span large portions of the design mission in most cases. To reduce base drag, the working points of the Coandă flap system should be chosen close to symmetric blowing operation ( $\eta_h = 0$ ). In addition, a complete deactivation of the active flow control system during cruise would counteract the findings in subsection 5.1.1. Figure 5.20 shows the lift and drag characteristics of the aerofoil under symmetric blowing conditions. The lift curves exhibit an interesting behaviour in the range of moderate angles of attack ( $4^\circ < \alpha < 9^\circ$ ). Here, low blowing rates ( $U_{jet}/U_\infty = 1$ ) appear to increase the lift coefficients and lift curve slopes whereas higher blowing rates ( $U_{jet}/U_\infty > 1$ ) reduce lift compared to the unblown case ( $U_{jet}/U_\infty = 0$ ). Due to the questionable modelling capabilities of the RANS method in the stall regions, the respective results have to be taken with caution. In terms of drag, high blowing rates are favourable as can be seen in Figure 5.20b. Again, the section drag coefficient  $c_d$  does not include the thrust force effect through blowing (Figure 5.10). The plotted drag values rather represent the base drag reduction due to separation control and possible clashing jets. The latter generate high pressure zones on the blunt trailing edge, thus reducing the net drag force. For an asymmetric blowing case, Figure 5.15 illustrates this effect by depicting the  $c_p$ -value on the Coanda surface which visibly attains positive values in the zone of jet clash. Introducing the propulsive effect of blowing would have an additional favourable impact on the drag balance

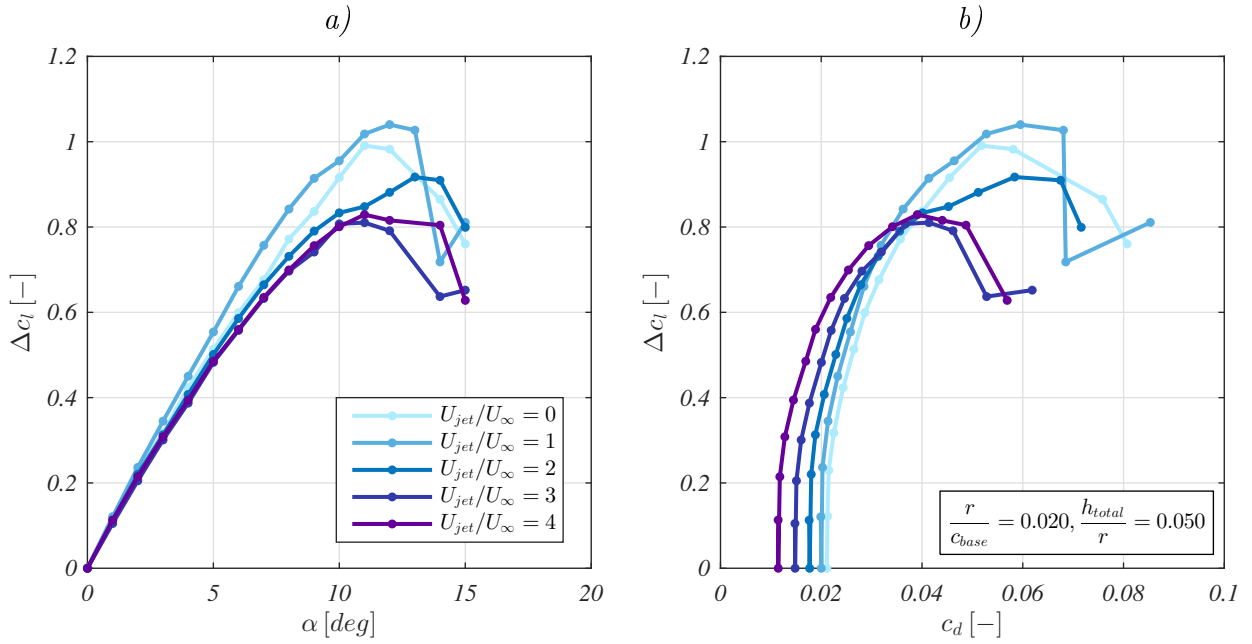


**Figure 5.20:** Lift (a) and drag (b) polar under different symmetric blowing conditions ( $\eta_h = 0$ ) (modified from STADLBERGER/HORNUNG, 2015b)

up to net thrust generation ( $c_d < 0$ ). However, this drag reduction measure must be traded off against the penalties that affect the efficiency of the propulsion system and of the entire aircraft system. This aspect will be addressed later in section 5.2.

### 5.1.4 Intermediate Results of Finite Wing Reactions

This subsection discusses the results of the cambering method (section 3.5) which are based on the previously presented two-dimensional section data (subsection 5.1.3). Most of the following results and discussions can also be found in STADLBERGER/HORNUNG (2015a). In the context of the SAGITTA configuration (section 4.2), the midboard span fraction (Figure 4.3), nominally covered by a conventional plain flap, is equipped with a Coandă flap featuring a radius-to-chord-ratio of  $\frac{r}{c} = 0.02$ . This value turned out to be a good compromise between maximum available control authority and base drag increase (subsection 5.1.3). The vortex lattice is modelled with the same discretisation parameters as applied during the method's validation (subsection 3.5.3).

Figure 5.21 shows the aerodynamic forces and moments generated by Coandă flap actuation  $\eta_h$  with a total-slot-height-to-chord-ratio of  $\frac{h_{total}}{c} = 0.001$ . The calculated aerodynamic 3D data describe the baseline flight state at zero angle of attack and zero sideslip ( $\alpha_\infty = 0^\circ$ ,  $\beta_\infty = 0^\circ$ ). The different jet velocity ratios  $\frac{U_{jet}}{U_\infty}$  correspond to varying total pressure ratios inside the Coandă flap plenum. In accordance with the two-dimensional section data (subsection 5.1.3), the lift coefficient  $C_L$  (Figure 5.21a), the pitching moment coefficient

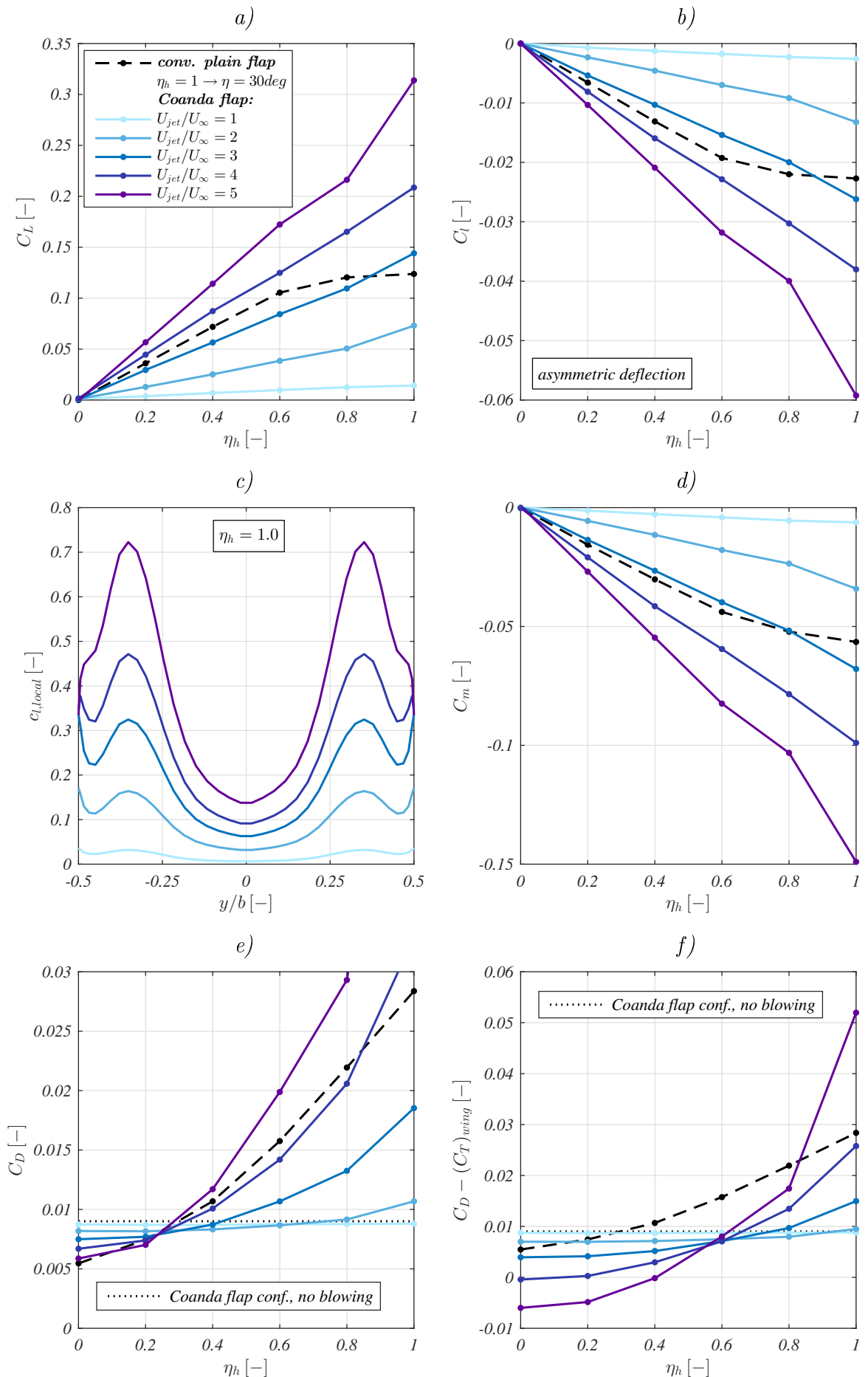


**Figure 5.21:** Aerodynamic reactions of the SAGITTA wing due to Coandă flap actuation,  $\alpha_\infty = 0deg$ ,  $\beta_\infty = 0deg$ ,  $\frac{h_{total}}{c} = 0.001$ ,  $\frac{\tau}{c} = 0.02$  (modified from STADLBERGER/HORNUNG, 2015a)

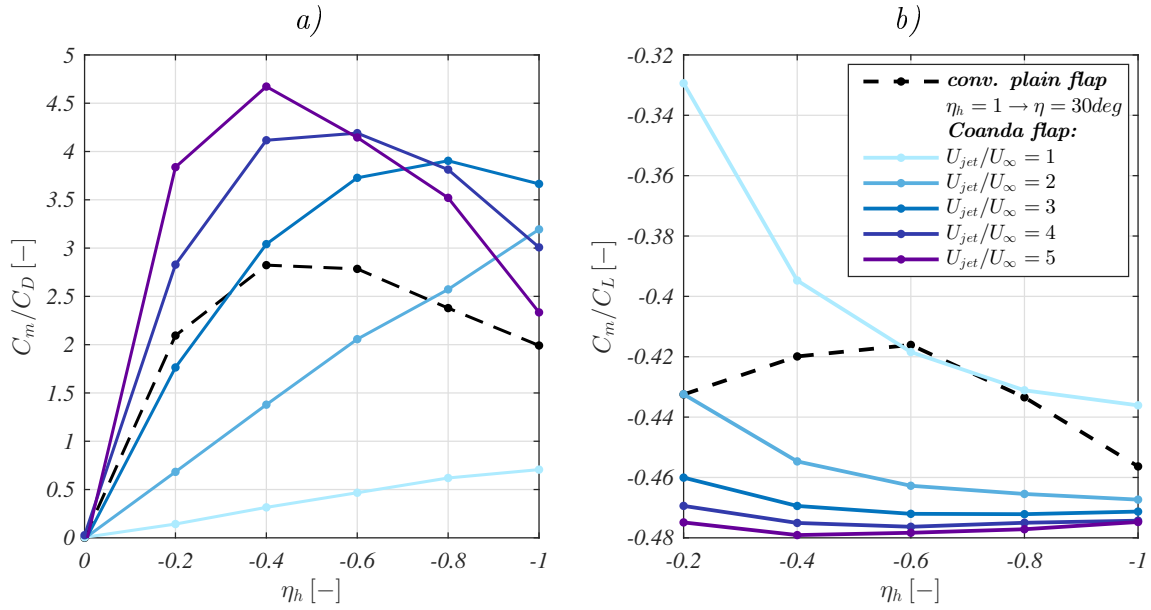


**Figure 5.22:** Pitch-to-drag ratio (a) and pitch-to-lift ratio (b) of the Coandă flap,  $\alpha_\infty = 0deg$ ,  $\beta_\infty = 0deg$ ,  $\frac{h_{total}}{c} = 0.001$ ,  $\frac{\tau}{c} = 0.02$  (modified from STADLBERGER/HORNUNG, 2015a)

$C_m$  (Figure 5.21d) and the roll moment coefficient  $C_l$  (Figure 5.21b) exhibit an approximately linear behaviour for all values of  $\frac{U_{jet}}{U_\infty}$ . Comparing the effectiveness of the Coandă flap and the nominal conventional flap, it can be seen that the jet outflow velocity has to exceed three times the free stream velocity value to attain the same control reactions. Note that the slope of the conventional flap curve depends on the chosen correlation between  $\eta$  and  $\eta_h$ . The plain flap curves are plotted such that a  $30^\circ$  plain flap deflection corresponds to a Coandă flap actuation value of  $\eta_h = 1$ .

Furthermore, the curves of pitching moment production efficiency  $\frac{C_m}{C_D}$  (Figure 5.22a) indicate that there is a chance to attain lower drag values with Coandă flaps than with the conventional flaps. In addition, their ratio of pitching moment and parasite downforce is about 10% better due to the very aft location of the rear suction peak (Figure 5.22b). This could be particularly interesting for the case where longitudinal trim is assured by use of Coandă flaps. Note that these results still do not include the thrust force produced by the jet outflow (Figure 5.10). When additionally incorporating the thrust effect, the net force in x-direction is further decreased as depicted by the curves of  $C_D - (C_T)_{wing}$  in Figure 5.21f where the wing thrust effect coefficient  $(C_T)_{wing}$  is defined as

$$(C_T)_{wing} = \frac{\dot{m} (U_{jet} - U_\infty) S_{Coanda\ flap}}{\frac{1}{2}\rho U_\infty^2 S_{ref}} \quad (5.1)$$

with  $S_{Coanda\ flap}$  denoting the wing area covered by the Coandă aerofoil. As can be seen at high blowing rates ( $\frac{U_{jet}}{U_\infty} > 4$ ), the fluidic flap system generates net thrust, i.e. negative drag, for low  $\eta_h$  values.

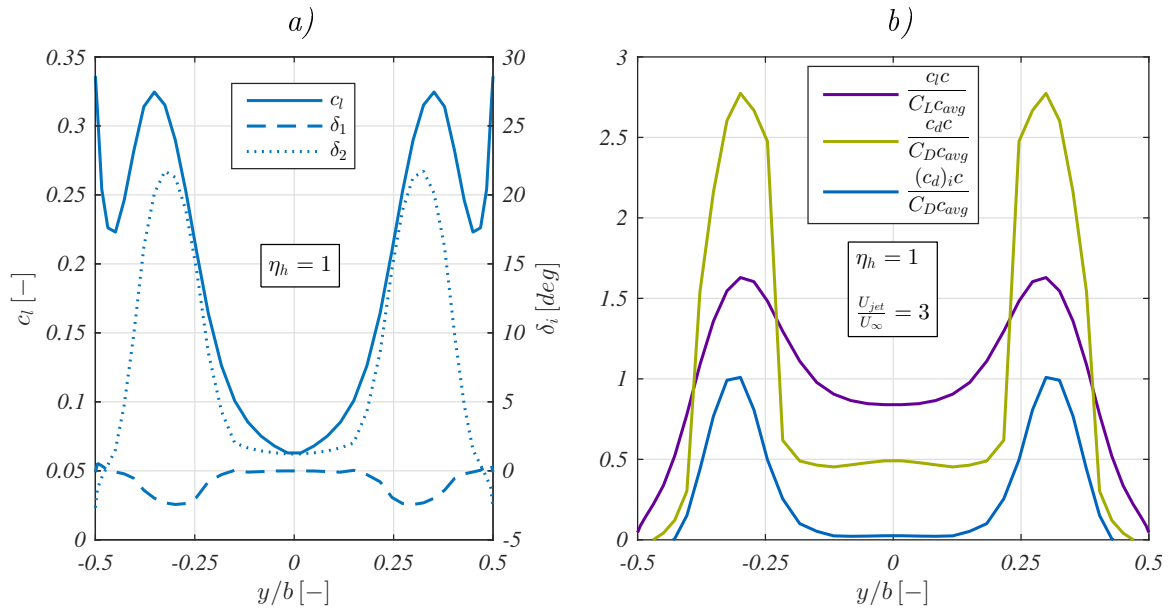


**Figure 5.23:** Vortex lattice modification angles over span (a) and span distribution of lift and drag fraction (b),  $\frac{U_{jet}}{U_\infty} = 3$ ,  $\alpha_\infty = 0deg$ ,  $\beta_\infty = 0deg$ ,  $\frac{h_{total}}{c} = 0.001$ ,  $\frac{z}{c} = 0.02$  (modified from STADLBERGER/HORNUNG, 2015a)

To illustrate the local aerodynamic modelling, Figure 5.23a shows the spanwise distribution of the local lift coefficient as well as the vortex lattice modification angles  $\delta_1$ ,  $\delta_2$  that have been determined iteratively by the proposed calculation method. As expected, the curves exhibit increased values at the span fractions that are covered by Coandă flaps. This can also be seen in Figure 5.23b which illustrates the lift and drag fraction ( $\frac{c_l c}{C_{Lc_{avg}}}$ ,  $\frac{c_d c}{C_{Dc_{avg}}}$ ) over span. The drag fraction distribution indicates that a large portion of total drag is produced at the Coandă flap sections where viscous and pressure drag is dominant compared to induced drag ( $\frac{(c_d)_i c}{C_{Dc_{avg}}}$ ).

## 5.2 Final Results of the Overall System

Finally, the combination of all submodels provides substantial information to evaluate the Coandă flap system as a whole. While the previous pages discussed the isolated Coandă flap effectiveness under the assumption of unlimited bleed air supply, this section investigates the control moment authority under installed conditions. This means that all submodels (engine, ducts, Coandă flaps, aircraft flight dynamics) now are combined to represent the crucial subsystem interactions (section 3.6). In particular, the incorporation of realistic engine throttle settings and associated available bleed air increases the significance of results.

In the context of the SAGITTA test case, various parameters are investigated to assess both effectiveness and efficiency of the overall system. Many of the following discussions compare

**Table 5.1:** Measured flap deflection angles during wind tunnel experiments

flap name	deflection angles
inboard plain flap (IB)	$-30deg \leq \eta \leq 30deg$
midboard plain flap (MB)	$-30deg \leq \xi \leq 30deg$
tip split flaps (upper, lower)	$0deg \leq \zeta \leq 55deg$

the Coandă flap version of the SAGITTA configuration with the reference case featuring conventional flaps (section 4.3). The control reactions of the latter are represented by look-up tables retrieved from wind tunnel data (HÖVELMANN ET AL., 2014). The ranges of measured flap deflection angles are summarised in Table 5.1. Unless specified differently, the following paragraphs assume that the span fractions of the conventional midboard (MB) plain flaps are equipped with the studied double-slotted circulation control concept. As a consequence of the results from subsection 5.1.3, the relative (circular) trailing edge radius of these Coandă flaps was set to  $\frac{r}{c_{base}} = 0.02$ .

In addition to the simplifications described in section 3.6, the subsystem masses of the conventional flap system and Coandă flap system are considered to be approximately identical. This relies on the assumption that the additional weight for ducts and plenum structures is compensated by the reduced weight of omitted actuators and hydraulic lines.

The following subsections present Coandă flap parameters at transonic flight velocities up to  $Ma_\infty = 0.8$ . Note that these results have to be taken with caution since the incompressible aerodynamic modelling does not account for compressible effects. For instance, recompression shock waves have to be expected on the upper wing surface at transonic Mach numbers ( $Ma_\infty \gtrsim 0.7$ ). Moreover, transonic flight speeds usually require supersonic Coandă jet flow to achieve sufficient control authority through sufficiently high jet outflow velocity ratios  $\frac{Ma_{jet}}{Ma_\infty}$ . For the following studies, the risk of supersonic jet detachment (subsection 2.2.5) has not been taken into account either.

## 5.2.1 Pitch Authority

The following results in this subsection seek to evaluate the pitch authority of the installed fluidic flight control system. In particular, the dependence on the engine thrust setting will be clearly visible.

**Coandă flap compared with conventional flap** For an exemplary operating point (loiter:  $H = 5000m$ ,  $Ma_\infty = 0.5$ ), the solid lines in Figure 5.24a represent the pitching moment increment  $(\Delta C_m)_{body}$  generated by the Coandă flap at different thrust settings  $\delta_T$ . The total slot opening area  $A_{slot}$  was set to the maximum value  $A_{slot,max}$  available in the data base.

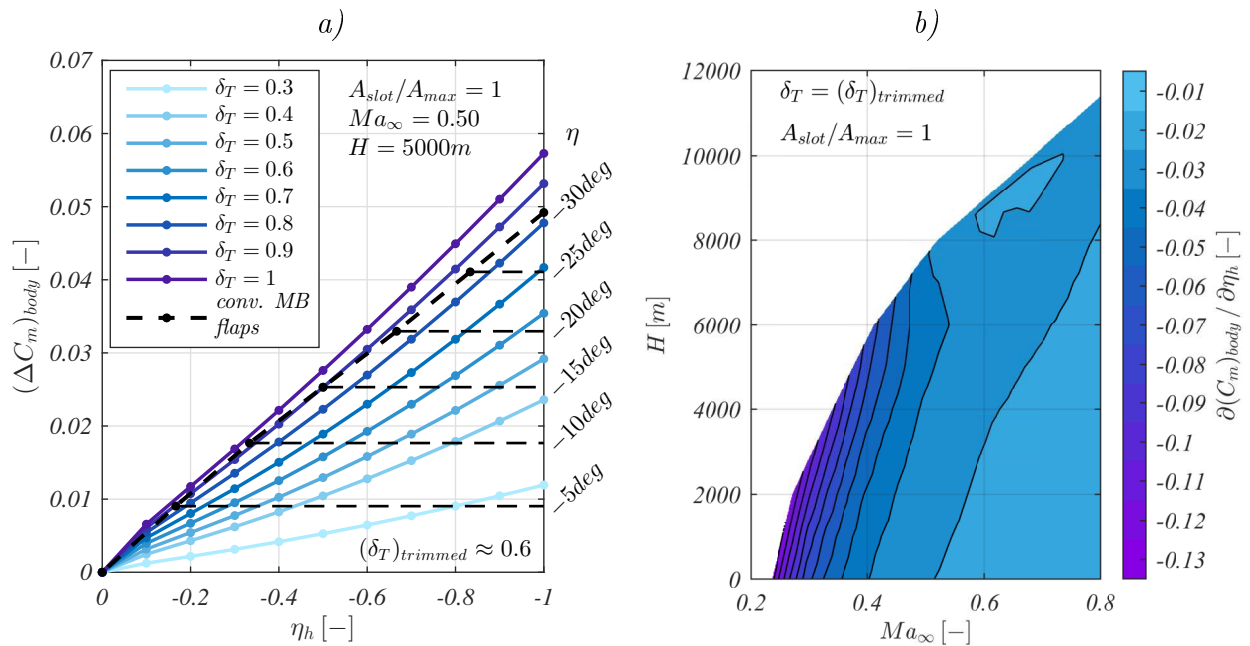


**Figure 5.24:** Pitch authority of the Coandă flap system at midboard position

As reference, the diagram also contains the pitch authority of the conventional midboard flap (dashed line). Note that the values of the x-axis were correlated such that the Coandă flap control parameter  $\eta_h = -1$  corresponds to the maximum upward plain flap deflection ( $\eta = -30deg$ ) that was measured during the wind tunnel tests. As can be seen for the trimmed thrust setting ( $(\delta_T)_{trimmed} \approx 0.6$ ), i.e. for zero specific excessive power  $SEP = 0$ , the Coandă flap system is capable to generate the same pitching moment as an equivalent plain flap deflection of  $\eta \approx -22deg$ . At full thrust, the Coandă flap becomes even more competitive in terms of pitch control authority. To give an idea of the Coandă flap effectiveness throughout the entire envelope, Figure 5.24b depicts the regressed control moment slopes  $\frac{\partial C_m}{\partial \eta_h}$  for different flight altitudes and Mach numbers. Since the jet outflow velocity ratio  $\frac{U_{jet}}{U_\infty}$  diminishes with increasing flight speed, also the Coandă pitch authority decreases. Even though high Mach numbers require higher thrust settings, the increased bypass pressure ratio cannot compensate the loss in relative Coandă jet velocity.

**Sustained coordinated turn** For the following results, solely the midboard Coandă flap is used for longitudinal trim and coordinated turn. The maximum sustained load factor represents trimmability and agility of the aircraft equipped with Coandă flap devices. It directly affects the minimum turn radius. As a result of automated trim calculations, Figure 5.25 depicts the envelope of the maximum sustained load factor. The maximum values of approx. 3 are located at low altitudes and high Mach numbers. In terms of minimum flight speed, it must be mentioned that the available thrust was the limiting factor rather than the Coandă flap capability of pitching moment generation.

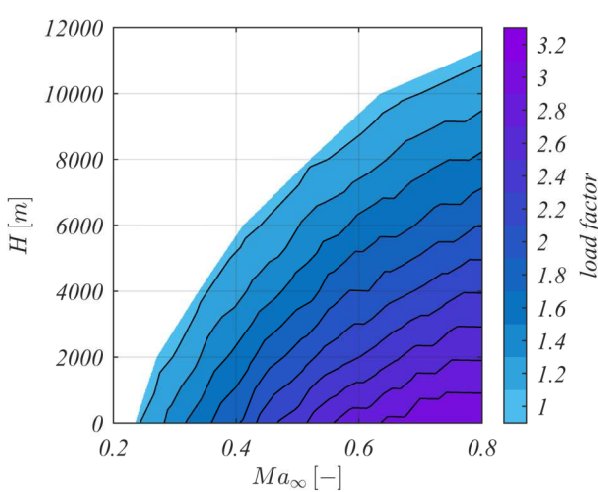


**Figure 5.25:** Sustained load factor during coordinated turn through Coandă flap trim

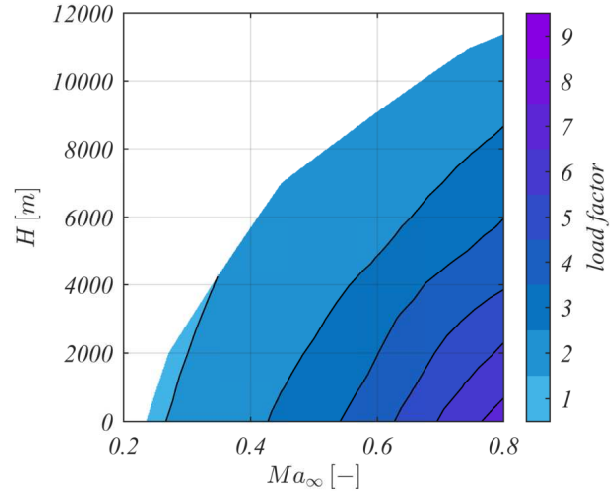


**Figure 5.26:** Maximum attained load factor during pull-up manoeuvre out of trimmed horizontal flight

**Dynamic Pull-up manoeuvre** To eliminate the limitation of available thrust, the pitch motion is simulated dynamically to evaluate the maximum attainable load factor. This unsteady pull-up manoeuvre is performed out of the trimmed horizontal flight state. The instantaneous setting of maximum pitching moment generation ( $\eta_h = -1$ ,  $A_{slot} = A_{slot,max}$ ) leads to a nose up motion increasing the angle of attack. As can be seen in Figure 5.26, load factors up to 6 can be attained by the modelled Coandă flap system.

## 5.2.2 Roll Authority

The following paragraphs evaluate the competitiveness of the Coandă flap in terms of roll authority.

**Coandă flap compared with conventional flap** The solid lines in Figure 5.27a represent the Coandă flap roll authority  $(\Delta C_l)_{body}$  for different thrust settings  $\delta_T$  at an exemplary operating point (loiter:  $H = 5000m$ ,  $Ma_\infty = 0.5$ ). The reference roll moment generated by an asymmetric conventional plain flap (MB) deflection is illustrated by the dashed line. The data is correlated such that a value of  $\eta_h = 1$  on the x-axis corresponds to the maximum available flap deflection  $\xi = 30deg$  tested in the wind tunnel. For trimmed thrust setting, the Coandă flap is capable to attain the same roll moment as a conventional plain flap deflection of  $\xi \approx 12deg$ . Even though the Coandă flap roll authority increases with higher thrust settings, its performance has to be judged inferior compared to the conventional flap. The flight envelope of roll moment slope  $\frac{\partial C_l}{\partial \eta_h}$  depicted in Figure 5.27b, illustrates the downward

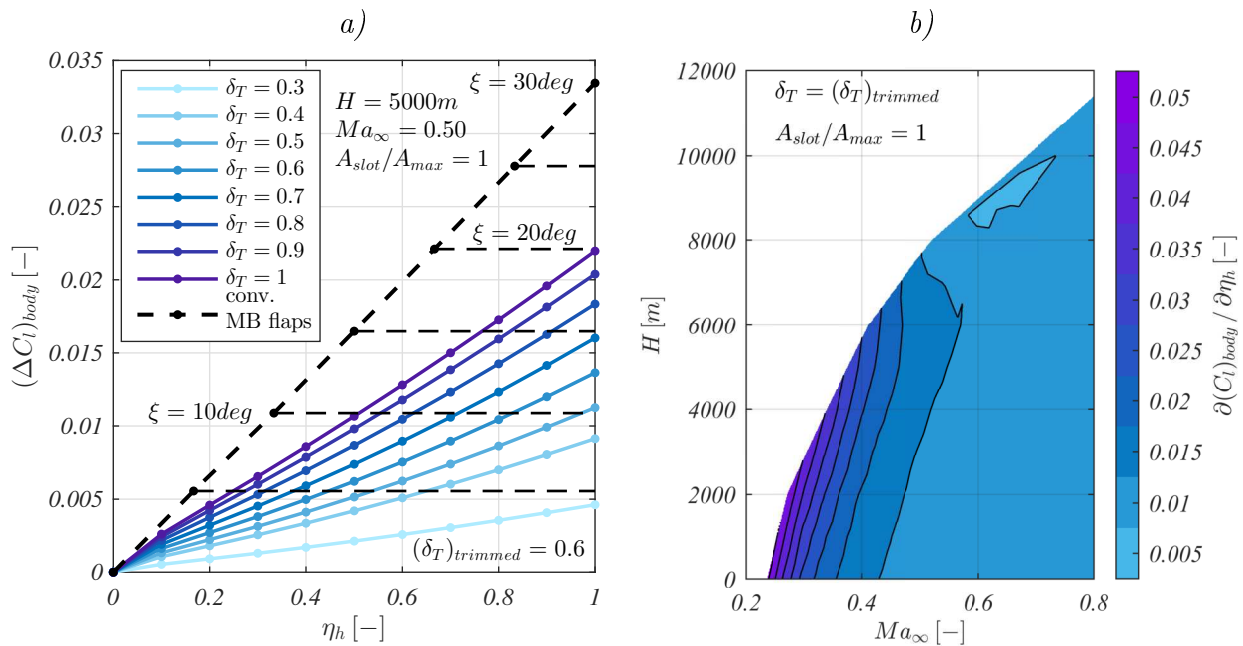


**Figure 5.27:** Roll authority of the Coandă flap system at midboard position

trend of roll authority for increasing flight velocities. As seen before, the higher thrust settings cannot compensate the reduced jet outflow velocity ratios  $\frac{U_{jet}}{U_\infty}$ .

**Dynamic Roll manoeuvre** As recommended by the military specifications MIL-F-8785C (MOORHOUSE/WOODCOCK, 1982), the roll agility is investigated by simulating roll manoeuvres with maximum control input ( $\eta_h = \pm 1$ ,  $A_{slot} = A_{slot,max}$ ). The manoeuvre is started at the respective trimmed horizontal flight state. For trimmed throttle position, Figure 5.28a shows that the necessary time  $T_{\Phi=45deg}$  to roll from wings level state to a bank angle of  $\Phi = 45^\circ$  is lower than 1s throughout the entire trimmable envelope. This corresponds to the highest level of agility (Level 1:  $T_{\Phi=45deg} \leq 1.4s$ ) for the SAGITTA aircraft class (class II). Note that the time period increases in areas of lower trimmed thrust settings where reduced bypass pressure ratios constrain Coandă flap effectiveness. At full thrust, these roll times can be reduced even more as can be seen in Figure 5.28b.

### 5.2.3 Yaw Authority

In theory, the Coandă flap concept is capable to generate yaw moments using the jet thrust effect active on one halfspan. The increased drag of the blunt trailing edge without blowing on the other halfspan additionally contributes to yaw moment generation. However, the yaw authority results presented in Figure 5.29a denote only poor yaw effectiveness. As demonstrated by the solid lines, the Coandă flap system only attains very low maximum yaw moments. These are almost one order of magnitude lower than those produced by the

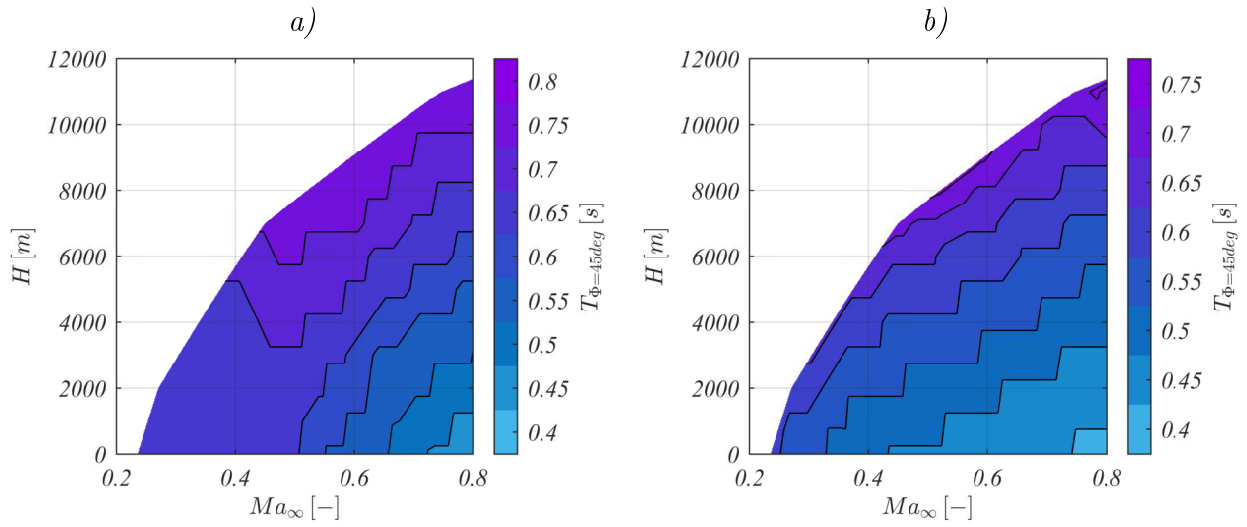


**Figure 5.28:** Time to pass a bank angle of  $\Phi = 45deg$  with trimmed throttle (a) and full throttle (b) during roll manoeuvre

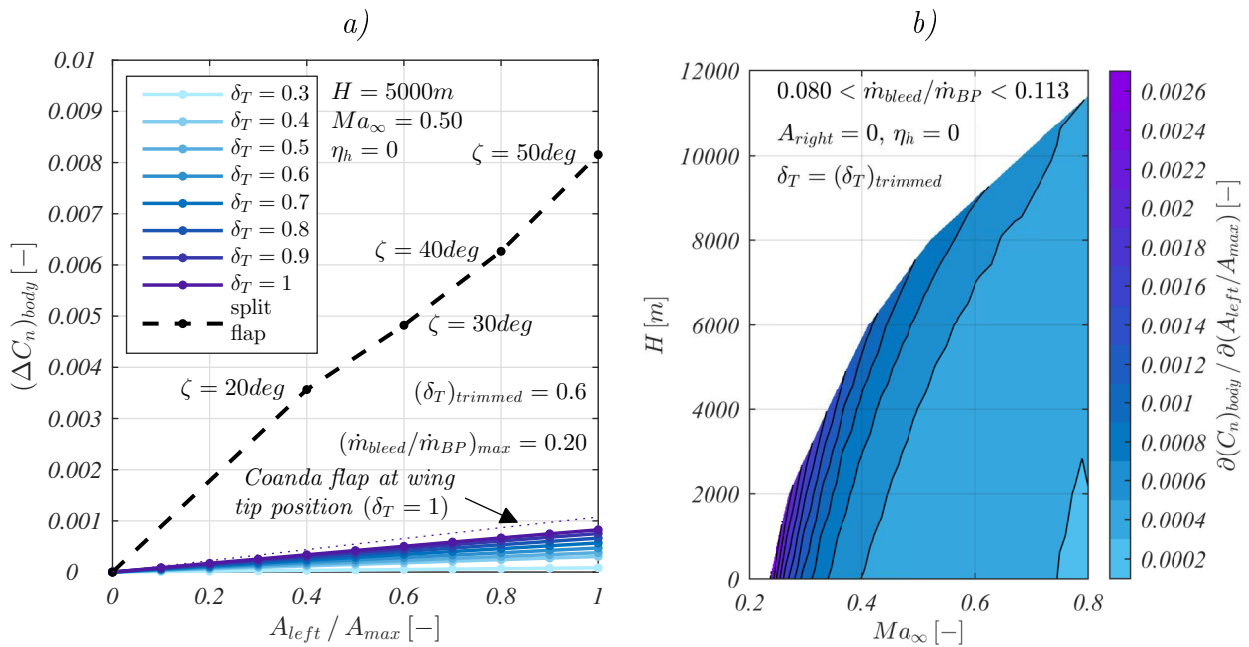


**Figure 5.29:** Yaw authority of Coandă flap system

lower tip split flap (dashed line). The thrust effect of about 20% of the bypass mass flow  $\dot{m}_{BP}$  in combination with a fairly short moment arm  $\Delta y_{MB}$  reveals too low to be competitive. Even if the Coandă flap were situated at the wing tip generating the same asymmetric thrust force, the resulting yaw moment would only increase by about 30% (dotted line). Still, the tip split flap concept of providing yaw authority through drag generation appears superior in this case. The Coandă flap yaw moment slope  $\frac{\partial C_n}{\partial(A_{slot}/A_{max})}$  diminishes even more at higher flight velocities due to reduced jet outflow velocity ratios  $\frac{U_{jet}}{U_\infty}$  (Figure 5.29b).

### 5.2.4 Efficiency

In the precedent subsections, the Coandă flap concept has been investigated in terms of maximum effectiveness. For the final evaluation, however, also the increased fuel consumption has to be taken into account. In this context, the following results enable conclusions about the Coandă flap system efficiency in comparison with a conventional flap configuration. The efficiency analysis in the subsequent paragraphs comprise two use cases of the Coandă flap during steady horizontal flight. First, solely the midboard Coandă flaps have been used to generate pitch control moments for trim. All other control devices remain in neutral position. Second, the aircraft is primarily trimmed by the inboard (IB) plain flaps (with gap covers) but additionally supported by the Coandă midboard flaps. This operation mode is considered to be more realistic as pneumatic power demand is kept low, still reducing the Coandă aerofoil base drag through steady blowing. In both cases, the trim calculations are performed for varying values of the slot opening area  $A_{slot}$ . At each operating point  $(H, Ma_\infty)$ , the configuration with least fuel flow  $\dot{m}_{fuel}$  was selected to compile the envelope of minimum fuel flow. The envelope mesh sizes of the calculated operating points are  $\Delta H = 1000m$  and  $\Delta U_\infty = 10 \frac{m}{s}$ .

**Longitudinal Trim with Coandă Flaps** The contour plots of Figure 5.30 contain the envelopes of the feasible flight states that could be trimmed solely by the midboard Coandă flap. Figure 5.30a and Figure 5.30c illustrate the Coandă flap settings  $A_{slot}$  and  $\eta_h$  that assure longitudinal trim at minimum fuel flow  $\dot{m}_{fuel}$ . Interestingly, the maximum slot opening areas  $A_{slot}$  are predominant at lower altitudes while they quickly decrease to low slot sizes at high altitudes. This trend is also naturally visible in the envelope for Coandă jet mass flow, i.e. bypass bleed mass flow  $\dot{m}_{bleed}$ . Note that the steplike appearance in x-direction is due to the relatively coarse discretisation of the envelope grid. At lower altitudes  $H$ , the reduced required thrust settings  $\Omega_{HP}^*$  (Figure 5.30e) lead to engine operating points that prefer higher bypass bleed fractions to achieve higher engine efficiencies (subsection 5.1.1). In contrast, bypass bleed air becomes more expensive at higher altitudes where the engine is approaching its design point  $\Omega_{HP}^* = 1$ . This tendency is underlined by Figure 5.31 which

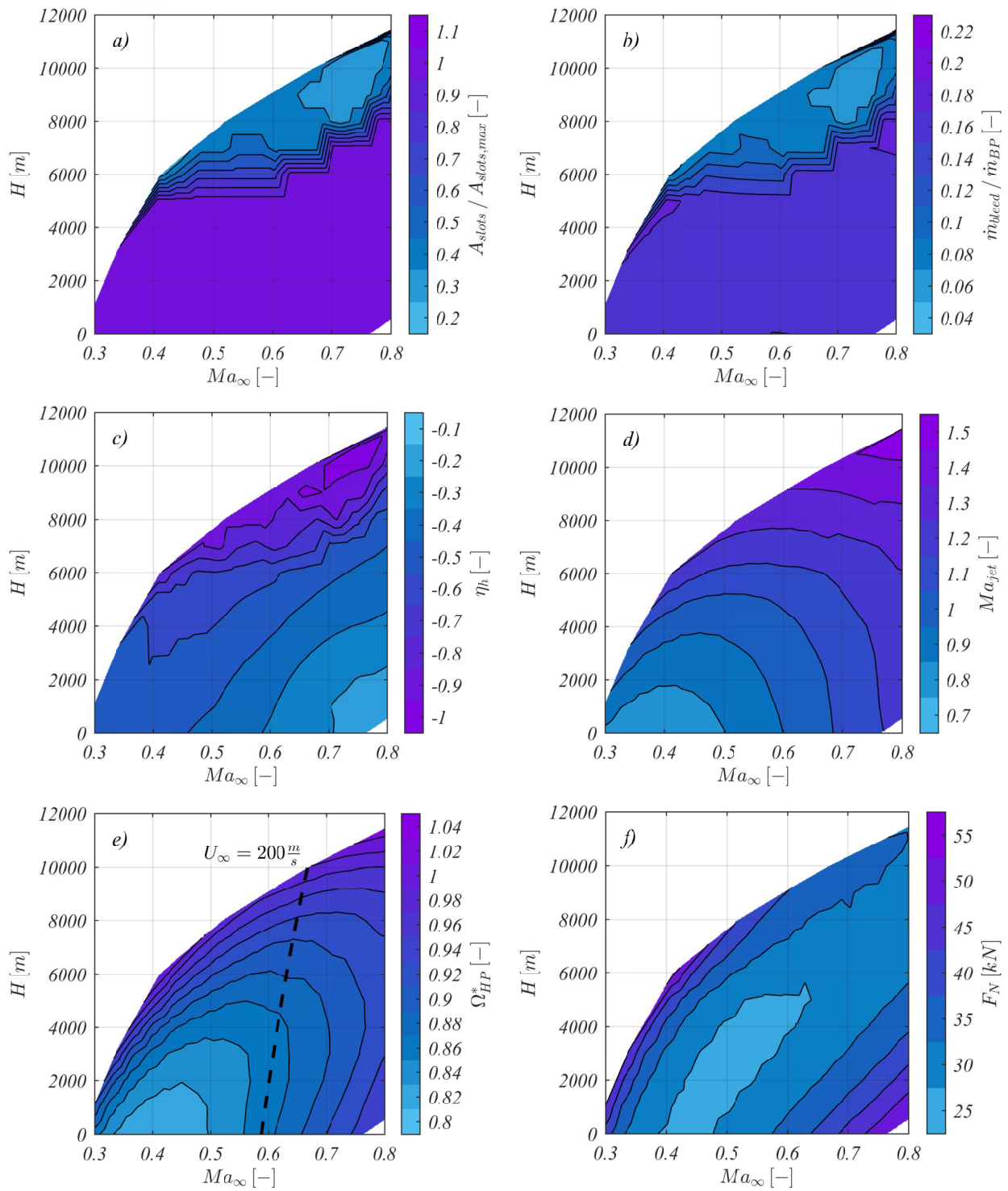


**Figure 5.30:** Envelopes of optimised Coandă system parameters during horizontal flight solely trimmed by the midboard Coandă flaps

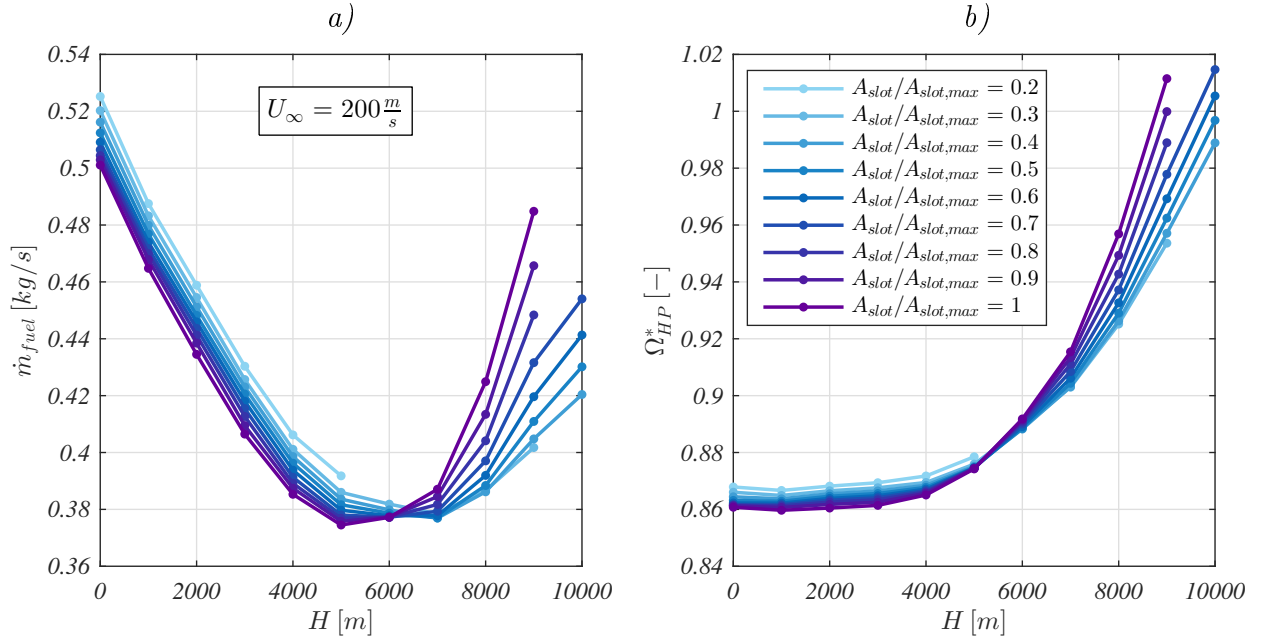


**Figure 5.31:** Dependency of optimum slot outlet area on altitude and engine thrust setting

depicts the necessary fuel flow  $\dot{m}_{fuel}$  (a) and thrust setting  $\Omega_{HP}^*$  (b) for various slot opening areas  $A_{slot}$  at an exemplary intermediate flight velocity of  $U_\infty = 200 \frac{m}{s}$ . At  $H \approx 5000$  m the required engine spool speed begins to rise rapidly above  $\Omega_{HP}^* > 0.88$  and smaller slot opening areas suddenly become more favourable when passing the line of  $H \geq 6000$  m.

To give an indication of fuel consumption throughout the flight envelope, Figure 5.32a depicts the necessary total fuel flow  $\dot{m}_{fuel}$  while Figure 5.32b shows the total specific fuel consumption ( $SFC_{total}$ ). The latter is based on the total thrust produced by the sum of mass flows that exit the engine nozzle and Coandă slots. While the total fuel flow  $\dot{m}_{fuel}$  is lowest in regions of minimum total drag, the  $SFC_{total}$  decreases at flight states with high angles of attack. For loiter phases, flight altitude and velocity are usually chosen close to the point of minimum fuel consumption  $\dot{m}_{fuel}$ . In contrast, for cruise flight the optimum in specific range  $\frac{U_\infty}{\dot{m}_{fuel}} [\frac{km}{kg}]$  determines the operating point of maximum distance covered by 1 kg of fuel. As can be seen in Figure 5.32c, the optimum cruise point is situated at high velocity and high altitude. To quantify the additional necessary fuel of the Coandă flap system w.r.t. to the conventional flap case, both total fuel mass flow values  $(\dot{m}_{fuel})_{Coanda}$  and  $(\dot{m}_{fuel})_{conv}$  are compared throughout the flight envelope. As analysed for the Coandă flap case before, also the reference aircraft configuration with conventional plain flaps implies the use of solely the midboard flaps (MB) for longitudinal trim. The relative fuel mass flow  $\frac{(\dot{m}_{fuel})_{Coanda}}{(\dot{m}_{fuel})_{conv}}$  of the Coandă flap compared to the conventional flap case gives an indication of the price that has to be paid for reduced observability (Figure 5.32d). As can be seen in the green coloured regions, the Coandă flap interestingly shows a potential to reduce fuel burn at low flight

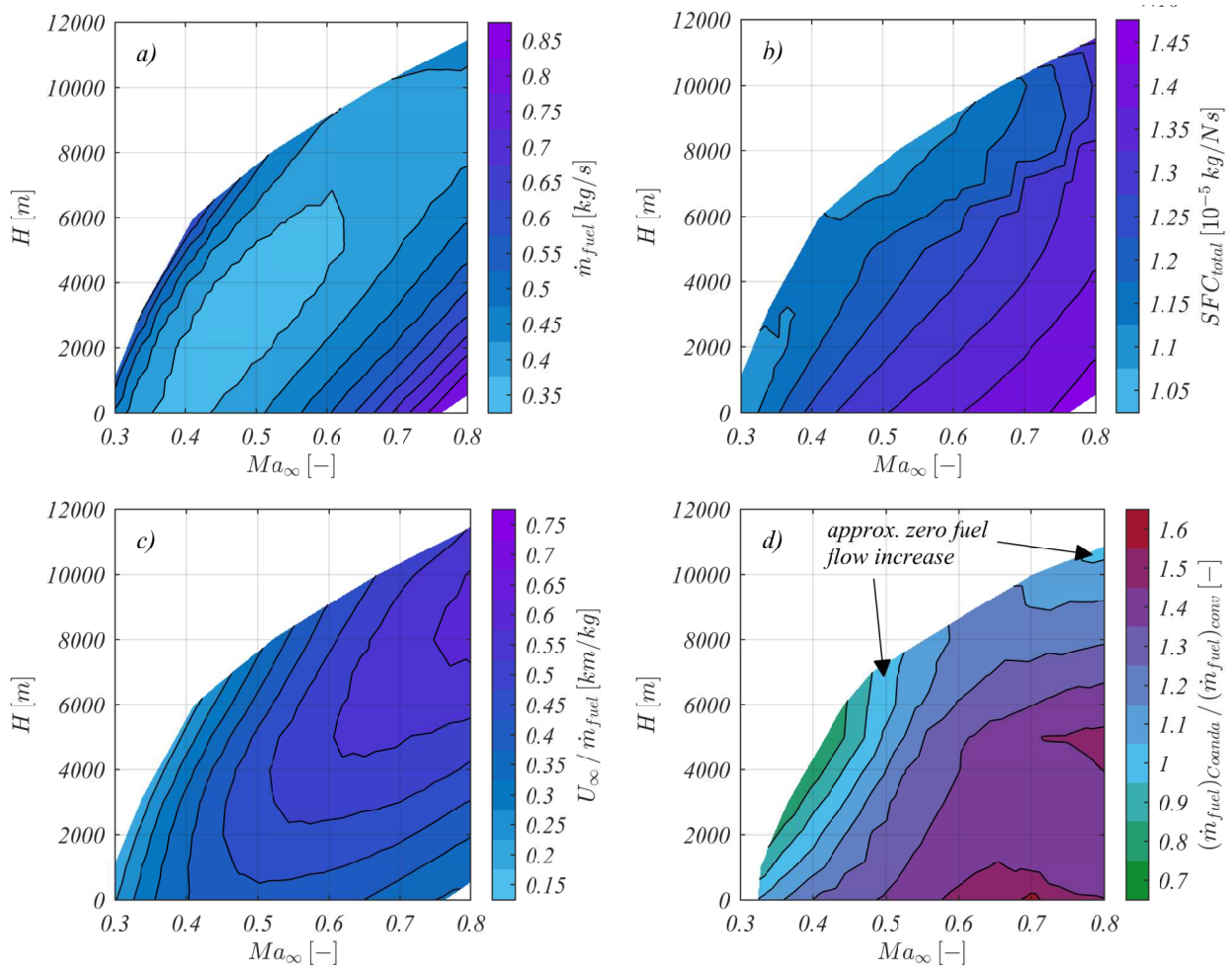


**Figure 5.32:** Aircraft system performance during horizontal flight solely trimmed by the midboard Coandă flaps

velocities, i.e. at high angles of attack. In contrast, at high velocities and low altitudes, the necessary fuel flow raises significantly by up to 40%. Increasing the flight level alleviates the penalty in fuel consumption and even shows an approximately neutral behaviour at high altitude cruise conditions ( $H \approx 11\,000\text{m}$ ,  $Ma \approx 0.8$ ). However, the neglect of compressibility leaves doubts of validity here.

**Coandă Flaps as Supporting Devices** The Coandă flap is considered to be a supporting trim device rather than the unique device for longitudinal trim. The inboard (gap covered) plain flaps are meant to generate the main portion of pitching moments while the Coandă flaps contribute with low blowing rates. Still, the steady jet outflow has to be strong enough to reduce the Coandă aerofoil base drag during cruise. Similar to the previous case, the trim calculations are performed for different slot opening settings  $A_{slot}$  and, additionally, for different values of  $\eta_h$ . For each operating point ( $H$ ,  $Ma_\infty$ ), the setting with least fuel flow  $\dot{m}_{fuel}$  is chosen to be assembled to the final envelope of operation. In this use case of

supporting Coandă flap, the pattern of slot opening area  $A_{slot}/A_{slot,max}$  and bypass bleed fraction  $\dot{m}_{bleed}/\dot{m}_{BP}$  for minimum fuel flow is similar to the precedent case of pure Coandă flap trim (Figure 5.33a,b). However, the Coandă flap control value  $\eta_h$  exhibits naturally lower magnitudes (Figure 5.33c). As can be seen in Figure 5.33e, the Coandă flap contributes a notably large portion (60%-80%) to the necessary trim moments at the majority of trim points. Interestingly, the conventional inboard flap (IB) does not take the role of the main longitudinal trim device. For low altitudes and high velocities, the minimum fuel burn is even achieved with zero or very small conventional plain flap deflections (Figure 5.33d). In these regions, the Coandă flap system generates nearly 100% of required trim pitching moment. In terms of thrust contribution, the fraction  $\frac{(F_N)_{Coanda}}{(F_N)_{total}}$  of net thrust due to the Coandă jets w.r.t. total thrust does not exceed 10% as seen in Figure 5.33f. Concerning fuel consumption, this use case leads to a slight reduction compared to the precedent case of a pure Coandă flap trim (Figure 5.34a,b,c). The line of zero increase in fuel flow w.r.t. to the conventional configuration is shifted towards higher velocities. So, a real potential for fuel savings could be identified for lower velocities (Figure 5.34d). However, the penalty at high velocities and low altitudes still exists.

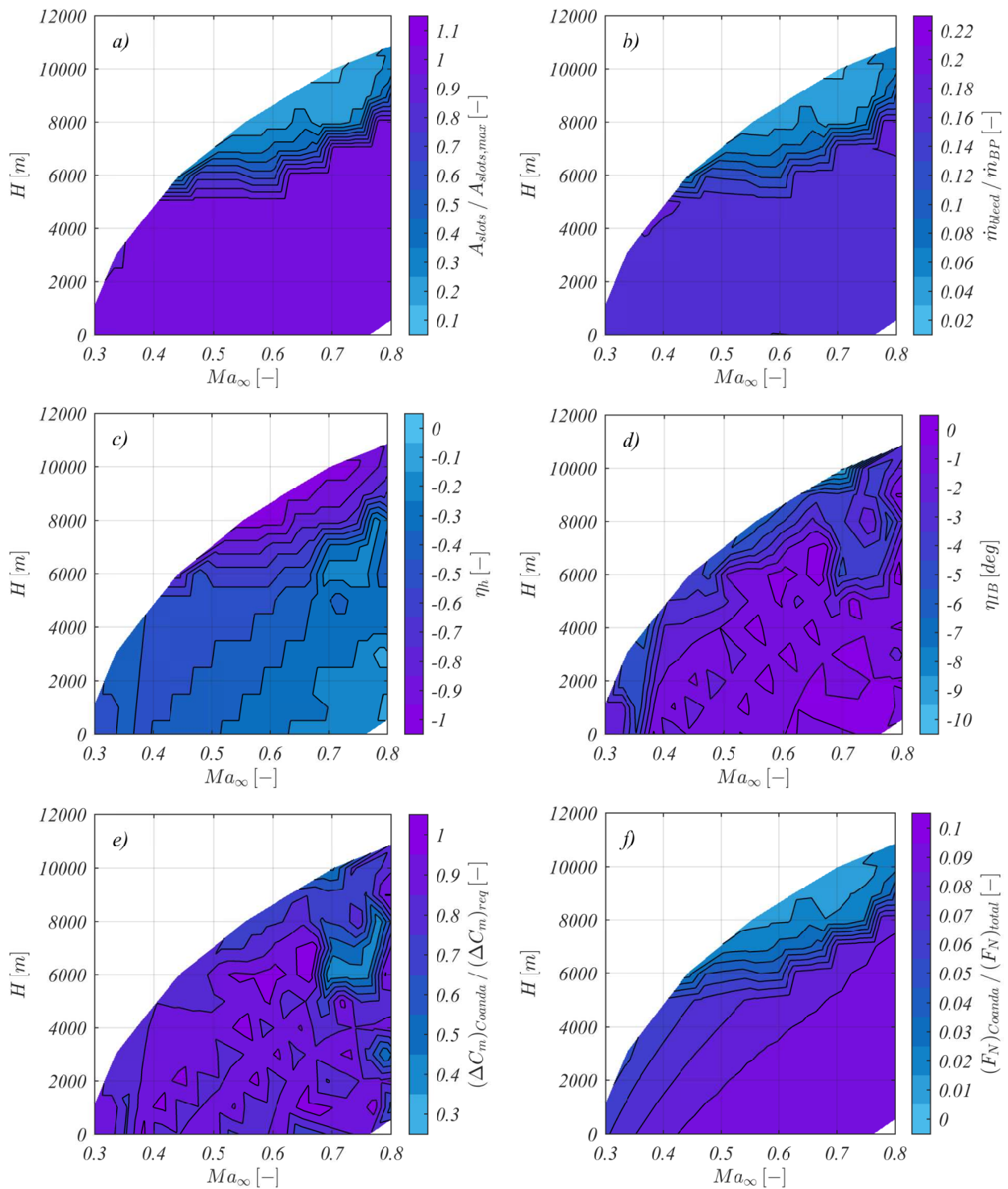


**Figure 5.33:** Envelopes of optimised Coandă system parameters during horizontal flight with trim support through midboard Coandă flaps

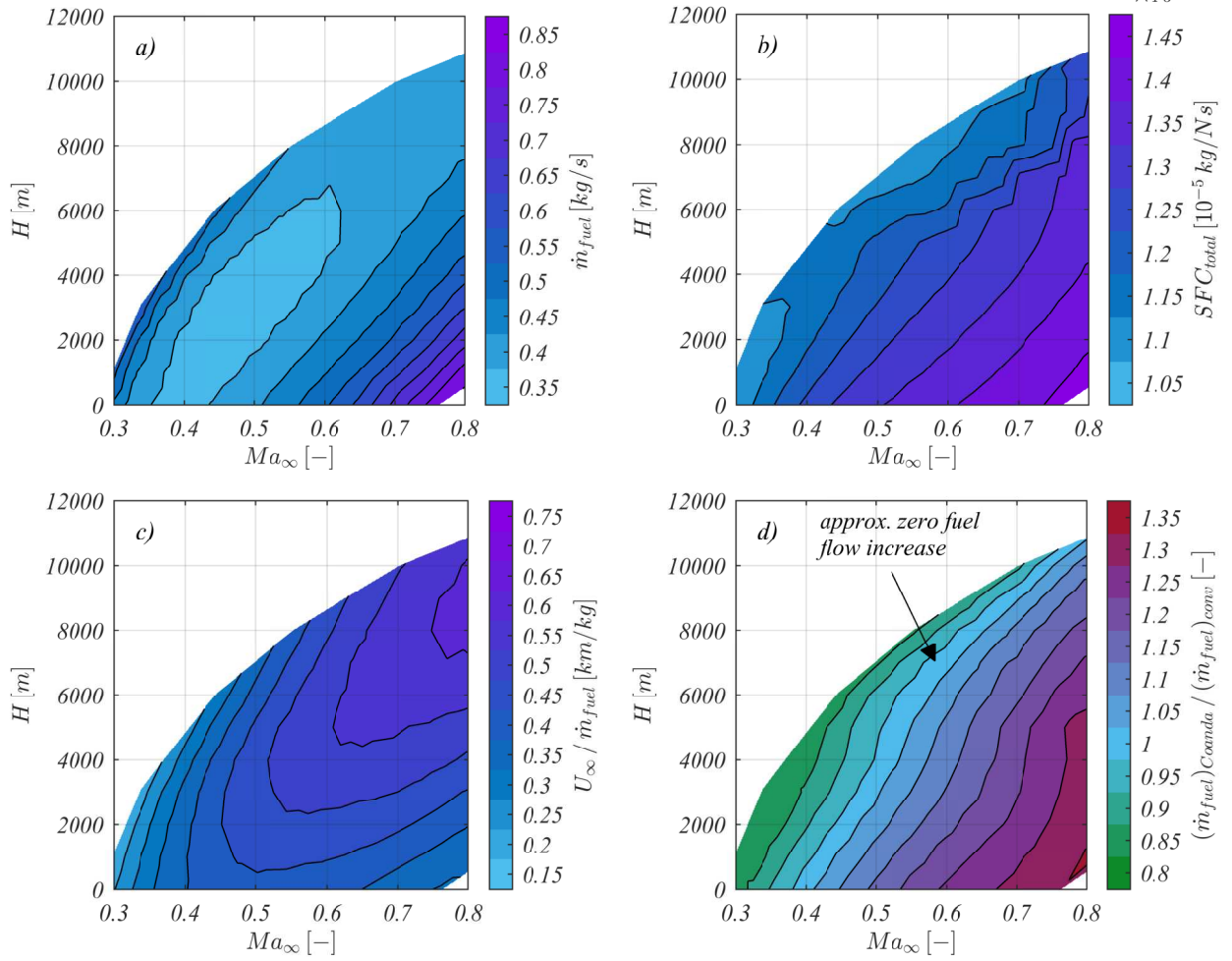


**Figure 5.34:** Aircraft system performance during horizontal flight with trim support through midboard Coandă flaps



# 6 Conclusion

In this thesis, a preliminary design method is proposed to model the entire functional chain of a Coandă flap system. This comprises the estimation of engine performance, total pressure losses inside ducts, aerodynamic characteristics of the Coandă aerofoil and flight dynamic reaction of the finite wing. Sufficient accuracy for early Coandă flap design stages could be proven through validation studies for the respective methods. Inside their custom implementations, novel enhancements of sophisticated approaches have been developed. They mainly comprise 2D RANS turbulence model modifications and extensions of a vortice lattice cambering method. Their respective implementations (MATLAB) enabled stable automated simulations of aerodynamic flow. The stipulated robustness was achieved in the scope of the performed studies. The latter included automated calculation campaigns with vast parameter variations as well as automated data matching algorithms to set up look-up tables for the final simulation of the overall system. Computational speed was absolutely acceptable in every step. Even for the 2D RANS simulations, several thousand data points could be calculated within a few days by means of standard IT infrastructure.

The presented methods were applied in the context of a low-aspect-ratio flying-wing configuration. It is virtually equipped with Coandă “flaps” for the purpose of flapless flight control. Extensive parameter studies have been performed within the practical boundaries of the available design space. Their results in combination with findings from literature research allow the deduction of several conclusions and design recommendations which are summarised in the subsequent section.

## 6.1 Summary of Results

The most important findings in this study can be summarised as follows:

- Whereas bypass bleed visibly degrades engine efficiency at spool speeds close to the design point ( $\Omega_{HP}^* = 1$ ), the low pressure spool process reacts favourably in the off-design regime ( $0.7 < \Omega_{HP}^* < 0.9$ ). Under the assumption of 100% thrust recovery from bleed air, the total specific thrust  $\frac{F_N}{\dot{m}_{fuel}}$  increases due to bypass bleed in the off-design operating points. For the modelled engine type, this could be traced back to the fact

that the increased bypass mass flow shifts the LP operating points in both turbine and compressor map towards higher LP spool speeds, and therefore to higher adiabatic efficiencies (subsection 5.1.1).

- Small pipe diameters below  $D \lesssim 5\text{cm}$  and extensively curved ducting can lead to a dramatical loss in outflow jet momentum  $(\dot{m} \cdot u)_{slot}$ . However, average duct diameters corresponding to approximately 25% of the engine bypass area ( $\frac{\dot{m}_{BP}}{\dot{m}_{engine}} \approx 1.5$ ) cause acceptable pressure losses ( $\frac{p_{t,slot}}{p_{t,BP}} \approx 7 - 10\%$ ) in the relatively short duct system ( $L_{total} \approx 5\text{m}$ ) of a low aspect ratio configuration ( $AR = 2$ ). Moreover, under the conditions of a choked outlet ( $Ma_{slot} = 1$ ), pressure losses inside the duct system remain essentially constant with increasing pressure ratios  $\frac{p_{t,BP}}{p_{\infty}}$  (subsection 5.1.2).
- Larger Coandă radii lead to an increased potential of lift and pitching moment generation. However, beyond radius-to-baseline-chord-ratios of  $\frac{r}{c_{base}} > 0.02$ , the gain in maximum effectiveness does not justify the base drag rise. In terms of control force efficiency  $\frac{\partial c_l / \partial \eta_h}{C_{\mu}}$  during dual-slot mode, the smallest tested radii led to highest efficiency values (subsection 5.1.3).
- In single-slot mode, the Coandă jet outflow velocity ratio has to reach at least unity ( $\frac{U_{jet}}{U_{\infty}} > 1$ ) to provoke positive aerodynamic reactions ( $\Delta c_l, \Delta c_m$ ) compared to the unblown case. Below this threshold, lift generation is scarcely existent or even exhibits negative values. In contrast, velocity ratios exceeding  $\frac{U_{jet}}{U_{\infty}} > 2$  led to reduced lift augmentations  $\frac{\partial c_l}{\partial C_{\mu}}$  for a Coandă radius of  $\frac{r}{c_{base}} = 0.02$ . For the same radius under symmetric double-slot-blowing conditions, a velocity ratio of  $\frac{U_{jet}}{U_{\infty}} = 1$  achieved the highest lift curve slope  $\frac{\partial c_l}{\partial \alpha}$  and maximum lift coefficient  $(c_l)_{max}$  while the values dropped for further increased  $C_{\mu}$ -values. Furthermore, double-slot-blowing with slight asymmetry ( $0.1 < \eta_h < 0.3$ ) revealed a potential to slightly reduce section drag (subsection 5.1.3).
- As confirmed by wind tunnel experiments from literature, smaller slot heights enable higher lift ( $\Delta c_l$ ) and pitching moment ( $\Delta c_m$ ) increments for identical outflow momentum fluxes  $C_{\mu}$ . Or expressed differently, the lift augmentation  $\frac{\partial c_l}{\partial C_{\mu}}$  increases for shrinking slot sizes. In dual-slot mode, larger total slot heights  $h_{total}$  cannot further increase the control force slope  $\frac{\partial c_l}{\partial \eta_h}$  significantly and even lead to reduced slopes. The same trend applies for the ratio of control force slope to blowing coefficient  $\frac{\partial c_l / \partial \eta_h}{C_{\mu}}$  (subsection 5.1.3).
- For incident angles well below leading edge separation, the Coandă flap effectiveness is essentially independent from angle of attack  $\alpha_{\infty}$  (subsection 5.1.3).
- Comparing the Coandă flap with a conventional plain flap of identical span (but relatively high flap chord fraction), the pitching moment authority relative to the parasite negative lift is more favourable. This is due to the existence of the pronounced trailing edge suction peak (subsection 5.1.4).

- In installed configuration under loiter conditions ( $H = 5000m$ ,  $Ma_\infty = 0.5$ ) at trimmed thrust ( $\delta_T \approx 0.6$ ), the Coandă flap is capable to produce essentially the same magnitude of pitching moment as the conventional reference flap. Roll authority is about half the conventional flap effectiveness in the same flight state. Compared to the lower tip split flap, Coandă flap yaw authority is poor and constitutes no more than about 10% of reference effectiveness (section 5.2).
- For trimmed horizontal flight at altitudes below  $6000m$ , larger slot sizes, i.e. higher bypass bleed fractions, are more favourable in terms of total fuel consumption  $\dot{m}_{fuel}$ . High blowing rates become more expensive in the high altitude regime ( $H > 6000m$ ). This applies for longitudinal trim solely achieved through the Coandă flap system as well as for the use case of assisting Coandă flap deflection (i.e. additionally to the conventional inboard plain flap) (section 5.2).
- Whereas the installed Coandă flap system revealed quite expensive ( $\Delta\dot{m}_{fuel} > +20\%$ ) at high flight speeds ( $Ma_\infty > 0.5$ ), a potential to reduce fuel consumption at low velocities could be identified compared to the conventional plain flap configuration (section 5.2).

## 6.2 Applicability and Validity

In principle, the presented method is applicable for both single-slotted and double-slotted Coandă aerofoil designs. While the first might be primarily interesting for fluidic high lift systems and STOL applications, the latter is preferable for flight control and aerodynamic morphing purposes. Redundancy issues and cross-bleed architectures are not considered in the current implementation.

In accordance to the assumptions listed in section 3.6 the most important limitations are repeated as follows: Since the two-dimensional RANS simulations for the estimation of Coandă flap effectiveness are restricted to incompressible flow, the results are only valid for flight Mach numbers  $Ma_\infty < 0.6$  and unchoked Coandă jet conditions ( $Ma_{jet} < 1$ ). However, tendencies can be derived also for higher velocities, even though the quantitative values have to be taken with caution. The aerodynamic data tables for the flight dynamic simulation contain only control increments ( $\Delta C_D$ ,  $\Delta C_Y$ ,  $\Delta C_L$ ,  $\Delta C_l$ ,  $\Delta C_m$ ,  $\Delta C_n$ ) which are based on zero angle of attack ( $\alpha_\infty = 0deg$ ). Especially at flight states with high incidences, uncertainty exists about the validity of simulation results. High local angles of attack ( $\alpha_{loc} > 10deg$ ) are likely to affect control effectiveness negatively. Moreover, the effects of possible vortex systems and non-linear lift are neglected.

## 6.3 Outlook

Since the circulation control technology is explicitly relevant for transonic flight regimes, the most obvious enhancement of the presented method is the extension for compressible flow up to free stream Mach numbers close to unity ( $Ma_\infty \approx 0.9$ ). This more realistic modelling requires advanced stabilisation techniques to achieve a robust convergence of the automated RANS calculations. Unsteady shock phenomena (e.g. buffeting) pose special challenges here. In addition, for sufficient accuracy, automated local mesh refinement at runtime could be an interesting but complex feature. Also, a relatively easy adaption of the automeshing could extend the applicability to blown flaps which have been subject of extensive investigation since the middle of the last century (e.g. WILLIAMS (1955); PFINGSTEN/RADESPIEL (2009); WICK ET AL. (2013)). Note that the jet wrap-around problem (subsection 2.4.2 and subsection 3.4.5) in the super-circulation regime is eliminated for blown plain flaps as the jet separation point is clearly defined by the sharp flap trailing edge.

Beneficial aspects of circulation control aerofoils might be interesting also for other aircraft missions and associated configurations. The potential of noise reduction compared to conventional high-lift systems could be attractive for civil applications where aircraft noise becomes more and more relevant (MUNRO ET AL., 2001). Furthermore, circulation control promises to enable the control of laminar flow over a wide range of flight conditions, thus reducing drag significantly (MCGOWAN ET AL., 2004). This aspect additionally contributes to the chance of reduced fuel consumption at moderate flight velocities ( $Ma_\infty \approx 0.5$ ) as shown in this work. Therefore, long endurance configurations (MALE/HALE) implying extended low speed loiter phases could be particularly interesting for the application of fluidic circulation control systems. Bypass bleed is capable to improve engine efficiency at off-design points. In addition, flight state dependent manipulation of the lift distribution could open new degrees of freedom for advanced fuel saving concepts. In every case, the implied feasibility studies in the preliminary design stages will require thorough models of the overall system. To this, the presented methods constitute a useful starting point to build far more than “paper planes” (see p. 1).

# References

- ABRAMSON, J. (1975): Two-Dimensional Subsonic Wind Tunnel Evaluation of a 20-Percent-Thick Circulation Control Airfoil, Tech. rep., David W. Taylor Naval Ship Research and Development Center, Bethesda (MD), USA.
- ABRAMSON, J. (1977): Two-Dimensional Subsonic Wind Tunnel Evaluation of Two Related Cambered 15-Percent Thick Circulation Control Airfoils, Tech. rep., David W. Taylor Naval Ship Research and Development Center, Bethesda (MD), USA.
- ABRAMSON, J. (2004): Characteristics of a Cambered Circulation Control Airfoil Having Both Upper and Lower Surface Trailing Edge Slots, Tech. rep., Naval Surface Warfare Center, Carderock Division, West Bethesda (MD), USA.
- ALEXANDER, M. G./ANDERS, S. G./JOHNSON, S. K./FLORANCE, J. P./KELLER, D. F. (2005): Trailing Edge Blowing on a Two-Dimensional Six-Percent Thick Elliptical Circulation Control Airfoil Up to Transonic Conditions: NASA/TM-2005-213545, Tech. rep., NASA Langley Research Center, Langley (VA), USA.
- ANDERSON, J. D./CORDA, S. (1980): Numerical lifting line theory applied to drooped leading-edge wings below and above stall, in: *Journal of Aircraft*, 17(12), pp. 898–904.
- AROLLA, S./DURBIN, P. (2013): Assessing the effects of streamline curvature on the aerodynamics of circulation control airfoil, in: 51st AIAA Aerospace Sciences Meeting, American Institute of Aeronautics and Astronautics, Grapevine (TX), USA, 7-10 January 2013.
- BAKER, W./PATERSON, E. (2006): RANS CFD Simulation of a Circulation-Control Foil: Validation of Performance, Flow Field, and Wall Jet, in: 3rd AIAA Flow Control Conference, Fluid Dynamics and Co-located Conferences, American Institute of Aeronautics and Astronautics, San Francisco (CA), USA, 5-8 June 2006.
- BARBERIE, F./HOOKER, J./ZEUNE, C. (2013): Low Speed Powered Lift Testing of a Transonic Cruise Efficient STOL Military Transport, in: 51st AIAA Aerospace Sciences Meeting, American Institute of Aeronautics and Astronautics, Grapevine (TX), USA, 7-10 January 2013.
- BERNHARDT, P. (2015): Numerische Strömungssimulation eines Flügelprofils mit aktiver Strömungskontrolle, Stud. Proj. Rep. LS-SA 15/08, Lehrstuhl für Luftfahrtsysteme, Technische Universität München, Munich, Germany.
- BRADSHAW, B. A./GEE, M. T. (1962): Turbulent Wall Jets with and without an External Stream, Tech. rep. 3252, Ministry of Supply, Aeronautical Research Council, London, UK.
- CARPENTER, P. W./SMITH, C. (1997a): Aeroacoustics and Aerodynamics of High-Speed Coanda Devices, Part 1: Conventional Arrangement of Exit Nozzle and Surface, in: *Journal of Sound and Vibration*, 208(5), pp. 777–801.

- CARPENTER, P. W./SMITH, C. (1997b): Aeroacoustics and Aerodynamics of High-Speed Coanda Devices, Part 2: Effects of Modifications for Flow Control and Noise Reduction, in: *Journal of Sound and Vibration*, 208(5), pp. 803–822.
- CELIC, A./HIRSCHEL, E. H. (2006): Comparison of Eddy-Viscosity Turbulence Models in Flows with Adverse Pressure Gradient, in: *AIAA Journal*, 44(10), pp. 2156–2169.
- CHANG, P. A./SLOMSKI, J./MARINO, T./EBERT, M. P./ABRAMSON, J. (2006): Full Reynolds-Stress Modeling of Circulation Control Airfoils, in: *Applications of Circulation Control Technology, Progress in Astronautics and Aeronautics*, pp. 445–468, American Institute of Aeronautics and Astronautics.
- CHEN, C./SEELE, R./WYGNANSKI, I. (2012): Separation and Circulation Control on an Elliptical Airfoil by Steady Blowing, in: *AIAA Journal*, 50(10), pp. 2235–2247.
- COANDA, H. (1961): Jet sustained aircraft, US Patent 2,988,303.
- CORNELIUS, K. C./LUCIUS, G. A. (1994): Physics of Coanda jet detachment at high-pressure ratio, in: *Journal of Aircraft*, 31(3), pp. 591–596.
- CZICHOS, H./HENNECKE, M. (2004): *Hütte: Das Ingenieurwissen*, 32. edition, Springer, Berlin, Germany and Heidelberg, Germany and New York (NY), USA.
- DRELA, M. (1989): XFOIL: An Analysis and Design System for Low Reynolds Number Airfoils, in: *Low Reynolds Number Aerodynamics, Vol. 54 of Lecture Notes in Engineering*, pp. 1–12, Springer, Berlin, Germany and Heidelberg, Germany.
- DUNHAM, J. (1968): A theory of circulation control by slot-blowing, applied to a circular cylinder, in: *Journal of Fluid Mechanics*, 33(03), pp. 495–514.
- DVORAK, F./STRASH, D./YORK, B./DASH, S. (1987): Improved algorithms for circulation-control airfoils in transonic flow, in: *25th AIAA Aerospace Sciences Meeting, American Institute of Aeronautics and Astronautics, Reno (NV), USA, 12-15 January 1987*.
- DVORAK, F. A. (1973): Calculation of turbulent boundary layers and wall jets over curved surfaces, in: *AIAA Journal*, 11(4), pp. 517–524.
- DVORAK, F. A./CHOI, D. H. (1983): Analysis of circulation-controlled airfoils in transonic flow, in: *Journal of Aircraft*, 20(4), pp. 331–337.
- DVORAK, F. A./KIND, R. J. (1979): Analysis Method for Viscous Flow over Circulation-Controlled Airfoils, in: *Journal of Aircraft*, 16(1), pp. 23–28.
- ENGLAR, R./JONES, G./ALLAN, B./LIN, J. (2009): 2-D Circulation Control Airfoil Benchmark Experiments Intended for CFD Code Validation, in: *47th AIAA Aerospace Sciences Meeting, American Institute of Aeronautics and Astronautics, Orlando (FL), USA, 5-8 January 2009*.
- ENGLAR, R. J. (1970): Two-Dimensional Transonic Wind Tunnel Tests of Three 15-Percent Thick Circulation Control Airfoils, Tech. rep. AD882075, David W. Taylor Naval Ship Research and Development Center, Bethesda (MD), USA.
- ENGLAR, R. J. (1971): Two-Dimensional Subsonic Wind Tunnel Tests of Two 15-Percent Thick Circulation Control Airfoils, Tech. rep., David W. Taylor Naval Ship Research and Development Center, Bethesda (MD), USA.

- ENGLAR, R. J. (1972): Two-Dimensional Subsonic Wind Tunnel Tests of a 30-Percent Thick Circulation Control Airfoil, Tech. rep., David W. Taylor Naval Ship Research and Development Center, Bethesda (MD), USA.
- ENGLAR, R. J. (1975): Experimental Investigation of the High Velocity Coanda Wall Jet Applied to Bluff Trailing Edge Circulation Control Airfoils, Tech. rep., David W. Taylor Naval Ship Research and Development Center, Bethesda (MD), USA.
- ENGLAR, R. J. (1979): Development of the A-6/Circulation Control Wing Flight Demonstrator Configuration, Tech. rep., David W. Taylor Naval Ship Research and Development Center, Bethesda (MD), USA.
- ENGLAR, R. J. (1981): Low-Speed Aerodynamic Characteristics of a Small, Fixed-Trailing-Edge Circulation Control Wing Configuration Fitted to a Supercritical Airfoil, Tech. rep., David W. Taylor Naval Ship Research and Development Center, Bethesda (MD), USA.
- ENGLAR, R. J./HEMMERLY, R. A./TAYLOR, D. W./MOORE, W. HORACE/SEREDINSKY, V./VALCKENAERE, W./JACKSON, J. A. (1981): Design of the Circulation Control Wing STOL Demonstrator Aircraft, in: *Journal of Aircraft*, 18(1), pp. 51–58.
- FALKNER, V. M. (1952): The Scope and Accuracy of Vortex Lattice Theory, Tech. rep. 2740, Ministry of Supply, Aeronautical Research Council, London, UK.
- FAROKHI, S. (2009): *Aircraft Propulsion*, 1. edition, John Wiley & Sons, Inc., Hoboken (NJ), USA.
- FASEL, H. F./GROSS, A./WERNZ, S. (2006): Investigation of Turbulent Coanda Wall Jets Using DNS and RANS, in: *Applications of Circulation Control Technology, Progress in Astronautics and Aeronautics*, pp. 401–420, American Institute of Aeronautics and Astronautics.
- FEKETE, G. I. (1963): Coanda Flow of a Two-Dimensional Wall Jet on the Outside of a Circular Cylinder, Tech. rep. No. 63-11, Mechanical Engineering Research Laboratories, McGill University, Montreal, Canada.
- FERZIGER, J. H./PERIĆ, M. (2002): *Computational methods for fluid dynamics*, 3. edition, Springer, Berlin, Germany and New York (NY), USA.
- FIELDING, J. P./MILLS, A./SMITH, H. (2010): Design and manufacture of the DEMON unmanned air vehicle demonstrator vehicle, in: *Proceedings of the Institution of Mechanical Engineers, Part G: Journal of Aerospace Engineering*, 224(4), pp. 365–372.
- FINK, R. (1978): USAF Stability and Control DATCOM, Tech. rep. AFWAL-TR-83-3048, McDonnell Douglas Corporation, Long Beach, USA.
- FLIGHT GLOBAL (1910): Photographer: Anonymous, CC-license: BY-SA 4.0, URL: <http://www.flightglobal.com/pdfarchive/view/1910/1910%20-%200883.html>, accessed on 11 February 2016.
- FORSTER, M./BIAVA, M./STEIJL, R. (2015): Optimisation of Coanda Surfaces for Transonic Circulation Control, in: *6th European Conference for Aeronautics and Space Sciences*, Kraków, Poland, 29 June - 3 July 2015.
- FORSTER, M./STEIJL, R. (2015): Numerical Simulation of Transonic Circulation Control, in: *53rd AIAA Aerospace Sciences Meeting*, American Institute of Aeronautics and Astronautics, Kissimmee (FL), USA, 5-9 January 2015.

- FRITH, S./WOOD, N. (2003): Effect of Trailing Edge Geometry on a Circulation Control Delta Wing, in: 21st AIAA Applied Aerodynamics Conference, Fluid Dynamics and Co-located Conferences, American Institute of Aeronautics and Astronautics, Orlando (FL), USA, 23-26 June 2003.
- FRITH, S./WOOD, N. (2004): Investigation of Dual Circulation Control Surfaces for Flight Control, in: 2nd AIAA Flow Control Conference, Fluid Dynamics and Co-located Conferences, American Institute of Aeronautics and Astronautics, Portland (OR), USA, 28 June - 1 July 2004.
- GHIA, U. K./GHIA, K. N./SHIN, C. T. (1982): High-Re Solutions for Incompressible Flow Using the Navier-Stokes Equations and a Multigrid Method, in: Journal of computational physics, 48(3), pp. 387–411.
- GOLOGAN, C. (2009): A Method for the Comparison of Transport Aircraft with Blown Flaps, Thesis, Technische Universität München, Munich, Germany.
- GRAMÜLLER, B./BOBLENZ, J./HÜHNE, C. (2014): PACS - Realization of an Adaptive Concept Using Pressure Actuated Cellular Structures, in: 63. Deutscher Luft- und Raumfahrtkongress der Deutschen Gesellschaft für Luft- und Raumfahrt e.V., Augsburg, Germany, 16-18 September 2014.
- HARLEY, C./WILDE, P./CROWTHER, W. (2009): Application of Circulation Control manoeuvre effectors for three axis control of a tailless flight vehicle, in: 47th AIAA Aerospace Sciences Meeting, American Institute of Aeronautics and Astronautics, Orlando (FL), USA, 5-8 January 2009.
- HARLOW, F. H./WELCH, J. E. (1965): Numerical Calculation of Time-Dependent Viscous Incompressible Flow of Fluid with Free Surface, in: Physics of Fluids (1958-1988), 8(12), pp. 2182–2189.
- HAWES, J. G./MAY JR, RALPH W (1951): Investigation at Low Speed of the Effectiveness and Hinge Moments of a Constant-Chord Ailavator on a Large-Scale Triangular Wing with Section Modification, Tech. rep. RM-L51A26, Langley Aeronautical Laboratory, Langley (VA), USA.
- HELLSTEN, A. (1998): Some improvements in Menter's  $k-\omega$  SST turbulence model, in: 29th AIAA Fluid Dynamics Conference, Fluid Dynamics and Co-located Conferences, American Institute of Aeronautics and Astronautics, Albuquerque (NM), USA, 15-18 June 1998.
- HOERNER, S. F./BORST, H. V. (1985): Fluid-Dynamic Lift: practical information on aerodynamic and hydrodynamic lift, 2. edition, Hoerner Fluid Dynamics, Albuquerque (NM), USA.
- HÖVELMANN, A./BREITSAMTER, C. (2012): Aerodynamic Characteristics of the SAGITTA Diamond Wing Demonstrator Configuration, in: 61. Deutscher Luft- und Raumfahrtkongress der Deutschen Gesellschaft für Luft- und Raumfahrt e.V., Berlin, Germany, 10-12 September 2012.
- HÖVELMANN, A./PFNÜR, S./BREITSAMTER, C. (2014): Flap Efficiency Analysis for the SAGITTA Diamond Wing Demonstrator Configuration, in: 63. Deutscher Luft- und Raumfahrtkongress der Deutschen Gesellschaft für Luft- und Raumfahrt e.V., Augsburg, Germany, 16-18 September 2014.

- IMBER, R./ROGERS, E. (1996): Investigation of a circular planform wing with tangential fluid ejection, in: 34th AIAA Aerospace Sciences Meeting, American Institute of Aeronautics and Astronautics, Reno (NV), USA, 15-18 January 1996.
- JABBAL, M./LIDDLE, S./CROWTHER, W. (2010): Active Flow Control Systems Architectures for Civil Transport Aircraft, in: *Journal of Aircraft*, 47(6), pp. 1966–1981.
- JABBAL, M./TOMASSO, V. (2014): Sensitivity Analysis of Active Flow Control Systems: Operating Parameters and Configuration Design, in: *Journal of Aircraft*, 51(1), pp. 330–335.
- JONES, G./ENGLAR, R. (2003): Advances In Pneumatic Controlled High Lift Systems Through Pulsed Blowing, in: 21st AIAA Applied Aerodynamics Conference, Fluid Dynamics and Co-located Conferences, American Institute of Aeronautics and Astronautics, Orlando (FL), USA, 23-26 June 2003.
- JONES, G./YAO, C.-S./ALLAN, B. (2006): Experimental Investigation of a 2D Supercritical Circulation-Control Airfoil Using Particle Image Velocimetry, in: 3rd AIAA Flow Control Conference, Fluid Dynamics and Co-located Conferences, American Institute of Aeronautics and Astronautics, San Francisco (CA), USA, 5-8 June 2006.
- JONES, G. S. (2005): Pneumatic Flap Performance for a 2D Circulation Control Airfoil, Steady and Pulsed, in: Proceedings of the 2004 NASA/ONR Circulation Control Workshop, Part 2; 845-888, NASA/CP-2005-213509/PT2, National Aeronautics and Space Administration.
- KATZ, J./PLOTKIN, A. (2001): Low speed aerodynamics, Vol. 13 of Cambridge aerospace series, 2. edition, Cambridge University Press, Cambridge, UK and New York (NY), USA.
- KOBAYASHI, R./FUJISAWA, N. (1983): Curvature Effects on Two-Dimensional Turbulent Wall Jets, in: *Ingenieur-Archiv*, 53(6), pp. 409–417.
- KURZKE, J. (1995): Advanced User-Friendly Gas Turbine Performance Calculations on a Personal Computer, in: ASME 1995 International Gas Turbine and Aeroengine Congress and Exposition, Houston (TX), USA, 5-8 June 1995.
- KURZKE, J. (1999): Gas Turbine Cycle Design Methodology: A Comparison of Parameter Variation With Numerical Optimization, in: *Journal of Engineering for Gas Turbines and Power*, 121(1), pp. 6–11.
- KURZKE, J. (2011): Transient Simulations During Preliminary Conceptual Engine Design, in: XX International Symposium on Air Breathing Engines, Gothenburg, Sweden, 12-16 September 2011.
- KWON, K./PARK, S. O. (2005): Aerodynamic Characteristics of an Elliptic Airfoil at Low Reynolds Number, in: *Journal of Aircraft*, 42(6), pp. 1642–1644.
- LAUNDER, B. E./REECE, G. J./RODI, W. (1975): Progress in the development of a Reynolds-stress turbulence closure, in: *Journal of Fluid Mechanics*, 68(03), pp. 537–566.
- LAUNDER, B. E./RODI, W. (1983): The Turbulent Wall Jet Measurements and Modeling, in: *Annual Review of Fluid Mechanics*, 15(1), pp. 429–459.
- LAUNDER, B. E./SPALDING, D. B. (1972): Lectures in mathematical models of turbulence, Academic Press, London, UK and New York (NY), USA.

- LEVINSKY, E. S./YEH, T. T. (1972): Analytical and experimental investigation of circulation control by means of a turbulent Coanda jet, Tech. rep., Air Vehicle Corporation, Ames Research Center, Washington D.C. and Springfield (VA), USA.
- LOTH, J. (2006): Advantages of Combining BLC Suction with Circulation Control High-Lift Generation, in: Applications of Circulation Control Technology, Progress in Astronautics and Aeronautics, pp. 3–21, American Institute of Aeronautics and Astronautics.
- LOTH, J. L./FANUCCI, J. B./ROBERTS, S. C. (1976): Flight Performance of a Circulation Controlled STOL Aircraft, in: Journal of Aircraft, 13(3), pp. 169–173.
- MADAVAN, N./ROGERS, M. (2010): Direct Numerical Simulation of Flow Around a Circulation Control Airfoil, in: 5th Flow Control Conference, Fluid Dynamics and Co-located Conferences, American Institute of Aeronautics and Astronautics, Chicago (IL), USA, 28 June - 1 July 2010.
- MATSUO, S./SETOGUCHI, T./KUDO, T./YU, S. (1998): Study on the Characteristics of Supersonic Coanda Jet, in: Journal of Thermal Science, 7(3), pp. 165–175.
- MCGOWAN, G./GOPALARATHNAM, A./JONES, G. S. (2004): Analytical and Computational Study of Adaptive Circulation Control Airfoils, in: 22nd AIAA Applied Aerodynamics Conference, American Institute of Aeronautics and Astronautics, Providence (RI), USA, 16-19 August 2004.
- MENTER, F. R. (1994): Two-equation eddy-viscosity turbulence models for engineering applications, in: AIAA Journal, 32(8), pp. 1598–1605.
- MENTER, F. R./KUNTZ, M./LANGTRY, R. (2003): Ten Years of Industrial Experience with the SST Turbulence Model, in: Turbulence, Heat and Mass Transfer, (4), pp. 625–632.
- MIKLOSOVIC, D./IMBER, R./BRITT-CRANE, M./COLANTONIO, K. (2012): Mid-span PIV Measurements of a Low Aspect Ratio Circulation Control Wing, in: 30th AIAA Applied Aerodynamics Conference, Fluid Dynamics and Co-located Conferences, American Institute of Aeronautics and Astronautics, New Orleans (LA), USA, 25-28 June 2012.
- MIN, B.-Y./LEE, W./ENGLAR, R./SANKAR, L. N. (2009): Numerical Investigation of Circulation Control Airfoils, in: Journal of Aircraft, 46(4), pp. 1403–1410.
- MONTERZINO, G. A. I./LAWSON, C. P. (2010): Development of a Pneumatic System to Enable Flight without Conventional Control Surfaces, in: 27th Congress of International Council of the Aeronautical Sciences, Nice, France, 19-24 September 2010.
- MOORHOUSE, D. J./WOODCOCK, R. J. (1982): Background Information and User Guide for MIL-F-8785C, Military Specification - Flying Qualities of Piloted Airplanes, Tech. rep. AFWAL-TR-81-3109, Air Force Wright Aeronautical Laboratories, Wright-Patterson Air Force Base, Ohio, USA.
- MUKHERJEE, R./GOPALARATHNAM, A. (2006): Poststall Prediction of Multiple-Lifting-Surface Configurations Using a Decambering Approach, in: Journal of Aircraft, 43(3), pp. 660–668.
- MUNRO, S./AHUJA, K./ENGLAR, R. (2001): Noise reduction through circulation control, in: 39th AIAA Aerospace Sciences Meeting, American Institute of Aeronautics and Astronautics, Reno (NV), USA, 8-11 January 2001.
- MÜNZBERG, H.-G./KURZKE, J. T. (1977): Gasturbinen: Betriebsverhalten und Optimierung, Springer Verlag, Berlin, Germany.

- NEUENDORF, R./WYGNANSKI, I. (1999): On a Turbulent Wall Jet Flowing over a Circular Cylinder, in: *Journal of Fluid Mechanics*, 381, pp. 1–25.
- NISHINO, T./HAHN, S./SHARIFF, K. (2010): Calculation of the Turbulence Characteristics of Flow Around a Circulation Control Airfoil Using LES (Invited Paper), in: 48th AIAA Aerospace Sciences Meeting, American Institute of Aeronautics and Astronautics, Orlando (FL), USA, 4-7 January 2010.
- NISHINO, T./SHARIFF, K. (2010): Numerical Study of Wind-Tunnel Sidewall Effects on Circulation Control Airfoil Flows, in: *AIAA Journal*, 48(9), pp. 2123–2132.
- NISHINO, T./SHARIFF, K. (2012): Effect of Jet Nozzle Lip Momentum Loss on Circulation Control Airfoil Performance, in: *AIAA Journal*, 50(3), pp. 551–558.
- NOVAK, C./CORNELIUS, K. (1986): An LDV investigation of a circulation control airfoil flowfield, in: 24th AIAA Aerospace Sciences Meeting, American Institute of Aeronautics and Astronautics, Reno (NV), USA, 6-9 January 1986.
- NOVAK, C./CORNELIUS, K./ROADS, R. (1987): Experimental investigations of the circular wall jet on a circulation control airfoil, in: 25th AIAA Aerospace Sciences Meeting, American Institute of Aeronautics and Astronautics, Reno (NV), USA, 12-15 January 1987.
- OWEN, F. K./OWEN, A. K. (2006): Measurement and Analysis of Circulation Control Airfoils, in: *Applications of Circulation Control Technology*, Progress in Aeronautics and Astronautics, pp. 105–112, American Institute of Aeronautics and Astronautics.
- PAJAYAKRIT, P./KIND, R. J. (2000): Assessment and Modification of Two-Equation Turbulence Models, in: *AIAA Journal*, 38(6), pp. 955–963.
- PFINGSTEN, K. C./RADESPIEL, R. (2009): Experimental and numerical investigation of a circulation control airfoil, in: 47th AIAA Aerospace Sciences Meeting, American Institute of Aeronautics and Astronautics, Orlando (FL), USA, 5-8 January 2009.
- PHILLIPS, W. F./SNYDER, D. O. (2000): Modern Adaptation of Prandtl’s Classic Lifting-Line Theory, in: *Journal of Aircraft*, 37(4), pp. 662–670.
- PRANDTL, L. (1923): *Applications of modern hydrodynamics to aeronautics*, Tech. rep. 116, Universität Göttingen, Göttingen, Germany.
- PUGLIESE, A./ENGLAR, R. (1979): Flight Testing the Circulation Control Wing, in: *Aircraft Systems and Technology Meeting*, Aircraft Design and Technology Meeting, American Institute of Aeronautics and Astronautics, New York (NY), USA, 20-22 August 1979.
- PULLIAM, T./JESPERSEN, D./BARTH, T. (1985): Navier-Stokes Computations for Circulation Controlled Airfoils, in: 18th Fluid Dynamics and Plasmadynamics and Lasers Conference, Fluid Dynamics and Co-located Conferences, American Institute of Aeronautics and Astronautics, Cincinnati (OH), USA, 16-18 July 1985.
- RAHMAN, N. U. (2009): *Propulsion and Flight Controls Integration for the Blended Wing Body Aircraft*, Thesis, Cranfield University, Cranfield, UK.
- RAYMER, D. P. (2012): *Aircraft design: A conceptual approach*, AIAA education series, 5. edition, American Institute of Aeronautics and Astronautics, Reston (VA), USA.
- REW, H. S./PARK, S. O. (1988): The interaction of two opposing, asymmetric curved wall jets, in: *Experiments in Fluids*, 6(4), pp. 243–252.

- ROBINSON, D. F./HASSAN, H. A. (1998): Further Development of the  $k$ -C (Enstrophy) Turbulence Closure Model, in: AIAA Journal, 36(10), pp. 1825–1833.
- DA ROCHA-SCHMIDT, L./BAIER, H. (2013): Morphing Skins and Gap Covers for Aerodynamic Control Surfaces, in: 62. Deutscher Luft- und Raumfahrtkongress der Deutschen Gesellschaft für Luft- und Raumfahrt e.V., Stuttgart, Germany, 10-12 September 2013.
- ROGERS, E./DONNELLY, M. (2004): Characteristics of a Dual-Slotted Circulation Control Wing of Low Aspect Ratio Intended for Naval Hydrodynamic Applications, in: 42nd AIAA Aerospace Sciences Meeting, American Institute of Aeronautics and Astronautics, Reno (NV), USA, 5-8 January 2004.
- RUMSEY, C. L. (2009): Exploring a Method for Improving Turbulent Separated-Flow Predictions with  $k$ - $\omega$  Models, Tech. rep., NASA Langley Research Center, Hampton (VA), USA.
- RUMSEY, C. L./GATSKI, T. B. (2001): Recent Turbulence Model Advances Applied to Multielement Airfoil Computations, in: Journal of Aircraft, 38(5), pp. 904–910.
- RUMSEY, C. L./NISHINO, T. (2011): Numerical study comparing RANS and LES approaches on a circulation control airfoil, in: International Journal of Heat and Fluid Flow, 32(5), pp. 847–864.
- SCHLECHT, R./ANDERS, S. (2007): Parametric Evaluation of Thin, Transonic Circulation-Control Airfoils, in: 45th AIAA Aerospace Sciences Meeting, American Institute of Aeronautics and Astronautics, Reno (NV), USA, 8-11 January 2007.
- SEUME, J./TEICHEL, S./BURNAZZI, M./SCHWERTER, M./BEHR, C./RUDENKO, A./SCHMITZ, A./DÖRBAUM, M./ATALAYER, C. (2013): SFB 880 - Efficient High Lift, in: 62. Deutscher Luft- und Raumfahrtkongress der Deutschen Gesellschaft für Luft- und Raumfahrt e.V., Stuttgart, Germany, 10-12 September 2013.
- SHIH, T.-H./LIOU, W. W./SHABBIR, A./YANG, Z./ZHU, J. (1994): A new  $k$ - $\varepsilon$  eddy viscosity model for high Reynolds number turbulent flows: model development and validation, Vol. no. 94-21 of ICOMP, National Technical Information Service, Springfield (VA), USA.
- SHREWSBURY, G. (1986): Numerical Evaluation of Circulation Control Airfoil Performance Using Navier-Stokes Methods, in: 24th AIAA Aerospace Sciences Meeting, American Institute of Aeronautics and Astronautics, Reno (NV), USA, 6-9 January 1986.
- SHUR, M./STRELETS, M./TRAVIN, A./SPALART, P. (1998): Turbulence modeling in rotating and curved channels - Assessment of the Spalart-Shur correction term, in: 36th AIAA Aerospace Sciences Meeting, American Institute of Aeronautics and Astronautics, Reno (NV), USA, 12-15 January 1998.
- SHUR, M. L./STRELETS, M. K./TRAVIN, A. K./SPALART, P. R. (2000): Turbulence Modeling in Rotating and Curved Channels: Assessing the Spalart-Shur Correction, in: AIAA Journal, 38(5), pp. 784–792.
- SIGLOCH, H. (2003): Technische Fluidmechanik, 4. edition, Springer, Berlin, Germany and Heidelberg, Germany and New York (NY), USA.
- SIVELLS, J. C./NEELY, R. H. (1947): Method for calculating wing characteristics by lifting-line theory using nonlinear section lift data, Tech. rep. TN1269, Langley Aeronautical Laboratory, Langley (VA), USA.

- SLOMSKI, J./GORSKI, J./MILLER, R./MARINO, T. (2002): Numerical simulation of circulation control airfoils as affected by different turbulence models, in: 40th AIAA Aerospace Sciences Meeting, American Institute of Aeronautics and Astronautics, Reno (NV), USA, 14-17 January 2002.
- SPALART, P./ALLMARAS, S. (1992): A one-equation turbulence model for aerodynamic flows, in: 30th AIAA Aerospace Sciences Meeting, American Institute of Aeronautics and Astronautics, Reno (NV), USA, 6-9 January 1992.
- SPALART, P. R./SHUR, M. (1997): On the sensitization of turbulence models to rotation and curvature, in: *Aerospace Science and Technology*, 1(5), pp. 297–302.
- SPALDING, D. B. (1961): A Single Formula for the “Law of the Wall”, in: *Journal of Applied Mechanics*, 28(3), pp. 455–458.
- SPALDING, D. B. (1972): A novel finite difference formulation for differential expressions involving both first and second derivatives, in: *International Journal for Numerical Methods in Engineering*, 4(4), pp. 551–559.
- STADLBERGER, K./HORNING, M. (2012): Design Drivers for Novel Flight Control Effectors for Low Aspect Ratio Flying-Wing Configurations, in: 61. Deutscher Luft- und Raumfahrtkongress der Deutschen Gesellschaft für Luft- und Raumfahrt e.V.
- STADLBERGER, K./HORNING, M. (2014): Challenges in the Modelling of Blown Circulation Control Aerofoils, in: 63. Deutscher Luft- und Raumfahrtkongress der Deutschen Gesellschaft für Luft- und Raumfahrt e.V., Augsburg, Germany, 16-18 September 2014.
- STADLBERGER, K./HORNING, M. (2015a): Aerodynamic Modelling of an Active Flow Control System for Flapless Flight Control in the Preliminary Design Stages, in: 5th CEAS Air & Space Conference, Delft, The Netherlands, 7-11 September 2015.
- STADLBERGER, K./HORNING, M. (2015b): Numerical Performance Analysis of a Coanda Aerofoil, in: 64. Deutscher Luft- und Raumfahrtkongress der Deutschen Gesellschaft für Luft- und Raumfahrt e.V., Rostock, Germany, 22-24 September 2015.
- SWANSON, R./RUMSEY, C./ANDERS, S. (2005): Progress Towards Computational Method for Circulation Control Airfoils, in: 43rd AIAA Aerospace Sciences Meeting, American Institute of Aeronautics and Astronautics, Reno (NV), USA, 10-13 January 2005.
- SWANSON, R. C./RUMSEY, C. L. (2009): Computation of circulation control airfoil flows, in: *Computers & Fluids*, 38(10), pp. 1925–1942.
- SWANSON, R. C./RUMSEY, C. L./ANDERS, S. G. (2006): Aspects of Numerical Simulation of Circulation Control Airfoils, in: *Applications of Circulation Control Technology, Progress in Astronautics and Aeronautics*, pp. 469–498, American Institute of Aeronautics and Astronautics.
- TAI, T. C./IDWELL, G. H. (1985): Numerical Optimization of Circulation Control Airfoil at High Subsonic Speed, in: *Journal of Aircraft*, 22(10), pp. 869–874.
- THOMPSON, J. F./SONI, B. K./WEATHERILL, N. P. (1999): *Handbook of grid generation*, 1. edition, CRC Press, Boca Raton and Fla.
- TOOREN, M./ROCCA, G./CHICIUDEAN, T. (2009): Further Steps towards Quantitative Conceptual Aircraft Design, in: BUTTAZZO, G./FREDIANI, A. (Editors), *Variational Analysis and Aerospace Engineering*, pp. 491–508, Springer New York, New York (NY), USA.

- USAF (2008): Photographer: Anonymous, License: public domain, URL: [https://upload.wikimedia.org/wikipedia/commons/f/fe/Avrocar\\_2.jpg](https://upload.wikimedia.org/wikipedia/commons/f/fe/Avrocar_2.jpg), accessed on 11 February 2016.
- VERSTEEG, H. K./MALALASEKERA, W. (2007): An introduction to computational fluid dynamics: The finite volume method, 2. edition, Pearson Education Ltd., Harlow, UK and New York (NY), USA.
- WAGNER, W. (2012): Strömung und Druckverlust, 7. edition, Vogel Buchverlag, Würzburg, Germany.
- WETZEL, D./GRIFFIN, J./LIU, F./CATTAFESTA, L. (2009): An Experimental Study of Circulation Control on an Elliptic Airfoil, in: 39th AIAA Fluid Dynamics Conference, Fluid Dynamics and Co-located Conferences, American Institute of Aeronautics and Astronautics, San Antonio (TX), USA, 22-25 June 2009.
- WICK, A./HOOKER, J./BARBERIE, F./ZEUNE, C. (2013): Powered Lift CFD Predictions of a Transonic Cruising STOL Military Transport, in: 51st AIAA Aerospace Sciences Meeting, American Institute of Aeronautics and Astronautics, Grapevine (TX), USA, 7-10 January 2013.
- WILCOX, D. (2007): Formulation of the  $k-\omega$  Turbulence Model Revisited, in: 45th AIAA Aerospace Sciences Meeting, American Institute of Aeronautics and Astronautics, Reno (NV), USA, 8-11 January 2007.
- WILCOX, D. C. (1998): Turbulence modeling for CFD, 2. edition, DCW Industries, La C nada (CA), USA.
- WILKERSON, J. B./MONTANA, P. S. (1982): Transonic Wind Tunnel Test of a 16-Percent-Thick Circulation Control Airfoil with One-Percent Asymmetric Camber, Tech. rep. ASED-82/03, David W. Taylor Naval Ship Research and Development Center, Bethesda (MD), USA.
- WILLIAMS, J. (1955): An Analysis of Aerodynamic Data on Blowing Over Trailing Edge Flaps for Increasing Lift, Tech. rep. C.P. No. 209, Ministry of Supply, Aeronautical Research Council, London, UK.
- WILLIAMS, R. M./HOWE, H. J. (1970): Two Dimensional Subsonic Wind Tunnel Tests on a 20 Percent Thick, 5 Percent Cambered Circulation Control Airfoil, Tech. rep. AD877764, Naval Ship Research and Development Center, Washington D.C., USA.
- WONG, C./HALE, C./CHAN, B./KONTIS, K. (2006): Experimental Studies on the Application of Circulation Control in Subsonic Flows, in: 44th AIAA Aerospace Sciences Meeting, American Institute of Aeronautics and Astronautics, Reno (NV), USA, 9-12 January 2006.
- WOOD, N./CONLON, J. (1983): The performance of a circulation control airfoil at transonic speeds, in: 21st AIAA Aerospace Sciences Meeting, American Institute of Aeronautics and Astronautics, Reno (NV), USA, 10-13 January 1983.
- WOOD, N. J./NIELSEN, J. N. (1986): Circulation control airfoils as applied to rotary-wing aircraft, in: Journal of Aircraft, 23(12), pp. 865–875.
- YOUNG, T. (1800): Outlines of Experiments and Inquiries Respecting Sound and Light, in: Philosophical Transactions of the Royal Society of London, (90), pp. 106–150.

ZACHAROS, A./KONTIS, K. (2006): Numerical Studies on an Active Flow Circulation Controlled Flap Concept for Aeronautical Applications, in: Transactions of the Japan Society for Aeronautical and Space Sciences, 49(163), pp. 25–30.



# Nomenclature

## Abbreviations

ADM	Aerodynamic Data Module
AFC	Active Flow Control
BSL	Baseline
c.g.	centre of gravity
CC	Circulation Control
CFRP	Carbon Fibre Reinforced Plastics
DNS	Direct Numerical Simulation
DOF	Degree Of Freedom
IR	Infra-Red
ISA	International Standard Atmosphere
LES	Large Eddy Simulation
M.A.C.	Mean Aerodynamic Chord
MTOW	Maximum Take-Off Weight
NACA	National Advisory Committee for Aeronautics
PDE	Partial Differential Equation
RANS	Reynolds Averaged Navier-Stokes
RCS	Radar Cross Section
SFC	Specific Fuel Consumption
SL	Sea Level ( $H = 0m$ )
SLE	System of Linear Equations
SST	Shear-Stress-Transport
SSTMod	SST model Modification
STOL	Short Take-Off and Landing
STR	Sustained Turn Rate
T/O	Take-Off
TRL	Technology Readiness Level
UAS	Unmanned Aerial System
VLM	Vortex Lattice Method
VTOL	Vertical Take-Off and Landing
WJC	Wall Jet Correction

## Greek Symbols

$\alpha_\infty$	free stream angle of attack	[deg]
$\alpha_{loc}$	local angle of attack at wing section	[deg]
$\beta_\infty$	free stream sideslip angle	[deg]
$\Delta C_D$	drag coefficient increment of finite wing	[-]
$\Delta C_L$	lift coefficient increment of finite wing	[-]
$\Delta C_l$	roll moment coefficient increment of finite wing	[-]
$\Delta C_m$	pitching moment coefficient increment of finite wing	[-]
$\Delta C_n$	yaw moment coefficient increment of finite wing	[-]
$\Delta C_Y$	side force coefficient increment of finite wing	[-]
$\delta_1, \delta_2$	local lattice modification angles	[deg]
$\delta_T$	throttle setting	[-]
$\eta_h$	outflow momentum ratio based on slot heights	[-]
$\Gamma$	vortex strength	[m <sup>2</sup> /s]
$\kappa$	ideal gas constant, $\kappa = 1.4$	[-]
$\lambda_{sep}$	separation loss factor of diverging pipe segment	[-]
$\lambda_{visc}$	pressure loss factor due to viscous effects	[-]
$\mu$	dynamic viscosity	[Pa s]
$\mu_t$	eddy viscosity due to turbulence	[Pa s]
$\mu_{eff}$	effective viscosity, $\mu_{eff} = \mu + \mu_t$	[Pa s]
$\nu$	kinematic viscosity	[m <sup>2</sup> /s]
$\nu_t$	kinematic eddy viscosity	[m <sup>2</sup> /s]
$\nu_{eff}$	effective kinematic viscosity, $\nu_{eff} = \nu + \nu_t$	[m <sup>2</sup> /s]
$\omega$	turbulence frequency	[1/s]
$\Omega_{HP}^*$	relative high pressure spool speed, $\Omega_{HP}^* = \frac{\Omega_{HP}}{(\Omega_{HP})_{design}}$	[rpm]
$\phi_{diff}$	diffusor angle	[deg]
$\Pi_{BP}$	bypass pressure ratio	[-]
$\Pi_{slot}$	slot pressure ratio	[-]
$\rho$	air density	[kg/m <sup>3</sup> ]
$\rho_\infty$	free stream air density	[kg/m <sup>3</sup> ]
$\sigma_{bend}$	pipe bend aspect ratio $\sigma_{bend} = \frac{r_{bend}}{d_P}$	[-]
$\Theta_{sep}$	jet separation angle on Coandă surface	[deg]
$v$	amplification factor inside wall jet marker function	[-]
$\varepsilon_{CP}$	correction factor to account for the deviation from perpendicularity	[-]
$\varphi_{0\%}$	leading edge sweep angle	[deg]

### Roman Symbols

$\dot{m}$	mass flow	[kg/s]
$\frac{\partial c_l / \partial \eta_h}{c_\mu}$	Coandă flap lift gain efficiency	[-]
$\frac{\partial c_l}{\partial c_\mu}$	lift augmentation	[-]
$\frac{\partial c_l}{\partial \eta_h}$	Coandă flap lift gain	[-]
$\frac{h}{r}$	ratio of slot height to Coandă radius	[-]
$\frac{r}{c_{base}}$	ratio of Coandă radius to baseline aerofoil chord	[-]
$\frac{U_{jet}}{U_\infty}$	jet outflow velocity ratio	[-]
$\bar{u}$	mean flow velocity inside the duct	[m/s]
$\vec{F}$	force vector	[m/s]
$\vec{n}$	normal vector	[m]
$\vec{r}_{AB}$	vector from point A to point B	[m]
$\vec{u}$	vector of local velocity	[m/s]
$\vec{V}_\Gamma$	vector of velocity induced by the potential flow vortex	[m/s]
$A$	cell surface area	[m <sup>2</sup> ]
$A_{slot}$	slot outflow area	[m <sup>2</sup> ]
$AR$	wing aspect ratio	[-]
$b$	wing span	[m]
$c$	wing section chord length	[m]
$C_D$	wing drag force coefficient	[-]
$c_d$	section drag coefficient (based on Coandă aerofoil chord length)	[-]
$C_L$	wing lift force coefficient	[-]
$C_l$	wing roll moment coefficient	[-]
$c_l$	section lift coefficient (based on Coandă aerofoil chord length)	[-]
$C_m$	wing pitching moment coefficient	[-]
$c_m$	section pitching moment coefficient (based on Coandă aerofoil chord length)	[-]
$C_v$	heat capacity at constant volume	[J/(kgK)]
$C_\mu$	jet outflow momentum flux coefficient, $C_\mu = \frac{U_{jet} \dot{m}_{jet}}{\frac{1}{2} \rho U_\infty^2 S_{ref}}$	[-]
$c_{avg}$	mean geometric wing chord, $c_{avg} = \frac{S_{ref}}{b}$	[m]
$c_{base}$	chord of unmodified baseline aerofoil	[m]
$c_{bend}$	coefficient to account for pressure losses inside pipe bends	[-]
$c_{Coanda}$	chord of Coandă aerofoil	[m]
$c_{l_\alpha}$	section lift curve slope	[-]
$c_p$	pressure coefficient	[-]
$C_T$	thrust effect coefficient	[-]

$D$	fluid element deformation tensor	[1/s]
$d_P$	local diameter of duct segment	[m]
$d_w$	normal distance from wall	[m]
$D_{hydr}$	hydraulic diameter (pipe segment)	[m]
$F_N$	net thrust generated by the engine	[N]
$f_{bend}$	pressure loss supplement factor of pipe bend	[-]
$F_D$	wall jet marker function	[-]
$H$	altitude	[m]
$h_l$	height of lower slot	[m]
$h_{total}$	total slot height, $h_{total} = h_u + h_l$	[m]
$h_u$	height of upper slot	[m]
$k$	turbulent kinetic energy	[m <sup>2</sup> /s <sup>2</sup> ]
$k_s$	sand grain height	[m]
$k_\phi$	diffusor correction factor	[-]
$k_{T,eff}$	effective thermal conductivity	[W/(mK)]
$L$	pipe segment length	[m]
$l_{CV}$	control volume length	[m]
$Ma$	Mach number	[-]
$p$	static pressure	[Pa]
$p_\infty$	ambient pressure	[Pa]
$p_{out}$	static pressure at duct outlet	[Pa]
$p_{t,BP}$	bypass total pressure	[Pa]
$p_{t,in}$	total pressure at duct inlet	[Pa]
$p_{t,out}$	total pressure at duct outlet	[Pa]
$q$	dynamic pressure, $q = \frac{1}{2}\rho V^2$	[Pa]
$R$	gas constant	[J/(kgK)]
$r$	radius of Coandă surface	[m]
$r_{bend}$	pipe bend radius	[m]
$Re$	Reynolds number based on the section chord length	[-]
$Re_d$	duct Reynolds number based on diameter, $Re_d = \frac{ud}{\nu}$	[-]
$SFC$	specific fuel consumption, $SFC = \frac{\dot{m}_{fuel}}{F_N}$	[g/kNs]
$T$	static temperature	[K]
$t/c$	relative aerofoil thickness	[-]
$T_0$	total temperature	[K]
$T_{t,in}$	total temperature at duct inlet	[K]
$u$	horizontal velocity component	[m/s]
$U_\infty$	free stream velocity	[m/s]

## Nomenclature

---

$u_\tau$	friction velocity	[m/s]
$u_\Theta$	tangential velocity on Coandă surface	[m/s]
$U_{jet}$	mean jet outflow velocity	[m/s]
$V$	cell volume	[m <sup>3</sup> ]
$v$	vertical velocity component	[m/s]
$y_{Coanda}$	normal distance from Coandă surface	[m]

## Subscripts

$BP$	bypass
$E$	eastern neighbour point of the considered control volume
$HP$	high pressure
$IB$	inboard flap position
$LP$	low pressure
$MB$	midboard flap position
$P$	centre point of the considered control volume
$W$	western neighbour point of the considered control volume



# List of Figures

1.1	Turbine driven aircraft Coandă-1910 (a) (FLIGHT GLOBAL, 1910) and U.S. military project Avro Canada VZ-9 Avrocar (b) (USAF, 2008) . . . . .	2
1.2	Illustration of Coandă effect . . . . .	2
1.3	Illustration of a circulation control aerofoil / Coandă aerofoil (modified from STADLBERGER/HORNUNG, 2014, 2015a,b) . . . . .	2
1.4	Structure of work . . . . .	5
2.1	Illustration of outflow process and wall jet (modified from STADLBERGER/HORNUNG, 2012, 2014) . . . . .	8
2.2	Typical velocity and turbulent shear stress profile of a wall jet . . . . .	8
2.3	Experimental and potential pressure distribution of an elliptical ( $t/c = 15\%$ ) circulation control aerofoil (created with data from ENGLAR, 1971) . . . . .	10
2.4	Lift increase due to blowing (created with data from ENGLAR, 1981) . . . . .	10
2.5	Maximum attained lift coefficient over free stream Mach number of an elliptical ( $t/c = 15\%$ ) circulation control aerofoil for different trailing edge shapes (created with data from ENGLAR, 1970) . . . . .	13
2.6	Lift coefficient over blowing coefficient of a circulation control aerofoil (CCW 244) for different slot heights (created with data from ENGLAR, 1975) . . . . .	13
2.7	Lift coefficient over blowing coefficient of an elliptical ( $t/c = 15\%$ ) circulation control aerofoil for different angles of attack (created with data from ENGLAR, 1971) . . . . .	16
2.8	Lift coefficient over outflow velocity ratio of an elliptical ( $t/c = 15\%$ ) circulation control aerofoil for different free stream Mach numbers (created with data from ENGLAR, 1970) . . . . .	16
2.9	Illustration of possible $C_{\mu}$ -stall phenomena: (a) leading edge separation, (b) jet wrap-around and (c) supersonic jet detachment (modified from CORNELIUS/LUCIUS (1994) and CARPENTER/SMITH (1997a)) . . . . .	17
2.10	Illustration of finite wing wind tunnel models (planforms reproduced from ROGERS/DONNELLY (2004) (a), HARLEY ET AL. (2009) (b) and FRITH/WOOD (2004) (c)) . . . . .	21
2.11	WVU Flight Demonstrator (a) and Grumman A-6A (b) as examples for flying circulation control demonstrators (LOTH, 2006) . . . . .	22
2.12	Flow fields (a,b) and pressure distributions (c,d) of successful (left) and failed (right) RANS simulations reproducing the wind tunnel test case from ENGLAR ET AL. (2009), $\alpha_{\infty} = 0deg$ , $\frac{U_{jet}}{U_{\infty}} = 6$ , $\frac{h_u}{c_{Coanda}} = 0.0022$ (simulated with the RANS method presented in section 3.4) . . . . .	27
3.1	Illustration of main subsystems of the fluidic flight control system . . . . .	31
3.2	Overview of the overall system modelling process . . . . .	33

3.3	Illustration of investigated Coandă flap concept (modified from STADLBERGER/HORNUNG, 2014, 2015a,b)	34
3.4	Illustration of subsystem model interactions	35
3.5	Illustration of a turbofan engine with bypass bleed concept	36
3.6	Illustration of duct model with discrete control volumes	39
3.7	Relative deviation of inviscid results from isentropic flow equations	43
3.8	Relative variation of results as function of discretisation	43
3.9	Illustration of the calculation procedure during a calculation campaign	49
3.10	Lift coefficient history of an exemplary calculation with increasing jet outflow velocity ratios $U_{jet}/U_{\infty}$	52
3.11	Flow field of “erroneous” calculations with leading edge separation (a) and jet wrap-around (b), $\alpha = 10deg$ , $\frac{r}{c_{base}} = 0.035$ , $\frac{U_{jet}}{U_{\infty}} = 5$ , $\frac{h_l}{c_{base}} = 0$	52
3.12	Circulation control aerofoil geometry of validation test case and used grid topology (STADLBERGER/HORNUNG, 2014)	55
3.13	Lift coefficient increment (a) and wall jet separation angle (b) with original turbulence model versions (BSL, SST) for different mesh sizes, $h_u = 0.5mm$ , $\alpha = 0deg$	56
3.14	Velocity (a), eddy viscosity (b) and blending function (c) of the wall jet with original turbulence model (BSL, SST), medium mesh size, $\frac{U_{jet}}{U_{\infty}} = 3$ , $C_{\mu} = 0.057$ , $h_u = 0.5mm$ , $\alpha = 0deg$	57
3.15	Lift coefficient increment (a) and wall jet separation angle (b) with turbulence model modifications activated individually and in combination for the medium mesh size, $h_u = 0.5mm$ , $\alpha = 0deg$ (modified from STADLBERGER/HORNUNG, 2015b)	58
3.16	Baseline blending function $F_1$ (a), corrective function $F_D$ (b) and corrected blending function $F_{1,corrected}$ (c) in the upper slot region of the blown trailing edge	58
3.17	Velocity (a), eddy viscosity (b) and blending function (c) of the wall jet with activated WJC, medium mesh size, $\frac{U_{jet}}{U_{\infty}} = 5$ , $C_{\mu} = 0.158$ , $h_u = 0.5mm$ , $\alpha = 0deg$ (modified from STADLBERGER/HORNUNG, 2015b)	59
3.18	Velocity (a), eddy viscosity (b) and SST modification function (c) of the wall jet with modified SST formulation for the medium mesh size, $\frac{U_{jet}}{U_{\infty}} = 2$ , $C_{\mu} = 0.025$ , $h_u = 0.5mm$ , $\alpha = 0deg$ (modified from STADLBERGER/HORNUNG, 2015b)	60
3.19	Lift generation of the Englar/Jones test case (ENGLAR ET AL., 2009) due to blowing for different slot heights, calculated with the medium mesh size for the author’s RANS method, $\alpha = 0deg$ (modified from STADLBERGER/HORNUNG (2015b) with data from BERNHARDT (2015))	61
3.20	Lift coefficient increment (a) and wall jet separation angle (b) with turbulence model modifications WJC and SSTMod for different mesh sizes, $h_u = 0.5mm$ , $\alpha = 0deg$	61
3.21	Illustration of a vortex lattice for a low aspect ratio wing (STADLBERGER/HORNUNG, 2015a)	63
3.22	Illustration of one horseshoe vortex (STADLBERGER/HORNUNG, 2015a)	63
3.23	Panel modification method I) from MUKHERJEE/GOPALARATHNAM (2006) and present method II) (modified from STADLBERGER/HORNUNG, 2015a)	63

3.24	Flow chart of the cambering method calculation process (STADLBERGER/HORNUNG, 2015a) . . . . .	66
3.25	Comparison of lift (a) and pitching moment (b) coefficient for the different 2D panel modification methods, $\alpha_\infty = 0deg$ , $\frac{x_{hinge} \delta_2}{c} = 0.8$ (modified from STADLBERGER/HORNUNG, 2015a) . . . . .	67
3.26	Planforms and specifications of conventional flap validation test cases RML51A26 (HAWES/MAY JR, RALPH W, 1951) and SAGITTA (HÖVELMANN ET AL., 2014) (modified from STADLBERGER/HORNUNG, 2015a) . . . . .	71
3.27	Relative change in aerodynamic reactions as a function of spanwise panel number	72
3.28	Relative change in aerodynamic reactions as a function of the relative hinge line position of $\delta_2$ , $N_x = 10$ , $N_y = 30$ . . . . .	72
3.29	Comparison of numerical results with experimental data for conventional flaps, $\alpha_\infty = 0deg$ , $\beta_\infty = 0deg$ (modified from STADLBERGER/HORNUNG, 2015a) . . . . .	73
3.30	Main blocks and signal flows inside the SIMULINK model . . . . .	74
4.1	Illustration of the SAGITTA design mission . . . . .	78
4.2	3-view of the SAGITTA configuration . . . . .	79
4.3	Illustration of the conventional reference flap scheme (top) and Coanda flap flight control concept (bottom) (modified from STADLBERGER/HORNUNG, 2014, 2015a) . . . . .	82
4.4	SAGITTA wind tunnel model with conventional plain flaps and two different types of tip split flaps (left: abandoned concept, right: investigated vortex flap concept) . . . . .	82
5.1	Bypass pressure ratio (a), specific thrust (b) and isentropic efficiencies (c, d) as a function of bypass bleed at standard conditions ( $H = 0m$ , $Ma = 0$ ) . . . . .	84
5.2	High pressure compressor (a) and turbine (b) map with operating lines for different bleed fractions at standard conditions ( $H = 0m$ , $Ma = 0$ ) . . . . .	86
5.3	Low pressure compressor (a) and turbine (b) map with operating lines for different bleed fractions at standard conditions ( $H = 0m$ , $Ma = 0$ ) . . . . .	87
5.4	Relative HP spool speed (a) and bypass pressure ratio (b) as a function of bypass bleed fraction . . . . .	88
5.5	Illustration of studied duct system . . . . .	88
5.6	Flow parameters along duct at ISA0m . . . . .	90
5.7	Relative pressure ratio (a) and relative momentum flux (b) at slot exit w.r.t. duct entrance values for different slot outlet areas . . . . .	91
5.8	Relative pressure ratio (a) and relative momentum flux (b) at slot exit w.r.t. duct entrance values for different diameter sizes of the nominal duct pipe, $D_{ref} = 0.185m$ . . . . .	92
5.9	Geometry of the studied NACA 64A012 circulation control aerofoil and used grid topology (STADLBERGER/HORNUNG, 2015b) . . . . .	93
5.10	Illustration of control volume used for the calculation of aerodynamic forces and moments . . . . .	94
5.11	Lift (a) and pitching moment (b) due to blowing through upper slot over jet velocity ratio ( $\eta_h = 1$ ) (modified from STADLBERGER/HORNUNG, 2015b) . . . . .	94
5.12	Lift due to blowing through upper slot for different slot heights and Coandă radii (a) and momentum flux coefficient (b) ( $\eta_h = 1$ ) (modified from STADLBERGER/HORNUNG, 2015b) . . . . .	95

5.13	Lift (a) and drag (b) due to double-slot-blowing for different Coandă radii (modified from STADLBERGER/HORNUNG, 2015a,b) . . . . .	96
5.14	Lift increase due to control parameter $\eta_h$ for different total slot heights and Coandă radii (modified from STADLBERGER/HORNUNG, 2015b) . . . . .	97
5.15	Flow field and $c_p$ on the trailing edge under double-slot-blowing conditions, $\frac{r}{c_{base}} = 0.02$ , $\frac{U_{jet}}{U_\infty} = 2$ , $\eta_h = 0.6$ (modified from STADLBERGER/HORNUNG, 2015b) . . . . .	97
5.16	Dependency of lift generation on angle of attack (modified from STADLBERGER/HORNUNG, 2015b) . . . . .	98
5.17	Dependency of lift of Coandă flap effectiveness on angle of attack (modified from STADLBERGER/HORNUNG, 2015b) . . . . .	98
5.18	Dependency of lift augmentation on slot height and blowing conditions ( $\eta_h = 1$ ) (modified from STADLBERGER/HORNUNG, 2015b) . . . . .	99
5.19	Ratio of Coandă flap effectiveness and momentum coefficient for different slot heights and Coandă radii (modified from STADLBERGER/HORNUNG, 2015b) . . . . .	99
5.20	Lift (a) and drag (b) polar under different symmetric blowing conditions ( $\eta_h = 0$ ) (modified from STADLBERGER/HORNUNG, 2015b) . . . . .	100
5.21	Aerodynamic reactions of the SAGITTA wing due to Coandă flap actuation, $\alpha_\infty = 0deg$ , $\beta_\infty = 0deg$ , $\frac{h_{total}}{c} = 0.001$ , $\frac{r}{c} = 0.02$ (modified from STADLBERGER/HORNUNG, 2015a) . . . . .	101
5.22	Pitch-to-drag ratio (a) and pitch-to-lift ratio (b) of the Coandă flap, $\alpha_\infty = 0deg$ , $\beta_\infty = 0deg$ , $\frac{h_{total}}{c} = 0.001$ , $\frac{r}{c} = 0.02$ (modified from STADLBERGER/HORNUNG, 2015a) . . . . .	102
5.23	Vortex lattice modification angles over span (a) and span distribution of lift and drag fraction (b), $\frac{U_{jet}}{U_\infty} = 3$ , $\alpha_\infty = 0deg$ , $\beta_\infty = 0deg$ , $\frac{h_{total}}{c} = 0.001$ , $\frac{r}{c} = 0.02$ (modified from STADLBERGER/HORNUNG, 2015a) . . . . .	103
5.24	Pitch authority of the Coandă flap system at midboard position . . . . .	105
5.25	Sustained load factor during coordinated turn through Coandă flap trim . . . . .	106
5.26	Maximum attained load factor during pull-up manoeuvre out of trimmed horizontal flight . . . . .	106
5.27	Roll authority of the Coandă flap system at midboard position . . . . .	107
5.28	Time to pass a bank angle of $\Phi = 45deg$ with trimmed throttle (a) and full throttle (b) during roll manoeuvre . . . . .	108
5.29	Yaw authority of Coandă flap system . . . . .	108
5.30	Envelopes of optimised Coandă system parameters during horizontal flight solely trimmed by the midboard Coandă flaps . . . . .	110
5.31	Dependency of optimum slot outlet area on altitude and engine thrust setting . . . . .	111
5.32	Aircraft system performance during horizontal flight solely trimmed by the midboard Coandă flaps . . . . .	112
5.33	Envelopes of optimised Coandă system parameters during horizontal flight with trim support through midboard Coandă flaps . . . . .	114
5.34	Aircraft system performance during horizontal flight with trim support through midboard Coandă flaps . . . . .	115
A.1	Vertical (a) and horizontal (b) velocity at the centre lines of the lid-driven cavity flow problem ( $Re = 1000$ ) in comparison with data from GHIA ET AL. (1982) . . . . .	155

A.2	Turbulent boundary layer on a flat plate for different running lengths ( $Re_x = \frac{U_\infty x}{\nu_\infty}$ ) . . . . .	156
A.3	Lift curve of unblown (cambered) elliptical circulation control aerofoil from ALEXANDER ET AL. (2005) . . . . .	157
A.4	Lift curve of unblown semi-elliptical circulation control aerofoil from ENGLAR ET AL. (2009) . . . . .	157



# List of Tables

2.1	Summary of qualitative circulation control sensitivities . . . . .	12
3.1	Empirical correction factor $k_\phi$ . . . . .	42
3.2	Turbulence model coefficients of Menter’s BSL model . . . . .	45
3.3	Law of under-relaxation for PDE solution . . . . .	48
3.4	Proposed threshold values for convergence detection . . . . .	52
3.5	Mesh sizes of mesh refinement study . . . . .	55
3.6	Main specifications of the SAGITTA wind tunnel model and test conditions	74
4.1	Requirements imposed on the SAGITTA configuration . . . . .	78
4.2	Main specifications of the SAGITTA configuration . . . . .	79
4.3	Specifications of generic engine . . . . .	81
5.1	Measured flap deflection angles during wind tunnel experiments . . . . .	104
A.1	Modelled double-slotted circulation control aerofoils . . . . .	156



# Appendix



# A Bibliography: Conducted Experiments on Coandă Aerofoils

Reference	Aerofoil shape	Trailing edge shape	Thickness [%]	Camber [%]	Radius ratio(s) $\frac{h}{c}$ [-]	Slot height ratio(s) $\frac{h}{c}$ [-]	Reynolds number [-]
WILLIAMS/HOWE, 1970	ellipse	circular	20.5	5	0.0525	0.0244	560,000; 890,000
ENGLAR, 1970	ENGLAR, 1971	elliptical, circular	15	0	>0.0122; 0.0403	0.016; 0.032; 0.081; 0.161	550,000; up to 2.500,000
ENGLAR, 1972	ellipse	circular	30	1.5	0.0601	0.014; 0.028; 0.056	570,000
ENGLAR, 1975	ellipse	circular	20	0	0.0910	0.013; 0.025; 0.032; 0.050; 0.100;	840,000
ABRAMSON, 1975	ellipse	circular	20	0	0.0392	0.032	240,000 to 420,000
ABRAMSON, 1977	ellipse	elliptical, spiral	15	1	various	various	375,000 to 520,000
ENGLAR, 1981	supercritical	circular	17	2	0.0094; 0.0188; 0.0367	0.008; 0.016; 0.032; 0.064; 0.128	1,200,000
WOOD/CONLON, 1983	ellipse	circular	20	3	0.038	0.044	up to 3,200,000
NOVAK ET AL., 1987	ellipse	circular	16	~0	0.067	0.030; 0.056; 0.100	1,000,000
ABRAMSON, 2004	ellipse	circular	17	1	0.0417	0.031; 0.048	1,400,000
JONES, 2005	supercritical	circular, elliptical, biconvex	17	4	0.020; >0.010; 0	various	650,000
ALEXANDER ET AL., 2005	ellipse	elliptical (3x)	6	0.75	>0.005; >0.007; >0.009	<0.140; <0.480	1,000,000
WONG ET AL., 2006	supercritical	circular	17	n/a	0.068	0.053	300,000
ENGLAR ET AL., 2009	ellipse	circular	20	0	0.095	0.011; 0.016; 0.022; 0.032; 0.053	500,000
WETZEL ET AL., 2009	ellipse	circular	20	0	0.0426	0.022; 0.045; 0.068	650,000
CHEN ET AL., 2012	ellipse	circular	30	0	0.2265	0.006; 0.012; 0.018	500,000



## B Bibliography: Tested Turbulence Models

Turbulence model	Number of equations	Model reference(s)	Application reference(s)
Spalart-Almaras (SA)	1	SPALART/ALLMARAS, 1992	SWANSON ET AL. (2005), version 1992 with Spalart-Shur-Correction ZACHAROS/KONTIS (2006), version 1992 BAKER/PATERSON (2006), version 1992 SWANSON ET AL. (2006), version 1992 standard and with Spalart-Shur-Correction MIN ET AL. (2009), version 1992 RUMSEY/NISHINO (2011), version 1992
Lauder $k-\epsilon$ ( $k-\epsilon$ )	2	LAUNDER/SPALDING, 1972 SHIH ET AL., 1994	SLOMSKI ET AL. (2002), version 1972 and version 1994 ZACHAROS/KONTIS (2006), version 1972 and version 1994
Wilcox $k-\omega$ ( $k-\omega$ )	2	WILCOX, 1998 WILCOX, 2007	FASEL ET AL. (2006), version 1988 FORSTER/STEJL (2015), version 1988 and version 2006
Menter Shear Stress Transport (SST)	2	MENTER, 1994	ZACHAROS/KONTIS (2006), version 1994 FASEL ET AL. (2006), version 1994 BAKER/PATERSON (2006), version 1994 SWANSON ET AL. (2006), version 1994 CHANG ET AL. (2006), version 1994 MIN ET AL. (2009), version 1994 RUMSEY/NISHINO (2011), version 1994 standard and with Hellsten-Correction FORSTER/STEJL (2015), version 1994
$k$ -enstrophy ( $k-\zeta$ )	2	ROBINSON, D. F./HASSAN, H. A., 1998	SWANSON ET AL. (2005), version 1998
EASM- $k-\omega$	2	RUMSEY/GATSKI, 2001	FASEL ET AL. (2006), version 2001 SWANSON ET AL. (2006), version 2001 RUMSEY/NISHINO (2011), version 2001
Full Reynolds Stress Model (RSM)	5 (2D)	LAUNDER ET AL., 1975	SLOMSKI ET AL. (2002), version 1975 ZACHAROS/KONTIS (2006), version 1975 CHANG ET AL. (2006), version 1975
Curvature Correction Method		Reference	Application reference(s)
Spalart-Shur-Correction		SHUR ET AL., 1998	SWANSON ET AL. (2005) SWANSON ET AL. (2006)
Hellsten		HELLSTEN, 1998	RUMSEY/NISHINO (2011)



## C Isentropic Flow Equations

For isentropic (frictionless, adiabatic) air flow, assuming a caloric ideal gas ( $\kappa = 1.4$ ), the static temperature  $T$ , static pressure  $p$  and static density  $\rho$  are given as follows

$$T = T_t \left( 1 + \frac{\kappa - 1}{2} Ma^2 \right)^{-1}$$

$$p = p_t \left( 1 + \frac{\kappa - 1}{2} Ma^2 \right)^{\frac{-\kappa}{\kappa - 1}}$$

$$\rho = \rho_t \left( 1 + \frac{\kappa - 1}{2} Ma^2 \right)^{\frac{-1}{\kappa - 1}}$$

where  $T_t$ ,  $p_t$  and  $\rho_t$  constitute the respective gas properties in total conditions and

$$Ma = \frac{u}{a}$$

$$a = \sqrt{\kappa RT}$$



## D Validation of 2D RANS Code

For RANS code validation, the subsequent sections contain the data of three test cases.

### D.1 Lid-Driven Cavity Flow

The classical lid-driven cavity problem is a widely-used steady incompressible test case for CFD code validation and performance assessment. The solution of the present code obtained with a non-uniform grid size of  $128 \times 128$  at  $Re = 1000$  is compared with data from literature (GHIA ET AL., 1982). As shown in Figure A.1, the results agree essentially well for both vertical (a) and horizontal (b) velocities at the respective centre lines of the square cavity.

### D.2 Turbulent Boundary Layer on a Flat Plate

To validate the used turbulence model (Menter's  $k-\omega/k-\varepsilon$  SST), the turbulent velocity profiles (Figure A.2a) on a flat plate are transformed to dimensionless values yielding  $u^+ = \frac{u}{u_\tau}$  where the dimensionless velocity  $u^+$  is calculated by use of the friction velocity  $u_\tau$ . The latter is given by  $u_\tau = \sqrt{\frac{\tau_w}{\rho_\infty}}$  depending on the wall shear stress  $\tau_w$  and the fluid density  $\rho_\infty$ . Finally, the dimensionless distance to the wall yields  $y^+ = \frac{yu_\tau}{\nu_\infty}$ . Compared with Spalding's law of the wall (SPALDING, 1961), the numerical solution of the boundary layer shows reasonable agreement as can be seen in Figure A.2b.

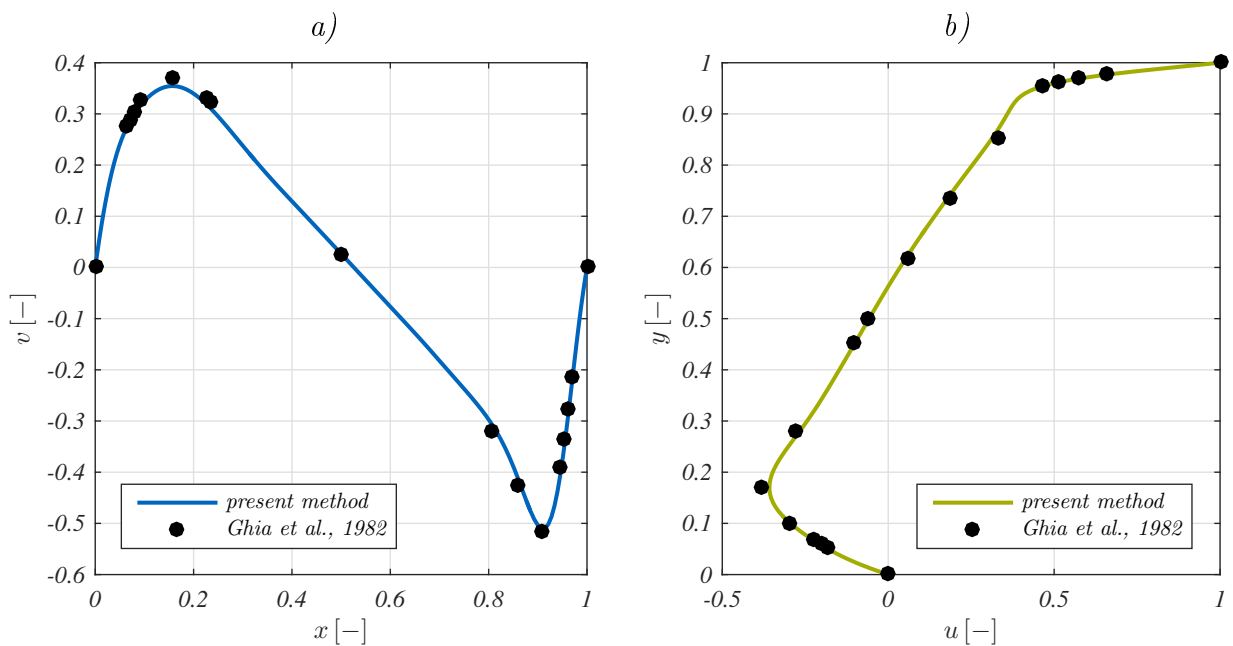


**Figure A.1:** Vertical (a) and horizontal (b) velocity at the centre lines of the lid-driven cavity flow problem ( $Re = 1000$ ) in comparison with data from GHIA ET AL. (1982)

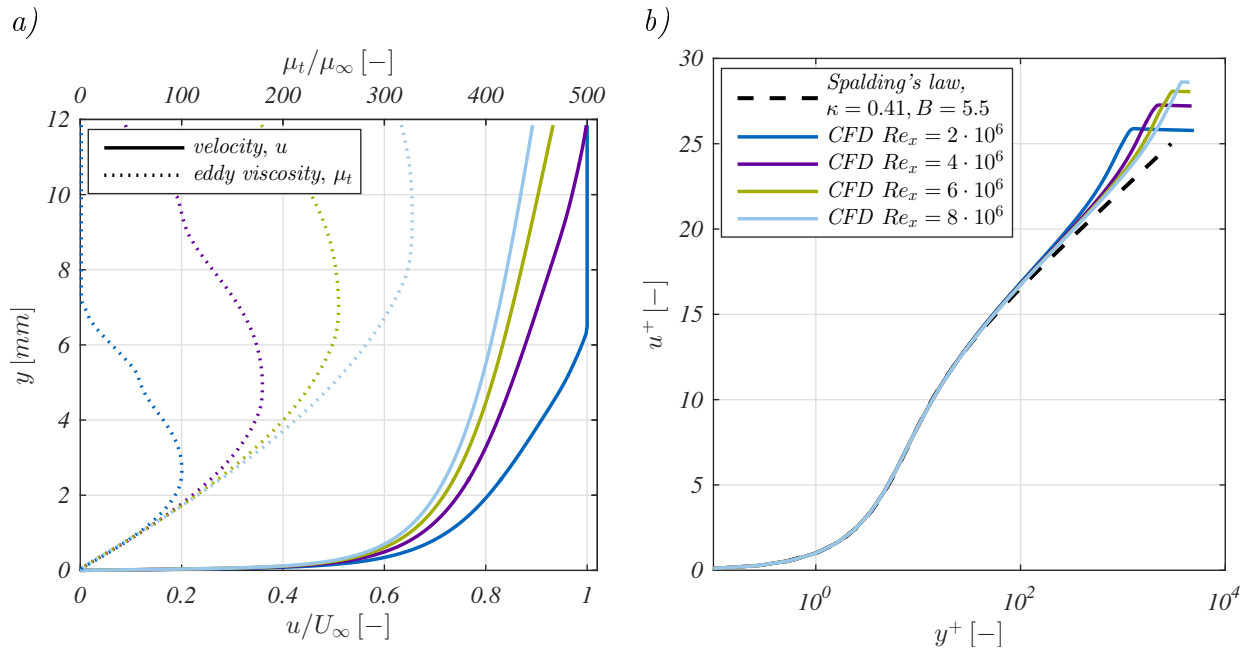


**Figure A.2:** Turbulent boundary layer on a flat plate for different running lengths ( $Re_x = \frac{U_\infty x}{\nu_\infty}$ )

**Table A.1:** Modelled double-slotted circulation control aerofoils

	ENGLAR ET AL. (2009)	ALEXANDER ET AL. (2005)
$t/c_{Coanda}$	20%	6%
$camber$	0%	0.75%
$r/c_{Coanda}$	0.095	$\sim 0.025$
$c_{Coanda} [m]$	0.22	0.71
$Re$	$\sim 500,000$	$\sim 1,000,000$
$h_{slot} [mm]$	0.23, 0.33, 0.46, 0.66, 1.09	0.53, 0.89, 1.42, 1.85



### D.3 Unblown Coandă Aerofoil

An unblown Coandă aerofoil under angle of attack serves as test case for the code validation on a convection-diffusion flow problem with non-orthogonal grid. Two wind tunnel experiments have been reproduced whose specifications are listed in Table A.1. For the first test case, Figure A.3 shows the reference curve for  $Re = 1 \times 10^6$  and the corresponding results from RANS calculations for a 6%-thick cambered elliptical aerofoil tested by ALEXANDER ET AL. (2005). While the average lift curve slopes agree essentially well, the experimental results exhibit significant deviations from linearity even at low angles of attack. Similar observations were also made by KWON/PARK (2005). Their wind tunnel experiments revealed

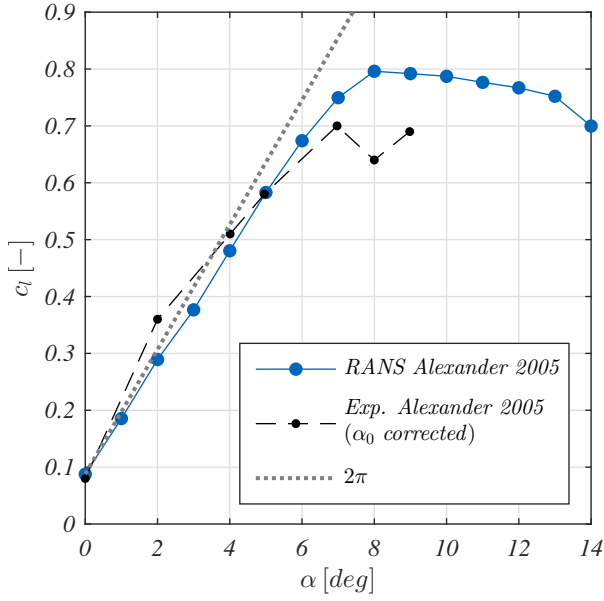


**Figure A.3:** Lift curve of unblown (cambered) elliptical circulation control aerofoil from ALEXANDER ET AL. (2005)

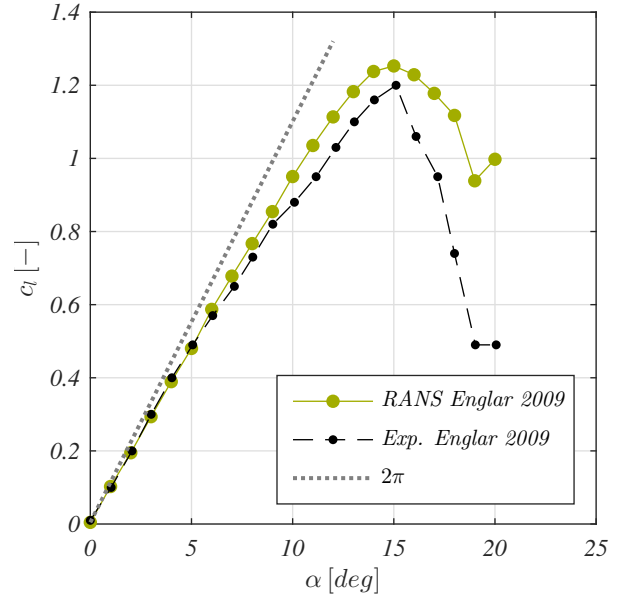


**Figure A.4:** Lift curve of unblown semi-elliptical circulation control aerofoil from ENGLAR ET AL. (2009)

that the Reynolds number has a significant effect on the lift curve slope of elliptical aerofoil sections. At higher subsonic Reynolds numbers ( $2 \times 10^6$ ), the lift curve slope falls below that of a conventional aerofoil. This might be expected due to separations at the trailing edge and the resulting thick wake layer. However, at low Reynolds numbers of about  $3 \times 10^5$  the lift curve slopes at low angles of attack can be much higher than  $\frac{\partial c_l}{\partial \alpha} > 2\pi$ . This is a consequence of early laminar separation from the lower side of the trailing edge combined with attached flow around nose and trailing edge suction side. In the case of a double-slotted aerofoil, the separation point is assumed to be defined by the contour steps formed by the slot lips. In addition, these laminar effects disappear when early transition is provoked by boundary layer trips as put into practice by ALEXANDER ET AL. (2005). Assuming that laminar flow effects are the explanation for the particular lift curve shape, the fully turbulent RANS simulation would be scarcely capable to reproduce these effects. However, even though the maximum lift was overestimated, the stall incidence could be reproduced quite accurately. Note that the original experimental curve was corrected by a zero lift angle of attack  $\alpha_0 \approx -1deg$  as would be approximately predicted by common methods from literature (HOERNER/BORST, 1985).

Better concordance of numerical and experimental results could be obtained with the test case from ENGLAR ET AL. (2009). As can be seen in Figure A.4, the RANS data agrees well in the region of low angles of attack while the numerical model overestimates produced lift at higher angles of attack. Despite the boundary layer trip, viscous flow separation

effects seem to weaken the real lift curve slope early before stall. If these effects are due to local laminar flow, is unknown. Again, maximum lift has been slightly overestimated while the stall incidence could be reproduced accurately even though the lift drop is significantly smoother for the numerical results.